



**HAL**  
open science

## Traitement d'antenne tensoriel

Francesca Raimondi

► **To cite this version:**

Francesca Raimondi. Traitement d'antenne tensoriel. Traitement du signal et de l'image [eess.SP]. Université Grenoble Alpes, 2017. Français. NNT : 2017GREAT043 . tel-01691607v2

**HAL Id: tel-01691607**

**<https://theses.hal.science/tel-01691607v2>**

Submitted on 22 Jan 2018

**HAL** is a multi-disciplinary open access archive for the deposit and dissemination of scientific research documents, whether they are published or not. The documents may come from teaching and research institutions in France or abroad, or from public or private research centers.

L'archive ouverte pluridisciplinaire **HAL**, est destinée au dépôt et à la diffusion de documents scientifiques de niveau recherche, publiés ou non, émanant des établissements d'enseignement et de recherche français ou étrangers, des laboratoires publics ou privés.

## **THÈSE**

Pour obtenir le grade de

## **DOCTEUR DE LA COMMUNAUTÉ UNIVERSITÉ GRENOBLE ALPES**

Spécialité : SIGNAL IMAGE PAROLE TELECOMS

Arrêté ministériel : 25 mai 2016

Présentée par

**Francesca Elisa Diletta RAIMONDI**

Thèse dirigée par **Pierre COMON**, CNRS

préparée au sein du

**Laboratoire Grenoble Images Parole Signal Automatique**

dans l'École Doctorale Électronique, Électrotechnique,  
**Automatique, Traitement du Signal (EEATS)**

# **Traitement d'antenne tensoriel**

Thèse soutenue publiquement le 22 septembre 2017,  
devant le jury composé de:

**M. Olivier J. Michel**

Professeur des universités, GIPSA-lab,  
Président du jury

**M. Pascal Chevalier**

Professeur du CNAM, Chaire d'Électronique  
(Conservatoire National des Arts et Métiers), Rapporteur

**M. Martin Haardt**

Professeur des universités, Ilmenau University of Technology,  
Rapporteur

**M. David Brie**

Professeur des universités, CRAN  
(Centre de Recherche en Automatique de Nancy), Examineur

**M. Pierre COMON**

Directeur de recherche, GIPSA-lab, CNRS,  
Directeur de thèse





# Tensor Array Processing

Francesca Elisa Diletta RAIMONDI

A thesis submitted for the degree of

Doctor of Philosophy  
in SIGNAL PROCESSING

Supervised by Pierre Comon

GRENOBLE ALPS UNIVERSITY  
GIPSA-lab, CNRS

September 22, 2017

## Thesis Committee:

<i>Chair :</i>	Olivier J. MICHEL	-	GIPSA-lab
<i>Reviewers :</i>	Pascal CHEVALIER	-	CNAM
	Martin HAARDT	-	Ilmenau University of Technology
<i>Examiner :</i>	David BRIE	-	CRAN
<i>Thesis advisor :</i>	Pierre COMON	-	GIPSA-lab



# Acknowledgments

A PhD is the outcome of several contributions (beside the endeavour and the efforts of the bewildered student), and I like to interpret it as a Bildungsroman. I am now three years older, hopefully wiser, and a grown up researcher.

First, a PhD work, as solitary as it may seem, is founded on a learning process alongside a guide who introduces the student into the world of scientific discovery. This guide, the supervisor, is then a mentor into a new world, science, with its own language, its own codes, its own culture. I can say that I owe that to a wonderful researcher, Pierre Comon: he taught me how to tell a good quality article from a bad one, how to communicate my ideas in a precise and synthetic fashion, and how to understand the requirements of the scientific community. I learned from him that every result should be justified and easily reproducible by other researchers. Whenever I needed his advice, he was there to provide me with a very thoughtful answer.

I thank all the invited members of my thesis committee: Martin Haardt who really helped me improving the quality of my work through his meticulous reading of this manuscript; Pascal Chevalier for his attentive reading and inspiring suggestions; David Brie and Olivier Michel for their interesting interpretation of my work.

A PhD work also benefits from the exchanges with the natural environment where it is conducted: and for me this was GIPSA-lab in Grenoble, in the department of signal and image processing (DIS). Several were the colleagues with whom I exchanged ideas during these three years. I am thankful for the interesting talks I had the pleasures to have with Olivier Michel, whose insight and intuition are of rare and great value. I also really appreciated being part of a greater project, the ERC DECODA: this allowed me to have very meaningful conversations, in particular with Rodrigo Cabral Farias, who is also a very good friend, Konstantin Usevich, Chengfang Ren, and Souleyman Sahnoun. I also thank my MSc mentor, Umberto Spagnolini, with whom I collaborated for the last chapter of this thesis. I learned a lot from him during the last few years, via his intuitions and pragmatism. I also thank Barbara Nicolas, who was my supervisor during my MSc project.

It was also very helpful to be part of the CICS team with weekly meetings and presentations around “complex systems”. I enjoyed then the very positive and interactive atmosphere thanks to my fellow colleagues, with whom it was a pleasure to share this experience. In particular, I want to thank Emmanuelle, for the beautiful friendship that we have, and our sacred gossip time together; my officemates Irina, Saloua and Karina, for their affection: they had to deal daily with the stressed version of me in the end, thank you for understanding my introversion in the cutest possible way; sweet Dana for our talkative daily strolls around the building; the GIPSA-doc team for their cheerful presence and debates: Marc, Alexandre, Quyen, Louis, Florent, Raphaël, Marion, Pierre N., Pierre M., Yasmin, Wei, Zhongyang and Guanghan, and all the others; Lucia for her helpful kindness;

I want to thank all my friends in Grenoble and scattered in every corner of the world that have enriched my life so far and in particular in the last few years. A warm thankful

thought to Perrine for our silliness together, and lots of laughs; to Angélique and Raphaël for our hikes and talks; Letizia for our intellectual connection and Jungian interests; Nina for our lunches and her colourful personality; Raluca and Vincent for our discussions and friendship; Sophie for her kindness; Pauline and Henri for their congeniality; my virtual Italian sense8s Alberto, Elide, Roberto, Andrea, Mirko, Sabrina, and Xavier in particular; my “girls only” group with Tiphaine, Angélique, Olha, and Audrey; my ASP friends Alessandra, Cristina, Boris, Michele; Ilaria, Valeria R., Elisa, Daniel, Francesca, Valeria Miranda, Valeria D. M., Giada, Cecio, Viola, Valerio, Ilaria P. from Italy that I would like to see more often; Tommaso for his friendship and advice.

I want to thank my Karate senseis from my past, for their training in this magnificent martial art, and all their life teachings, as well as my training mates at the dojo of sensei Marchini. From the last two years, I want to thank my Iyengar Yoga teacher Juliette who introduced me to the endlessly profound world of yoga and pranayama, that changed my life forever. I could not find a more resourceful and gifted teacher.

I want to thank my family, and in particular my two wonderful as much as different sisters: Laura for being the best cheerleader and singing teacher ever and for laughing together at each other and at the world, and Valeria for our deep exchange about psychology and existence, nothing is ever prosaic with you two at my side; my mother for her support and anxious affection; my grandfather, who was a bright mathematician and who was so affectionate and who would be so proud of me; my father for his levity and Italian sense of humour; all my grandparents for their affection and their teachings; Valentina for her fondness; Alessandro for his relentless optimism and wittiness.

I want to thank above all Josselin for loving me, for being there for me, for being the best lover, life companion, yoga mate, hiking pal, intellectual partner, French teacher and French cook (especially when I was hungry and composing this manuscript) that I could wish for. You really supported me with endless empathy, infinite curiosity for the complex human being that I am, and always believed in me when I had ceased to.

Last, but not least, I want to thank our marvellous Russian Blue, Artù, for loving me in his feline way, purring me out of anguish, meowing out of love and hunger, attention seeking, and curling up on my lap even and especially when I was working at this thesis.

Namaste.

# Abstract

## English Abstract

Source estimation and localization are a central problem in array signal processing, and in particular in telecommunications, seismology, acoustics, biomedical engineering, and astronomy. Sensor arrays, i.e. acquisition systems composed of multiple sensors that receive source signals from different directions, sample the impinging wavefields in space and time. Hence, high resolution techniques such as MUSIC make use of these two elements of diversities: space and time, in order to estimate the signal subspace generated by impinging sources, as well as their directions of arrival. This is generally done through the estimation of second or higher orders statistics, such as the array spatial covariance matrix, thus requiring sufficiently large data samples. Only recently, tensor analysis has been applied to array processing using as a third mode (or diversity), the space shift translation of a reference subarray, with no need for the estimation of statistical quantities. Tensor decompositions consist in the analysis of multidimensional data cubes of at least three dimensions through their decomposition into a sum of simpler constituents, thanks to the multilinearity and low rank structure of the underlying model. Thus, tensor methods provide us with an estimate of source signatures, together with directions of arrival, in a deterministic way. This can be achieved by virtue of the separable and low rank model followed by narrowband sources in the far field. This thesis deals with source estimation and localization of multiple sources via these tensor methods for array processing. Chapter 1 presents the physical model of narrowband elastic sources in the far field, as well as the main definitions and assumptions. Chapter 2 reviews the state of the art on direction of arrival estimation, with a particular emphasis on high-resolution signal subspace methods. Chapter 3 introduces the tensor formalism, namely the definition of multi-way arrays of coordinates, the main operations and multilinear decompositions. Chapter 4 presents the subject of tensor array processing via rotational invariance. Chapter 5 introduces a general tensor model to deal with multiple physical diversities, such as space, time, space shift, polarization, and gain patterns of narrowband elastic waves. Subsequently, Chapter 6 and Chapter 8 establish a tensor model for wideband coherent array processing. We propose a separable coherent focusing operation through bilinear transform and through a spatial resampling, respectively, in order to ensure the multilinearity of the interpolated data. We show via computer simulations that the proposed estimation of signal parameters considerably improves, compared to existing narrowband tensor processing and wideband MUSIC. Throughout the chapters we also compare the performance of tensor estimation to the Cramér-Rao bounds of the multilinear model, which we derive in its general formulation in Chapter 7. Moreover, in Chapter 9 we propose a tensor model via the diversity of propagation speed for seismic waves and illustrate an application to real seismic data from an Alpine glacier. Finally, the last part of this thesis in Chapter 10 moves to the parallel subject of multidimensional spectral factorization of seismic ways, and illustrates an application to the estimation of the impulse response of the Sun for helioseismology.

**Keywords**

Tensor, Array, Wideband, Source Separation, Localization, Direction of Arrival, Seismic

**Resumé en Français**

L'estimation et la localisation de sources sont des problèmes centraux en traitement d'antenne, en particulier en télécommunication, sismologie, acoustique, ingénierie médicale ou astronomie. Une antenne de capteurs est un système d'acquisition composé par de multiples capteurs qui reçoivent des ondes en provenance de sources de directions différentes: elle échantillonne les champs incidents en espace et en temps. Pour cette raison, des techniques haute résolution comme MUSIC utilisent ces deux éléments de diversité, l'espace et le temps, afin d'estimer l'espace signal engendré par les sources incidentes, ainsi que leur direction d'arrivée. Ceci est généralement atteint par une estimation préalable de statistiques de deuxième ordre ou d'ordre supérieur, comme la covariance spatiale de l'antenne, qui nécessitent donc de temps d'observation suffisamment longs. Seulement récemment, l'analyse tensorielle a été appliquée au traitement d'antenne, grâce à l'introduction, comme troisième modalité (ou diversité), de la translation en espace d'une sous-antenne de référence, sans faire appel à l'estimation préalable de quantités statistiques. Les décompositions tensorielles consistent en l'analyse de cubes de données multidimensionnelles, au travers de leur décomposition en somme d'éléments constitutifs plus simples, grâce à la multilinéarité et à la structure de rang faible du modèle sous-jacent. Ainsi, les mêmes techniques tensorielles nous fournissent une estimée des signaux eux-mêmes, ainsi que de leur direction d'arrivée, de façon déterministe. Ceci peut se faire en vertu du modèle séparable et de rang faible vérifié par des sources en bande étroite et en champs lointain. Cette thèse étudie l'estimation et la localisation de sources par des méthodes tensorielles de traitement d'antenne. Le premier chapitre présente le modèle physique de source en bande étroite et en champs lointain, ainsi que les définitions et hypothèses fondamentales. Le deuxième chapitre passe en revue l'état de l'art sur l'estimation des directions d'arrivée, en mettant l'accent sur les méthodes haute résolution à sous-espace. Le troisième chapitre introduit la notation tensorielle, à savoir la définition des tableaux de coordonnées multidimensionnels, les opérations et décompositions principales. Le quatrième chapitre présente le sujet du traitement tensoriel d'antenne au moyen de l'invariance par translation. Le cinquième chapitre introduit un modèle tensoriel général pour traiter de multiples diversités à la fois, comme l'espace, le temps, la translation en espace, les profils de gain spatial et la polarisation des ondes élastiques en bande étroite. Par la suite, les sixième et huitième chapitres établissent un modèle tensoriel pour un traitement d'antenne bande large cohérent. Nous proposons une opération de focalisation cohérente et séparable par une transformée bilinéaire et par un ré-échantillonnage spatial, respectivement, afin d'assurer la multilinéarité des données interpolées. Nous montrons par des simulations numériques que l'estimation proposée des paramètres des signaux s'améliore considérablement, par rapport au traitement tensoriel classique en bande étroite, ainsi qu'à MUSIC cohérent bande large. Egalement, tout au long de la thèse, nous comparons les performances de l'estimation tensorielle avec la borne de Cramér-Rao du modèle multilinéaire associé, que nous développons, dans sa forme la plus générale, dans le septième chapitre. En outre, dans le neuvième chapitre nous illustrons une application à des données sismiques réelles issues d'une campagne de mesure sur un glacier alpin, grâce à la diversité de vitesse de propagation. Enfin, le dixième et dernier chapitre de cette thèse traite le sujet parallèle de la factorisation spectrale multidimensionnelle d'ondes sismiques, et présente une application à l'estimation de la réponse

impulsionnelle du soleil pour l'héliosismologie.

**Keywords**

Tenseur, Antenne, Bande Large, Séparation de Sources, Localization, Direction d'Arrivée, Sismique

**This work was supported by the ERC Grant AdG-2013-320594 "DECODA".**



# Contents

<b>Introduction</b>	<b>3</b>
I.1. Space-Time Processing . . . . .	3
I.2. Main Applications . . . . .	3
I.3. Classic Approaches in 2D . . . . .	4
I.4. Tensor Arrays . . . . .	5
I.5. Contribution and Outline . . . . .	7
<b>I. Tensor Decompositions for Source Localization: State of the Art</b>	<b>9</b>
<b>1. Sensor Arrays: Parametric Modeling for Wave Propagation</b>	<b>11</b>
1.1. Introduction . . . . .	11
1.2. Narrowband Wave Propagation for Array Processing . . . . .	12
1.2.1. Far Field Approximation of Narrowband Waves . . . . .	12
1.2.2. Parametric Modeling for Sensor Arrays: Directions of Arrival . . . . .	13
1.2.3. General Array Geometries . . . . .	15
1.2.4. Uniform Linear Arrays . . . . .	16
1.2.5. Uniform Rectangular Arrays . . . . .	17
1.2.6. Uniform Circular Arrays . . . . .	17
1.3. The Signal Subspace and the Spatial Covariance . . . . .	18
1.3.1. Assumptions and Fundamental Definitions . . . . .	18
1.3.2. Array Manifold and Signal Subspace . . . . .	19
1.4. Polarized Waves . . . . .	20
1.4.1. The 3C Sensor Response . . . . .	20
1.4.2. Vector Sensor Arrays . . . . .	22
1.4.3. Another Polarization Model . . . . .	24
1.5. Wideband Sources . . . . .	24
1.5.1. Wideband Scalar Wavefields . . . . .	24
1.5.2. Polarized wideband sources . . . . .	25
1.6. Seismic Waves . . . . .	26
1.7. Parameters of Interest . . . . .	28
1.8. The Sample Covariance Matrix . . . . .	29
<b>Appendices</b>	<b>30</b>
1.A. Signal Complex Envelope . . . . .	30
<b>2. Signal Parameter Estimation in 2D</b>	<b>31</b>
2.1. Introduction . . . . .	31
2.2. Performance of an Estimator . . . . .	31
2.3. Spectral and Parametric Approaches . . . . .	33

2.4.	Beamforming . . . . .	33
2.5.	Spectral MUSIC . . . . .	35
2.5.1.	Evaluation of spectral MUSIC . . . . .	36
2.6.	ESPRIT . . . . .	37
2.6.1.	Signal Copy . . . . .	40
2.6.2.	Evaluation of ESPRIT . . . . .	40
2.7.	Signal Subspace for Polarized Sources . . . . .	41
2.8.	Signal Subspace for Wideband Sources . . . . .	41
2.8.1.	Virtual arrays . . . . .	42
2.8.2.	Linear Interpolation . . . . .	43
2.8.3.	Interpolation through Spatial Resampling . . . . .	44
2.8.4.	Wideband Polarized Waves . . . . .	45
2.9.	Dealing with Correlation . . . . .	45
2.9.1.	Correlated Noise . . . . .	45
2.9.2.	Correlated Sources . . . . .	46
<b>3.</b>	<b>Multi-Way Arrays and Tensors</b>	<b>49</b>
3.1.	Introduction . . . . .	49
3.2.	Tensor Arrays: Notations and Operations . . . . .	49
3.2.1.	From Multilinear Operators to Multi-Way Arrays . . . . .	49
3.2.2.	Notations and Terminology . . . . .	50
3.2.3.	Multi-Way Operations . . . . .	53
3.3.	Tensor Decompositions . . . . .	54
3.3.1.	Decomposable Tensors and Tensor Rank . . . . .	54
3.3.2.	Tucker Decomposition and Multilinear Rank . . . . .	55
3.3.3.	Canonical-Polyadic Decomposition (CPD) and Tensor Rank . . . . .	56
3.3.4.	CPD Factors, Normalization and Scaling . . . . .	58
3.3.5.	Uniqueness of the CPD . . . . .	59
3.3.6.	Advantages of the Tensor Formalism when $D \geq 3$ . . . . .	61
3.4.	Multilinear Normal Distributions . . . . .	61
3.5.	Algorithms for Exact Decompositions . . . . .	63
3.5.1.	Computation of the CPD through Joint Diagonalization . . . . .	63
3.6.	Tensor Approximation . . . . .	64
3.6.1.	An Approximation Problem in Additive Noise . . . . .	64
3.6.2.	Existence and Degeneracies . . . . .	65
3.6.3.	Algorithms for Tensor Approximation . . . . .	66
3.7.	Physical Diversity and Coherence . . . . .	67
<b>4.</b>	<b>Tensor Array Processing with Multiple Rotational Invariances</b>	<b>71</b>
4.1.	Introduction . . . . .	71
4.2.	Multidimensional Subspace Methods . . . . .	71
4.3.	CPD through Multiple Invariances . . . . .	72
4.3.1.	CPD Factors, Normalization and Scaling . . . . .	73
4.4.	Identifiability of the CPD Model . . . . .	74
4.4.1.	Incoherent Sources Scenario . . . . .	75
4.4.2.	Coherent Source Scenario . . . . .	76
4.5.	Physical Meaning of Coherences . . . . .	77
4.6.	DoA Estimation . . . . .	78
4.6.1.	General 3D DoA Estimation . . . . .	79

4.6.2.	2D DoA Estimation . . . . .	79
4.6.3.	1D DoA Estimation for ULAs . . . . .	80
4.7.	Source Signature Extraction . . . . .	81
4.8.	Advantages of Tensor Decomposition for Sensor Arrays . . . . .	81

## **II. Contribution: Wideband Multiple Diversity Tensor Array Processing** **83**

### **5. Multiple Diversity Array Processing** **85**

5.1.	Contribution . . . . .	85
5.2.	Physical Diversities . . . . .	85
5.3.	Tensor Decomposition of Polarized Waves . . . . .	88
5.3.1.	The Long Vector MUSIC . . . . .	88
5.3.2.	Tensor MUSIC . . . . .	89
5.3.3.	Tensor CPD for Vector Sensor Arrays . . . . .	90
5.3.4.	CPD Factors, Normalization and Scaling . . . . .	91
5.3.5.	Coherent Sources . . . . .	92
5.3.6.	Physical Meaning of Coherences . . . . .	92
5.3.7.	Estimation of Source, DoAs and Polarization Angles . . . . .	92
5.3.8.	Computer Results . . . . .	93
5.4.	Directivity Gain Pattern Diversity . . . . .	96
5.4.1.	CPD Factors, Normalization and Scaling . . . . .	96
5.4.2.	Diversity of Space Shift and Gain Pattern . . . . .	97
5.4.3.	Physical Meaning of Coherences . . . . .	98
5.4.4.	Estimation of Sources and DoA . . . . .	98
5.4.5.	Computer Results . . . . .	99

### **6. Wideband Tensor DoA Estimation** **103**

6.1.	Contribution . . . . .	103
6.2.	Tensor Model for Wideband Waves . . . . .	104
6.2.1.	Space Shift and Gain Pattern Diversity in Wideband . . . . .	104
6.2.2.	Polarization Diversity in Wideband . . . . .	105
6.2.3.	Multiple Diversity in Wideband . . . . .	106
6.3.	Tensor Wideband Processing . . . . .	106
6.3.1.	Virtual Subarrays . . . . .	107
6.3.2.	Bilinear Transform . . . . .	107
6.3.3.	Bilinear Interpolation . . . . .	109
6.3.4.	Noise Correlation Induced by Interpolation . . . . .	109
6.3.5.	Interpolation in the Presence of Polarization . . . . .	110
6.4.	CPD Factors, Normalisation and Scaling . . . . .	110
6.5.	Algorithms . . . . .	111
6.5.1.	Estimation of Factor Matrices . . . . .	112
6.5.2.	Estimation of Signal Parameters . . . . .	113
6.6.	Computer Results . . . . .	114
6.6.1.	Space Shift in Wideband . . . . .	116
6.6.2.	Polarization in Wideband . . . . .	120
6.7.	Conclusion . . . . .	123

<b>7. Cramér-Rao Bound for Source Estimation and Localization</b>	<b>125</b>
7.1. Contribution . . . . .	125
7.2. Cramér-Rao Bounds . . . . .	125
7.2.1. Log-Likelihood . . . . .	125
7.2.2. Fisher Information Matrix (FIM) . . . . .	126
7.3. Derivatives Required for the FIM . . . . .	127
7.3.1. Complex Derivatives . . . . .	127
7.3.2. Derivatives w.r.t. sources . . . . .	128
7.3.3. Derivatives w.r.t. DoAs . . . . .	128
7.3.4. Derivatives w.r.t. polarization parameters . . . . .	129
7.4. Interpolation errors . . . . .	130
<b>8. Tensor Wideband Estimation through Spatial Resampling</b>	<b>133</b>
8.1. Contribution . . . . .	133
8.2. Space Shift Diversity in Wideband . . . . .	133
8.2.1. Linear Arrays . . . . .	134
8.2.2. Planar Arrays . . . . .	135
8.2.3. Tensor Resampling . . . . .	137
8.3. Polarization Diversity in Wideband . . . . .	137
8.3.1. Tensor Resampling . . . . .	138
8.4. Estimation of Signal Parameters . . . . .	139
8.5. Computer results . . . . .	140
8.5.1. Space Shift in Wideband . . . . .	140
8.5.2. Polarization in Wideband . . . . .	145
8.6. Conclusions and Perspectives . . . . .	147
<b>Appendices</b>	<b>148</b>
8.A. Array 1D Interpolation . . . . .	148
8.A.1. Sinc Interpolation . . . . .	148
8.A.2. Spatial Interpolation . . . . .	148
<b>9. Tensor Decomposition of Seismic Volume Waves</b>	<b>149</b>
9.1. Contribution . . . . .	149
9.2. Context . . . . .	149
9.3. Physical model and assumptions . . . . .	150
9.4. Speed diversity in tensor format . . . . .	151
9.4.1. Estimation of Signal Parameters . . . . .	153
9.5. Numerical simulations . . . . .	154
9.6. Application to Real Seismic Data . . . . .	159
9.6.1. Windowing and Alignment . . . . .	159
9.6.2. Working Frequencies and Filtering . . . . .	160
9.7. Application to the Argentière Glacier . . . . .	160
9.7.1. Speed Diversity - Narrowband . . . . .	162
9.7.2. Repetition Diversity . . . . .	165
9.7.3. Space Shift Diversity - Wideband . . . . .	168
9.8. Conclusion and perspectives . . . . .	170
<b>Appendices</b>	<b>171</b>
9.A. Justification of Assumption A 9.3 . . . . .	171

<b>III. Contribution: Multidimensional Spectral Factorization</b>	<b>173</b>
<b>10. Multidimensional Factorization of Seismic Waves</b>	<b>175</b>
10.1. Contribution . . . . .	175
10.2. The Helical Coordinate System . . . . .	176
10.3. Cepstral Factorization . . . . .	177
10.4. The Effect of the Helical Transform on the Multidimensional Factorization Problem . . . . .	181
10.5. Helical Mapping for Wavefield Propagation . . . . .	185
10.6. Application to Physical Systems . . . . .	186
<b>Appendices</b>	<b>190</b>
10.A. Proof for Propagative Systems . . . . .	190
10.B. Algorithms . . . . .	192
 <b>Conclusion and Perspectives</b>	 <b>195</b>
 <b>Résumé en Français</b>	 <b>201</b>



# List of Figures

I.1.	Data Matrix . . . . .	5
I.2.	Data tensor . . . . .	6
1.1.	Acquisition system . . . . .	11
1.2.	Direction of arrival . . . . .	15
1.3.	DoA in 2D . . . . .	16
1.4.	Uniform Linear Array (ULA) . . . . .	16
1.5.	Regular planar arrays . . . . .	17
1.6.	Plane of particle motion . . . . .	21
1.7.	Orientation and ellipticity of the polarization ellipse . . . . .	23
1.8.	3C sensor . . . . .	23
1.9.	Particle motion of seismic volume waves . . . . .	26
2.1.	Space shift - ESPRIT . . . . .	37
2.2.	Virtual arrays . . . . .	43
2.3.	Spatial resampling . . . . .	45
3.1.	Third order tensor . . . . .	50
3.2.	Tensor Fibers . . . . .	51
3.3.	Tensor slices . . . . .	51
3.4.	Decomposable tensor . . . . .	54
3.5.	CPD of a tensor . . . . .	57
3.6.	CPD of a matrix . . . . .	60
4.1.	Space shift diversity: narrowband . . . . .	72
5.1.	Polarization diversity: narrowband . . . . .	94
5.2.	MSE vs SNR: polarization, narrowband . . . . .	95
5.3.	Gain pattern diversity: narrowband . . . . .	99
5.4.	MSE vs SNR: gain patterns, narrowband . . . . .	101
5.5.	MSE vs directivity: gain patterns, narrowband . . . . .	101
5.6.	MSE vs sensor spacing: gain patterns, narrowband . . . . .	102
6.1.	Virtual subarrays . . . . .	108
6.2.	Space shift diversity, wideband . . . . .	116
6.3.	MSE vs sample size: tensor narrowband estimation . . . . .	117
6.4.	MSE vs SNR: space shift, wideband . . . . .	118
6.5.	Noise covariance matrix after interpolation . . . . .	119
6.6.	Polarization diversity: wideband . . . . .	120
6.7.	MSE vs SNR: polarization, wideband . . . . .	121
6.8.	Noise covariance matrix after interpolation . . . . .	122
8.1.	Interpolation, linear subarrays . . . . .	134

8.2. Interpolation, linear uniform subarrays . . . . .	134
8.3. Interpolation, linear uniform global array . . . . .	135
8.4. Interpolation, planar subarrays . . . . .	136
8.5. Interpolation, uniform rectangular global array . . . . .	136
8.6. MSE vs SNR: space shift, wideband, ULA . . . . .	142
8.7. MSE vs angular separation: space shift, wideband, ULA . . . . .	143
8.8. MSE vs sensor number: space shift, wideband, ULA . . . . .	144
8.9. MSE vs SNR: polarization, wideband, ULA . . . . .	146
9.1. Propagation speed diversity . . . . .	152
9.2. RMSE vs SNR: propagation speed, broadside . . . . .	156
9.3. RMSE vs SNR: propagation speed, endfire . . . . .	157
9.4. RMSE vs angular separation: propagation speed, broadside . . . . .	158
9.5. RMSE vs angular separation: propagation speed, endfire . . . . .	158
9.6. Pictures of the Argentière glacier . . . . .	160
9.7. Geophone . . . . .	161
9.8. Glacier structure . . . . .	161
9.9. Example of a deep seismic event . . . . .	163
9.10. Optimized working frequency for P wave . . . . .	164
9.11. DoA estimation of deep seismic events, propagation speed, narrowband . . . . .	164
9.12. P and S waves from the same seismic cluster . . . . .	165
9.13. Welch periodogram of P and S waves from the same seismic cluster . . . . .	166
9.14. WB DoA estimation of deep seismic events, wideband . . . . .	169
10.1. 2D admissible regions . . . . .	180
10.2. Semi-causal cepstrum via a helix . . . . .	182
10.3. Semi-causal cepstrum for a separable function . . . . .	184
10.4. Simulated 2D data and impulse response . . . . .	187
10.5. Estimation of the impulse response - Dirac source . . . . .	188
10.6. Estimation of the impulse response - random source . . . . .	188
10.7. Approximation error and correlation . . . . .	188
10.8. Solar Data Volume . . . . .	189
10.9. Estimation of the impulse response of the Sun . . . . .	189
10.10. Pearson correlation of the solutions . . . . .	189
10.11. Data Matrix . . . . .	203
10.12. Data tensor . . . . .	205

## Acronyms

**3C** three-component sensor

**ALS** Alternating Least Squares

**ALSCOLOR** Proposed ALS algorithm for correlated noise

**BF** Beamforming

**BSS** Blind Source Separation

**CPD** Canonical Polyadic Decomposition

**CRB** Cramér-Rao Bound

**CSS** Coherent Signal Subspace

**DFT** Discrete Fourier Transform

**DoA** Direction of Arrival

**ESPRIT** Estimation of Signal Parameters via Rotational Invariance Techniques

**EVD** Eigenvalue Decomposition

**FIM** Fisher Information Matrix

**FIR** Finite Impulse Response

**FT** Fourier Transform

**HOSVD** High Order Singular Value Decomposition

**IFT** Inverse Fourier Transform

**LCMV** Linearly Constrained Minimum Variance

**LS** Least Squares

**LV MUSIC** Long Vector MUSIC

**MC** Monte Carlo

**MI ESPRIT** Multiple Invariance ESPRIT

**ML** Maximum Likelihood

**MLE** Maximum Likelihood Estimator

**MSE** Mean Square Error

**MUSIC** Multiple Signal Characterization

**NMF** Non Negative Matrix Factorization

**NSHP** Non-Symmetric Half Plane

<b>NSHS</b>	Non-Symmetric Half Space
<b>PDE</b>	Partial Differential Equations
<b>RMSE</b>	Root Mean Square Error
<b>SNR</b>	Signal to Noise Ratio
<b>SVD</b>	Singular Value Decomposition
<b>T-MUSIC</b>	Tensor MUSIC
<b>TDL</b>	Tapped Delay Line
<b>TKD</b>	Tucker Decomposition
<b>TLS</b>	Total Least Squares
<b>UCA</b>	Uniform Circular Array
<b>ULA</b>	Uniform Linear Array
<b>URA</b>	Uniform Rectangular Array
<b>WB</b>	Wideband

## Main Notations

$j$	$\sqrt{-1}$
$\mathbf{v}$	vector: in bold lower case
$v_i$	$i$ -th element of $\mathbf{v}$
$\mathbf{A}$	matrix: in bold upper case
$\mathbf{I}_L$	identity matrix of size $L \times L$
$\mathbf{a}_i$	$i$ -th column of $\mathbf{A}$
$\bar{\mathbf{g}}$	vector $\mathbf{g}$ without its first entry
$\tilde{\mathbf{x}}$	vector related to a virtual array or interpolated vector
$A_{ij}$	$\{i, j\}$ element of $\mathbf{A}$
$\mathbf{A}^\top$	transpose of $\mathbf{A}$
$\mathbf{A}^*$	complex conjugate of $\mathbf{A}$
$\mathbf{A}^H$	conjugate transpose of $\mathbf{A}$
$\mathbf{A}^\dagger$	Moore-Penrose pseudoinverse of $\mathbf{A}$
$\mathbf{v}^\top \mathbf{u}$	scalar product between real vectors $\mathbf{v}$ and $\mathbf{u}$
$\mathbf{v}^H \mathbf{u}$	scalar product between complex vectors $\mathbf{v}$ and $\mathbf{u}$
$\mathbf{v} \otimes \mathbf{u}$	outer (tensor) product between two vectors
$\mathbf{A} \boxtimes \mathbf{B}$	Kronecker product between $\mathbf{A}$ and $\mathbf{B}$
$\mathbf{A} \odot \mathbf{B}$	Khatri-Rao product between $\mathbf{A}$ and $\mathbf{B}$
$\mathbf{A} \square \mathbf{B}$	Hadamard (element-wise) product
$\mathbf{A} \oslash \mathbf{B}$	Hadamard (element-wise) division
$\mathcal{T} \bullet_d \mathbf{A}$	mode- $d$ product
$\ \mathcal{A}\ $	Frobenius norm of $\mathcal{A}$
$\ \mathbf{v}\ _D$	weighted Euclidean norm, $\sqrt{\mathbf{v}^H \mathbf{D}^{-1} \mathbf{v}}$

$\mathcal{T}$	tensor: in bold calligraphic font
$\mathcal{T}_{ijk}$	$\{i, j, k\}$ element of $\mathcal{T}$
$\mathbf{T}_{(d)}$	mode- $d$ unfolding of $\mathcal{T}$
$\text{vec}\{\mathcal{T}\}$	vectorization of $\mathcal{T}$
$\dot{\mathbf{d}}(\theta)$	derivative $\partial \mathbf{d} / \partial \theta$

# Introduction



## I.1. Space-Time Processing

In the beginning of signal processing, statistics and engineering problems revolved around parameter estimation and the corresponding performance. The parameters of interest were mainly related to time, as recorded data was essentially a function of time. Therefore, signals could be characterized in time domain, or, equivalently, in frequency domain.

Subsequently, following the expansion of applications, recorded signals also became a function of sensor position, thus developing a spatial dependence. The spatial part of the processor is an aperture (or antenna) in the continuous space domain, and it is an array in the discrete space domain [151]. Since signals became space-time processes, spatial as well as temporal parameters became the object of a whole new field, named sensor array signal processing, or just array processing. Array processing is a joint space-time processing, aimed at fusing data collected at several sensors [79]. Prior information on the acquisition system (*i.e.* array geometry, sensor characteristics, etc.) is used in order to estimate signal parameters. Since a sensor array samples the impinging wavefields in space and time, the spatial and temporal fusion takes place in the multidimensional space-time domain. The main issues in array processing are given by the array configuration, the characteristics of the signals and the characteristics of the noise, and the estimation objective [151], such as the Directions of Arrival (DoAs) of possibly simultaneous emitters.

## I.2. Main Applications

Signal parameter estimation in array processing has given rise to a huge variety of applications, as listed below.

### Radar

The first application of antenna arrays was provided by source localization in radar. Most radar systems are active, in that the antenna is used for transmission and reception of signals at the same time. Reflection of the ground is a major problem commonly referred to as *clutter*, involving spatially spread interferences. Non military applications include air-traffic control. The spatial parameters of interest may vary: active systems can estimate velocity (Doppler frequency), range, and DoAs, whereas passive systems can only estimate the DoAs.

### Astronomy

In astronomy, antenna arrays are very long passive systems (the baseline can reach thousands of kilometers) that measure and study celestial objects with very high resolution.

### Sonar

Active sonar systems process the echoes of acoustic signals transmitted underwater, whereas passive sonar systems study incoming acoustic waves, through arrays of hydrophones. The main difference between active sonars and radars is given by the propagation conditions: the propagation of acoustic waves in the ocean is more complex and problematic than the propagation of electromagnetic waves in the atmosphere, due to dispersion, dissipation, and variation of propagation speed with depth. Major instances of noise are ambient noise, self noise and *reverberation*. The most important application is the detection and tracking of submarines. Deformable arrays are often towed underwater, with a linear array structure [79].

### Communications

Another major domain for array processing is provided by telecommunications (both terrestrial and satellite based). Communication signals are typically point-like sources, and they generally arrive at the distant receiver as plane waves, after being reflected several times by buildings and hills. These multiple reflections are called multipath and can produce severe signal fading. Estimation performance can also be degraded by other interfering signals, or inter-user interference. In this context, *smart antennas* refers to adaptive arrays for wireless communications: they implement adaptive spatial processing in addition to the adaptive temporal processing already used [151].

### Seismology

Exploration or reflection seismology is another important area of array processing, aimed at deriving an image of the earth structure and physical properties of various layers. Active systems, measuring reflections through various layers, are designed according to the propagation of elastic waves through an inhomogeneous medium. On the other hand, passive seismic makes use of several seismometers, separated by hundreds of meters, to detect natural low frequency earth movements over periods of hours or days [151]. The latter application is addressed in Chapter 9.

### Medical technology

Medical applications have also offered a very fertile ground for array processing. Electrocardiography (ECG) is used to monitor heart health; electroencephalography (EEG) and magnetoencephalography (MEG) are used to localize brain activity [79]. Tomography is the cross-sectional imaging of objects from transmitted or reflected waves. It has had great success for medical diagnosis [151].

## I.3. Classic Approaches in 2D

At first, the original approach for space-time processing was provided by spatial filtering, or Beamforming (BF), consisting in amplifying signals arriving from certain directions, while attenuating all the others [152]. However, although very simple, beamforming suffers from a severe limitation: its performance directly depends on the array aperture, regardless of the number of data samples, and of the Signal to Noise Ratio (SNR). This seriously limits its resolution, *i.e.* its ability to distinguish closely spaced sources. Resolution is intuitively easy to understand in the context of spectral methods, like BF: as whenever two peaks are visible in correspondence with two actual emitters, the latter are said to be resolved.

Recorded data consist of matrices, whose rows correspond to the various sensors (space) and columns correspond to recorded time samples (time), as in Figure I.1. Since the signal parameters of interest, such as the DoA, are spatial in nature, most 2D approaches rely on the estimation of the cross-covariance information among the sensors, *i.e.* the spatial covariance matrix, thus requiring sufficiently large data samples.

A real breakthrough in array processing was provided by subspace methods [131, 126], when the eigen-structure of the covariance matrix was explicitly exploited through spectral decomposition techniques, such as the Eigenvalue Decomposition (EVD). Thanks to the low-rank structure of received data, the eigenvectors corresponding to the largest eigenvalues span the signal subspace, whereas the remaining eigenvectors span the noise

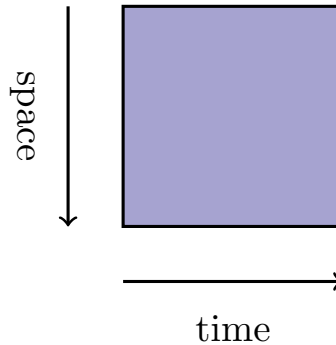


Figure I.1.: Data matrix in traditional array processing

subspace. Hence, high resolution techniques such as MUSIC [131] make use of these two elements of diversities: space and time, in order to estimate the signal subspace generated by impinging sources, as well as their directions of arrival. This is generally done through the estimation of the array spatial covariance matrix. Higher order statistics can also be used [83] to get rid of Gaussian noise, and increase the number of detectable sources.

In addition, the shift-invariant structure of the acquisition system can be exploited whenever the global array is given by two identical subarrays, each being the translated version of the other. This is the core idea of the ESPRIT algorithm [126].

In the absence of model mismatch, the resolution capability of subspace methods is not limited by the array aperture, provided the data size and SNR are large enough [79].

Furthermore, if impinging wavefields are not scalar, but vector valued, wave polarization becomes a useful property that can improve source localization, provided sensors are sensitive to different components and these components can be calibrated separately. This is the case of the *vector-sensor*, *i.e.* a sensor that measures all the orthogonal components of elastic or electromagnetic waves at the same time [95, 96].

In traditional methods, the vector sensor components are generally stacked one after another into a long vector, for a given observation time, thus losing their multidimensional structure.

At first, BF and subspace methods were conceived for narrowband waves, which can be quite a realistic assumption in radar and telecommunications, as the signal spectral bandwidth is often negligible, compared to the array aperture. However, in many other applications, such as sonar and seismology, received signals are wideband in nature. The natural extension of array processing to the wideband case is based on the Discrete Fourier Transform (DFT), followed by an optimal or suboptimal combination of the information at different frequency bins. An optimal solution is provided by the Coherent Signal Subspace (CSS): all the frequency contributions are aligned to the same reference subspace at a central frequency, through linear transformations [157].

## I.4. Tensor Arrays

We note that the EVD of the estimated covariance matrix is equivalent to the Singular Value Decomposition (SVD) of the corresponding raw data. SVD is a matrix factorization deriving its uniqueness from two constraints: a diagonal core containing distinct non-negative singular values, and orthonormal matrices containing left and right singular vectors, respectively. This orthogonality constraint is often arbitrary and physically

unjustified.

Standard matrix factorizations, such as the SVD, are indeed effective tools for feature selection, dimensionality reduction, signal enhancement, and data mining [22]. However, as we mentioned in the previous section, they can deal with data having only two modes, *e.g.* space-time arrays. In many applications, such as chemometrics and psychometrics, but also text mining, clustering, social networks, telecommunications, etc., the data structure is highly multidimensional, as it contains higher order modes, such as trials, experimental conditions, subjects, and groups, in addition to the intrinsic modes given by space and time/frequency [22]. Clearly, the flat perspective of matrix factorization cannot describe the complex multidimensional structure, whereas tensor decompositions are a natural way to jointly grasp the multilinear relationships between various modes, and extract unique and physically meaningful information.

Tensor factorization consists in the analysis of multidimensional data cubes of at least three dimensions. This is achieved through their decomposition into a sum of simpler constituents, thanks to the multilinearity and low rank structure of the underlying model. The Canonical Polyadic Decomposition (CPD), one of the most widespread decompositions of multi-way arrays, expands a multi-way array into a sum of multilinear terms. This can be interpreted as a generalization of bilinear matrix factorizations such as the SVD. However, unlike the SVD, the CPD does not require any orthogonality constraints, as it is unique under mild conditions. This means that we can jointly and uniquely recover all the factor matrices corresponding to tensor modalities, starting from the noisy data tensor [88].

Only recently, tensor analysis has been applied to array processing of narrowband waves in [136], as a deterministic generalization of ESPRIT [126] to more than one translation, with no need for the estimation of statistical quantities. This means that the acquisition system needs to be made of a reference subarray, repeated in space through multiple translations. Hence, the third mode or diversity is provided by space shift, in addition to space and time. Afterwards, the tensor formalism was extended to deal with polarized waves in [57], via CPD, with polarization as a third mode instead of space shift. See Figure I.2 for an illustration of a 3-way array.

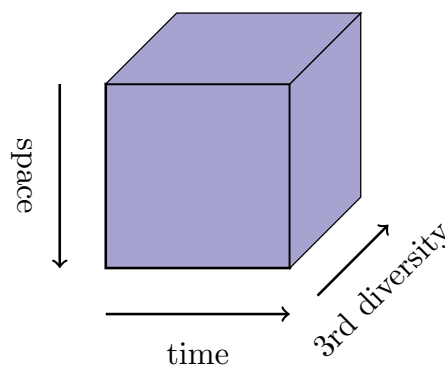


Figure I.2.: 3-way array in tensor array processing

Tensor decompositions allow to jointly and uniquely recover all the modalities related to signal parameters, *i.e.* DoAs, polarization angles, and received signals. Thus, tensor methods provide us with an estimate of source signatures, together with directions of arrival, in a deterministic way. This can be achieved by virtue of the separable and low rank model followed by narrowband sources in the far field. Since tensor CPD methods

do not need any estimation of data covariance or higher order statistics, they can handle shorter data samples.

## I.5. Contribution and Outline

This thesis deals with the estimation and localization of multiple sources via tensor methods for array processing, using various modalities. We include several physical diversities into the tensor model, in addition to space and time: space shift, polarization, gain patterns of directional sensors, and propagation speed of seismic waves. At the beginning of my PhD, I was interested in a tensor model for narrowband waves, in particular, polarized and seismic waves. Only afterwards, I extended all our results to the study of wideband waves using frequency diversity, further developing the corresponding tensor formulation.

The main practical difficulty of the tensor formalism is due to the requirement of multilinearity, corresponding to the separability of the underlying model. While in many situations, such as for narrowband far-field sources, the physical model is separable, there are still as many cases in which it is not. This thesis is an example of the possibility to use tensors even in difficult situations, such as in the case of wideband waves, thus overcoming this problem.

**Contributions** Throughout my PhD, my work gave rise to the following contributions, which are listed below in chronological order.

- At first, we extended tensor analysis to the seismic volume waves, using the diversity of propagation speed as a third mode. This was published in a journal article for *Signal Processing*, Elsevier [117].
- We also presented our work on the tensor model for narrowband polarized elastic waves, and its performance bounds, at a national French conference in *Signal Processing* [115].
- Our interest for seismic waves lead us to publish a journal article for *Signal Processing*, Elsevier, on multidimensional factorization of seismic data cubes for helioseismology [118].
- We introduced the use of directional sensors, proposing gain patterns as a physical diversity of its own in an article for *IEEE Signal Processing Letters* [116].
- After realizing that the speed diversity of seismic waves in our article [117] could be interpreted as a frequency diversity, we decided to extend the tensor formalism to generic wideband waves. Our idea of using spatial interpolation for linear uniform arrays was first presented at ICASSP 2016 in Shanghai [119].
- We further developed the original idea in [119] using bilinear transformations in a journal article, published by *IEEE Transactions on Signal Processing* [114].

This PhD thesis is organized as follows. The presentation is divided into three parts: Part I describes the state of the art of sensor arrays and tensor analysis; Part II and Part III explain my contribution for tensor array processing and multidimensional factorization, respectively.

Chapter 1 presents the physical model of narrowband elastic sources in the far field, as well as the main definitions and assumptions. Chapter 2 reviews the state of the art on direction of arrival estimation, with a particular emphasis on high-resolution signal subspace methods.

Chapter 3 introduces the tensor formalism, namely the definition of multi-way arrays of coordinates, the main operations and multilinear decompositions. Chapter 4 presents the subject of tensor array processing via rotational invariance.

Chapter 5 introduces a general tensor model for narrowband elastic waves, dealing with multiple physical diversities, such as space, time, space shift, polarization, and gain patterns .

Subsequently, Chapter 6 and Chapter 8 establish a tensor model for wideband coherent array processing. We propose a separable coherent focusing operation through bilinear transform and through a spatial resampling, respectively, in order to ensure the multilinearity of the interpolated data. We show via computer simulations that the proposed estimation of signal parameters considerably improves, compared to existing narrowband tensor processing and wideband MUSIC. Throughout the chapters we also compare the performance of tensor estimation to the Cramér-Rao bounds of the multilinear model, which we derive in its general formulation in Chapter 7. Moreover, in Chapter 9 we propose a tensor model via the diversity of propagation speed for seismic waves and illustrate an application to real seismic data from an Alpine glacier.

Finally, the last part of this thesis in Chapter 10 moves to the parallel subject of multidimensional spectral factorization of seismic ways, and illustrates an application to the estimation of the impulse response of the Sun for helioseismology.

## **Part I.**

# **Tensor Decompositions for Source Localization: State of the Art**



# 1. Sensor Arrays: Parametric Modeling for Wave Propagation

## 1.1. Introduction

This first chapter formulates a general model for array processing of various impinging waves (electromagnetic or acoustic signals). A sensor array is generally an acquisition system composed of multiple sensors located at different positions. This set of sensors receives and samples impinging sources in space and time, measuring physical quantities such as electromagnetic field, pressure, particle displacement or velocity. An illustration is given in Figure 1.1.

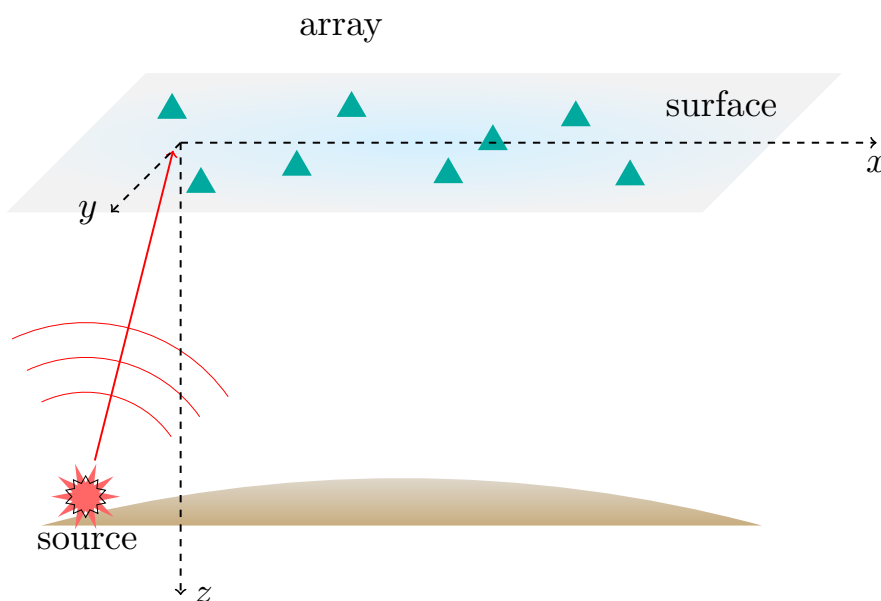


Figure 1.1.: Acquisition system for array processing

Array processing consists in filtering signals in a space-time field, by exploiting their spatial characteristics, in order to estimate their parameters of interest [151]. In Section 1.2 we define and describe the narrowband model, through the introduction of the direction of arrival as the main parameter of interest. In Section 1.3 we postulate some simple assumptions for the acquisition configuration, and for incoming signals, such as the far field approximation, and noise correlation structure. We state some statistical assumptions about data collection and basic geometrical properties of the sensor array are reviewed. Moreover, we define the concepts of array manifold, signal subspace and noise subspace.

In Sections 1.4 and 1.5 we extend the model in Section 1.2 to polarized, wideband and seismic waves through linear algebra tools. We parameterize polarized signals with

respect to both their direction of arrival and their polarization parameters. In Section 1.6 we briefly describe the main properties of seismic waves.

In Section 1.7 we build a vector of parameters of interest. Finally, in Section 1.8 we derive the sample covariance matrix as an important tool carrying spatial information on impinging sources.

## 1.2. Narrowband Wave Propagation for Array Processing

### 1.2.1. Far Field Approximation of Narrowband Waves

Many physical phenomena can be described by wave propagation through a medium, such as electromagnetic waves through space or acoustic waves through a guide, as described by the homogeneous wave equation

$$\nabla^2 \mathbf{E} - \frac{1}{c^2} \frac{\partial^2 \mathbf{E}}{\partial t^2} = 0 \quad (1.1)$$

where  $c$  refers to the propagation speed in the medium of interest. If  $\|\boldsymbol{\eta}\| = 1/c$ , any function of the form  $f(t - \mathbf{p}^\top \boldsymbol{\eta})$  is a solution to (1.1) at radius  $\mathbf{p}$  and time  $t$ : it indicates a wave propagating in the direction of *slowness vector*  $\boldsymbol{\eta}$  with propagation speed  $1/\|\boldsymbol{\eta}\|$ . At first we will only consider one of the scalar components of the vector field  $\mathbf{E}(\mathbf{p}, t)$ , whereas in Section 1.4 we will cover the model of the vector wavefield for elastic waves.

An emitting narrowband source  $E(\mathbf{0}, t) = s(t)e^{j\omega_c t}$  can be seen as the boundary condition for (1.1). The corresponding far field solution is given by

$$E(\mathbf{p}, t) = s(t - \mathbf{p}^\top \boldsymbol{\eta}) e^{j\omega_c(t - \mathbf{p}^\top \boldsymbol{\eta})} \approx s(t) e^{j(\omega_c t - \mathbf{p}^\top \boldsymbol{\kappa})} \quad (1.2)$$

provided  $s(t)$  is a slowly varying envelope function, compared with the carrier  $e^{j\omega_c t}$ , and for  $\|\mathbf{p}\| \ll c/B_s$  where  $B_s$  is the bandwidth of  $s(t)$ . In (1.2)  $\boldsymbol{\kappa}$  refers to the wave-vector, pointing in the direction of propagation and with modulus  $\|\boldsymbol{\kappa}\| = \omega_c/c = 2\pi/\lambda$ , where  $\lambda$  indicates the wavelength [79]. Denote by  $\omega$  the radial frequency: we will restrict our interest to bandpass complex envelopes, that are limited in bandwidth to the region  $|\omega_L| \leq 2\pi B_s/2$  with  $\omega_L \triangleq \omega - \omega_0$ . We refer to Section 1.A for the definition of complex envelope.

In the near field the wavefront (*i.e.* all the points sharing equal phase) corresponds to a sphere of radius  $\Delta$ , whereas in the far field the radius is so large with respect to the size of the array, that the field curvature becomes negligible and the wavefront can be approximated by a plane. Therefore, spherical waves can be approximated by plane waves in the far field.

If the medium is linear, the superposition principle allows us to model multiple waves propagating simultaneously:

$$x(\mathbf{p}, t) = \sum_{r=1}^R s_r(t) e^{j(\omega_c t - \mathbf{p}^\top \boldsymbol{\kappa}_r)} + n(\mathbf{p}, t) \quad (1.3)$$

where  $n(\mathbf{p}, t)$  refers to additive noise. Since (1.3) is a function of both space and time, it is particularly adequate to model signals with different space-time parameters, as we will see in Section 1.2.2.

### 1.2.2. Parametric Modeling for Sensor Arrays: Directions of Arrival

Array processing consists in merging time and space information measured at different sensors, in order to estimate relevant signal parameters. As much as one single sensor samples a signal in time, an array made of multiple sensors samples a wavefield in space. An antenna array is then a system exploiting two kinds of physical diversity: time and space simultaneously. Since we can associate to each sensor in space a given time delay due to finite propagation speed  $c$  (cf. (1.2)), we will need a time-space processing approach and make full use of our knowledge on the geometry and sensor characteristics of the acquisition system. The model in (1.3) is used in array processing for the estimation of relevant signal parameters, such as the DoA, detailed in the present section, source polarization, detailed in Section 1.4, source waveforms and temporal frequency.

We consider  $R$  radiating *narrowband* sources in the far-field,  $s_r$ ,  $1 \leq r \leq R$ , arriving from directions defined by unit vectors  $\mathbf{d}(\theta_r)$ ,  $\theta_r$  being a pair of angles in 3D, or a single angle in 2D (cf. Section 1.2.3). These sources impinge on an arbitrary array of  $L$  sensors located at positions  $\mathbf{p}_\ell$  in space,  $1 \leq \ell \leq L$ .

We shall state the main assumptions:

**A 1.1.** Impinging sources are described by *plane waves*. This is equivalent to the *far-field* configuration described in Section 1.2.1. The distance of the source from the receiving array is much greater than the array aperture: this is equivalent to assuming a planar wavefront at the sensor level. Moreover, sensors and sources are considered point-like, as their size is negligible with respect to the source-to-sensor distance (point-source and point-like sensors).

**A 1.2.** Complex envelopes have a *band-limited spectrum*:  $|\omega_L| \leq 2\pi B_s/2$  with  $\omega_L \triangleq \omega - \omega_0$ .

**A 1.3.** The *narrowband* assumption requires that

$$\Delta\tau_{max} B_s \ll 1 \quad (1.4)$$

where  $B_s$  is the bandwidth of source envelope  $s$  and  $\Delta\tau_{max}$  is the maximum travel time between any two elements of the array.<sup>1</sup> This is equivalent to requiring that the array aperture  $\Delta p = \Delta\tau_{max}/c$  (converted into wavelengths) be much less than the inverse relative source bandwidth  $B_s$ :

$$\Delta p \ll c/B_s \quad \iff \quad \Delta p/\lambda \ll f/B_s \quad (1.5)$$

where  $f = \omega/(2\pi)$ . This allows us to represent envelope  $s$  as slowly varying:  $s(t-\tau) \approx s(t)$ .

**A 1.4.** *Narrowband in base-band*. Signals of interest are the product of a varying amplitude (complex envelope)  $s_r(t)$  and a high-frequency signal  $e^{j\omega t}$  (cf. Section 1.2.1). We assume that the spectral supports of both parts do not overlap (this is sometimes referred to as the Bedrosian condition)<sup>2</sup>. Under this condition, one can work in base-band with the complex envelope of the low-pass signal. For this type of signal, a time delay of the original signal is equivalent to a phase shift of the complex envelope, as expressed in (1.2).

<sup>1</sup> For an linear array the maximum travel time refers to a source arriving along the array axis (*endfire*).

<sup>2</sup>We recall the Bedrosian theorem [9]: The Hilbert transform of the product of two complex valued functions  $f, g : \mathbb{R} \rightarrow L^2(\mathbb{R})$  with non-overlapping Fourier spectra ( $F(\omega) \approx 0$  for  $|\omega| > a$  and  $G(\omega) \approx 0$  for  $|\omega| < a$  where  $a$  is a positive constant) is given by the product of the low-frequency signal  $f$  and the Hilbert transform of the high-frequency signal  $g$ :  $H\{f(x)g(x)\} = f(x)H\{g(x)\}$ ,  $x \in \mathbb{R}$ .

**A 1.5.** *Dissipation* at the antenna scale is excluded, as the array dimensions are negligible with respect to dissipation characteristic length.

**A 1.6.** Sources propagate in a *non-dispersive medium i.e.* their propagation speed is independent of frequency.

**A 1.7.** *Homogeneous and isotropic medium at the antenna level:* ray-paths can be approximated by straight lines.

From (1.3), the signal received at the  $\ell$ -th sensor at time  $t$  can be modeled as:

$$x_\ell(t) = \sum_{r=1}^R g_\ell(\theta_r) s_r(t) e^{-j\omega\tau_\ell(\theta_r)} + n_\ell(t) \quad (1.6)$$

where  $s_r(t)$  is the complex envelope of the  $r$ -th source,  $t \in \{1, 2, \dots, T\}$ ,  $g_\ell(\theta_r)$  is the sensor gain of the  $\ell$ -th sensor, and  $n_\ell(t)$  is an additive noise. It is assumed that the output in (1.6) is proportional to the wavefield (1.3) measured at its location. Notice that we dropped the carrier term  $e^{j\omega t}$ , which is equivalent to converting the signal to the baseband and reducing it to its complex envelope [79].

The delay of arrival  $\tau_\ell(\theta)$  is directly related to sensor locations and DoAs via the expression

$$\tau_\ell(\theta_r) = \mathbf{p}_\ell^\top \boldsymbol{\kappa}_r = \mathbf{p}_\ell^\top \mathbf{d}(\theta_r)/c \quad (1.7)$$

$c$  being the wave propagation speed. After introducing the notion of steering element,

$$\mathbf{a}_\ell(\theta_r) = g_\ell(\theta_r) e^{-j\omega\tau_\ell(\theta_r)} \quad (1.8)$$

(1.6) simplifies to

$$x_\ell(t) = \sum_{r=1}^R \mathbf{a}_\ell(\theta_r) s_r(t) + n_\ell(t) \quad (1.9)$$

The array output vector  $\mathbf{x}(t) = [x_1(t), \dots, x_L(t)]^\top$  is then obtained by

$$\mathbf{x}(t) = \sum_{r=1}^R \mathbf{a}_r s_r(t) \in \mathbb{C}^L \quad (1.10)$$

with steering vector  $\mathbf{a}_r = \mathbf{a}(\theta_r) = [a_1(\theta_r), \dots, a_L(\theta_r)]^\top$ . After arranging all the steering elements into a steering matrix and the complex envelopes into a vector of signal waveforms

$$\begin{cases} \mathbf{A}(\boldsymbol{\theta}) = [\mathbf{a}(\theta_1), \dots, \mathbf{a}(\theta_R)] \in \mathbb{C}^{L \times R} \\ \mathbf{s}(t) = [s_1(t), \dots, s_R(t)]^\top \in \mathbb{C}^R \end{cases} \quad (1.11)$$

(1.10) writes

$$\mathbf{x}(t) = \mathbf{A}(\boldsymbol{\theta}) \mathbf{s}(t) \in \mathbb{C}^L \quad (1.12)$$

which constitutes the general formulation for array processing. The  $r$ -th column of  $\mathbf{A}(\boldsymbol{\theta})$ , denoted  $\mathbf{a}_r$  or  $\mathbf{a}(\theta_r)$  in the remainder, is the value of the *array manifold* taken at  $\theta = \theta_r$  (cf. Section 1.3).

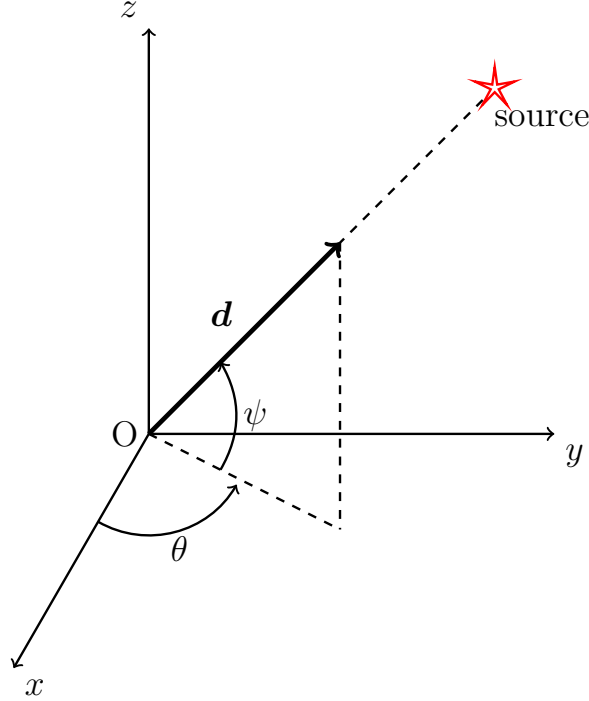


Figure 1.2.: Direction of Arrival (DoA) in 3D

### 1.2.3. General Array Geometries

The DoA is defined by two angles in 3D: the azimuth  $\theta \in (-\pi, \pi]$  and the elevation  $\psi \in [-\pi/2, \pi/2)$ , as illustrated in Figure 1.2. The unit vector pointing in the direction of the source is then expressed by

$$\mathbf{d}(\theta, \psi) = \begin{bmatrix} \cos \theta \cos \psi \\ \sin \theta \cos \psi \\ \sin \psi \end{bmatrix} \quad (1.13)$$

On the other hand, in 2D the sources lie in the same plane as a planar array, *i.e.*  $\psi = 0$ , as illustrated in Figure 1.3: the DoA is then defined by azimuth  $\theta$  only, leading to directional vector

$$\mathbf{d}(\theta) = \begin{bmatrix} \cos \theta \\ \sin \theta \end{bmatrix} \quad (1.14)$$

Hence, in a 3D space, the DoA parameter matrix  $\Theta$  is an  $R \times 2$  matrix, whereas in 2D it is a  $R \times 1$  vector (see Section 1.7 for more details).

In the remainder we will consider mostly 2D settings, as in Figure 1.3, *i.e.*

**A 1.8.** Sources and antennas are assumed coplanar, without any loss of generality. Vectors  $\mathbf{p}_\ell$  and  $\mathbf{d}(\theta)$  are thus both in  $\mathbb{R}^2$ , and we shall use the notation  $\mathbf{p}_\ell = [p_\ell^x, p_\ell^y]^\top$  and  $\mathbf{d}(\theta) = [\cos \theta, \sin \theta]^\top$ . This permits to parameterize DoAs by a single angle, azimuth  $\theta_r$ . Therefore, unless otherwise specified,  $\boldsymbol{\theta} = [\theta_1, \dots, \theta_R]^\top$ , leading to a time delay at sensor  $\ell$  of the form

$$\tau_\ell(\theta_r) = (p_\ell^x \cos \theta_r + p_\ell^y \sin \theta_r)/c \quad (1.15)$$

We state an important definition of the ability of a sensor array to correctly estimate any DoA:

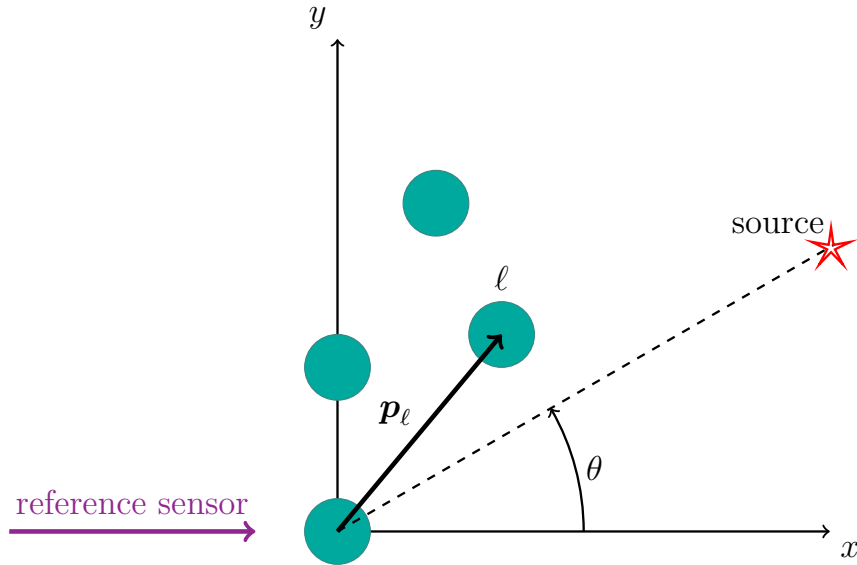


Figure 1.3.: Acquisition system and DoA in 2D

**Definition 1.1.** The sensor position vectors  $\{\mathbf{p}_1, \dots, \mathbf{p}_L\}$  are said to be *resolvent* with respect to a direction  $\mathbf{v} \in \mathbb{R}^2$ , if

$$\exists k, \ell : \mathbf{v} = \mathbf{p}_k - \mathbf{p}_\ell \quad \text{s.t.} \quad 0 \leq \|\mathbf{v}\| \leq \lambda/2 \quad (1.16)$$

where  $\lambda$  refers to the wavelength of the impinging signal.

### 1.2.4. Uniform Linear Arrays

The most common array configuration is the Uniform Linear Array (ULA), with  $\mathbf{p}_\ell = [(\ell - 1)p_0, 0]^\top$ , *i.e.* there are  $L$  elements located on the  $x$ -axis with uniform spacing equal to  $p_0$  [151], as in Figure 1.4. We have chosen the first sensor position as the origin of the coordinate system.

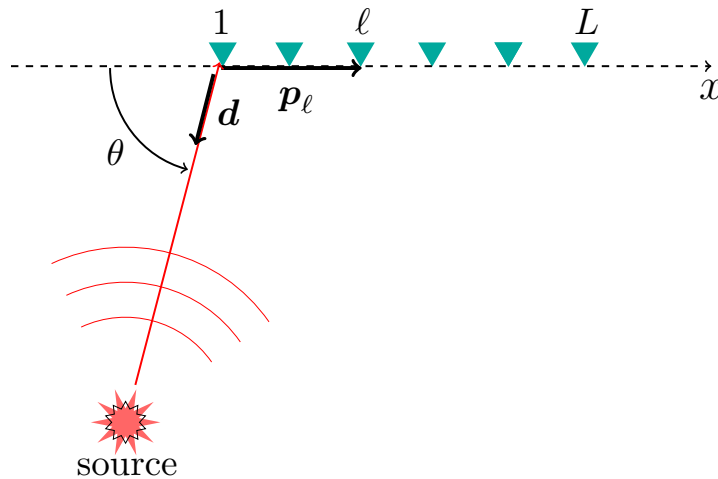


Figure 1.4.: Uniform Linear Array (ULA)

In this case, if all the sensors share the same directivity pattern  $g(\theta)$ , the resulting steering vector is Vandermonde:

$$\mathbf{a}(\theta) = g(\theta)[1 e^{-j\kappa_0 p_0 \cos \theta}, \dots, e^{-j\kappa_0 (L-1)p_0 \cos \theta}] \quad (1.17)$$

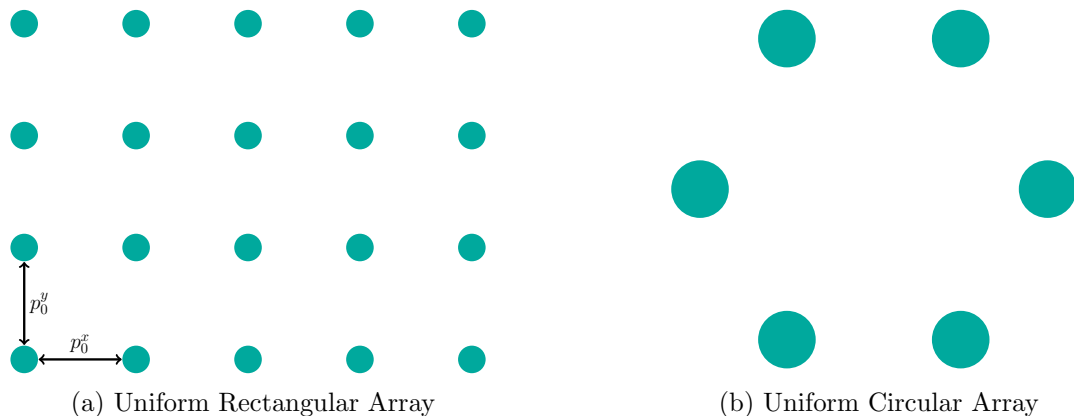


Figure 1.5.: Regular planar array geometries

The space-time field is band-limited in wavenumber space [151]:

$$|\kappa| \leq \frac{2\pi}{\lambda} \triangleq \kappa_0 \quad (1.18)$$

with  $\kappa = \kappa_0 \cos \theta = 2\pi \cos \theta / \lambda$ . This implies a spatial sampling condition upon inter-sensor spacing:

$$p_0 \leq \frac{\lambda}{2} \quad (1.19)$$

as wavenumber and position are dual FT variables. A ULA with  $p_0 = \frac{\lambda}{2}$  is referred to as a *standard* ULA.

### 1.2.5. Uniform Rectangular Arrays

Analogously, for Uniform Rectangular Array (URA) as in Figure 1.5a, with  $p_\ell^x = (\ell^x - 1)p_0^x$ ,  $1 \leq \ell^x \leq L^x$  and  $p_\ell^y = (\ell^y - 1)p_0^y$ ,  $1 \leq \ell^y \leq L^y$ , we would have two conditions:

$$\begin{cases} |\kappa^x| \leq \frac{2\pi}{\lambda} \implies p_0^x \leq \frac{\lambda}{2} \\ |\kappa^y| \leq \frac{2\pi}{\lambda} \implies p_0^y \leq \frac{\lambda}{2} \end{cases} \quad (1.20)$$

### 1.2.6. Uniform Circular Arrays

Another array configuration in 2D is the Uniform Circular Array (UCA), as in Figure 1.5b, where

$$\mathbf{p}_\ell = \rho \begin{bmatrix} \cos(2\pi(\ell - 1)/L) \\ \sin(2\pi(\ell - 1)/L) \end{bmatrix} \quad (1.21)$$

A sampling theorem argument indicates [151]

$$L \geq 2 \left( \frac{2\pi\rho}{\lambda} \right) + 1 \quad (1.22)$$

which ensures that the spacing between two consecutive elements is  $d_{circ} \leq \frac{\lambda}{2}$ .

In the remainder, we will use the following assumption on sensor spacing  $\Delta\mathbf{p}_\ell = \mathbf{p}_{\ell+1} - \mathbf{p}_\ell$ :

**A 1.9.** Two consecutive sensors are always spaced by less than  $\lambda/2$ :  $\|\Delta\mathbf{p}_\ell\| \leq \lambda/2, \forall \ell$ .

## 1.3. The Signal Subspace and the Spatial Covariance

### 1.3.1. Assumptions and Fundamental Definitions

We can assume the following properties, that we will use regularly throughout this thesis:

**A 1.10.** The number of sources,  $R$ , *i.e.* the model order, is known.

**A 1.11.** Noise spatial coherency is known. Therefore, one can always consider (thanks to spatial whitening) that the noise covariance matrix  $\Sigma_n$  is proportional to identity:  $\Sigma_n = \mathbb{E}[\mathbf{n}(t)\mathbf{n}(t)^H] = \sigma^2\mathbf{I}$ , where  $\sigma$  may be unknown, after whitening is applied. This hypothesis refers to the *spatial whiteness* of noise: the noise processes at different sensors are considered to be identically distributed and uncorrelated from one another.

**A 1.12.** Finally, noise is additive and Gaussian complex circular:  $\mathbb{E}[\mathbf{n}(t)\mathbf{n}(t)^T] = \mathbf{0}$ .

In Section 2.9 we address the case of spatially correlated noise.

Moreover, whenever we talk about the signal subspace, we use the following assumptions:

**A 1.13.** The number of sources of interest,  $R$ , is smaller than the number of sensors  $L$ :  $R < L$ .

**A 1.14.** Incident signals are uncorrelated to noise.

Whenever not specified, we will assume that

**A 1.15.** Received sources are uncorrelated, *i.e.*  $\mathbb{E}[s_r(t)s_q(t)] = 0$ ,  $\forall q \neq r$ . Moreover, received sources  $s_r$  are assumed complex Gaussian zero mean random processes with variance  $\sigma_r^2$ .

As for the signal covariance matrix  $\mathbf{R}_S = \mathbb{E}[\mathbf{s}(t)\mathbf{s}(t)^H]$ , we distinguish between a few cases:

1. If the  $R$  sources are uncorrelated, the matrix  $\mathbf{R}_S$  is diagonal and hence full rank (or nonsingular);
2. If the  $R$  sources are partially correlated, the matrix  $\mathbf{R}_S$  is nondiagonal and nonsingular but with worse conditioning<sup>3</sup> than the uncorrelated case;
3. If the  $R$  sources are highly correlated, the matrix  $\mathbf{R}_S$  is nondiagonal and nearly singular (very bad conditioned).
4. If the  $R$  sources are fully correlated or *coherent*, the matrix  $\mathbf{R}_S$  is nondiagonal and rank-deficient (or singular).

---

<sup>3</sup> We define the *condition number* of a matrix  $\mathbf{A}$  as  $\kappa(\mathbf{A}) = \|\mathbf{A}\| \cdot \|\mathbf{A}^{-1}\|$ . If we use the  $l^2$  norm,  $\kappa(\mathbf{A}) = \frac{\sigma_{max}(\mathbf{A})}{\sigma_{min}(\mathbf{A})}$ , where  $\sigma_{max}$  and  $\sigma_{min}$  are the largest and the smallest singular values of matrix  $\mathbf{A}$ .  $\kappa(\mathbf{A}) \in [1, \infty)$ : if  $\mathbf{A}$  is unitary ( $\mathbf{A}^T = \mathbf{A}^{-1}$ ),  $\kappa(\mathbf{A}) = 1$ ; if  $\mathbf{A}$  is singular,  $\kappa(\mathbf{A}) = \infty$ . If  $\kappa(\mathbf{A})$  is close to 1, matrix  $\mathbf{A}$  is said to be well conditioned and its inverse can be computed with good numerical accuracy; if it is much larger than 1,  $\mathbf{A}$  is said to be ill conditioned and its inverse will be subject to large numerical errors [53].

Impinging sources are said *incoherent* if they are not fully correlated. In Section 2.9 we address the case of correlated sources.

Additional hypotheses or notations are progressively introduced when needed:

**A 1.16.** Identical sensor responses (calibration): all sensors have the same gain:  $g_\ell(\theta) = g(\theta) \forall \ell$ , or they have unit gain in all directions:  $g_\ell(\theta) = 1 \forall \ell, \forall \theta$ .

**A 1.17.** The number of time samples  $T$  is greater than the number of sensors  $L$ :  $T > L$ .

### 1.3.2. Array Manifold and Signal Subspace

The  $R$  vectors  $\mathbf{a}_r = \mathbf{a}(\theta_r) \in \mathbb{C}^L$ , *i.e.* the columns of steering matrix  $\mathbf{A}(\boldsymbol{\theta})$ , are elements of a set (not a subspace) named *array manifold* or  $\mathcal{A}$  [126], composed of all obtained steering vectors as  $\theta$  ranges over the entire parameter space<sup>4</sup>. In order to avoid ambiguities, we make a further assumption:

**A 1.18.** The map from the set of DoAs  $\boldsymbol{\theta} = [\theta_1, \dots, \theta_R]$  to  $\mathcal{R}\{\mathbf{A}(\boldsymbol{\theta})\}$ , the subspace spanned by the columns of  $\mathbf{A}(\boldsymbol{\theta})$ , is injective. This can be assured by proper array design.

If  $R < L$  (fewer sources than sensors, Assumption A 1.13), in the absence of noise, the array output  $\mathbf{x}(t) = \mathbf{A}(\boldsymbol{\theta})\mathbf{s}(t) = \sum_{r=1}^R \mathbf{a}_r s_r(t)$  is constrained into an  $R$  dimensional subspace of  $\mathbb{C}^L$ , termed *signal subspace* or  $S_X$ , that is spanned by the columns  $\mathbf{a}_r$  of steering matrix  $\mathbf{A}(\boldsymbol{\theta})$ :

$$S_X = \mathcal{R}\{\mathbf{A}(\boldsymbol{\theta})\} = \left\{ \sum_{r=1}^k s_r \mathbf{a}_r \quad \mid \quad k \in \mathbb{N}, \mathbf{a}_r \in \mathcal{A}, s_r \in \mathbb{C} \right\} \quad (1.23)$$

The *noise subspace* is defined as the orthogonal complement in  $\mathbb{C}^L$  of the signal subspace,  $S_X^\perp$ , thanks to assumptions A 1.11, A 1.13, A 1.14 and A 1.15.

Since the signal parameters of interest are related to space, the spatial covariance is fundamental for their estimation:

$$\begin{aligned} \mathbf{R}_X &= \mathbb{E} [\mathbf{x}(t)\mathbf{x}(t)^H] = \\ &= \mathbf{A}\mathbb{E} [\mathbf{s}(t)\mathbf{s}(t)^H] \mathbf{A}^H + \mathbb{E} [\mathbf{n}(t)\mathbf{n}(t)^H] = \\ &= \mathbf{A}\mathbf{R}_S\mathbf{A}^H + \sigma^2 \mathbf{I} \end{aligned} \quad (1.24)$$

where we used assumption A 1.11. Let us apply a spectral factorization to the array spatial covariance, by sorting the eigenvalues in descending order:

$$\mathbf{R}_X = \mathbf{A}\mathbf{R}_S\mathbf{A}^H + \sigma^2 \mathbf{I} = \mathbf{U}\boldsymbol{\Lambda}\mathbf{U}^H \quad (1.25)$$

where  $\mathbf{U}$  is unitary and  $\boldsymbol{\Lambda} = \text{Diag}\{\lambda_1, \lambda_2, \dots, \lambda_L\}$ , with  $\lambda_1 \geq \lambda_2 \geq \dots \geq \lambda_L$ . Hence, (1.25) can be written as

$$\mathbf{R}_X = \mathbf{U}_S\boldsymbol{\Lambda}_S\mathbf{U}_S^H + \mathbf{U}_N\boldsymbol{\Lambda}_N\mathbf{U}_N^H \quad (1.26)$$

with  $\boldsymbol{\Lambda}_S = \text{Diag}\{\lambda_1, \lambda_2, \dots, \lambda_R\}$  and  $\boldsymbol{\Lambda}_N = \sigma^2 \mathbf{I}$ , which is equivalent to  $\lambda_{R+1} = \lambda_{R+2} = \dots = \lambda_L = \sigma^2$ . Notice that  $\mathbf{U}_S = [\mathbf{u}_1 | \dots | \mathbf{u}_R]$  is formed by the  $R$  eigenvectors corresponding to the first leading eigenvalues and spanning the signal subspace, and  $\mathbf{U}_N = [\mathbf{u}_{R+1} | \dots | \mathbf{u}_L]$  is composed of the remaining eigenvectors, spanning the noise subspace. If matrix  $\mathbf{R}_X$  is full rank, the following facts are verified:

<sup>4</sup>For azimuth only estimation,  $\mathbf{A}(\boldsymbol{\theta})$  is a rope waving in  $\mathbb{C}^L$ ; for both azimuth and elevation estimation,  $\mathbf{A}(\boldsymbol{\theta})$  is a sheet in  $\mathbb{C}^L$ .

1. the columns of  $\mathbf{U}_S$  span the same space as the columns of  $\mathbf{A}$  *i.e.* the column space of  $\mathbf{A}$  and  $\mathbf{U}_S$  coincide:  $\mathcal{R}\{\mathbf{A}\} = \mathcal{R}\{\mathbf{U}_S\}$ ;
2. the columns of  $\mathbf{U}_N$  span its orthogonal complement (*i.e.* the left null space of  $\mathbf{A}$ )<sup>5</sup>.

Even more so, the columns of  $\mathbf{U}_S$  are an orthonormal basis for the column space of  $\mathbf{A}$ , and the columns of  $\mathbf{U}_N$  are an orthonormal basis for the left null space of  $\mathbf{A}$ . The signal subspace and noise subspace correspond to the column space and the left null space of  $\mathbf{A}$  respectively, with projectors

$$\begin{cases} \mathbf{\Pi}_S = \mathbf{U}_S \mathbf{U}_S^H = \mathbf{A} (\mathbf{A}^H \mathbf{A})^{-1} \mathbf{A}^H \\ \mathbf{\Pi}_N = \mathbf{U}_N \mathbf{U}_N^H = \mathbf{I} - \mathbf{A} (\mathbf{A}^H \mathbf{A})^{-1} \mathbf{A}^H \end{cases} \quad (1.27)$$

## 1.4. Polarized Waves

### 1.4.1. The 3C Sensor Response

Sections 1.2.1 and 1.2.2 refer to a scalar wavefield, whereas the present section will derive a parametric modeling for elastic vector wavefields, or polarized waves [3]. For the more general formulation of electromagnetic waves, we refer the interested reader to [96].

Let us introduce the concept of seismic *vector sensor*, measuring particle motion along three orthogonal directions. The measured physical quantity is the particle displacement recorded by the three components of a geophone, located at a given point in space, along the direction of the  $x$ -,  $y$ -, and  $z$ - axes of its reference system. The  $z$ -axis is required to be perpendicular to the earth's surface.

Analogously to the scalar array output described in Section 1.2.2, the vector sensor output excited by a single source  $s(t)$  is then expressed as:

$$\mathbf{x}(t) = \mathbf{k}(\boldsymbol{\vartheta}) s(t) + \mathbf{n}(t) \in \mathbb{C}^3 \quad (1.28)$$

where  $\mathbf{k}(\boldsymbol{\vartheta})$  refers to the response vector of the sensor and is parameterized by four angles  $\boldsymbol{\vartheta} = [\theta, \psi, \alpha, \beta]$ : azimuth  $\theta$ , elevation  $\psi$ , orientation angle  $\alpha$ , and ellipticity angle  $\beta$ .

A narrowband polarized wave  $s(t)$  induces an elliptical particle motion  $\mathbf{x}(t)$  that is restricted to a plane [3]. This polarization plane is spanned by the vectors of a  $3 \times 2$  matrix  $\mathbf{H}$ , that we choose as an orthonormal basis, as in Figure 1.6.

The restriction of the particle motion within this plane is expressed through  $\mathbf{x}(t) \in \mathcal{R}\{\mathbf{H}\}$ , or, equivalently,

$$\mathbf{x}(t) = \mathbf{H}(\theta, \psi) \boldsymbol{\xi}(\alpha, \beta, t) + \mathbf{n}(t) \quad (1.29)$$

where  $\boldsymbol{\xi} \in \mathbb{C}^2$  describes the elliptical motion. Notice that  $\boldsymbol{\xi} \in \mathbb{C}^2$  is directly related to polarization parameters and has a unique and separable representation:

$$\boldsymbol{\xi} = \mathbf{W}(\alpha) \mathbf{w}(\beta) s(t) \quad (1.30)$$

where matrix  $\mathbf{W}$  performs a rotation of the ellipse principal axis of angle  $\alpha \in (-\pi/2, \pi/2]$ , and vector  $\mathbf{w}$  draws the ellipse with ellipticity  $\beta \in [-\pi/4, \pi/4]$ :

$$\mathbf{W}(\alpha) = \begin{bmatrix} \cos \alpha & \sin \alpha \\ -\sin \alpha & \cos \alpha \end{bmatrix}, \quad \mathbf{w}(\beta) = \begin{bmatrix} \cos \beta \\ j \sin \beta \end{bmatrix} \quad (1.31)$$

<sup>5</sup> The left null space of the linear map represented as the  $L \times R$  matrix  $\mathbf{A}$  is defined as the null space of  $\mathbf{A}^H$ :  $\text{Left Null}\{\mathbf{A}\} = \{\mathbf{v} \in \mathbb{C}^L \mid \mathbf{A}^H \mathbf{v} = \mathbf{0}\}$  [53].

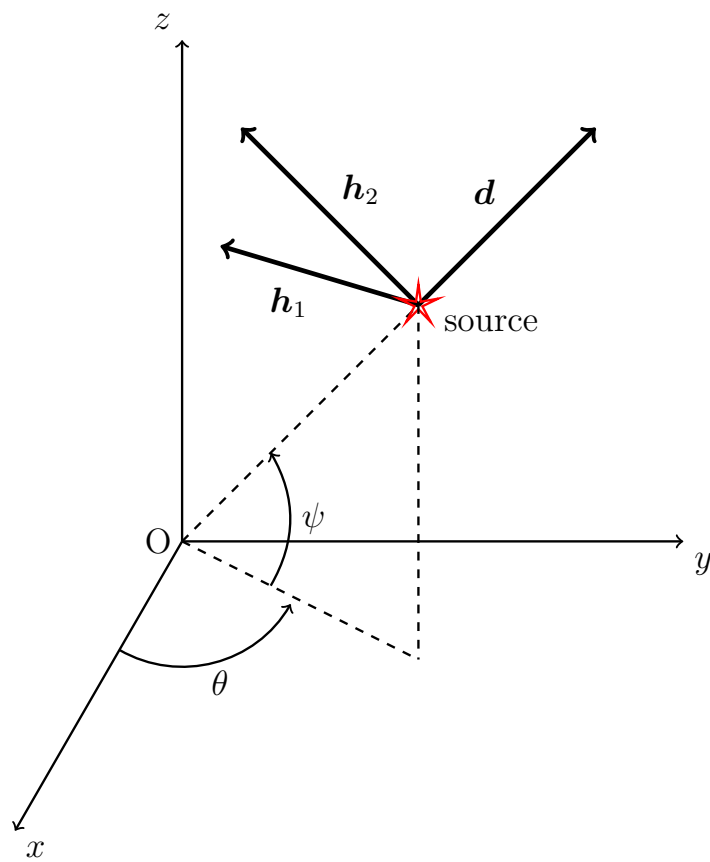


Figure 1.6.: Plane of particle motion

Finally, the resulting sensor output for  $R$  impinging sources writes:

$$\mathbf{x}(t) = \sum_{r=1}^R \mathbf{k}_r s_r(t) + \mathbf{n}(t) \in \mathbb{C}^3 \quad (1.32)$$

$$\text{with} \quad \mathbf{k}_r = \mathbf{H}(\theta_r, \psi_r) \mathbf{W}(\alpha_r) \mathbf{w}(\beta_r) \quad (1.33)$$

This model completely separates DoA, polarization parameters and time.

We can distinguish between two kinds of seismic waves:

1. *Transverse waves*: the plane of particle motion is perpendicular to the direction of propagation. This means that the columns of matrix  $\mathbf{H}$  are an orthonormal basis for the plane perpendicular to  $\mathbf{d}$ , as in Figure 1.7a:

$$\mathbf{H}_T = [\mathbf{h}_1, \mathbf{h}_2] = \begin{bmatrix} -\sin \theta & -\cos \theta \sin \psi \\ \cos \theta & -\sin \theta \sin \psi \\ 0 & \cos \psi \end{bmatrix} \quad (1.34)$$

Notice that  $\{\mathbf{d}, \mathbf{h}_1, \mathbf{h}_2\}$  forms a right orthonormal triad.

2. *Tilted generalized Rayleigh waves*: the polarization plane spanned by the ellipse semi-axes contains  $\mathbf{d}$  and  $\mathbf{h}_2$ , as in Figure 1.7b. This means that

$$\mathbf{H}_{TGR} = [\mathbf{d}, \mathbf{h}_2] = \begin{bmatrix} \cos \theta \cos \psi & -\cos \theta \sin \psi \\ \sin \theta \cos \psi & -\sin \theta \sin \psi \\ \sin \psi & \cos \psi \end{bmatrix} \quad (1.35)$$

Particular degenerate cases are *longitudinal* or *P-waves*, where  $\alpha = \beta = 0$  (the particles move along the direction of propagation); and *Rayleigh waves*, which are elliptically polarized surface waves with  $\psi = \alpha = 0$ . See Section 1.6 for more details about seismic waves and polarization.

### 1.4.2. Vector Sensor Arrays

The present section combines results from Sections 1.4.1 and 1.2.2, deriving the parametric model for an array composed of  $L$  vector, *i.e.* three-component sensors (3Cs) [3], as in Figure 1.8.

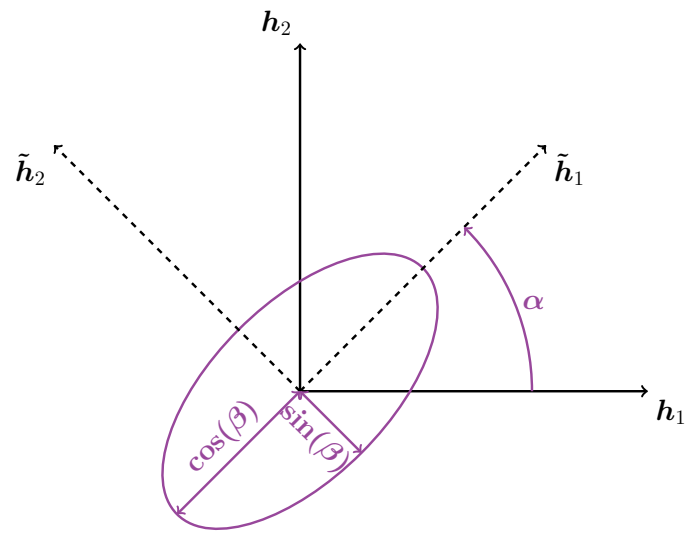
The array output at time  $t$  is given by an  $L \times 3$  matrix

$$\mathbf{X}(t) = [\mathbf{y}_1^T, \dots, \mathbf{y}_L^T] \quad (1.36)$$

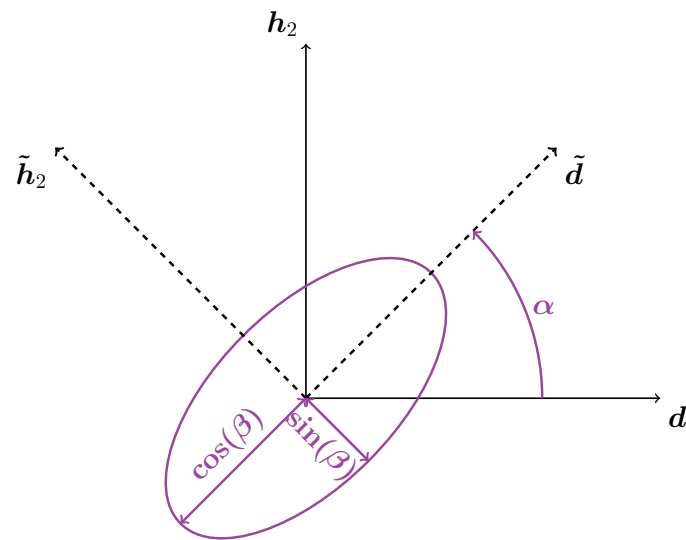
If all previous assumptions are verified, combining (1.10) and (1.32) yields

$$\begin{aligned} \mathbf{X}(t) &= \sum_{r=1}^R \mathbf{a}_r \otimes \mathbf{k}_r s_r(t) + \mathbf{N}(t) = \\ &= \mathbf{A} \mathbf{S}(t) \mathbf{K}^T + \mathbf{N}(t) \end{aligned} \quad (1.37)$$

with steering vector  $\mathbf{a}_r = \mathbf{a}(\theta_r, \psi_r)$ , and polarization vector  $\mathbf{k}_r = \mathbf{k}(\theta_r, \psi_r, \alpha_r, \beta_r)$ . Moreover,  $\mathbf{S}(t) = \text{Diag}\{s_1(t), \dots, s_R(t)\}$ ,  $\mathbf{K} = [\mathbf{k}_1, \dots, \mathbf{k}_R]$  refers to the  $3 \times R$  sensor response matrix, and  $\mathbf{A} = [\mathbf{a}_1, \dots, \mathbf{a}_R]$  refers to the  $L \times R$  array steering matrix.



(a) Polarization ellipse - TR waves



(b) Polarization ellipse - TGR waves

Figure 1.7.: Orientation and ellipticity of the polarization ellipse

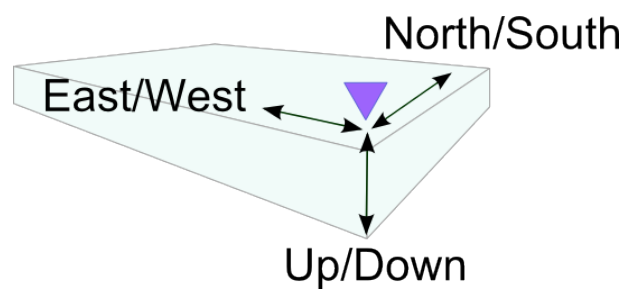


Figure 1.8.: 3C sensor

We can vectorize the array output matrix at time  $t$  as the  $\mathbb{C}^{3L}$  vector  $\mathbf{x}(t) = \text{vec}\{\mathbf{X}\}$ :

$$\begin{aligned}\mathbf{x}(t) &= \sum_{r=1}^R \mathbf{k}_r \boxtimes \mathbf{a}_r s_r(t) + \mathbf{n}(t) = \\ &= \mathbf{K} \boxtimes \mathbf{A} \mathbf{s}(t) + \mathbf{n}(t)\end{aligned}\quad (1.38)$$

where  $\mathbf{s}(t) = \text{vec}\{\mathbf{S}(t)\}$  and  $\mathbf{n}(t) = \text{vec}\{\mathbf{N}(t)\}$ . Notice that the polarized signal subspace is spanned by column vectors  $\{\mathbf{k}_1 \boxtimes \mathbf{a}_1, \dots, \mathbf{k}_R \boxtimes \mathbf{a}_R\}$ .

### 1.4.3. Another Polarization Model

In many polarimetric applications, such as RADAR, the vector sensor has  $P$  components: we can model the signal received at component  $p$  by multiplying its amplitude by  $\rho_p$  and shifting its phase by  $\phi_p$ , relative to the first (reference) component  $p = 1$  [92, 44]:

$$\mathbf{k}(\boldsymbol{\rho}, \boldsymbol{\phi}) = [1, \rho_1 e^{j\phi_1}, \dots, \rho_P e^{j\phi_P}]^\top \quad (1.39)$$

where  $\boldsymbol{\rho} = [1, \rho_1, \dots, \rho_P]^\top$ , and  $\boldsymbol{\phi} = [1, \phi_1, \dots, \phi_P]^\top$ . Thus polarimetric models in (1.37) and (1.38) attain a decoupled form

$$\begin{cases} \mathbf{X}(t) = \sum_{r=1}^R \mathbf{a}_r \otimes \mathbf{k}_r s_r(t) + \mathbf{N}(t) \in \mathbb{C}^{L \times P} \\ \mathbf{x}(t) = \sum_{r=1}^R \mathbf{k}_r \boxtimes \mathbf{a}_r s_r(t) + \mathbf{n}(t) \in \mathbb{C}^{LP} \end{cases} \quad (1.40)$$

in which steering vector  $\mathbf{a}_r = \mathbf{a}(\theta_r, \psi_r)$ , and polarization vector  $\mathbf{k}_r = \mathbf{k}(\boldsymbol{\rho}_r, \boldsymbol{\phi}_r)$  depend on distinct parameters. DoA and polarization information are then decoupled.

## 1.5. Wideband Sources

### 1.5.1. Wideband Scalar Wavefields

Let us consider a wideband wavefield with carrier  $\omega_c$ :  $E(\mathbf{p}, t) = s(t - \mathbf{p}^\top \boldsymbol{\kappa}) e^{j\omega_c t}$  measured at position  $\mathbf{p}$  and time  $t$ , and its Fourier Transform (FT)

$$E(\mathbf{p}, \omega) = \int_{-\infty}^{\infty} E(\mathbf{p}, t) e^{-j\omega t} dt \quad (1.41)$$

If the spectral bandwidth  $B_s$  of the complex envelope  $s(\cdot)$  is not negligible in (1.5), a time delay is not equivalent to a phase shift anymore:  $s(t - \tau) \neq s(t) e^{-j\omega\tau}$ . However, thanks to the time shift theorem of FT  $\mathcal{F}(\cdot)$ , a translation in time domain translates into a phase shift in frequency domain:

$$s(t - \tau) \longleftrightarrow \hat{s}(\omega) e^{-j\omega\tau} \quad (1.42)$$

where  $\hat{s} = \mathcal{F}(s)$ . Therefore, in order to use the spatial information of the acquisition system, we need to work with Fourier transformed data.

The real wideband signal received at the  $\ell$ th sensor at time  $t$  can be modeled as

$$x_\ell(t) = \sum_{r=1}^R g_\ell(\theta_r) s_r(t - \tau_\ell(\theta_r)) + n_\ell(t), \quad (1.43)$$

where  $s_r(t)$  is the signal transmitted by the  $r$ th source,  $t \in \{1, 2, \dots, T\}$ ,  $g_\ell(\theta_r)$  is the gain of the  $\ell$ th sensor,  $\tau_\ell(\theta_r)$  was defined in (1.7) and  $n_\ell(t)$  is an additive noise. We make one further assumption:

**A 1.19.** Sensor gains  $g_\ell$  are *a priori* unknown functions unless otherwise specified, real (which is actually equivalent to assuming that their phase is known) and independent of frequency.

Denote by  $x(\omega)$  the FT of  $x(t)$ . In this framework, thanks to (1.42), model (1.43) can be equivalently rewritten in the frequency domain:

$$x_\ell(\omega) = \sum_{r=1}^R a_\ell(\omega, \theta_r) s_r(\omega) + n_\ell(\omega) \quad (1.44)$$

where  $x_\ell(\omega) = \mathcal{F}\{x_\ell(t)\}$  is the FT of  $x_\ell(t)$ , and  $\omega = \omega_1, \dots, \omega_Q$  if we take the Discrete Fourier Transform (DFT);  $n_\ell(\omega)$  refers to a circular Gaussian white noise process at the  $\ell$ -th sensor, thanks to Assumption 1.12. Notice that the steering element

$$a_\ell(\omega, \theta_r) = g_\ell(\theta_r) e^{-j\omega\tau_\ell(\theta_r)} \quad (1.45)$$

is now a function of both frequency and DoA.

Alternatively, in vector form, (1.44) becomes

$$\begin{aligned} \mathbf{x}(\omega) &= \sum_{r=1}^R \mathbf{a}(\omega, \theta_r) s_r(\omega) + \mathbf{n}(\omega) = \\ &= \mathbf{A}(\omega, \boldsymbol{\theta}) \mathbf{s}(\omega) + \mathbf{n}(\omega) \end{aligned} \quad (1.46)$$

where matrix  $\mathbf{A}(\omega, \boldsymbol{\theta}) \in \mathbb{C}^{L \times R}$  depends on the vector of DoAs,  $\boldsymbol{\theta} = [\theta_1, \dots, \theta_R]^\top$ . Thanks to Assumption 1.11, noise  $\mathbf{n}(\omega)$  is circular complex white Gaussian, with covariance  $\sigma^2 \mathbf{I}$ . The  $r$ -th column of  $\mathbf{A}(\omega, \boldsymbol{\theta})$ , denoted  $\mathbf{a}_r(\omega) = \mathbf{a}(\omega, \theta_r)$  in the remainder, is the value of the *array manifold* for radial frequency  $\omega$  taken at  $\theta = \theta_r$ . Therefore, the array manifold and the signal subspace are now frequency dependent. Moreover, notice that also spatial covariance  $\mathbf{R}_X$  in (1.24) becomes frequency dependent:

$$\mathbf{R}_X(\omega) = \mathbb{E} [\mathbf{x}(\omega) \mathbf{x}(\omega)^H] \quad (1.47)$$

## 1.5.2. Polarized wideband sources

This section combines the wideband scalar model in Section 1.5.1 with wave polarization in Section 1.4. For this purpose, we will need a further assumption:

**A 1.20.** The polarization parameters  $\alpha$  and  $\beta$  of impinging wavefronts are independent of frequency.

Wideband output in (1.38) and polarized output (1.46) combined together yield a  $L \times 3$  wideband polarized output:

$$\begin{aligned} \mathbf{X}(\omega) &= \sum_{r=1}^R \mathbf{a}_r(\omega) \otimes \mathbf{k}_r s_r(\omega) + \mathbf{N}(\omega) = \\ &= \mathbf{A}(\omega) \mathbf{S}(\omega) \mathbf{K}^\top + \mathbf{N}(\omega) \end{aligned} \quad (1.48)$$

with steering vector  $\mathbf{a}_r(\omega) = \mathbf{a}(\omega, \theta_r, \psi_r)$ , and polarization vector  $\mathbf{k}_r = \mathbf{k}(\theta_r, \psi_r, \alpha_r, \beta_r)$ . Moreover,  $\mathbf{S}(\omega) = \text{Diag}\{s_1(\omega), \dots, s_R(\omega)\}$ ,  $\mathbf{K} = [\mathbf{k}_1, \dots, \mathbf{k}_R]$  refers to the  $3 \times R$  sensor response matrix, and  $\mathbf{A}(\omega) = [\mathbf{a}_1(\omega), \dots, \mathbf{a}_R(\omega)]$  refers to the  $L \times R$  array steering matrix.

We can vectorize the array output matrix at frequency  $\omega$  as the  $\mathbb{C}^{3L}$  vector  $\mathbf{x}(\omega) = \text{vec}\{\mathbf{X}(\omega)\}$

$$\begin{aligned}\mathbf{x}(\omega) &= \sum_{r=1}^R \mathbf{k}_r \boxtimes \mathbf{a}_r(\omega) s_r(\omega) + \mathbf{n}(\omega) = \\ &= \mathbf{K} \boxtimes \mathbf{A}(\omega) \mathbf{s}(\omega) + \mathbf{n}(\omega)\end{aligned}\quad (1.49)$$

where  $\mathbf{s}(\omega) = \text{vec}\{\mathbf{S}(\omega)\}$  and  $\mathbf{n}(\omega) = \text{vec}\{\mathbf{N}(\omega)\}$ . Notice that the polarized signal subspace at frequency  $\omega$  is spanned by column vectors  $\{\mathbf{k}_1 \boxtimes \mathbf{a}_1(\omega), \dots, \mathbf{k}_R \boxtimes \mathbf{a}_R(\omega)\}$ .

## 1.6. Seismic Waves

The importance of sensor arrays for the analysis of seismic waves was illustrated in [123]. As we briefly mentioned in Section 1.4, [3] made a simple inventory of seismic waves according to their polarization type. More generally, we can distinguish between *volume* or *body* waves and *surface* waves [133, 134].

### Volume or body waves

Two types of waves can propagate through a homogeneous isotropic solid medium, one corresponding to changes in dilatation and the other to rotation [134].

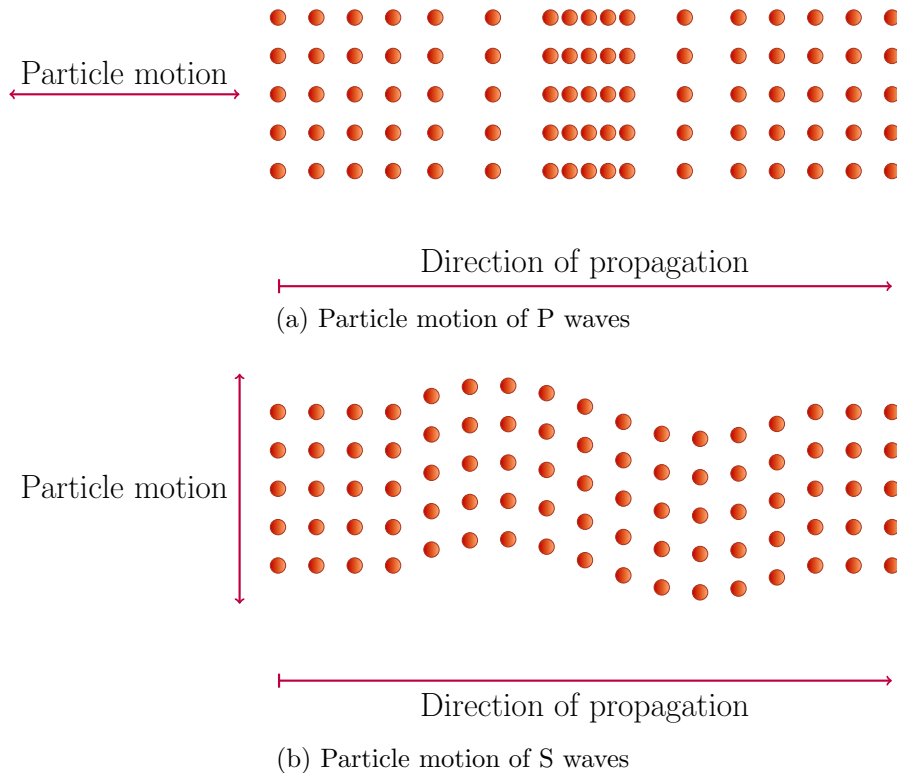


Figure 1.9.: Particle motion of seismic volume waves

- P waves (or *primary*, *dilatational*, *compressional*, *irrotational*, *longitudinal* waves). Since their particle motion is parallel to the direction of propagation, as in Figure 1.9a, they are linearly polarized.

- S, SH, SV waves (or *transverse, shear, rotational, secondary*): their particle motion lies in the plane perpendicular to the direction of propagation, as in Figure 1.9b. They can be linearly or elliptically polarized.

Linear polarization refers to the fact that more coherent seismic energy is located in one principal direction of particle motion [98].

Seismic events originating at depth, one has to deal with a double arrival of elastic body waves: P waves and S waves. They have different propagation velocities and a variable frequency content: the former tend to have a higher frequency content and are characterized by higher propagation speed than the latter. Hence, the P wave arrives first, whereas the S wave is the second arrival observed on seismic records. P waves and S waves have theoretical velocities  $v_1$  and  $v_2$ , respectively, given by Ref. [133]:

$$\begin{cases} v_1 = \left( \frac{\lambda+2\mu}{\rho} \right)^{\frac{1}{2}} \\ v_2 = \left( \frac{\mu}{\rho} \right)^{\frac{1}{2}} \end{cases} \quad (1.50)$$

where  $\lambda$  and  $\mu$  are *Lamé's constants* and  $\rho$  is the density of the medium. Since they are positive constants,  $v_1$  is greater than  $v_2$ . In particular, the velocity of the S wave ranges from zero up to 70% of the velocity of the P wave. For fluids  $\mu$  is zero,  $v_2 = 0$  and therefore S waves do not propagate. Typical velocities are in the  $1.5\text{km/s}$  (in water) to  $6.5\text{km/s}$  range, increasing with loss of porosity, cementation, age and depth [134].

For the physical model of wave propagation, the following property is assumed:

**A 1.21.** P and S waves propagate at velocities  $v_1$  and  $v_2$ , respectively, under the approximation of non-dispersive medium A 1.6.

## Surface waves

When the  $xy$ -plane separates two media with different properties, solutions decreasing like  $e^{-\kappa z}$  (evanescent waves) exist under certain conditions. Their amplitude decreases exponentially with the distance from the interface, and their energy is tied to the surface [134].

- Rayleigh waves, surface elliptically polarized waves with the ellipse major axis corresponding to the direction of propagation. They propagate along a free surface of a solid, where free means contact with vacuum or with air, as the elastic constant and density of air are negligible compared with that of rocks. Rayleigh waves are often referred to as *ground roll*. They are dispersive, low velocity, low frequency, with a broad flat spectrum [133].
- Other examples include Stoneley waves, Love waves, Tube waves.

## 1.7. Parameters of Interest

In the first part of this chapter we described the model of plane waves with unknown wavenumber impinging into the array. The parameters of interest  $\boldsymbol{\vartheta}$  enter into the model in a non linear way. The problem of estimating the source wavenumbers or angles of arrivals of multiple plane waves is referred to as Direction of Arrival or DoA estimation. This problem is widespread in many scientific domains, such as radar, sonar, seismic, medical diagnosis and astronomy [151]. The narrowband model we refer to in the remainder is developed in Section 1.2.2, whereas the wideband model can be found in Section 1.5.1.

As we explained in Section 1.2.3, in 3D for a single plane wave, the parameters of interest form a vector:  $\boldsymbol{\vartheta} = [\theta, \psi]^\top \in \mathbb{R}^2$ ; in 2D it is a scalar  $\boldsymbol{\vartheta} = \theta \in \mathbb{R}$ . With  $R$  sources, this corresponds to

$$\boldsymbol{\Theta} = [\boldsymbol{\theta}, \boldsymbol{\psi}] = \begin{bmatrix} \theta_1 & \psi_1 \\ \vdots & \vdots \\ \theta_R & \psi_R \end{bmatrix} \in \mathbb{R}^{R \times 2}, \quad \boldsymbol{\theta} = \begin{bmatrix} \theta_1 \\ \vdots \\ \theta_R \end{bmatrix} \in \mathbb{R}^R \quad (1.51)$$

respectively. In the case of polarized waves, we might also be interested in estimating the polarization parameters  $\boldsymbol{\phi} = [\alpha, \beta]^\top \in \mathbb{R}^2$ , or, for  $R$  sources:

$$\boldsymbol{\Xi} = [\boldsymbol{\alpha}, \boldsymbol{\beta}] = \begin{bmatrix} \alpha_1 & \beta_1 \\ \vdots & \vdots \\ \alpha_R & \beta_R \end{bmatrix} \in \mathbb{R}^{R \times 2} \quad (1.52)$$

We can arrange all parameters of interest into a vector  $\boldsymbol{\vartheta}$ :

1. For scalar wavefields in 3D, we have:

$$\begin{aligned} \boldsymbol{\vartheta} &= [\boldsymbol{\theta}^\top, \boldsymbol{\psi}^\top]^\top = \\ &= [\theta_1, \dots, \theta_R, \psi_1, \dots, \psi_R]^\top \in \mathbb{R}^{2R} \end{aligned} \quad (1.53)$$

2. For scalar wavefields in 2D, we have:

$$\boldsymbol{\vartheta} = \boldsymbol{\theta} = [\theta_1, \dots, \theta_R]^\top \in \mathbb{R} \quad (1.54)$$

3. For vector wavefields in 3D, we have:

$$\begin{aligned} \boldsymbol{\vartheta} &= [\boldsymbol{\theta}^\top, \boldsymbol{\psi}^\top, \boldsymbol{\alpha}^\top, \boldsymbol{\beta}^\top]^\top = \\ &= [\theta_1, \dots, \theta_R, \psi_1, \dots, \psi_R, \alpha_1, \dots, \alpha_R, \beta_1, \dots, \beta_R]^\top \in \mathbb{R}^{4R} \end{aligned} \quad (1.55)$$

4. For vector wavefields in 2D, we have:

$$\begin{aligned} \boldsymbol{\vartheta} &= [\boldsymbol{\theta}^\top, \boldsymbol{\alpha}^\top, \boldsymbol{\beta}^\top]^\top = \\ &= [\theta_1, \dots, \theta_R, \alpha_1, \dots, \alpha_R, \beta_1, \dots, \beta_R]^\top \in \mathbb{R}^{3R} \end{aligned} \quad (1.56)$$

In many cases, we might also be interested in extracting the source signatures  $\{s_1(t), \dots, s_R(t)\}$ , which can be stored in a  $T \times R$  matrix

$$\boldsymbol{S} = \begin{bmatrix} s_1(1) & \dots & s_R(1) \\ \vdots & \ddots & \vdots \\ s_1(T) & \dots & s_R(T) \end{bmatrix} = [\boldsymbol{s}_1, \dots, \boldsymbol{s}_R] \quad (1.57)$$

or a vector  $\boldsymbol{\xi} = [\boldsymbol{s}_1^\top, \dots, \boldsymbol{s}_R^\top]^\top \in \mathbb{C}^{TR}$ .

Other problems, which are beyond the scope of this thesis, include the following:

1. Array *calibration*, *i.e.* the estimation of the positions and gains of sensors:  
 sensor position matrix  $\mathbf{P} = [\mathbf{p}_1, \dots, \mathbf{p}_L]^T \in \mathbb{R}^{L \times 3}$ ;  
 sensor gain patterns  $[g_1(\theta), \dots, g_L(\theta)]$ .
2. ARMA modeling and parameter estimation.
3. Estimation of the range of near field sources.

The next chapter will introduce high resolution DoA and polarization estimation for both narrowband and wideband impinging wavefields. We will restrain our interest to the signal subspace approach (cf. Section 1.3 for the definition of signal and noise subspace).

## 1.8. The Sample Covariance Matrix

In Section 1.2.2 we derived the spatial covariance matrix in (1.24), assuming we dispose of an infinite observation period. However, the natural estimate of this quantity is the sample covariance matrix. To this purpose, we can use either the narrowband snapshot model in time domain or in frequency domain. In time domain we have:

$$\hat{\mathbf{R}}_X = \frac{1}{T} \sum_{t=1}^T \mathbf{x}(t)\mathbf{x}(t)^H = \mathbf{X}\mathbf{X}^H \quad (1.58)$$

where appears the  $L \times T$  data matrix  $\mathbf{X} = [\mathbf{x}(1), \dots, \mathbf{x}(T)]$ .

If there are multiple independent and identically distributed complex Gaussian snapshots available,  $\mathbf{X}_1, \dots, \mathbf{X}_{N_S}$ , we define the sample covariance matrix as [151]

$$\hat{\mathbf{R}}_X = \frac{1}{N_S} \sum_{j=1}^{N_S} \mathbf{X}_j \mathbf{X}_j^H \quad (1.59)$$

On the other hand, after DFT with  $Q$  frequency bins, frequency dependent spatial covariance in (1.47) is estimated as:

$$\hat{\mathbf{R}}_X(\omega_q) = \frac{1}{N_S} \sum_{j=1}^{N_S} \mathbf{x}_j(\omega_q)\mathbf{x}_j(\omega_q)^H \quad (1.60)$$

If we do not impose our knowledge of the array manifold upon it,  $\hat{\mathbf{R}}_X$  is the Maximum Likelihood Estimator (MLE) of the spectral matrix, and its spectral representation is

$$\hat{\mathbf{R}}_X = \hat{\mathbf{U}}_S \hat{\mathbf{\Lambda}}_S \hat{\mathbf{U}}_S^H + \hat{\mathbf{U}}_N \hat{\mathbf{\Lambda}}_N \hat{\mathbf{U}}_N^H \quad (1.61)$$

The sampling process generates a sequence of Gaussian random vectors (cf. Assumptions A 1.12 and A 1.15), we assume that resulting vectors at different time instants  $t$ , in different frequency bins  $\omega_q$  and different observation snapshots are statistically independent [151]. Therefore, one can prove that the time domain model and the frequency domain model, for the narrowband case, have identical spatial statistics, resulting in identical subsequent processing [151]. This means that if the sources are narrowband, the two equations in (1.58) and (1.60) have the same spatial structure, allowing us to work indifferently in time or frequency domain.

# Appendix

## 1.A. Signal Complex Envelope

A time series  $x(t)$  can be considered a *pass-band* signal if its spectral support is limited and it does not include the origin:

$$[-f_0 - W, -f_0 + W] \cup [f_0 - W, f_0 + W], \quad \text{with } \infty > f_0 > W > 0 \quad (1.62)$$

Every *pass-band* signal can be associated with an *analytic* signal  $\hat{x}(t)$  whose support does not contain positive frequencies:

$$\hat{X}(f) = \sqrt{2} U_+(f) X(f) \longleftrightarrow \hat{x}(t) = \frac{1}{\sqrt{2}} [x(t) + jH\{x(t)\}] \quad (1.63)$$

where  $U_+(\cdot)$  indicates the Heaviside step function, and  $H\{x(t)\}$  refers to the Hilbert transform of real signal  $x(t)$ . Since a real signal is characterized by even spectral symmetry, it can be represented by its analytic signal without loss of information.

The complex envelope of  $x(t)$  around frequency  $f_0$ , or *base-band* signal, is obtained from the analytic signal by a mere translation in frequency:

$$\check{X}(f) = \hat{X}(f + f_0) \longleftrightarrow \check{x}(t) = \hat{x}(t)e^{-j2\pi f_0 t} \quad (1.64)$$

For a given carrier at frequency  $f_0$ , a complex envelope around  $f_0$  is in bijection with a complex number representing the modulus and the phase of the carrier.

## 2. Signal Parameter Estimation in 2D

### 2.1. Introduction

After introducing in Chapter 1 the basics of the sensor array model, we dedicate the present chapter to the problem of high resolution signal parameter estimation. In particular, the parameters of interest are represented by directions of arrival, polarization features and source signatures. The term 2D in the title refers to traditional matrix approaches, relying on time and space information: in the time model of (1.12) data can be described by a matrix  $\mathbf{X} \in \mathbb{C}^{L \times T}$  for the narrowband case, and a matrix  $\mathbf{X} \in \mathbb{C}^{L \times Q}$  for the wideband case. Useful information is derived by sampling impinging wavefields in time and space, and through the computation of the spatial covariance matrix in (1.58) and (1.60). Whenever other physical dimensions are present, such as polarization, data are vectorized as in (1.38) and (1.49), so that their inner structure is lost and the main representation remains a long matrix  $\mathbf{X} \in \mathbb{C}^{3L \times T}$  in time domain, and  $\mathbf{X} \in \mathbb{C}^{3L \times Q}$  in frequency domain.

In Section 2.2 we lay the basis for the evaluation of the performance of an estimator, through the definition of the log-likelihood and the performance bound (Cramér-Rao Bound). In Section 2.3 we introduce the two main approaches for signal parameter estimation: spectral and parametric methods.

After briefly introducing beamforming in Section 2.4, we detail the main high resolution signal subspace methods, MUSIC and ESPRIT, in Sections 2.5 and 2.6, respectively. These algorithms are evaluated and compared with the performance bound of Section 2.2 and in terms of computational cost. Sections 2.7 and 2.8 extend the signal subspace to the separation of polarized and wideband waves.

Finally, in Section 2.9 we discuss the case of correlated noise and correlated sources, *i.e.* when Assumptions A 1.11 and A 1.15 are not verified.

### 2.2. Performance of an Estimator

The  $N_S$  snapshots  $\mathbf{x}_j(t)$  or  $\mathbf{x}_j(\omega)$  introduced in Section 1.8 are statistically independent, so we can deal with one single snapshot and combine the results at the end.

As previously stated, thanks to Assumptions A 1.12, the observation  $\mathbf{x}(t)$  or  $\mathbf{x}(\omega)$  is a complex Gaussian random vector  $\mathbf{x}$  whose mean  $\boldsymbol{\mu}(\boldsymbol{\vartheta})$  and covariance  $\mathbf{R}_X(\boldsymbol{\vartheta})$  depend on real parameter vector  $\boldsymbol{\vartheta}$ . In the remainder, in the light of Section 1.7,  $\boldsymbol{\vartheta}$  is an arbitrary vector of parameters, and it does not necessarily indicate an angle [151].

The variance of any unbiased estimator is bounded by the Cramér-Rao Bound (CRB): if  $\boldsymbol{\vartheta}$  is modeled as deterministic, the performance of the estimator is bounded by the classical CRB; if it is modeled as a random variable, we need a Bayesian CRB, and if it is partially random, we need a hybrid CRB. In the remainder we will assume that  $\boldsymbol{\vartheta}$  is fully deterministic.

The *likelihood*, *i.e.* the probability density for a single snapshot is then given by

$$p(\mathbf{x}|\boldsymbol{\vartheta}) = \frac{1}{\det\{\pi\mathbf{R}_X(\boldsymbol{\vartheta})\}} \exp\left\{-\left(\mathbf{x}^H - \boldsymbol{\mu}^H(\boldsymbol{\vartheta})\right)\mathbf{R}_X^{-1}(\boldsymbol{\vartheta})\left(\mathbf{x} - \boldsymbol{\mu}(\boldsymbol{\vartheta})\right)\right\} \quad (2.1)$$

where  $\mathbf{x} \in \mathbb{C}^L$  is a complex Gaussian random variable and  $\boldsymbol{\vartheta} \in \mathbb{R}^D$  is the real deterministic vector we want to estimate. In Chapter 7 we will develop the subject of the estimation of a complex parameter vector.

For i.i.d. snapshots, the likelihood is the product

$$p(\mathbf{x}_1, \dots, \mathbf{x}_{N_S}|\boldsymbol{\vartheta}) = \prod_{j=1}^{N_S} \frac{1}{\det\{\pi\mathbf{R}_X(\boldsymbol{\vartheta})\}} \exp\left\{-\left(\mathbf{x}_j^H - \boldsymbol{\mu}^H(\boldsymbol{\vartheta})\right)\mathbf{R}_X^{-1}(\boldsymbol{\vartheta})\left(\mathbf{x}_j - \boldsymbol{\mu}(\boldsymbol{\vartheta})\right)\right\} \quad (2.2)$$

The *log-likelihood* corresponding to (2.2) is given by

$$\begin{aligned} \mathcal{L}_x(\boldsymbol{\vartheta}) &= \mathcal{L}(\mathbf{x}_1, \dots, \mathbf{x}_{N_S}|\boldsymbol{\vartheta}) = \log[p(\mathbf{x}_1, \dots, \mathbf{x}_{N_S}|\boldsymbol{\vartheta})] = \\ &= -N_S \log[\det\{\mathbf{R}_X(\boldsymbol{\vartheta})\}] - \sum_{j=1}^{N_S} \left(\mathbf{x}_j^H - \boldsymbol{\mu}^H(\boldsymbol{\vartheta})\right)\mathbf{R}_X^{-1}(\boldsymbol{\vartheta})\left(\mathbf{x}_j - \boldsymbol{\mu}(\boldsymbol{\vartheta})\right) - N_S L \log \pi \end{aligned} \quad (2.3)$$

In many cases of interest, either  $\boldsymbol{\mu}(\boldsymbol{\vartheta})$  or  $\mathbf{R}_X(\boldsymbol{\vartheta})$  (but not both) are a function of parameter vector  $\boldsymbol{\vartheta}$ .

We denote the covariance matrix of an unbiased estimator as

$$\mathbf{C}(\boldsymbol{\vartheta}) = \mathbb{E}\left[\left(\hat{\boldsymbol{\vartheta}} - \boldsymbol{\vartheta}\right)\left(\hat{\boldsymbol{\vartheta}} - \boldsymbol{\vartheta}\right)^T\right] \quad (2.4)$$

The multiple parameter CRB states that [151]

$$\mathbf{C}(\boldsymbol{\vartheta}) \geq \mathbf{C}_{CRB}(\boldsymbol{\vartheta}) \triangleq \mathbf{F}^{-1} \quad (2.5)$$

for any unbiased estimate of  $\boldsymbol{\vartheta}$ . The matrix inequality means that  $\mathbf{C}(\boldsymbol{\vartheta}) - \mathbf{C}_{CRB}$  is a non negative definite matrix.  $\mathbf{F}$  denotes the Fisher Information Matrix (FIM):

$$\mathbf{F} \triangleq -\mathbb{E}\left[\nabla_{\boldsymbol{\vartheta}}\left(\nabla_{\boldsymbol{\vartheta}}\left(\mathcal{L}_x(\boldsymbol{\vartheta})\right)\right)^T\right] \quad (2.6)$$

with elements

$$F_{ij} \triangleq -\mathbb{E}\left[\frac{\partial \mathcal{L}_x(\boldsymbol{\vartheta})}{\partial \vartheta_i} \frac{\partial \mathcal{L}_x(\boldsymbol{\vartheta})}{\partial \vartheta_j}\right] = -\mathbb{E}\left[\frac{\partial^2 \mathcal{L}_x(\boldsymbol{\vartheta})}{\partial \vartheta_i \partial \vartheta_j}\right] \quad (2.7)$$

The result (2.5) also provides a bound on the variance of any unbiased estimate of scalar element  $\vartheta_i$ :

$$\text{Var}(\hat{\vartheta}_i - \vartheta_i) \geq [\mathbf{C}_{CRB}(\boldsymbol{\vartheta})]_{ii} = [\mathbf{F}^{-1}]_{ii} \quad (2.8)$$

The effect of considering multiple snapshots with respect to the single snapshot case is that the CRB is divided by  $N_S$ .

When we generate multiple realizations of the same process, we estimate the variance  $\text{Var}(\hat{\vartheta}_i - \vartheta_i)$  through  $N$  Monte Carlo (MC) trials, by computing the Mean Square Error (MSE):

$$\text{MSE}(\vartheta_i) = \frac{1}{N} \sum_{n=1}^N (\hat{\vartheta}_n - \vartheta_i)^2 \quad (2.9)$$

In order to assess the performance of the unbiased estimator, we are also interested in plotting its MSE as a function of the Signal to Noise Ratio (SNR) in *dB*:

$$\text{SNR} = 10 \log_{10} \frac{P_s}{P_n} \quad (2.10)$$

where  $P_s$  and  $P_n$  refer to average signal and noise power. We are interested in comparing  $\text{MSE}(\vartheta_i)$  with the SNR. An estimator is said efficient if it reaches the CRB, *i.e.* when its variance equals the CRB:  $\mathbf{C}(\vartheta) = \mathbf{C}_{CRB}(\vartheta)$ . The Maximum Likelihood Estimator (MLE), which maximizes the log-likelihood, is asymptotically (for  $N_S \rightarrow \infty$ ) efficient. Many other estimators come close to the CRB for high SNR: the value of the SNR at which this convergence occurs is referred to as *threshold*. Estimators with a lower threshold SNR are said to have a better threshold behavior.

## 2.3. Spectral and Parametric Approaches

Before introducing the estimation of signal parameters of interest, we need to make a further assumption:

**A 2.1.** In what follows, the number of impinging sources  $R$  is supposed to be known.

In Chapter 1 we modeled the array output as a function of signal parameters such as the Directions of Arrival (DoAs)  $\theta_r, \psi_r$  and wave polarization angles  $\alpha_r, \beta_r$ . The goal of array processing is to estimate these parameters, starting from the the array output  $\mathbf{x}(t)$ .

We can distinguish between two main approaches [79]:

1. The spectral approach maximizes a spectrum-like scalar function of the parameters of interest, looking for its  $R$  highest peaks. We can include into this class beamforming and the most known signal subspace method, spectral MUSIC.
2. The parametric approach requires a simultaneous search for all parameters, providing more accurate but also more computationally expensive solutions. We can include into this class both deterministic and stochastic MLEs, sub-space approximations, root-MUSIC and ESPRIT.

Subspace methods such as MUSIC, root-MUSIC and ESPRIT achieve higher resolution than conventional beamforming techniques and are thus called *high resolution methods*. We will briefly introduce beamforming, but we will detail in particular MUSIC and ESPRIT, as they are among the most versatile and widespread high resolution methods for signal parameter estimation, though not implying the heavy computational burden of MLE [79, 17]. Notice that MUSIC, ESPRIT and the deterministic ML belong to the general class of subspace-fitting algorithms [153, 142].

## 2.4. Beamforming

Beamforming (BF) builds a specific spatial response of the array (*i.e.* a beam pointing to the desired source, and hopefully nulls towards other interferences) in order to estimate the signature of the sources impinging on the array in the presence of noise. The steering directions that result in maximum output power are the DoA estimates. An exhaustive

search involves the presteering of the array in a given look direction  $\theta \in (-\pi, \pi]$ , by applying a sensor dependent time delay  $T_\ell(\theta) = T_0 + \tau_\ell(\theta)$ :

$$x_\ell^{ps}(t, \theta) = x_\ell(t + T_\ell(\theta)) \quad \ell = 0, \dots, L-1 \quad (2.11)$$

where  $T_0$  is a bulk delay such that  $T_\ell(\theta) > 0, \forall \ell$  [51]. The BF output is then given by  $y(t, \theta) = \sum_{\ell=1}^L x_\ell^{ps}(t, \theta)$ . A time interpolation is then necessary for a correct implementation of presteering delays in order to extrapolate signal values at given time delays between two original samples. The effect of presteering in a source direction  $\theta = \theta_r$  is a spatial alignment of all the waveforms on all sensors, corresponding to a local maximum energy output when  $\theta = \theta_r$ :  $x_\ell^{ps}(t, \theta_r) \approx s_r(t + T_0), \forall \ell$ .

The steering operation of narrowband BF can be achieved through a linear combination of spatial samples through weight vector  $\mathbf{w} \in \mathbb{C}^L$ , in the same manner that a Finite Impulse Response (FIR) filter linearly combine temporally sampled data [152]:

$$y(t) = \sum_{\ell=1}^L w_\ell^* x_\ell(t) = \mathbf{w}^H \mathbf{x}(t) \quad (2.12)$$

with associated output power

$$P(\mathbf{w}) = \frac{1}{T} \sum_{t=1}^T |y(t)|^2 = \frac{1}{T} \sum_{t=1}^T \mathbf{w}^H \mathbf{x}(t) \mathbf{x}(t)^H \mathbf{w} = \mathbf{w}^H \hat{\mathbf{R}}_X \mathbf{w} \quad (2.13)$$

where we observe the sample covariance matrix  $\hat{\mathbf{R}}_X$ . The spatial resolution depends on the size in wavelengths of the array aperture. However, when the signal bandwidth increases, its performance degrades. One of the first Tapped Delay Line (TDL) time domain solutions was provided for this purpose by [47] and involves a TDL scheme (or FIR filters for the discrete case). A temporal filter is applied to each wideband recorded signal to compensate for the phase difference of different frequency components; this is equivalent to a temporal and spatial sampling of the propagating wavefield: [89, 52]

$$y(k) = \sum_{l=1}^L \sum_{i=0}^{J-1} w_{li}^* x_\ell(k - iT_s) = \mathbf{w}^H \mathbf{x}(k) \quad (2.14)$$

where  $J$  is the length of the filter corresponding to the TDL,  $T_s$  is the delay between adjacent lags of the TDL. We also need to properly define long vectors  $\mathbf{w}, \mathbf{x} \in \mathbb{C}^{LJ}$ . For the sake of simplicity, we will assume  $T_s$  equal to sampling period. Analogously to the frequency response of a FIR filter<sup>1</sup>, when the signal is a complex plane wave with DoA  $\theta$  and frequency  $\omega$ , we have:

$$y(k) = e^{j\omega k} \sum_{l=1}^L \sum_{i=0}^{J-1} w_{li}^* e^{j\omega(\tau_\ell(\theta)+i)} = e^{j\omega k} \gamma(\omega, \theta) \quad (2.15)$$

where the beamformer response  $\gamma$  is a function of steering vector  $\mathbf{a}(\omega, \theta)$ :

$$\gamma(\omega, \theta) = \mathbf{w}^H \mathbf{a}(\omega, \theta) \quad (2.16)$$

<sup>1</sup>The analogy of BF and FIR filtering is closest when the sensor array is a ULA and we fix a single temporal frequency  $\omega_0$ , if we establish a mapping between temporal frequency for the FIR filter and the cosine of the DoA for the beamformer:  $\omega = \omega_0 p_0 \cos(\theta)/c$ .

The beampattern is given by its square modulus  $|\gamma(\omega, \theta)|^2$ .

The type of beamformer will depend on the procedure for choosing weight vector  $\mathbf{w}$ : the most common examples are Bartlett and Capon beamformers, and Linearly Constrained Minimum Variance (LCMV) beamformer [152]. When the number of sources increases, the performance of time domain beamforming rapidly degrades and is by far exceeded by high resolution techniques.

## 2.5. Spectral MUSIC

The interest in the subspace approach is mainly due to the introduction of the Multiple Signal Characterization (MUSIC) algorithm and its performance capability [131]: received data are used to estimate the signal subspace described in Section 1.3, and then this information is used to estimate signal parameters such as the DoA [79, 151]. MUSIC parameter estimation relies on a fundamental assumption on the acquisition system:

**A 2.2.** The array manifold  $\mathcal{A} = \mathbf{a}(\theta)$  is assumed to be known.

In the absence of noise, the steering vectors are the intersections between the signal subspace  $S_X$  and the array manifold  $\mathcal{A}$  (see Section 1.3 for their definitions). However, in the presence of noise, with probability one there are no intersections:  $\hat{S}_X \cap \mathcal{A} = \emptyset$ . The idea behind MUSIC is to look for elements in  $\mathcal{A}$  that are closest to  $\hat{S}_X$ .

As many spectral methods, MUSIC relies on the spectral decomposition of the covariance matrix in (1.26):

$$\mathbf{R}_X = \mathbf{U}_S \mathbf{\Lambda}_S \mathbf{U}_S^H + \mathbf{U}_N \mathbf{\Lambda}_N \mathbf{U}_N^H \quad (2.17)$$

As previously mentioned in Section 1.3, the noise eigenvectors  $\mathbf{U}_N$  are orthogonal to the array manifold  $\mathcal{A} = \{\mathbf{a}(\theta_1), \dots, \mathbf{a}(\theta_R)\}$ :

$$\mathbf{a}(\theta_r)^H \mathbf{U}_N = 0, \quad r = 1, \dots, R \quad (2.18)$$

The projector and orthogonal projector of the signal subspace in (1.27) is derived from the noise eigenvectors of the estimated covariance matrix  $\hat{\mathbf{R}}$ :

$$\begin{cases} \hat{\mathbf{\Pi}}_S = \hat{\mathbf{U}}_S \hat{\mathbf{U}}_S^H \\ \hat{\mathbf{\Pi}}_N = \hat{\mathbf{U}}_N \hat{\mathbf{U}}_N^H = \mathbf{I} - \hat{\mathbf{U}}_S \hat{\mathbf{U}}_S^H \end{cases} \quad (2.19)$$

We can then define the normalized MUSIC spatial spectrum:

$$P_{\text{MU}}(\theta) = \frac{\mathbf{a}(\theta)^H \mathbf{a}(\theta)}{\mathbf{a}(\theta)^H \hat{\mathbf{\Pi}}_N \mathbf{a}(\theta)} = \frac{\mathbf{a}(\theta)^H \mathbf{a}(\theta)}{\mathbf{a}(\theta)^H (\mathbf{I} - \hat{\mathbf{\Pi}}_S) \mathbf{a}(\theta)} \quad (2.20)$$

to be maximized. In the presence of noise  $\hat{\mathbf{U}}_N \neq \mathbf{U}_N$  and the denominator is not zero, but its value decreases significantly. Therefore, as suggested by (2.18), the spectrum in (2.20) has peaks in correspondence of the true DoAs  $\theta_r$ . Alternatively, one can minimize

$$P_{\text{MU}}(\theta) = \mathbf{a}(\theta)^H \hat{\mathbf{\Pi}}_N \mathbf{a}(\theta) = \mathbf{a}(\theta)^H (\mathbf{I} - \hat{\mathbf{\Pi}}_S) \mathbf{a}(\theta) \quad (2.21)$$

The steps of the algorithm are the described in Algorithm 2.1.

Notice that MUSIC is a two-steps sub-optimal algorithm, involving an unconstrained estimation of a set of  $R$  vectors  $\mathbf{u}_r$  and then the maximization of a 1D function  $P_{\text{MU}}(\theta)$ .

---

**Algorithm 2.1 Spectral MUSIC**


---

- 1: Compute either  $\hat{\mathbf{U}}_S$  or  $\hat{\mathbf{U}}_N$ :
  1. either through an Eigenvalue Decomposition (EVD) on sample covariance matrix  $\hat{\mathbf{R}}_X$ ;
  2. or through an Singular Value Decomposition (SVD) on raw data matrix  $\mathbf{X}$  (recommended for computational reasons).
- 2: Plot the MUSIC spectrum  $P_{\text{MU}}(\theta, \psi)$  and chose the  $R$  maxima. For 2D systems, in particular, the azimuth is given by

$$\theta_r = \arg \max_{\theta \in (-\pi, \pi]} P_{\text{MU}}(\theta) \quad (2.22)$$


---

another version of MUSIC, named root-MUSIC was proposed by [5] for ULAs, which exhibits a threshold for lower SNR than spectral MUSIC, but with the same asymptotic properties. DoAs are given by the  $R$  roots of a polynomial  $P_{\text{MU},z}(z) = \mathbf{a}_z(1/z)^\top \hat{\mathbf{\Pi}}_N \mathbf{a}_z(z)$ , that are inside the unit circle and closest to the unit circle, with  $\mathbf{a}_z(z) = [1 \ z \ \dots \ z^{L-1}]^\top$  and

$$P_{\text{MU},z}(z)|_{z=e^{-j\omega p_0 \cos \theta/c}} = P_{\text{MU}}(\theta) \quad (2.23)$$

In the absence of noise, these roots would be exactly on the unit circle. Root-MUSIC can benefit from the spatial backward-forward smoothing techniques described in Section 2.9. The Unitary root-MUSIC algorithm implements backward-forward root-MUSIC through a unitary transformation [108].

### 2.5.1. Evaluation of spectral MUSIC

The performance of MUSIC in comparison to the CRB can be found in [151, 140, 141].

#### Main advantages

- Arbitrary array configurations.
- Multiple parameter estimation (azimuth, elevation, range, polarization, etc.): it is possible to estimate  $F$  parameter per source, *i.e.*  $RF$  signal parameters.
- Since its search assumes that one single source is present, MUSIC only looks for  $F$  parameters, instead of  $RF$ . Hence, it is less computationally expensive than the ML methods.
- High resolution compared to beamforming.
- Asymptotically unbiased and efficient, if the noise is white Gaussian. For uncorrelated signal and high SNR, spectral MUSIC is close to the CRB.

#### Drawbacks

- Complete knowledge of the array manifold (sensor positions and gains) is required, *i.e.* array calibration is necessary.

- The exhaustive search over the parameter space is computationally very expensive, as it is an  $F$ -dimensional search for  $RF$  maxima.
- The 1D search for  $R$  parameters is finite-sample biased.
- Sensitive to low SNR and calibration errors; the threshold occurs at a higher SNR than Maximum Likelihood (ML) algorithms.
- Degradation if sources are correlated. Cannot deal directly with the fully correlated case.

## 2.6. ESPRIT

The Estimation of Signal Parameters via Rotational Invariance Techniques (ESPRIT) algorithm proposed by [126] applies whenever steering matrix  $\mathbf{A}$  has a *shift structure*: *i.e.* the acquisition system is composed of two identical subarrays,  $Z_X$  and  $Z_Y$ , translated from each other by a known displacement vector  $\delta$ , as in Figure 2.1. This property is named *translational invariance*.

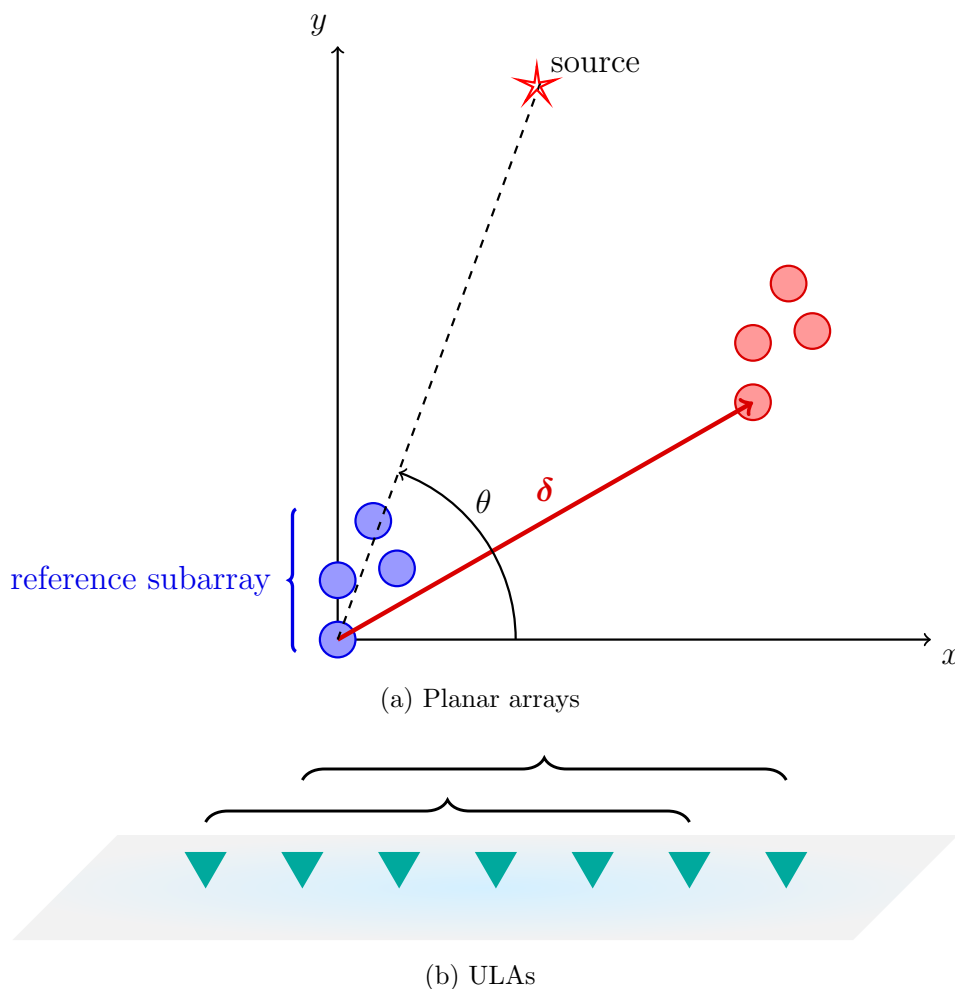


Figure 2.1.: Illustration of space shift between two identical subarrays

Thus, in order to reduce the computational complexity of signal subspace methods,

ESPRIT introduces a space shift constraint into the acquisition system in (1.9):

$$\begin{cases} x_\ell(t) = \sum_{r=1}^R a_\ell(\theta_r) s_r(t) + n_{x_\ell}(t) \\ y_\ell(t) = \sum_{r=1}^R a_\ell(\theta_r) e^{-j\omega\delta^\top \mathbf{d}_r/c} s_r(t) + n_{y_\ell}(t) \end{cases} \quad (2.24)$$

where  $a_\ell(\theta_r) = g_\ell(\theta_r) e^{-j\omega\tau_\ell(\theta_r)}$ . In [126] the translation  $\delta$  is assumed to be collinear with the  $x$ -axis:  $\delta = [\delta, 0, 0]$ , leading to  $e^{-j\omega\delta^\top \mathbf{d}_r/c} = e^{-j\omega\delta \cos \theta_r/c}$ , without restricting the generality. We also assume the problem is in 2D, with sources coplanar to the acquisition plane. The array output in vector form in (1.12) becomes

$$\begin{cases} \mathbf{x}(t) = \mathbf{A} \mathbf{s}(t) = \mathbf{A}_X \mathbf{s}(t) \in \mathbb{C}^L \\ \mathbf{y}(t) = \mathbf{A} \Phi \mathbf{s}(t) = \mathbf{A}_Y \mathbf{s}(t) \in \mathbb{C}^L \end{cases} \quad (2.25)$$

where  $\mathbf{x}(t)$  and  $\mathbf{y}(t)$  correspond to measurements recorded on the first and second subarrays respectively, and shift invariance

$$\mathbf{A}_Y = \mathbf{A}_X \Phi \quad (2.26)$$

Diagonal  $R \times R$  matrix  $\Phi$  is a unitary operator that relates the measurements from subarray  $Z_X$  to those from subarray  $Z_Y$ :

$$\Phi = \text{Diag}\{e^{j\varpi_1}, \dots, e^{j\varpi_R}\} \quad (2.27)$$

with phase shifts  $\varpi_r = -\omega\delta \cos \theta_r/c$ . Notice that in the complex field  $\Phi$  is a simple scaling operator, but it is isomorphic to the real 2D rotation operator (thus giving origin to the name ESPRIT). The general idea is to exploit the rotational invariance of the signal subspace introduced by the translational invariance of the sensor array, by estimating the diagonal elements of  $\Phi$ , without having to know  $\mathbf{A}$ .

Then we have the acquisition system output:

$$\mathbf{z}(t) = \begin{bmatrix} \mathbf{x}(t) \\ \mathbf{y}(t) \end{bmatrix} = \bar{\mathbf{A}} \mathbf{s}(t) + \mathbf{n}_z(t) \in \mathbb{C}^{2L} \quad (2.28)$$

where  $\bar{\mathbf{A}} = \begin{bmatrix} \mathbf{A} \\ \mathbf{A} \Phi \end{bmatrix} \in \mathbb{C}^{2L \times R}$  and  $\mathbf{n}_z(t) = \begin{bmatrix} \mathbf{n}_x(t) \\ \mathbf{n}_y(t) \end{bmatrix}$ , and covariance matrix from (1.25) and (1.26):

$$\begin{aligned} \mathbf{R}_Z &= \bar{\mathbf{A}} \mathbf{R}_S \bar{\mathbf{A}}^H + \sigma^2 \mathbf{I} = \\ &= \mathbf{U}_S \Lambda_S \mathbf{U}_S^H + \mathbf{U}_N \Lambda_N \mathbf{U}_N^H \end{aligned} \quad (2.29)$$

As discussed in Section 1.3,  $\mathcal{R}\{\mathbf{U}_S\} = \mathcal{R}\{\bar{\mathbf{A}}\}$ : there must exist a unique nonsingular transformation  $\mathbf{T}$  such that

$$\mathbf{U}_S = \bar{\mathbf{A}} \mathbf{T} \quad (2.30)$$

Through the invariance structure of the array we can decompose  $\mathbf{U}_S \in \mathbb{C}^{2L \times R}$  into  $\mathbf{U}_X, \mathbf{U}_Y \in \mathbb{C}^{L \times R}$

$$\mathbf{U}_S = \begin{bmatrix} \mathbf{U}_X \\ \mathbf{U}_Y \end{bmatrix} = \begin{bmatrix} \mathbf{A} \mathbf{T} \\ \mathbf{A} \Phi \mathbf{T} \end{bmatrix} \quad (2.31)$$

from which we infer  $\mathcal{R}\{\mathbf{U}_X\} = \mathcal{R}\{\mathbf{U}_Y\} = \mathcal{R}\{\mathbf{A}\}$ . From (2.31) we derive

$$\mathbf{U}_Y = \mathbf{U}_X \Psi \quad (2.32)$$

with

$$\mathbf{\Psi} = \mathbf{T}^{-1} \mathbf{\Phi} \mathbf{T} \quad (2.33)$$

Notice that (2.32) is the equivalent relationship to shift invariance  $\mathbf{A}_Y = \mathbf{A}_X \mathbf{\Phi}$  in (2.26) in terms of signal subspace eigenvectors, and that the eigenvalues of  $\mathbf{\Psi}$  correspond to the diagonal elements of  $\mathbf{\Phi}$ . Since  $R < L$ , this is an overdetermined set of equations. In practice, since we have estimates for these signal subspaces, (2.32) becomes:

$$\hat{\mathbf{U}}_X \hat{\mathbf{\Psi}} = \hat{\mathbf{U}}_Y \quad (2.34)$$

Linear system (2.34) can be solved through a Least Squares (LS), if the whole error is attributed to  $\hat{\mathbf{U}}_Y$ , with solution

$$\hat{\mathbf{\Psi}}_{LS} = \hat{\mathbf{U}}_X^\dagger \hat{\mathbf{U}}_Y \quad (2.35)$$

or a Total Least Squares (TLS) approach, if both  $\hat{\mathbf{U}}_X$  and  $\hat{\mathbf{U}}_Y$  are considered noisy:

$$(\hat{\mathbf{U}}_X + \mathbf{E}_X) \hat{\mathbf{\Psi}} = (\hat{\mathbf{U}}_Y + \mathbf{E}_Y) \quad (2.36)$$

where  $\mathbf{E}_X$  and  $\mathbf{E}_Y$  must have minimum Frobenius norm. Linear system (2.36) has solution

$$\hat{\mathbf{\Psi}}_{TLS} = -\mathbf{V}_{12} \mathbf{V}_{22}^{-1} \quad (2.37)$$

where  $\mathbf{V}_{12}$  and  $\mathbf{V}_{22}$  are  $R \times R$  matrices defined by the eigendecomposition of the  $2R \times 2R$  matrix

$$\begin{bmatrix} \hat{\mathbf{U}}_X^H \\ \hat{\mathbf{U}}_Y^H \end{bmatrix} \begin{bmatrix} \hat{\mathbf{U}}_X & \hat{\mathbf{U}}_Y \end{bmatrix} = \begin{bmatrix} \hat{\mathbf{V}}_{11} & \hat{\mathbf{V}}_{12} \\ \hat{\mathbf{V}}_{21} & \hat{\mathbf{V}}_{22} \end{bmatrix} \mathbf{\Lambda}_V \begin{bmatrix} \hat{\mathbf{V}}_{11}^H & \hat{\mathbf{V}}_{21}^H \\ \hat{\mathbf{V}}_{12}^H & \hat{\mathbf{V}}_{22}^H \end{bmatrix} \quad (2.38)$$

The steps of the algorithm are the described in Algorithm 2.2.

---

### Algorithm 2.2 LS and TLS ESPRIT

---

- 1: Compute  $\hat{\mathbf{U}}_S$ :
    1. either through an EVD on sample covariance matrix  $\hat{\mathbf{R}}_Z$
    2. or through an SVD on raw data matrix  $\mathbf{Z}$  (recommended for computational reasons).
  - 2: Select  $\hat{\mathbf{U}}_X$  and  $\hat{\mathbf{U}}_Y$  by decomposing  $\hat{\mathbf{U}}_S$  from (2.31).
  - 3: Obtain  $\hat{\mathbf{\Psi}}_{LS}$  from (2.35) or  $\hat{\mathbf{\Psi}}_{TLS}$  from (2.37).
  - 4: Find the eigenvalues of  $\hat{\mathbf{\Psi}}_{LS}$  or  $\hat{\mathbf{\Psi}}_{TLS}$ :  $\hat{\lambda}_1, \dots, \hat{\lambda}_R$ .
  - 5: Find the arguments of the steering complex exponentials from (2.27) as  $\hat{\omega}_r = \arg\{\hat{\lambda}_r\}$ ,  $r = 1, 2, \dots, R$ .
- 

LS and TLS ESPRIT have the same asymptotic behavior (for  $N_s \rightarrow \infty$ ), but TLS ESPRIT has better threshold behavior, with a slight increase in computational complexity. We inform the interested reader that another effective formulation of this approach is given by Unitary ESPRIT [59], that we do not discuss further.

### 2.6.1. Signal Copy

Estimation of signals as a function of time from a previously estimated DoA is termed *signal copy* [126]. Sometimes we are not only interested in the signal parameters, but also in signal signatures themselves.

Although the steering matrix  $\bar{\mathbf{A}}$  is not supposed to be known, we can exploit the relationship  $\mathbf{U}_S = \bar{\mathbf{A}}\mathbf{T}$  to find it:

$$\bar{\mathbf{A}} = \mathbf{U}_S \mathbf{T}^{-1} \quad (2.39)$$

where  $\mathbf{T}^{-1}$  is derived from (2.33) as the eigenvector matrix of  $\Psi$ .

Once we have estimated the steering matrix from (2.39), the simplest solution for the signal copy problem consists in a linear estimator with a squared cost function in the metric of the noise  $\Sigma_n$ .<sup>2</sup> This is equivalent to an oblique projection of the data matrix  $\mathbf{X}$  on the column space of  $\bar{\mathbf{A}}$ ,  $\mathcal{R}\{\bar{\mathbf{A}}\}$ :

$$\hat{\mathbf{S}} = \mathbf{W}^H \mathbf{Z} \quad (2.40)$$

with

$$\begin{aligned} \mathbf{W} &= \Sigma_n^{-1} \bar{\mathbf{A}} [\bar{\mathbf{A}}^H \Sigma_n^{-1} \bar{\mathbf{A}}]^{-1} = \\ &= \Sigma_n^{-1} \mathbf{U}_S [\mathbf{U}_S^H \Sigma_n^{-1} \mathbf{U}_S]^{-1} \mathbf{T}^{-H} \end{aligned} \quad (2.41)$$

Notice that the  $r$ -th column of  $\mathbf{W}$ ,  $\mathbf{w}_r$ , is a weight vector that enhances the signal from the  $r$ -th DoA and reject those from other directions. This is equivalent to a *spatial matched filter*.

Since we only have an estimate of the steering matrix  $\bar{\mathbf{A}}$ , at low SNR we may resort to a more robust TLS approach (see [126] for details).

### 2.6.2. Evaluation of ESPRIT

The performance of ESPRIT in comparison with the CRB can be found in [151, 103].

#### Main advantages

- High resolution compared to beamforming, and comparable to that of MUSIC.
- Knowledge of the array manifold (sensor positions and gains) is not required: only translation  $\boldsymbol{\delta}$  needs to be known.
- The structure of the subarray is arbitrary.
- Computationally efficient, much less expensive than the ML methods and than MUSIC (no need for an exhaustive search).
- Computational advantage especially pronounced for high dimensional parameter estimation: ESPRIT computational load grows linearly, whereas MUSIC load grows exponentially.
- Can estimate other signal parameters, such as the source signatures and correlation structure.

---

<sup>2</sup>When the noise is Gaussian, this estimator is ML.

- Robust to array imperfections (*e.g.* nonidentical subarrays) [126].
- TLS ESPRIT delivers estimates with insignificant finite sample bias.
- With row weighting, ESPRIT is close to the CRB above threshold.

### Main drawbacks

- A space shift constraint on the acquisition system.

## 2.7. Signal Subspace for Polarized Sources

When MUSIC was proposed in [131], the possibility of including wave polarization into the construction of the array manifold was briefly discussed. If we consider the vectorization of the data matrix at time  $t$  in (1.38)

$$\mathbf{x}(t) = \sum_{r=1}^R \mathbf{k}_r \boxtimes \mathbf{a}_r s_r(t) + \mathbf{n}(t) \in \mathbb{C}^{3L} \quad (2.42)$$

we can derive a  $3L \times 3L$  sample covariance matrix  $\hat{\mathbf{R}}_X$ . The array manifold is then given by  $\mathbf{k}(\theta, \psi, \alpha, \beta) \boxtimes \mathbf{a}(\theta, \psi)$ , leading to a *vector* MUSIC spectrum similar to (2.20)

$$P_{\text{MU}}(\theta, \psi, \alpha, \beta) = \frac{[\mathbf{k}^H \boxtimes \mathbf{a}^H] [\mathbf{k} \boxtimes \mathbf{a}]}{[\mathbf{k}^H \boxtimes \mathbf{a}^H] \hat{\mathbf{\Pi}}_N [\mathbf{k} \boxtimes \mathbf{a}]} \quad (2.43)$$

Afterwards, the vector sensor array model described in Section 1.4 was applied by [95, 96] to DoA estimation for acoustic and electromagnetic sources. Both ML DoA and polarization estimation were the subject of [66], with the derivation of the CRB and an application to remote sensing. A MUSIC-based method was proposed by [160] for DoA and polarization estimation. On the other hand, ESPRIT was also extended to polarized sources for DoA and polarization estimation: see [159, 86] for details. Finally, a comprehensive analysis and comparison of beamforming and MUSIC for polarized wavefronts can be found in [42].

## 2.8. Signal Subspace for Wideband Sources

Wideband extensions have been developed for beamforming, signal subspace and parametric methods [34]. In this section we will only detail the signal subspace approach for wideband sources: we will focus on high resolution methods such as MUSIC (cf. Section 2.5) and ESPRIT (cf. Section 2.6), that are based on a partition of the observation space into signal and noise subspaces, usually via low-rank approximations.

As introduced in Section 1.5.1, the data covariance matrix of the wideband case depends on frequency:

$$\mathbf{R}_X(\omega) = \mathbb{E} [\mathbf{x}(\omega) \mathbf{x}(\omega)^H] \quad (2.44)$$

If  $N_S$  independent snapshots,  $\mathbf{x}_1(\omega), \dots, \mathbf{x}_{N_S}(\omega)$ , are available, we define the sample spectral matrix as [151]

$$\hat{\mathbf{R}}_X(\omega) = \frac{1}{N_S} \sum_{j=1}^{N_S} \mathbf{x}_j(\omega) \mathbf{x}_j^H(\omega) \quad (2.45)$$

In Section 1.5.1 we Fourier transformed the dynamical model (1.6) into its frequency domain formulation (1.44), which is formally static for every fixed radial frequency  $\omega$ . We can then define and compute as many signal subspaces as there are frequency bins.

The major issue of wideband processing will be to effectively combine all these independent contributions. Two techniques can be considered, which jointly process the information in all frequency bands:

a) Incoherent signal-subspace processing: the wide frequency range can be divided into non-overlapping frequency bins, and the above mentioned narrowband signal subspace methods are applied to each narrow band separately. All the individual narrowband results are then combined through a simple averaging operation [79].

b) Coherent Signal Subspace (CSS) [157, 23, 80, 46, 36] relies on an approximately coherent combination of the spatial signal subspaces at different frequencies through the MUSIC algorithm. Through the same CSS process, ESPRIT was extended to the wideband case by [69, 102].

### 2.8.1. Virtual arrays

We will describe the CSS approach, as it provides better results: in order to steer all the frequency contributions in (2.45), it is necessary to first steer the corresponding subspaces towards a common subspace defined at a reference radial frequency  $\omega_0$ . For this purpose, the steering complex exponential  $e^{-j\omega\tau_\ell(\theta_r)}$  in (1.44) needs to become constant, in order to constitute a coherent contribution.

Since sensor gains do not depend on frequency, thanks to Assumption A 1.19, this steering operation leads to defining a virtual array for each radial frequency  $\omega$ , defined by sensor positions  $\tilde{\mathbf{p}}_\ell(\omega)$ , related to the actual sensor positions  $\mathbf{p}_\ell$  by

$$[\omega\tilde{\mathbf{p}}_\ell(\omega) - \omega_0\mathbf{p}_\ell]^\top \mathbf{d}(\theta) \equiv 0, \text{ mod } 2\pi c, \quad (2.46)$$

where  $\omega_0$  is fixed. This equation is satisfied if the term within brackets is orthogonal to  $\mathbf{d}(\theta_r)$  for every DoA  $\theta_r$ ,  $1 \leq r \leq R$ ; but this requires a prior knowledge of DoAs [157]. On the other hand, a sufficient condition is clearly that

$$\tilde{\mathbf{p}}_\ell(\omega) = \frac{\omega_0}{\omega} \mathbf{p}_\ell \quad (2.47)$$

which this time does not depend on  $\theta$ ; this also corresponds to the spatial resampling proposed in [23, 80, 46], as will be detailed in Section 2.8.3. An illustration of virtual arrays, *i.e.* shrunk or stretched arrays satisfying (2.47), is provided in Figure 2.2. This second (sufficient) condition in (2.47) will be retained in the present work.

#### Remark

More generally, if gains depended on frequency, the condition in (2.46) would become

$$\exp \left\{ \frac{j}{c} [\omega\tilde{\mathbf{p}}_\ell(\omega) - \omega_0\mathbf{p}_\ell]^\top \mathbf{d}(\theta) \right\} = \frac{g_\ell(\omega, \theta)}{g_\ell(\omega_0, \theta)} \quad (2.48)$$

Satisfying (2.48) would then always require prior knowledge of DoAs.

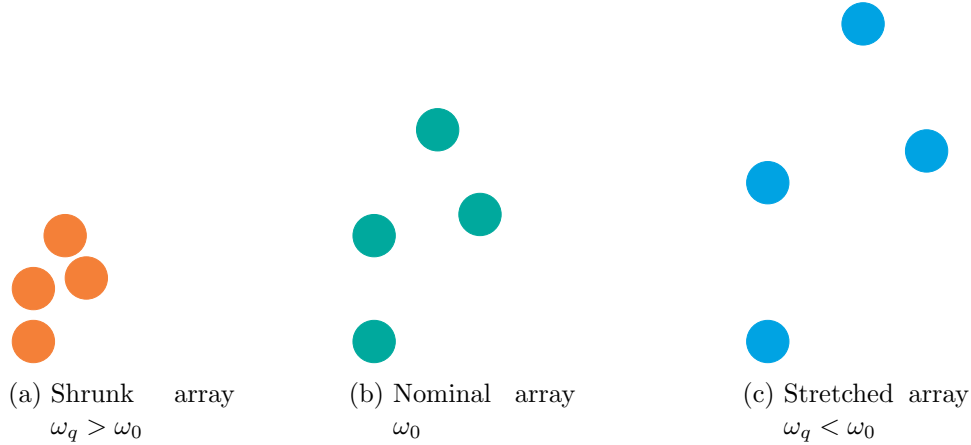


Figure 2.2.: Illustration of virtual arrays

### 2.8.2. Linear Interpolation

Equation (2.46) defines virtual arrays with identical array manifolds, but does not provide the signals that would be measured by the latter. It is hence necessary to devise an interpolator to compute the corresponding synthetic measurements. Moreover, to preserve the separation between noise and signal subspaces, it is suitable to map  $\mathbf{a}(\omega, \theta)$  to the same manifold  $\mathbf{a}(\omega_0, \theta)$  via a *multiplication* by some matrix  $\mathbf{U}(\omega, \omega_0, \theta) \in \mathbb{C}^{L \times L}$ , which we call focusing matrix. It turns out that this is possible exactly only for at most  $L$  distinct values of  $\theta$ . There are thus two possibilities.

- Either the DoAs are unknown, and a focusing matrix  $\mathbf{U}(\omega, \omega_0, \theta)$  can be computed so as to satisfy the following relationship only approximately [46]:

$$\mathbf{U}(\omega, \omega_0, \Theta_k) \mathbf{a}(\omega, \theta) \approx \mathbf{a}(\omega_0, \theta) \quad (2.49)$$

in an angular sector  $\theta \in \Theta_k$  of limited extent, where  $\omega_0$  is a fixed reference frequency. These focusing matrices can be obtained by solving in the LS sense the linear system  $\mathbf{U}(\omega, \omega_0, \Theta_k) \mathbb{A}(\omega, \Theta_k) \approx \mathbb{A}(\omega_0, \Theta_k)$ , where  $\Theta_k$  contains  $I$  discrete angular values  $\theta_i$ ,  $1 \leq i \leq I$ , and matrix  $\mathbb{A}(\omega, \Theta_k)$  is built with the corresponding columns  $\mathbf{a}(\omega, \theta_i)$ ; see [45] for further details on how to assess the accuracy of an array interpolator.

- Or the  $R$  DoAs are approximately known in advance,  $R \leq L$ , and it is possible to satisfy (2.49) exactly for these approximate DoAs; see [157] for more details.

In the state of the art [157, 46], the previously explained interpolation method is used as a preprocessing for subspace methods (such as MUSIC), in order to solve the problem of coherently averaging the estimated covariance matrices. This is illustrated below, as the covariance matrix depends on radial frequency  $\omega$ :

$$\begin{aligned} \mathbf{R}_X(\omega) &= \mathbb{E} [\mathbf{x}(\omega) \mathbf{x}(\omega)^H] = \\ &= \mathbf{A}(\omega, \theta) \mathbb{E} [\mathbf{s}(\omega) \mathbf{s}(\omega)^H] \mathbf{A}(\omega, \theta)^H + \mathbb{E} [\mathbf{n}(\omega) \mathbf{n}(\omega)^H] = \\ &= \mathbf{A}(\omega, \theta) \mathbf{R}_S(\omega) \mathbf{A}(\omega, \theta) + \sigma^2 \mathbf{I} \end{aligned} \quad (2.50)$$

where  $\mathbf{x}(\omega)$  was derived in (1.46). As a consequence, in order to estimate the DoAs by a coherent average over different values of  $\omega$ , it is necessary to first steer all estimated  $\hat{\mathbf{R}}(\omega)$

towards a subspace defined at a reference radial frequency  $\omega_0$  [157, 23, 80, 46]. After this focusing operation, in every angular sector  $\Theta_k$  we can use contributions of all frequencies to build an averaged estimate of the covariance matrix:

$$\begin{aligned}\bar{\mathbf{R}}(\Theta_k) &= \sum_{\omega} \tilde{\mathbf{R}}_X(\omega) = \sum_{\omega} \tilde{\mathbf{x}}(\omega) \tilde{\mathbf{x}}(\omega)^H = \\ &= \sum_{\omega} \mathbf{U}(\omega, \omega_0, \Theta_k) \mathbf{x}(\omega) \mathbf{x}(\omega)^H \mathbf{U}(\omega, \omega_0, \Theta_k)^H\end{aligned}\quad (2.51)$$

where we interpolated our data:  $\tilde{\mathbf{x}}(\omega) = \mathbf{U}(\omega, \omega_0, \Theta_k) \mathbf{x}(\omega)$ , corresponding to a virtual array with sensor positions  $\tilde{p}_\ell(\omega)$  in (2.47). From (1.46) and (2.49) we obtain

$$\bar{\mathbf{R}}(\Theta_k) \approx \sum_{\omega} \mathbf{A}(\omega_0, \theta) \mathbf{R}_s(\omega) \mathbf{A}(\omega_0, \theta)^H + \tilde{\mathbf{R}}_n(\omega) \quad (2.52)$$

where  $\mathbf{R}_s(\omega)$  denotes the covariance of the sources at radial frequency  $\omega$  and  $\tilde{\mathbf{R}}_n(\omega)$  the noise covariance transformed by matrix  $\mathbf{U}(\omega, \omega_0, \Theta_k)$  in the considered sector, *i.e.*  $\theta \in \Theta_k$ . These linear transformations allow to compute observations received on virtual arrays, each being a stretched or shrunk version of the nominal reference array at radial frequency  $\omega_0$ .

### 2.8.3. Interpolation through Spatial Resampling

As pointed out in [23], the CSS approach through focusing matrices can be replaced by a spatial resampling of recorded data if the array is a ULA. This approach does not require any prior approximate knowledge of the source DoAs. In fact, if the array is a ULA, the sufficient condition in (2.47) becomes

$$\begin{aligned}\tilde{p}_\ell(\omega) &= \frac{\omega_0}{\omega} p_\ell \\ \implies \tilde{p}(\omega)(\ell - 1) &= \frac{\omega_0}{\omega} p_0(\ell - 1) \\ \implies \tilde{p}(\omega) &= p_0 \frac{\omega_0}{\omega} = p_0 \frac{\lambda}{\lambda_0}\end{aligned}\quad (2.53)$$

where  $p_0$  is the nominal inter-sensor distance of the array and  $\lambda_0$  is the reference wavelength of the CSS. Hence, the CSS can be built by introducing a modified sampling interval  $\tilde{p}(\omega) \neq p_0$ , so that the product  $\omega \tilde{p}(\omega)$  is kept constant, without any prior assumption on the position of the sources. The same idea was exploited in [80], where this approach also implies an alignment of wideband sources in the spatial frequency domain, by treating the output of a discrete array as the result of the spatial sampling of a continuous array. An illustration of spatial resampling is provided in Figure 2.3.

The Fourier Transform (FT) of the wideband field incident on the ULA at position  $p$  at frequency  $\omega$  is then

$$x(p, \omega) = \sum_{r=1}^R s_r(\omega) \exp \{-j\omega p \cos \theta_r / c\} + n(p, \omega) \quad (2.54)$$

which yields a discretized expression for  $p_\ell = (\ell - 1)p_0$ .

The result of the resampling of the sensor output with sensor spacing  $\tilde{p}(\omega)$  is an alignment of the steering matrix, that becomes constant for all the considered frequencies



Figure 2.3.: Illustration of spatial resampling

within the common bandwidth of the sources. The adjusted sensor output at virtual position  $\tilde{p}_\ell(\omega) = p_0 \frac{\omega_0}{\omega} (\ell - 1)$ ,

$$\tilde{x}(\ell, \omega) = \sum_{r=1}^R s_r(\omega) \exp \{-j\omega_0 p_0 (\ell - 1) \cos \theta_r / c\} + \tilde{n}(\ell, \omega) \quad (2.55)$$

leads to a constant focused steering matrix  $\tilde{\mathbf{A}}(\omega) = \mathbf{A}(\omega_0)$  in the system (1.46). After Discrete Fourier Transform (DFT) with  $Q$  frequency bins, we have

$$\tilde{\mathbf{x}}(\omega_q) = \mathbf{A}(\omega_0) \mathbf{s}(\omega_q) + \tilde{\mathbf{n}}(\omega_q), \quad 1 \leq q \leq Q \quad (2.56)$$

Note that the values that would occur at virtual positions  $\tilde{p}_\ell(\omega_q)$  satisfying (2.53) are estimated, provided that the Nyquist criterion is satisfied: in order to avoid spatial aliasing, the spatial period must always respect the condition  $\tilde{p}(\omega_q) \leq \frac{\pi c}{\omega_q}$ ,  $\forall q$ , which is equivalent to  $p_0 \leq \lambda_0/2$  from (2.53).

In practice, the resampling of received data at the virtual sensors can be achieved through a simple interpolation approach, as described in Section 8.A.

### 2.8.4. Wideband Polarized Waves

When received signals are wideband polarized waves, as described in Section 1.5.2, the derivation of a coherent approach through MUSIC for DoA estimation is straightforward [16].

Seismic sources, previously introduced in Section 1.6, are an important example of well studied wideband and polarized waves [133]. In [35] ESPRIT was adapted to process wideband seismic waves for a joint DoA and velocity estimation, using an incoherent approach.

## 2.9. Dealing with Correlation

### 2.9.1. Correlated Noise

If Assumption A 1.11 is not verified, the noise space covariance matrix is known, but not proportional to identity:  $\Sigma_n = \mathbb{E} [\mathbf{n}(t)\mathbf{n}(t)^H] \neq \sigma^2 \mathbf{I}$ .

If the noise is not spatially white, but exhibits a covariance  $\Sigma_n$ , it is possible to prewhiten the sensor output through multiplication by  $\Sigma_n^{-1/2}$ :  $\Sigma_n^{-1/2}\mathbf{x}(t)$ , where  $\Sigma_n^{-1/2}$  is the positive definite Hermitian square root factor of  $\Sigma_n^{-1}$ .

Without prewhitening, the methods relying on the eigendecomposition of the data covariance matrix  $\mathbf{R}_X$  can be adapted through the generalized eigendecomposition of matrix pencil  $\{\hat{\mathbf{R}}_X, \Sigma_n\}$  [126]:

$$\hat{\mathbf{R}}_X \hat{\mathbf{U}} = \Sigma_n \hat{\mathbf{U}} \hat{\Lambda} \quad (2.57)$$

The signal subspace estimate is then given by the eigenvectors corresponding to the first leading  $R$  eigenvalues:

$$\hat{\mathbf{U}}_S = \Sigma_n [\hat{\mathbf{u}}_1 | \dots | \hat{\mathbf{u}}_R] \quad (2.58)$$

### 2.9.2. Correlated Sources

If Assumption A 1.15 is not verified, the sources can be correlated:  $\exists r, q \mid \mathbb{E}[s_r(t)s_q(t)] = \rho\sigma_r\sigma_q$ , with  $\rho \neq 0$ . If  $0 < \rho < 1$ , the condition number of matrix  $\mathbf{R}_S$  increases exponentially with  $\rho$ , but  $\mathbf{R}_S$  remains nonsingular or full rank. If  $\rho = 1$ , the sources are fully correlated, or *coherent*, and the signal covariance matrix  $\mathbf{R}_S$  has rank smaller than  $R$  (rank deficient), hence it is singular (see Section 1.3.1 for more details).

MUSIC and ESPRIT are known to yield high resolution and asymptotically unbiased estimates even when the sources are partially correlated. Theoretically, these methods encounter difficulties only when the sources are fully correlated, because subspace algorithms rely on the assumption of nonsingularity of matrix  $\mathbf{R}_S$ . However, in practice, their performance is considerably degraded even when the signals are highly correlated, for example in the case of multipath propagation. Hence, the fully correlated case is a good model for the highly correlated case encountered in many practical situations [151, 132].

In order to solve this problem in the context of beamforming, [50] used the particular Toeplitz structure (*i.e.* the entries along each diagonal are equal) of the spatial covariance when the array is a ULA and the sources and the noise are both uncorrelated. If the sources are coherent, the array covariance does not have this structure anymore. The idea proposed by [50] uses the sample covariance constrained to have this structure by averaging each diagonal. The entries along the  $i$ -th diagonal are then replaced by their average:

$$\bar{R}_i^{(Toeplitz)} = \frac{1}{L-i} \sum_{j=1}^{L-i} R_{i,i+j}, \quad j = 0, \dots, L-1 \quad (2.59)$$

*Spatial smoothing* proposed by [41] is a preprocessing technique that restore the full rank of a singular spatial covariance matrix  $\mathbf{R}_S$ . Spatial smoothing requires a regular array geometry, such as the ULA configuration described here, with inter-sensor spacing  $p_0$ . We compose a set of  $M$  ULA subarrays of length  $L^s > R$ : each subarray is shifted by one from the previous subarray [151, 132]. The  $m$ -th subarray is given by

$$\mathbf{x}_m(t) = \mathbf{A} \mathbf{B}_m \mathbf{s}(t) + \mathbf{n}_m(t). \quad (2.60)$$

with diagonal  $R \times R$  matrix  $\mathbf{B}_m = \text{Diag}\{e^{j\omega p_0(m-1)\cos\theta_1/c}, \dots, e^{j\omega p_0(m-1)\cos\theta_R/c}\}$ . Since each subarray has spatial covariance

$$\mathbf{R}_m = \mathbf{A} \mathbf{B}_m \mathbf{R}_S \mathbf{B}_m^H \mathbf{A}^H + \sigma^2 \mathbf{I} \quad (2.61)$$

it is possible to derive an average *forward* covariance

$$\bar{\mathbf{R}}^{(f)} = \frac{1}{M} \sum_{m=1}^M \mathbf{R}_m \quad (2.62)$$

The following result can be proved [132]:

**Theorem 2.1.** If the number of subarrays is equal or greater than the number of sources,  $M \geq R$ , then the average covariance  $\bar{\mathbf{R}}^{(f)}$  is nonsingular, regardless of the number of correlated signals.

Since  $\bar{\mathbf{R}}^{(f)}$  is a spatial matrix with the same structure as  $\mathbf{R}^{(f)}$ , one can easily apply the same signal subspace algorithms such as MUSIC to this smoothed covariance.

As a result of spatial smoothing, the sensitivity to source correlation is reduced, providing a better threshold behavior. The price to pay for this increased robustness is a reduced effective aperture of the array. If there are  $R_c \leq R$  coherent wavefronts, the number of subarrays  $M$  must be greater than the number of sources, according to Theorem 2.1:  $M = L - L^s + 1 \geq R$ , implying a minimum size of each subarray  $L^s = L + 1 - R$ . In the incoherent case, from Assumption A 1.13, we only needed  $L \geq R + 1$  sensors. Moreover, in order to separate  $R$  sources, each subarray must have a size  $L^s \geq R + 1$ , implying  $L \geq 2R$ .

Similarly, [110] extended the forward smoothing of (2.62) and symmetrically defined the backward smoothing, with subarrays related to (2.60) by a permutation matrix  $\mathbf{Q}$  inverting the order of the sensors within the array (from  $L$  to 1). For a ULA, we have

$$\begin{aligned} \mathbf{x}_m^{(b)}(t) &= \mathbf{Q} \mathbf{x}_m(t)^* = \mathbf{A} \mathbf{B}_m^{(b)} \mathbf{s}(t)^* + \mathbf{Q} \mathbf{n}_m(t)^* \\ \mathbf{R}_m^{(b)} &= \mathbf{A} \mathbf{B}_m^{(b)} \mathbf{R}_S^* \mathbf{B}_m^{(b)H} \mathbf{A}^H + \sigma^2 \mathbf{I} \end{aligned} \quad (2.63)$$

where  $\mathbf{B}_m^{(b)} = \text{Diag}\{e^{j\omega p_0(L+m-2)\cos\theta_1/c}, \dots, e^{j\omega p_0(L+m-2)\cos\theta_R/c}\}$ .

This leads to the smoothed *backward* covariance

$$\bar{\mathbf{R}}^{(b)} = \frac{1}{M} \sum_{m=1}^M \mathbf{R}_m^{(b)} \quad (2.64)$$

and a *backward-forward* smoothed covariance that is singular under mild conditions:

$$\bar{\mathbf{R}}^{(bf)} = \frac{1}{2}(\bar{\mathbf{R}}^{(b)} + \bar{\mathbf{R}}^{(f)}) \quad (2.65)$$

Since we use each subarray twice, if we want to separate  $R$  signals regardless of their correlation, we need  $M \geq R/2$  of minimum length  $L^s = L + 1 - R/2$ , with  $L \geq \frac{3}{2}R$ .

Finally, [158] extended spatial smoothing to arbitrary array configurations, through spatial interpolation. For *weighted* spatial smoothing and for rectangular arrays, see [151] and references therein.



# 3. Multi-Way Arrays and Tensors

## 3.1. Introduction

This chapter intends to give a basic introduction on tensor formalism and tensor decomposition techniques, as well as their physical interpretation. Section 3.2 refers to the fundamentals of multidimensional arrays: the definition of tensor and its relation to a multi-way array of coordinates, as well as some notations and operations. Section 3.3 presents tensor decompositions such as the CPD and their properties, and also its link to the tensor rank. Tensor normal distributions and the separable covariance structure are described in Section 3.4. The main algorithms for tensor decomposition and approximation are detailed in Sections 3.6 and 3.5, respectively. Finally, Section 3.7 discloses the interesting concept of coherence of tensor modalities, and its relation to new identifiability conditions on the tensor model.

## 3.2. Tensor Arrays: Notations and Operations

### 3.2.1. From Multilinear Operators to Multi-Way Arrays

From a practical perspective, a tensor is a multidimensional array. More formally, a  $D$ -order tensor is an element of the tensor product of  $D$  vector spaces, each with its own coordinate system [75, 24]. In order to define the tensor product, we need first to introduce multilinear functions [26]:

**Definition 3.1.** Assume  $\mathcal{S}_d$  are  $D$  vector spaces,  $1 \leq d \leq D$ , and  $f$  is the map

$$\begin{aligned} f : \mathcal{S}_1 \times \cdots \times \mathcal{S}_D &\longmapsto \mathbb{K} \\ (\mathbf{x}_1, \dots, \mathbf{x}_D) &\longrightarrow f(\mathbf{x}_1, \dots, \mathbf{x}_D) \end{aligned} \quad (3.1)$$

Map  $f$  is said *multilinear* if it is linear w.r.t. every variable  $\mathbf{x}_d$ ,  $1 \leq d \leq D$ , i.e.  $\forall d, \forall \alpha, \beta \in \mathbb{K}$ :

$$f(\mathbf{x}_1, \dots, \alpha \mathbf{x}_d + \beta \mathbf{y}_d, \dots, \mathbf{x}_D) = \alpha f(\mathbf{x}_1, \dots, \mathbf{x}_d, \dots, \mathbf{x}_D) + \beta f(\mathbf{x}_1, \dots, \mathbf{y}_d, \dots, \mathbf{x}_D) \quad (3.2)$$

The field  $\mathbb{K}$  can coincide with the real field  $\mathbb{R}$  or the complex field  $\mathbb{C}$ . In the remainder, we will always assume  $\mathbb{K} = \mathbb{C}$ .

Through multilinearity, we can define the following equivalence relationship and the relative quotient space:

**Definition 3.2.** Given the following equivalence:

$$(\mathbf{x}, \mathbf{y}, \mathbf{z}) \sim (\mathbf{x}', \mathbf{y}', \mathbf{z}') \iff \exists \alpha, \beta, \gamma \in \mathbb{K} : (\mathbf{x}', \mathbf{y}', \mathbf{z}') = (\alpha \mathbf{x}, \beta \mathbf{y}, \gamma \mathbf{z}) \quad (3.3)$$

with  $\alpha\beta\gamma = 1$ , a *tensor of order three* is an element of the quotient space by this equivalence, denoted as  $\mathcal{S}_1 \otimes \mathcal{S}_2 \otimes \mathcal{S}_3 = \mathcal{S}_1 \times \mathcal{S}_2 \times \mathcal{S}_3 / \sim$ .

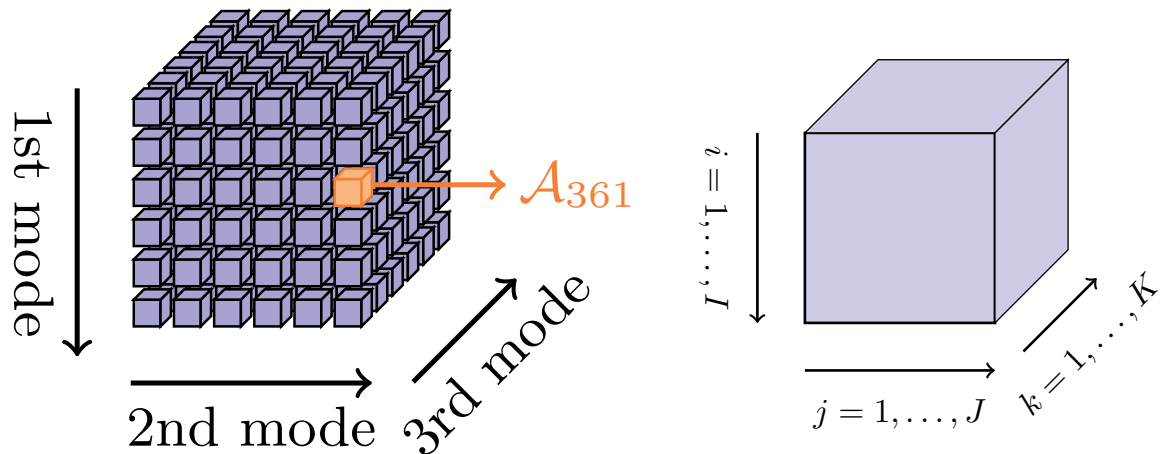
Once we fix the bases of the tensor space, a tensor of order  $D$  can be represented by an array of coordinates, where  $D$  is the number of its modes or dimensions. Real life examples of these diversities include space, time, frequency, repetitions (cf. Section 5.2). We will denote a  $D$ -way array by  $\mathcal{X} \in \mathbb{C}^{I_1 \times \dots \times I_D}$ , and its entries by  $X_{i_1, \dots, i_D}$ . For example, for  $D = 3$ , a tensor is an element of the vector space  $\mathcal{S}_1 \otimes \mathcal{S}_2 \otimes \mathcal{S}_3$ . Let us choose a basis  $\mathbf{e}_i^{(d)}$  for each of the vector spaces  $\mathcal{S}_d$ . Then any tensor  $\mathcal{X} \in \mathbb{C}^{I \times J \times K}$  has coordinates  $X_{ijk}$  defined by [27]

$$\mathcal{X} = \sum_{i=1}^I \sum_{j=1}^J \sum_{k=1}^K \mathcal{X}_{ijk} \mathbf{e}_i^{(1)} \otimes \mathbf{e}_j^{(2)} \otimes \mathbf{e}_k^{(3)} \quad (3.4)$$

NB: with an abuse of notation, we will often refer to tensor  $\mathcal{X}$  through its array representation  $\mathcal{X}$ . However, it is important to recall that an array of coordinates does not suffice to define a tensor: we also need to define spaces and bases.

Notice that a first-order tensor is a vector, a second-order tensor is a matrix, and tensor of order three or higher are called higher order tensors [75].

### 3.2.2. Notations and Terminology



(a) Tensor elements - reproduction from [22]

(b) Tensor indices - reproduction from [75]

Figure 3.1.: A third order tensor  $\mathcal{A} \in \mathbb{C}^{I \times J \times K}$

As previously stated on page xxi, we use the following notations:

- Scalars are denoted by lowercase letters:  $a$ .
- Vectors are denoted by boldface lowercase letters:  $\mathbf{a}$ , with elements  $a_i$ .
- Matrices are denoted by boldface capital letters:  $\mathbf{A}$  with columns  $\mathbf{a}_{\cdot j}$  or simply  $\mathbf{a}_j$  and rows  $\mathbf{a}_{i \cdot}$ . Matrix elements are denoted by  $A_{ij}$ .
- Higher order tensors are denoted by boldface Euler script letters,  $\mathcal{A}$ , with elements  $\mathcal{A}_{ijk}$  for  $D = 3$ . A third order tensor has three indices, as shown in Figure 3.1.

*Subarrays* are obtained when a subset of the indices is fixed.

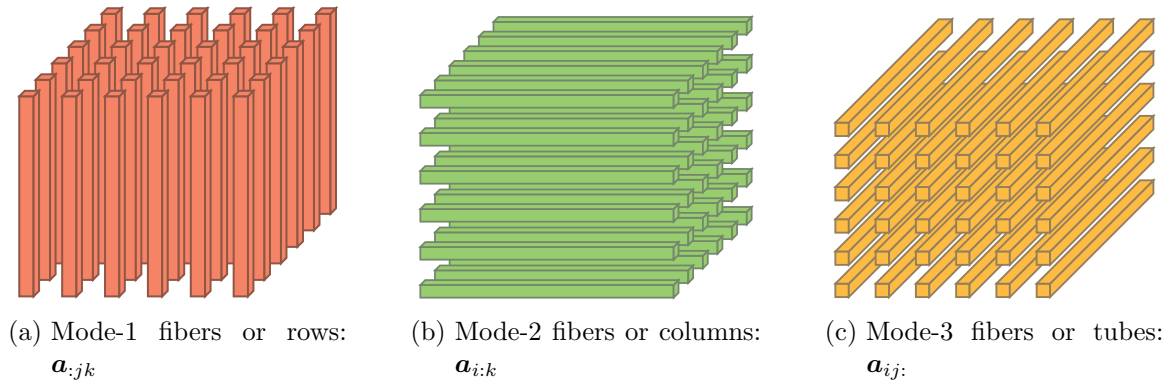


Figure 3.2.: Illustration of tensor fibers - reproduction from [75]

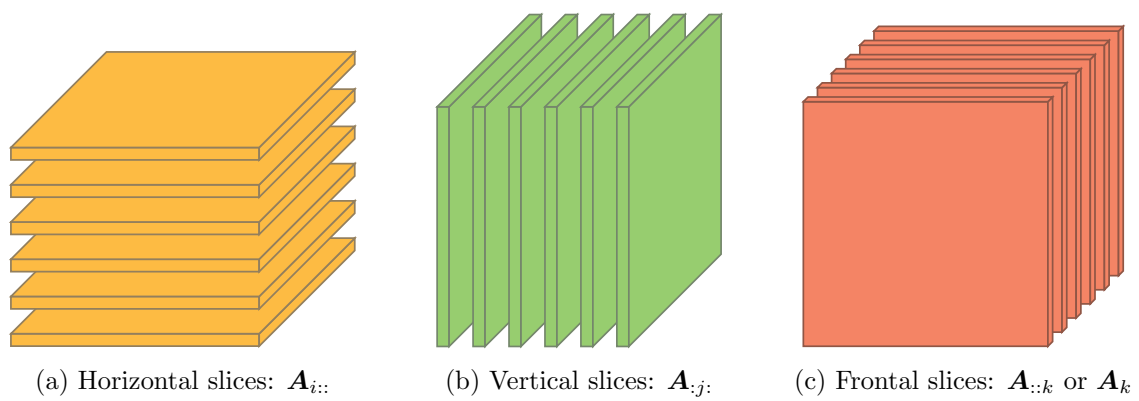


Figure 3.3.: Illustration of tensor slices - reproduction from [75]

1. *Fibers* are obtained by fixing all indices except one: fibers are always represented by column vectors. Rows  $\mathbf{a}_{:jk}$  are mode-1 fibers (in Figure 3.2a), whereas columns  $\mathbf{a}_{i:k}$  are mode-2 fibers (in Figure 3.2b). Moreover, *tubes*  $\mathbf{a}_{ij:}$  are mode-3 fibers (in Figure 3.2c).
2. *Slices* are obtained by fixing all but two indices, *i.e.* slices are 2D sections of a tensor:  $\mathbf{A}_{i:}$  (“horizontal” slices, in Figure 3.3a),  $\mathbf{A}_{:j}$  (“vertical” slices, in Figure 3.3b) and  $\mathbf{A}_{:,k}$  (“frontal” slices, in Figure 3.3c). Alternatively, the  $k$ -th “frontal” slice can be represented by the more compact form  $\mathbf{A}_k$ .

**Definition 3.3.** The inner product between two tensors of the same size:  $\mathcal{X}, \mathcal{Y} \in \mathbb{C}^{I_1 \times \dots \times I_D}$ :

$$\langle \mathcal{X}, \mathcal{Y} \rangle = \sum_{i_1=1}^{I_1} \dots \sum_{i_D=1}^{I_D} \mathcal{X}_{i_1 \dots i_D} \mathcal{Y}_{i_1 \dots i_D}^* \quad (3.5)$$

with associated Frobenius norm  $\|\mathcal{X}\| = \sqrt{\langle \mathcal{X}, \mathcal{X} \rangle}$ .

**Definition 3.4.** A tensor  $\mathcal{X} \in \mathbb{C}^{I_1 \times \dots \times I_D}$  is *diagonal* if  $X_{i_1 \dots i_D} \neq 0 \Leftrightarrow i_1 = i_2 = \dots = i_D$ , *i.e.* it has non zero elements only on its diagonal.

It is often useful to store the elements of a  $D$ -way array into a matrix, through *unfoldings* or *flattenings*, depending on the arbitrary order choice. The most used *matricizations* are given by the mode- $d$  unfoldings, *i.e.* matrices whose number of rows equals the  $d$ -th tensor dimension [26, 75]:

**Definition 3.5.** The mode- $d$  unfolding of a tensor  $\mathcal{X} \in \mathbb{C}^{I_1 \times \dots \times I_D}$  is denoted by  $\mathbf{X}_{(d)}$  and arranges the mode- $d$  fibers as columns of the resulting matrix.

It is easily verified that the Frobenius norm of any unfolding is equal to the tensor norm in Definition 3.3:

$$\|\mathcal{X}\| = \|\mathbf{X}_{(d)}\|, \quad \forall d \quad (3.6)$$

Reformatting of tensors in general is called *reshaping*. Through the reshaping operation we can unvectorize a tensor, as the reverse of the vectorization operation [22]. For example, in 2D we have the following  $\text{vec}\{\cdot\}$  and  $\text{unvec}\{\cdot\}$  operations:

**Definition 3.6.** The vectorization of a matrix  $\mathbf{X} = [\mathbf{x}_1, \dots, \mathbf{x}_J] \in \mathbb{C}^{I \times J}$  stacks its columns (or mode-2 fibers)  $\mathbf{x}_j$  into a vector:

$$\begin{cases} \mathbf{x} = \text{vec}\{\mathbf{X}\} = [\mathbf{x}_1^\top, \dots, \mathbf{x}_J^\top]^\top \in \mathbb{C}^{IJ} \\ x_{(i-1)J+j} = X_{ij} \end{cases} \quad (3.7)$$

Through the reshape operation (similar to the reshape MATLAB function) we can recover the original matrix  $\mathbf{X}$ :

$$\text{reshape}(\mathbf{x}, I, J) = [\mathbf{x}(1 : I), \mathbf{x}(I + 1 : 2I), \dots, \mathbf{x}(IJ - I + 1 : IJ)] \in \mathbb{C}^{I \times J} \quad (3.8)$$

For higher order tensors, we can define a similar vectorization operation. We define it for  $D = 3$ , but it is easily extended to higher order tensors [22]:

**Definition 3.7.** The vectorization of a tensor  $\mathcal{X} \in \mathbb{C}^{I \times J \times K}$  is defined as the vectorization of the associated mode-1 unfolding  $\mathbf{X}_{(1)} \in \mathbb{C}^{I \times JK}$ . Hence, it stacks all its mode-1 fibers  $\mathbf{x}_{:jk}$  into a vector:

$$\begin{aligned} \mathbf{x} &= \text{vec}\{\mathcal{X}\} = \text{vec}\{\mathbf{X}_{(1)}\} = [\text{vec}\{\mathbf{X}_{::1}\}, \dots, \text{vec}\{\mathbf{X}_{::K}\}]^\top \\ &= [\mathbf{x}_{:11}^\top, \mathbf{x}_{:21}^\top, \dots, \mathbf{x}_{:J1}^\top, \dots, \mathbf{x}_{:1K}^\top, \mathbf{x}_{:2K}^\top, \dots, \mathbf{x}_{:JK}^\top]^\top \in \mathbb{C}^{IJK} \end{aligned} \quad (3.9)$$

We adopt the usual definition [10] where the  $\text{vec}\{\cdot\}$  operation takes indices in lexicographical order. Then we have the identity [10, 75]:  $\text{vec}\{\mathbf{a}\mathbf{b}^\top\} = \mathbf{b} \boxtimes \mathbf{a}$ , for any pair of vectors  $(\mathbf{a}, \mathbf{b})$ . More generally:

$$\begin{aligned} \text{vec}\{\mathbf{a} \otimes \mathbf{b} \otimes \mathbf{c}\} &= \mathbf{c} \boxtimes \mathbf{b} \boxtimes \mathbf{a} \\ \text{vec}\{\mathbf{a}^{(1)} \otimes \dots \otimes \mathbf{a}^{(D)}\} &= \mathbf{a}^{(D)} \boxtimes \dots \boxtimes \mathbf{a}^{(1)} \end{aligned} \quad (3.10)$$

N.B. Although there exists an objectively better definition [24], allowing to preserve the order of the  $\boxtimes$  products, it is rarely used in the literature.

### 3.2.3. Multi-Way Operations

We define two fundamental operations, increasing and decreasing tensor order, respectively. Tensor product increases order  $D$ :

**Definition 3.8.** The *tensor product*  $\mathcal{A} \otimes \mathcal{B}$  between tensor  $\mathcal{A} = [A_{ij}] \in \mathcal{S}_1 \otimes \mathcal{S}_2$  and tensor  $\mathcal{B} = [B_{lm}] \in \mathcal{S}_3 \otimes \mathcal{S}_4$  is tensor  $\mathcal{C} = [C_{ijlm} = A_{ij}B_{lm}] \in \mathcal{S}_1 \otimes \mathcal{S}_2 \otimes \mathcal{S}_3 \otimes \mathcal{S}_4$

An example of tensor product is the outer product of two vectors  $\mathbf{a} \in \mathbb{C}^{I_a}$  and  $\mathbf{b} \in \mathbb{C}^{I_b}$ :  $\mathbf{a} \otimes \mathbf{b} = \mathbf{a}\mathbf{b}^\top \in \mathbb{C}^{I_a \times I_b}$ . Notice that the outer product of multiple vectors is a higher order tensor:  $\mathbf{a}^{(1)} \otimes \mathbf{a}^{(2)} \otimes \dots \otimes \mathbf{a}^{(D)} \in \mathbb{C}^{I_1 \times \dots \times I_D}$ , whereas the Kronecker product of multiple vectors remains a vector:  $\mathbf{a}^{(1)} \boxtimes \mathbf{a}^{(2)} \boxtimes \dots \boxtimes \mathbf{a}^{(D)} \in \mathbb{C}^{I_1 \dots I_D}$ .

**Definition 3.9.** The *contraction* or *mode- $d$  product*  $\bullet_d$  between tensor  $\mathcal{A}$  of order  $D$  and tensor  $\mathcal{A}'$  of order  $D'$  consists in a summation over a pair of indices. The result is a tensor  $\mathcal{B} = \mathcal{A} \bullet_d \mathcal{A}'$  of order  $D + D' - 2$ .

For  $(D, D', d) = (3, 3, 2)$

$$\mathcal{B}_{ijpq} = \sum_{\ell} \mathcal{A}_{i\ell j} \mathcal{A}'_{p\ell q} \quad (3.11)$$

Matrix multiplication is an example of mode-1 product between two matrices,  $\mathcal{B} = \mathcal{A}\mathcal{A}' = \mathcal{A}^\top \bullet_1 \mathcal{A}'$ , with  $B_{im} = \sum_{\ell} A_{i\ell} A'_{\ell m}$ . When the mode- $d$  product is between a matrix  $\mathbf{U} \in \mathbb{C}^{J \times I_d}$  and a higher order tensor  $\mathcal{X} \in \mathbb{C}^{I_1 \times \dots \times I_D}$ , as a rule, we sum over the second index of the matrix,

$$(\mathcal{X} \bullet_d \mathbf{U})_{i_1 \dots i_{d-1} j i_{d+1} \dots i_D} = \sum_{i_d=1}^{I_d} \mathcal{X}_{i_1 \dots i_D} U_{j i_d} \quad (3.12)$$

This can also be expressed in terms of unfolded tensors:  $\mathcal{Y} = \mathcal{X} \bullet_d \mathbf{U} \Leftrightarrow \mathbf{Y}_{(d)} = \mathbf{U}\mathbf{X}_{(d)}$ . As an example, the mode-3 product  $\mathcal{A} \bullet_3 \mathcal{M}$  between a matrix and a third order tensor gives the third order tensor:  $\mathcal{B}_{ipq} = \sum_{\ell} M_{i\ell} \mathcal{A}_{p\ell q}$ .

A natural extension of the mode- $d$  product is the following:

**Definition 3.10.** The *multilinear product* of a tensor with each matrix of a list  $\mathbf{A} = \{\mathbf{A}^{(1)}, \dots, \mathbf{A}^{(D)}\}$ , where  $\mathbf{A}^{(d)} \in \mathbb{C}^{J_d \times I_d}$  is a set of  $D$  independent mode- $d$  products. Alternatively, we can express a multilinear product through unfoldings and Kronecker products:

$$\begin{aligned} \mathcal{Y} &= \mathcal{X} \bullet_1 \mathbf{A}^{(1)} \bullet_2 \mathbf{A}^{(2)} \dots \bullet_D \mathbf{A}^{(D)} \Leftrightarrow \\ \mathbf{Y}_{(d)} &= \mathbf{A}^{(d)} \mathbf{X}_{(d)} \left( \mathbf{A}^{(D)} \boxtimes \dots \boxtimes \mathbf{A}^{(d+1)} \boxtimes \mathbf{A}^{(d-1)} \boxtimes \dots \boxtimes \mathbf{A}^{(1)} \right)^\top \end{aligned} \quad (3.13)$$

When a tensor defines a multilinear operator, the mode- $d$  product with a matrix is related to a change of basis, through multilinear product [26]. For  $D = 3$  we have three independent mode- $d$  products:

**Proposition 3.1.** If a linear change of basis is made in  $\mathcal{S}_1$ ,  $\mathcal{S}_2$ , and  $\mathcal{S}_3$  ( $\mathbf{x}' = \mathbf{A}\mathbf{x}$ ,  $\mathbf{y}' = \mathbf{B}\mathbf{y}$ ,  $\mathbf{z}' = \mathbf{C}\mathbf{z}$ ), then the array  $\mathcal{T}'$  defining the multilinear map  $f$  in the new coordinate system is a function of  $\mathcal{T}$ :

$$\begin{cases} \mathcal{X}' = (\mathbf{A}, \mathbf{B}, \mathbf{C}) \cdot \mathcal{X} = \mathcal{X} \bullet_1 \mathbf{A} \bullet_2 \mathbf{B} \bullet_3 \mathbf{C} \\ \mathcal{X}'_{ijk} = \sum_{pqr} A_{ip} B_{jq} C_{kr} \mathcal{X}_{pqr} \end{cases} \quad (3.14)$$

We recall then the definition of a tensor in relation to multilinear changes of bases:

**Definition 3.11.** A tensor of order  $D$  is an element of  $\mathcal{S}_1 \otimes \dots \otimes \mathcal{S}_D$ , and can be represented by a  $D$ -way array once bases of spaces  $\mathcal{S}_d$  have been fixed. Under multilinear transformations, the array of coordinates changes according to (3.14).

### 3.3. Tensor Decompositions

#### 3.3.1. Decomposable Tensors and Tensor Rank

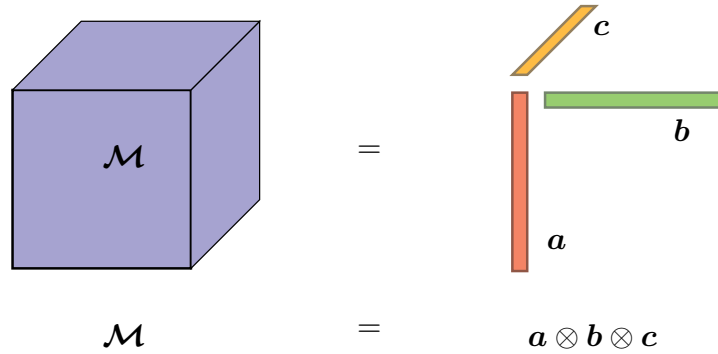


Figure 3.4.: A decomposable third order tensor - reproduction from [75]

The tensors of order  $D$  spanning the corresponding tensor space as defined in Definition 3.2 are very characteristic: they can be decomposed into an outer product of  $D$  vectors. Figure 3.4 illustrates a decomposable tensor of order  $D = 3$ . This leads us to the following definition:

**Definition 3.12.** A *decomposable* tensor, or *rank-1* tensor, is given by the outer product of vectors:  $\mathcal{D} = \mathbf{a} \otimes \mathbf{b} \otimes \dots \otimes \mathbf{c}$ , with elements  $D_{ij\dots k} = a_i b_j \dots c_k$ .

Decomposable tensors correspond to the discretization of a function of  $D$  separable variables (see Section 3.7 for more details).

**Proposition 3.2.** Any tensor  $\mathcal{T}$  can be decomposed into a linear combination of  $R$  decomposable tensors  $\mathcal{D}(r)$ :

$$\mathcal{M} = \sum_{r=1}^R \varsigma_r \mathcal{D}(r) \quad (3.15)$$

where coefficients  $\varsigma_r$  can be always chosen to be real positive, and decomposable tensors  $\mathcal{D}(r)$  to have unit norm, *i.e.* the product  $\|\mathbf{a}(r)\| \|\mathbf{b}(r)\| \cdots \|\mathbf{c}(r)\| = 1$ , but other choices are possible (cf. Section 3.3.4).

**Definition 3.13.** The minimum value  $R$  for which (3.15) holds is called *tensor rank*.

Unlike matrix rank, tensor rank may exceed all dimensions and depends on the choice for field  $\mathbb{K}$ .

In the remainder, we will generally state results for 3-order tensor decompositions. The generalization to  $D$ -order tensors is straightforward.

### 3.3.2. Tucker Decomposition and Multilinear Rank

The Tucker Decomposition (TKD) is a form of higher order principal component analysis.

**Definition 3.14.** The TKD  $\mathcal{M} = (\mathbf{A}, \mathbf{B}, \mathbf{C}) \cdot \mathcal{G} = \mathcal{G} \bullet_1 \mathbf{A} \bullet_2 \mathbf{B} \bullet_3 \mathbf{C}$  is given by a multilinear transformation of a dense but typically small core tensor  $\mathcal{G} \in \mathbb{C}^{P \times Q \times R}$ :

$$\begin{cases} \mathcal{M} = \sum_{p=1}^P \sum_{q=1}^Q \sum_{r=1}^R \mathcal{G}_{pqr} \mathbf{a}_p \otimes \mathbf{b}_q \otimes \mathbf{c}_r \\ M_{ijk} = \sum_p \sum_q \sum_r \mathcal{G}_{pqr} A_{ip} B_{jq} C_{kr} \end{cases} \quad (3.16)$$

The columns of factor matrices  $\mathbf{A} \in \mathbb{C}^{I \times P}$ ,  $\mathbf{B} \in \mathbb{C}^{J \times Q}$  and  $\mathbf{C} \in \mathbb{C}^{K \times R}$  represent the principal components along each mode, whereas the entries of the core tensor describe interactions between the components. The term on the left of (3.16) refers to the  $i, j, k$  entry of the multi-way array, so that a total number of  $I \times J \times K$  terms are known. The term on the right indicates the number of unknowns:  $(P \times Q \times R) + IP + JQ + KR$ . If the number of unknowns is smaller than the number of equations, there will generally be no solution. This is the case when both core tensor  $\mathcal{G}$  is diagonal and factor matrices  $\mathbf{A}$ ,  $\mathbf{B}$  and  $\mathbf{C}$  are orthonormal.  $R_1 = P$  refers to the *row rank*, *i.e.* the dimension of the space spanned by mode-1 fibers;  $R_2 = Q$  refers to the *column rank*, *i.e.* the dimension of the space spanned by mode-2 fibers, and so on. For  $D \geq 3$ ,  $R_1, \dots, R_D$  can be different. For generic  $D$ , we have:

**Definition 3.15.** The  $d$ -rank of tensor  $\mathcal{M} \in \mathbb{C}^{I_1 \times \cdots \times I_D}$  is the dimension of the vector space spanned by its mode- $d$  fibers:

$$R_d = \text{rank}_d\{\mathcal{M}\} = \text{column rank of } \mathbf{M}_{(d)} \leq I_d \quad (3.17)$$

The  $D$ -tuple  $(R_1, \dots, R_D)$  is called the *multilinear rank* of tensor  $\mathcal{M}$ .

If we only apply the orthonormality constraint to (3.16), we obtain HOSVD [26]. If we only keep a diagonal core tensor, we obtain the polyadic decomposition defined in Section 3.3.3. TKD is used to compress data or to find the  $D$  sub-spaces spanned by the

tensor fibers. On the other hand, the polyadic decomposition is used to factorize data into components easy to interpret. Thus, there exist two main instances of constrained TKD, with factor orthonormality or diagonal core constraints: HOSVD of Definition 3.18 and the polyadic decomposition of Definition 3.17.

**Definition 3.16.** The multilinear SVD or High Order Singular Value Decomposition (HOSVD) consists in a TKD with orthonormal factor matrices:

$$\mathcal{M} = \mathcal{S} \bullet_1 \mathbf{U}_1 \bullet_2 \mathbf{U}_2 \bullet_3 \mathbf{U}_3 \quad (3.18)$$

We can derive factor matrices  $\mathbf{U}_d$  via the SVD of mode- $d$  unfoldings  $\mathbf{M}_{(d)} = \mathbf{U}_d \Sigma_d \mathbf{V}_d^H$ . The columns of factor matrices  $\mathbf{U}_d$  are interpreted as multilinear singular vectors, and the norm of the slices of the core are multilinear singular values, these slices being mutually orthogonal.

### 3.3.3. Canonical-Polyadic Decomposition (CPD) and Tensor Rank

Consider the expression in (3.15), defining the tensor rank, as any tensor can be decomposed into a sum of rank-1 tensors. For  $D = 3$ , it takes the form below:

$$\mathcal{M} = \sum_{r=1}^R \varsigma_r \mathbf{a}(r) \otimes \mathbf{b}(r) \otimes \mathbf{c}(r) \quad (3.19)$$

We denote  $A_{ir}$ ,  $B_{jr}$  and  $C_{kr}$  the coordinates of vectors  $\mathbf{a}(r)$  in basis  $\mathbf{e}_i^{(1)}$ ,  $\mathbf{b}(r)$  in basis  $\mathbf{e}_j^{(2)}$ , and  $\mathbf{c}(r)$  in basis  $\mathbf{e}_k^{(3)}$  respectively. Then,  $\mathcal{M}$  can be expressed as

$$\begin{aligned} \mathcal{M} &= \sum_{r=1}^R \varsigma_r \left( \sum_{i=1}^I A_{ir} \mathbf{e}_i^{(1)} \right) \otimes \left( \sum_{j=1}^J B_{jr} \mathbf{e}_j^{(2)} \right) \otimes \left( \sum_{k=1}^K C_{kr} \mathbf{e}_k^{(3)} \right) = \\ &= \sum_{ijk} \left( \sum_{r=1}^R \varsigma_r A_{ir} B_{jr} C_{kr} \right) \mathbf{e}_i^{(1)} \otimes \mathbf{e}_j^{(2)} \otimes \mathbf{e}_k^{(3)} \end{aligned} \quad (3.20)$$

From (3.4), we derive the basis-dependent expression of array coordinates in (3.21), as represented in Figure 3.5:

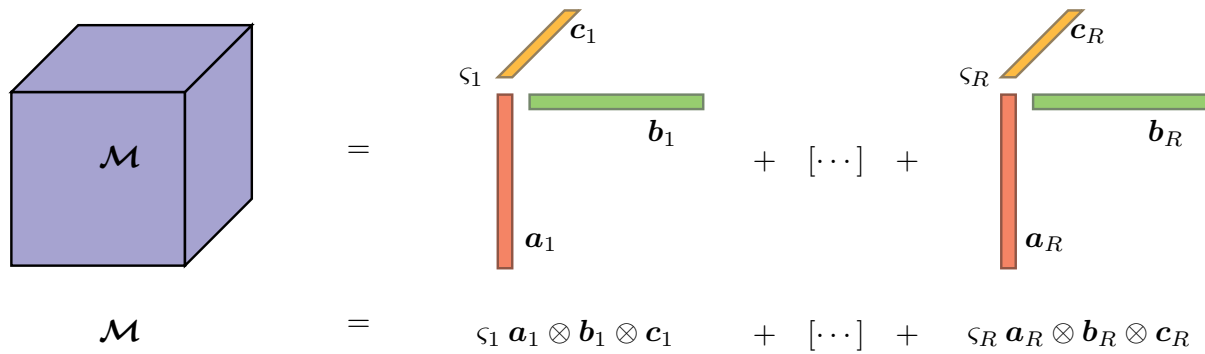
**Definition 3.17.** The *Polyadic decomposition* is indicated by  $\mathcal{M} = (\mathbf{A}, \mathbf{B}, \mathbf{C}) \cdot \mathcal{L} = \mathcal{L} \bullet_1 \mathbf{A} \bullet_2 \mathbf{B} \bullet_3 \mathbf{C}$  where  $R \times R \times R$  core tensor  $\mathcal{L} = \text{Diag}\{\boldsymbol{\varsigma}\}$  is diagonal:

$$\begin{cases} \mathcal{M} = \sum_{r=1}^R \varsigma_r \mathbf{a}_r \otimes \mathbf{b}_r \otimes \mathbf{c}_r \\ M_{ijk} = \sum_{r=1}^R \varsigma_r A_{ir} B_{jr} C_{kr} \end{cases} \quad (3.21)$$

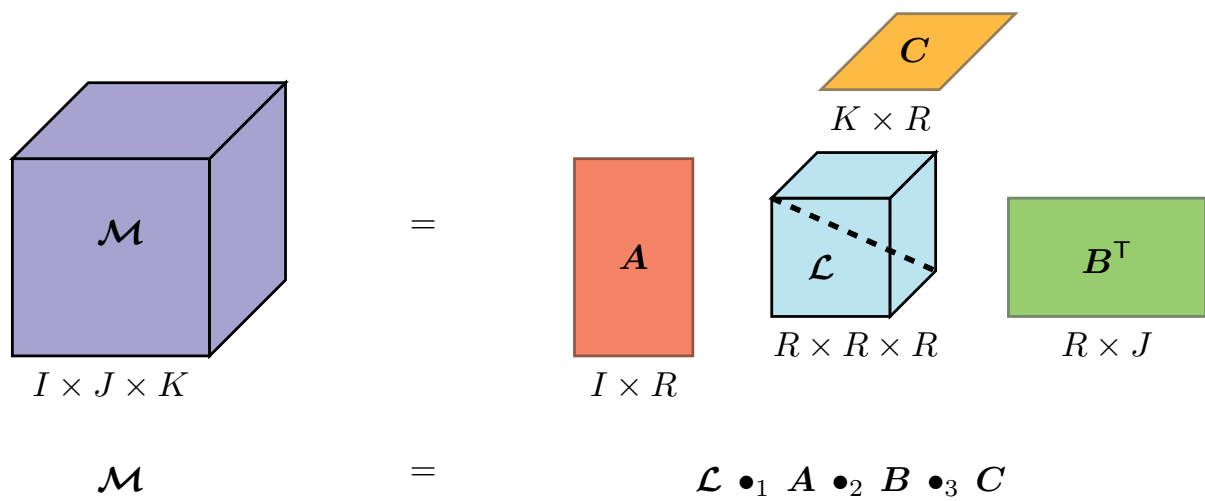
where  $\mathcal{L} = \text{Diag}\{\boldsymbol{\varsigma}\}$  is diagonal, and  $\boldsymbol{\varsigma} = [\varsigma_1, \dots, \varsigma_R]^T$ .

Notice that the Polyadic Decomposition in (3.21) is equivalent to (3.15) in terms of array coordinates, thus revealing tensor rank<sup>1</sup>. If  $R$  is not too large, this decomposition is unique (up to the equivalence relation of Definition 3.2) and is referred to as Canonical Polyadic Decomposition (CPD) (see [135, 26] and references therein. Uniqueness, which is the main motivation in resorting to tensors, will be treated in Section 3.3.5 .

<sup>1</sup>The problem of estimating the rank of a given tensor is NP hard. In practice, it is often determined numerically by fitting different rank- $R$  CPD models [75].



(a) CPD as a sum of rank-1 terms



(b) CPD as a linear change of basis

Figure 3.5.: Illustration of the CPD of a 3-order tensor - reproduction from [22]

It is often useful to express the CPD of a  $D$ -order tensor  $\mathcal{M}$  through tensor unfoldings and vectorization [21]:

$$\begin{cases} \mathcal{M} = (\mathbf{A}^{(1)}, \dots, \mathbf{A}^{(D)}) \cdot \mathcal{L} = \sum_{r=1}^R \varsigma_r \mathbf{a}_r^{(1)} \otimes \dots \otimes \mathbf{a}_r^{(D)} \\ \mathbf{M}_{(n)} = \mathbf{A}^{(n)} \mathbf{L}(\mathbf{A}^{(D)} \odot \dots \odot \mathbf{A}^{(n+1)} \odot \mathbf{A}^{(n-1)} \odot \dots \odot \mathbf{A}^{(1)})^\top \\ \text{vec}\{\mathcal{M}\} = (\mathbf{A}^{(D)} \odot \dots \odot \mathbf{A}^{(1)})_{\mathcal{S}} = \sum_{r=1}^R \varsigma_r \mathbf{a}_r^{(D)} \boxtimes \dots \boxtimes \mathbf{a}_r^{(1)} \end{cases} \quad (3.22)$$

For  $D = 3$  and  $\varsigma_r = 1 \forall r$ , we have three mode- $d$  unfolding representations of CPD [75]:

$$\begin{cases} \mathbf{M}_{(1)} = \mathbf{A}(\mathbf{C} \odot \mathbf{B})^\top \\ \mathbf{M}_{(2)} = \mathbf{B}(\mathbf{C} \odot \mathbf{A})^\top \\ \mathbf{M}_{(3)} = \mathbf{C}(\mathbf{B} \odot \mathbf{A})^\top \end{cases} \quad (3.23)$$

Moreover, when  $D = 3$ , we can express CPD in terms of “frontal” (or “horizontal”, or “lateral”) slices:

$$\begin{cases} \mathbf{M}_{::k} = \mathbf{A} \mathbf{D}_k(\mathbf{c}_{k:}) \mathbf{B}^\top \text{ where } \mathbf{D}_k(\mathbf{c}_{k:}) = \text{Diag}\{\mathbf{c}_{k:}\} \\ \mathbf{M}_{:j} = \mathbf{A} \mathbf{D}_j(\mathbf{b}_{j:}) \mathbf{C}^\top \text{ where } \mathbf{D}_j(\mathbf{b}_{j:}) = \text{Diag}\{\mathbf{b}_{j:}\} \\ \mathbf{M}_{i::} = \mathbf{B} \mathbf{D}_i(\mathbf{a}_{i:}) \mathbf{C}^\top \text{ where } \mathbf{D}_i(\mathbf{a}_{i:}) = \text{Diag}\{\mathbf{a}_{i:}\} \end{cases} \quad (3.24)$$

For simplicity, “frontal” slices can be expressed merely by  $\mathbf{M}_k = \mathbf{M}_{::k}$ .

### 3.3.4. CPD Factors, Normalization and Scaling

A CPD is said to be *essentially unique* if there exist a unique set  $\{\varsigma_r, \mathcal{D}(r), 1 \leq r \leq R\}$  such that equality holds in (3.15). However, even if the CPD is unique, there exist several ways of writing (3.15). In fact, writing a decomposable tensor as the outer product of vectors is subject to scaling indeterminacies, which actually stem from multilinearity properties of tensors [26], since

$$\alpha \mathbf{a} \otimes \beta \mathbf{b} \otimes \gamma \mathbf{c} = \mathbf{a} \otimes \mathbf{b} \otimes \mathbf{c} \quad (3.25)$$

if  $\alpha\beta\gamma = 1$ . Even if the above vectors are of unit Euclidean norm, there remain two scaling indeterminacies of unit modulus. As a consequence, attention should be paid to the difference between CPD or *essential* uniqueness, and uniqueness of factor matrices appearing in (3.21).

The *trivial indeterminacies* intrinsic in the array representation (3.21),  $\mathcal{M} = (\mathbf{A}, \mathbf{B}, \mathbf{C}) \cdot \mathcal{I}$ , are of two orders:

1. Arbitrary scaling of components for any  $R \times R$  invertible diagonal matrices  $\Delta_1, \Delta_2, \Delta_3$  satisfying  $\Delta_1 \Delta_2 \Delta_3 = \mathbf{I}$ :

$$\mathcal{M} = (\mathbf{A} \Delta_1, \mathbf{B} \Delta_2, \mathbf{C} \Delta_3) \cdot \mathcal{I} \quad (3.26)$$

or, equivalently,

$$\mathcal{M} = \sum_{r=1}^R (\alpha_r \mathbf{a}_r) \otimes (\beta_r \mathbf{b}_r) \otimes (\gamma_r \mathbf{c}_r) \text{ with } \alpha_r \beta_r \gamma_r = 1 \forall r \quad (3.27)$$

2. Permutation of the rank-1 terms, for any  $R \times R$  permutation matrix  $\mathbf{\Pi}$ :

$$\mathcal{M} = (\mathbf{A}\mathbf{\Pi}, \mathbf{B}\mathbf{\Pi}, \mathbf{C}\mathbf{\Pi}) \cdot \mathcal{I} \quad (3.28)$$

In practice, it is more convenient to fix the trivial indeterminacies of unit modulus in (3.21). It is often common to assume that the columns of factor matrices  $\mathbf{A}$ ,  $\mathbf{B}$ , and  $\mathbf{C}$ , have unit norm, with the weights absorbed into vector  $\boldsymbol{\varsigma} = [\varsigma_1, \dots, \varsigma_R]$ . As suggested in [128], for a  $D$ -order CPD, we generally fix  $(D - 1)R$  parameters without restricting the generality (cf. Sections 4.3.1, 5.3.4, 5.4.1, and 6.4 for examples of physics related constraints).

### 3.3.5. Uniqueness of the CPD

The unconstrained TKD is not unique, as factor matrices are rotation invariant:

$$(\mathbf{A}, \mathbf{B}, \mathbf{C}) \cdot \mathcal{G} = (\mathbf{A}\mathbf{U}^{-1}, \mathbf{B}\mathbf{V}^{-1}, \mathbf{C}\mathbf{W}^{-1})(\mathcal{G} \bullet_1 \mathbf{U} \bullet_2 \mathbf{V} \bullet_3 \mathbf{W}) \quad (3.29)$$

However, the subspaces spanned by factor vectors are unique [21], even though we might simplify the core structure as sparse or orthogonal, thus minimizing the interactions between components.

In order to better understand the interest of tensor CPD, we illustrate the case of rank- $R$  tensor decompositions of order two, which are not unique. This is the model usually employed in Blind Source Separation (BSS) and Non Negative Matrix Factorization (NMF) [21]:

$$\mathbf{M} = \sum_{r=1}^R \varsigma_r \mathbf{a}_r \otimes \mathbf{b}_r = \sum_{r=1}^R \varsigma_r \mathbf{a}_r \mathbf{b}_r^\top = \mathbf{A}\mathbf{L}\mathbf{B}^\top \quad (3.30)$$

where  $\mathbf{L} = \text{Diag}\{\varsigma_1, \dots, \varsigma_R\} \in \mathbb{C}^{R \times R}$  is a normalizing matrix, the columns of  $\mathbf{B}$  represent the unknown sources, and the columns of  $\mathbf{A}$  represent the associated mixing vectors, as represented in Figure 3.6. It is clear that, when  $D = 2$  (the multi-way array is a matrix), if model (3.30) is unconstrained, it admits infinite combinations of  $\mathbf{A}$  and  $\mathbf{B}$ :  $\mathbf{A}\mathbf{T}$ ,  $\mathbf{B}\mathbf{T}$ , where  $\mathbf{T}$  is orthogonal, *i.e.*  $\mathbf{T}^\top = \mathbf{T}^{-1}$ . For example, if the SVD of  $\mathbf{M}$  is  $\mathbf{U}\mathbf{\Sigma}\mathbf{V}^\top$ , we can choose  $\mathbf{A} = \mathbf{U}\mathbf{\Sigma}\mathbf{T}$ , and  $\mathbf{B} = \mathbf{V}\mathbf{T}$ . Therefore, uniqueness is attained thanks to restrictive constraints such as orthogonality (EVD and SVD) or triangularity (QR factorization), statistical independence, nonnegativity, etc. (cf. [22] for details). For example, the SVD is generically unique because  $\mathbf{U}$  and  $\mathbf{V}$  are orthonormal, and  $\mathbf{\Sigma}$  is diagonal [75]. On the other hand, the CPD of tensors of order  $D \geq 3$  is unique under mild conditions.

A necessary condition for uniqueness for CPD is that the number of equations be at least as large as the number of unknowns: for a tensor of order  $D$  and dimensions  $I_1 \times \dots \times I_D$ , we have

$$\left( \sum_{d=1}^D I_d - D + 1 \right) R \leq \prod_{d=1}^D I_d \quad (3.31)$$

(3.31) induces an upper bound on tensor rank, the *expected rank*  $R^0$ :

$$R \leq R^0 = \left\lfloor \frac{\prod_{d=1}^D I_d}{\left( \sum_{d=1}^D I_d - D + 1 \right)} \right\rfloor \quad (3.32)$$

Notice that we subtract  $(D - 1)R$  degrees of freedom because, in order to fix scaling indeterminacies, we fix  $(D - 1)R$  terms (see Section 3.3.4).

$$\begin{aligned}
 M &= \sigma_1 \mathbf{a}_1 \mathbf{b}_1^\top + [\dots] + \sigma_R \mathbf{a}_R \mathbf{b}_R^\top \\
 M &= \sigma_1 \mathbf{a}_1 \mathbf{b}_1^\top + [\dots] + \sigma_R \mathbf{a}_R \mathbf{b}_R^\top
 \end{aligned}$$

(a) CPD as a sum of rank-1 terms

$$\begin{aligned}
 M &= \mathbf{A} \mathbf{L} \mathbf{B}^\top \\
 M &= \mathbf{A} \mathbf{L} \mathbf{B}^\top
 \end{aligned}$$

(b) CPD as a linear change of basis

Figure 3.6.: Illustration of the CPD of a matrix - reproduction from [22]

The *typical rank* is any rank that occurs with probability greater than zero (this probability is generally estimated through MC experiments that randomly draw each entry from a continuous distribution).

For  $I \times J$  matrices, the expected and typical ranks are equal to  $\min\{I, J\}$ , whereas for tensors they may differ, and there may be more than one typical rank in  $\mathbb{R}$  (in  $\mathbb{C}$  there is only one typical rank). If only one typical rank exists, it occurs with probability one and is called *generic* [27].

In general, only the weak upper bound on the rank of a third order tensor is known [82]:

$$\text{rank}\{\mathcal{M}\} \leq \min\{IJ, JK, IK\} \quad (3.33)$$

A sufficient condition for the uniqueness of the CPD has been given by Kruskal for 3-way arrays [81, 26, 21]:

$$2R + 2 \leq \kappa_A + \kappa_B + \kappa_C \quad (3.34)$$

and was later generalized to  $D$ -way arrays by [135]:

$$2R + D - 1 \leq \sum_{d=1}^D \kappa_d \quad (3.35)$$

where  $\kappa_d$  denotes the Kruskal rank of the  $d$ -th factor matrix of the CPD. This condition is also necessary for  $D = 2, 3$  [75].

**Definition 3.18.** The Kruskal rank of a matrix  $\mathbf{A}$ ,  $\kappa(\mathbf{A})$ , is the largest number  $\kappa$  such that any combination of  $\kappa$  columns is full rank. Therefore,  $\kappa(\mathbf{A}) \leq \text{rank}\{\mathbf{A}\}$ .

A necessary condition for (3.35) to hold is that  $D \geq 3$  [88]. However, less stringent conditions guaranteeing almost surely a unique solution can be found, for instance, in [88, 26, 19]:

$$R(I + J + K - 2) < IJK \quad (3.36)$$

*i.e.* if  $R < R^0$ , or in [31]:

$$R \leq K \text{ and } R(R - 1) \leq \frac{I(I - 1)J(J - 1)}{2} \quad (3.37)$$

Notice that (3.36) and (3.37) are both valid for  $D = 3$ .

Tensor uniqueness conditions are milder and more natural, compared to matrix factorizations, as they only require the components to be sufficiently diverse and their number not too large. Sometimes prior knowledge of data properties, such as statistical independence, sparsity, Vandermonde structure, non negativity and orthogonality can be used as constraints to relax the uniqueness condition of CPD [21].

### 3.3.6. Advantages of the Tensor Formalism when $D \geq 3$

We enumerate hereafter some of the advantages offered by multilinear algebra tools.

1. Tensors are multi-way arrays that admit a compact representation and are typically overdetermined, *i.e.* the number of equations is greater than the number of unknowns. This enhances the robustness to noise and to missing data.
2. Tensor methods are able to directly operate on raw data, with no need to estimate higher order statistics: they can be considered deterministic and can deal with data of very short duration.
3. Flexibility in the choice of constraints, with less restrictive conditions than orthonormality or triangularity.
4. Uniqueness of decompositions under milder assumptions.

## 3.4. Multilinear Normal Distributions

Let  $\mathbf{x}$  be a  $I \times 1$  vector of random variables from a standard normal distribution,  $\mathbf{x} \sim \mathcal{N}(\mathbf{0}, \mathbf{I})$ , and  $\mathbf{y} = \mathbf{U}\mathbf{x}$  its linear transformation through a non singular  $I \times I$  matrix  $\mathbf{U}$ . Then,  $\mathbf{y} \sim \mathcal{N}(\mathbf{0}, \mathbf{\Sigma})$ , where  $\mathbf{\Sigma} = \mathbf{U}\mathbf{U}^H$ .

Now let  $\mathbf{X}$  be a  $I_1 \times I_2$  random matrix, and  $\mathbf{Y} = \mathbf{U}_1 \mathbf{X} \mathbf{U}_2^T = \mathbf{X} \bullet_1 \mathbf{U}_1 \bullet_2 \mathbf{U}_2$  its bilinear transformation through non singular matrices  $\mathbf{U}_1 \in \mathbb{C}^{I_1 \times I_1}$  and  $\mathbf{U}_2 \in \mathbb{C}^{I_2 \times I_2}$ . Then,  $\text{Cov}[\mathbf{Y}] = \mathbf{\Sigma}_1 \otimes \mathbf{\Sigma}_2$ , where  $\mathbf{\Sigma}_j = \mathbf{U}_j \mathbf{U}_j^H$ ,  $j = 1, 2$ . This covariance is said *separable*, as it can be divided into a row covariance  $\mathbf{\Sigma}_1$  and a column covariance  $\mathbf{\Sigma}_2$ . If the elements of  $\mathbf{X}$  follow a standard normal distribution, then the bilinearly transformed matrix  $\mathbf{Y}$  follows a matrix zero mean normal distribution:  $\mathbf{Y} \sim \mathcal{N}(\mathbf{0}, \mathbf{\Sigma}_1 \otimes \mathbf{\Sigma}_2)$ .

Let us increase the dimension and generalize this to random arrays. We introduce the definition of tensor multivariate normal distribution [67]:

**Definition 3.19.** We say that the multivariate random variable  $\mathcal{X} \in \mathbb{C}^{I_1 \times I_2 \times \dots \times I_D}$  follows an array Gaussian distribution of mean  $\mathcal{M}$  and covariance  $\mathcal{C} = \Sigma_1 \otimes \dots \otimes \Sigma_D \in \mathbb{C}^{I_1 \times I_1} \otimes \dots \otimes \mathbb{C}^{I_D \times I_D}$ , a tensor of order  $2D$ , and we write  $\mathcal{X} \sim \mathcal{AN}(\mathcal{M}, \mathcal{C})^2$ , if

$$p(\mathcal{X} | \mathcal{M}, \Sigma_1, \dots, \Sigma_D) = (2\pi)^{-I/2} |\mathcal{C}|^{-1/2} \exp\left(-\left\|(\mathcal{X} - \mathcal{M}) \bullet \mathcal{C}^{-1/2}\right\|^2 / 2\right) \quad (3.38)$$

with  $I = \prod_{d=1}^D I_d$ , and  $\mathcal{C}^{-1/2} = \{\Sigma_1^{-1/2}, \dots, \Sigma_D^{-1/2}\}$ , and  $|\mathcal{C}|^{-1/2} = \prod_{d=1}^D |\Sigma_d|^{-I/(2I_d)}$ .<sup>3</sup>

**Definition 3.20.** The covariance  $\mathcal{C}$  of a multivariate random variable  $\mathcal{X} \in \mathbb{C}^{I_1 \times I_2 \times \dots \times I_D}$  is said separable, since it can be expressed as the outer product of matrices  $\Sigma_d$ :  $\mathcal{C} = \Sigma_1 \otimes \dots \otimes \Sigma_D$  [67].

**Definition 3.21.** The  $I_1 \times I_2 \times \dots \times I_D$  array  $\mathcal{X} \sim \mathcal{AN}(\mathbf{0}, \mathbf{I}_{I_1} \otimes \dots \otimes \mathbf{I}_{I_D})$  is said to be standard Gaussian.

If we apply a multilinear transformation  $\{\mathbf{U}_1, \dots, \mathbf{U}_D\}$  on tensor  $\mathcal{X} = \sum_{r=1}^R \mathbf{a}_r^{(1)} \otimes \dots \otimes \mathbf{a}_r^{(D)}$ , its CPD nature is not modified:

$$\mathcal{Y} = (\mathbf{U}_1, \dots, \mathbf{U}_D) \cdot \mathcal{X} = \sum_{r=1}^R \mathbf{U}_1 \mathbf{a}_r^{(1)} \otimes \dots \otimes \mathbf{U}_D \mathbf{a}_r^{(D)} \quad (3.39)$$

Thus, the CPD is stable under multilinear transformations.

Similarly, we state the following results for the effects on the covariance structure after multilinear transformation of a random multi-way array [67]:

**Proposition 3.3.** If  $\text{Cov}[\mathcal{X}] = \Sigma_1 \otimes \dots \otimes \Sigma_D$  and  $\mathcal{Y} = \mathcal{X} \bullet_d \mathbf{G}$ , then

$$\text{Cov}[\mathcal{Y}] = \Sigma_1 \otimes \dots \otimes \Sigma_{d-1} \otimes (\mathbf{G} \Sigma_d \mathbf{G}^\top) \otimes \Sigma_{d+1} \otimes \dots \otimes \Sigma_D \quad (3.40)$$

This implies that the class of separable covariance arrays is stable under the action of mode- $d$  products. More generally,

**Proposition 3.4.** Let  $\mathcal{X} \sim \mathcal{AN}(\mathcal{M}, \mathbf{I}_{I_1} \otimes \dots \otimes \mathbf{I}_{I_D})$  and  $\{\mathbf{U}_1, \dots, \mathbf{U}_D\}$  be a multilinear transformation, and  $\Sigma_d = \mathbf{U}_d \mathbf{U}_d^\text{H}$ . Then, the multilinear product  $\mathcal{Y} = (\mathbf{U}_1, \dots, \mathbf{U}_D) \cdot \mathcal{X}$  has the following properties:

1.  $\mathbb{E}[\mathcal{Y}] = (\mathbf{U}_1, \dots, \mathbf{U}_D) \cdot \mathbb{E}[\mathcal{X}]; \quad \text{Cov}[\mathcal{Y}] = \Sigma_1 \otimes \dots \otimes \Sigma_D$
2.  $\mathbb{E}[\mathbf{Y}_{(d)}] = \mathbf{U}^{(d)} \mathbb{E}[\mathbf{X}_{(d)}] (\mathbf{U}^{(D)} \boxtimes \dots \boxtimes \mathbf{U}^{(d+1)} \boxtimes \mathbf{U}^{(d-1)} \boxtimes \dots \boxtimes \mathbf{U}^{(1)})^\top;$   
 $\mathbb{E}[\mathbf{Y}_{(d)} \mathbf{Y}_{(d)}^\text{H}] = \Sigma_d \prod_{i \neq d} \text{trace}\{\Sigma_i\}$
3.  $\mathbb{E}[\text{vec}\{\mathcal{Y}\}] = (\mathbf{U}_D \boxtimes \dots \boxtimes \mathbf{U}_1) \mathbb{E}[\text{vec}\{\mathcal{X}\}]; \quad \text{Cov}[\text{vec}\{\mathcal{Y}\}] = \Sigma_D \boxtimes \dots \boxtimes \Sigma_1$

Moreover, the probability density of  $\mathcal{Y}$ ,  $\text{vec}\{\mathcal{Y}\}$ ,  $\mathbf{Y}_{(d)}$ , remain Gaussian.

<sup>2</sup> $\mathcal{AN}$  denotes Array Normal.

<sup>3</sup>We recall that, as in Definition 3.10, the multilinear product between a tensor  $\mathcal{X}$  of order  $D$  and a collection of matrices  $\mathbf{A} = \{\mathbf{A}_1, \dots, \mathbf{A}_D\}$  is defined as a set of  $D$  independent mode- $d$  products:  $\mathcal{X} \bullet \mathbf{A} = \mathcal{X} \bullet_1 \mathbf{A}_1 \cdots \bullet_D \mathbf{A}_D$ .

## 3.5. Algorithms for Exact Decompositions

We recall the expression (3.21) of the  $R$ -term trilinear model for the 3-way array  $\mathcal{M}$ :

$$\begin{cases} \mathcal{M} = \sum_{r=1}^R \varsigma_r \mathbf{a}_r \otimes \mathbf{b}_r \otimes \mathbf{c}_r \\ M_{ijk} = \sum_{r=1}^R \varsigma_r A_{ir} B_{jr} C_{kr} \end{cases} \quad (3.41)$$

We shall describe an algebraic approximate solution for the exact CPD<sup>4</sup>, though joint diagonalization of two matrices.

### 3.5.1. Computation of the CPD through Joint Diagonalization

A direct decomposition algorithm has been proposed in [85]: it takes as inputs the  $K$  matrix slabs  $\mathbf{M}_k = \mathbf{M}_{::k}$  and the number of factors  $R$ , and returns the estimates of matrices  $\mathbf{A}$ ,  $\mathbf{B}$  and  $\mathbf{C}$ . The uniqueness of such a solution is guaranteed provided that the  $R$  column vectors corresponding to two of the ways are linearly independent, and the  $R$  column vectors associated with the third way have the property that no two are collinear (see below). The trilinear model (3.41) can be rewritten as  $K$  slices  $\mathbf{M}_k$  of size  $I \times J$ , according to (3.24):

$$\mathbf{M}_k = \sum_{r=1}^R (\mathbf{a}_r \otimes \mathbf{b}_r) C_{kr} = \sum_{r=1}^R \mathbf{a}_r C_{kr} \mathbf{b}_r^\top = \mathbf{A} \mathbf{D}_k(\mathbf{c}_{k:}) \mathbf{B}^\top \quad (3.42)$$

where  $\mathbf{D}_k(\mathbf{c}_{k:}) = \text{Diag}\{\mathbf{c}_{k:}\}$  and coefficients  $\varsigma_r$  were pulled in factor matrix  $\mathbf{B}$ .

The following more constraining identifiability conditions are employed, which concurrently imply the Kruskal condition in Equation (3.34):

**IC1** The columns of  $\mathbf{A}$  are linearly independent *i.e.*  $\kappa_A = R$ .

**IC2** The columns of  $\mathbf{B}$  are linearly independent *i.e.*  $\kappa_B = R$ .

**IC3** Every pair of columns of  $\mathbf{C}$  is linearly independent *i.e.*  $\kappa_C = 2$ .

Each condition refers to one way of the array: the first two conditions state that there must be at least  $R$  factors present in two ways. The third requires that no two factors are linked by a proportional relationship along the other way.

The decomposition proposed in [85] exploits the comparison between the two following linear combinations, for every vector of weights  $\boldsymbol{\rho} \in \mathbb{R}^K$ :

$$\begin{cases} \mathbf{M}(\boldsymbol{\rho}) = \sum_{k=1}^K \rho_k \mathbf{M}_k \\ \mathbf{C}(\boldsymbol{\rho}) = \sum_{k=1}^K \rho_k \mathbf{D}_k(\mathbf{c}_{k:}) \end{cases} \quad (3.43)$$

As particular combination we denote  $\mathbf{M}_+ = \sum_{k=1}^K \mathbf{M}_k$  and  $\mathbf{C}_+ = \sum_{k=1}^K \mathbf{D}_k(\mathbf{c}_{k:})$ . The following result constitutes the theoretical basis of the decomposition algorithm (see [85] for more details on its implementation):

**Theorem 3.1.** If conditions **IC1** and **IC2** hold,  $\mathbf{A}$  and  $\mathbf{B}$  have a left inverse and

1. the columns of matrix  $\mathbf{A}$  are the eigenvectors of the matrix  $\mathbf{M}(\boldsymbol{\rho}) \mathbf{M}_+^\dagger$ ; the corresponding eigenvalues are the diagonal entries of  $\mathbf{C}(\boldsymbol{\rho}) \mathbf{C}_+^{-1}$ .

<sup>4</sup>Exact is intended as in the absence of additive noise

2. matrix  $\mathbf{B}$  can be obtained as  $\mathbf{B} = (\mathbf{C}_+^{-1} \mathbf{A}^\dagger \mathbf{M}_+)^\top$ ;
3. the columns of matrix  $\mathbf{C}$  can be obtained thanks to the relation  $\mathbf{D}_k(\mathbf{c}_{k:}) = \mathbf{A}^\dagger \mathbf{M}_k (\mathbf{B}^\top)^\dagger$ .

*Sketch of proof.* From (3.42), we have  $\mathbf{M}_k = \mathbf{A} \mathbf{D}_k(\mathbf{c}_{k:}) \mathbf{B}^\top$ , and  $\mathbf{M}_+ = \mathbf{A} \mathbf{C}_+ \mathbf{B}^\top$ . Hence for any  $k$ ,  $\mathbf{M}_k \mathbf{M}_+^\dagger \mathbf{A} = \mathbf{A} \mathbf{D}_k(\mathbf{c}_{k:}) \mathbf{C}_+^{-1}$ .

## 3.6. Tensor Approximation

### 3.6.1. An Approximation Problem in Additive Noise

In practice, we admit that observations  $\mathcal{X}$ , related to the model  $\mathcal{M}$ , are corrupted by an additive noise  $\mathcal{N}$ . In other words, the observation model becomes  $\mathcal{X} = \mathcal{M} + \mathcal{N}$ , and the goal is to fit (3.22) with the data. In any case, when the data are noisy, the fit alone cannot determine the rank [75]. In practice, the presence of noise requires a fit of a multilinear model of lower rank, *i.e.* with  $R < \text{rank}\{\mathcal{X}\}$ , leading to an *approximation problem*. The fact that the set of rank- $R$  tensors is not closed when  $R > 1$  may raise difficulties (see Section 3.6.2 for the question of existence of a rank- $R$  approximant). The reasons why we cannot resort to an exact decomposition with  $\tilde{R} = \text{rank}\{\mathcal{X}\}$  is that generally, the real rank  $\tilde{R}$  is unknown and that decompositions with larger rank are not unique [27] (see Section 3.3.5 for the question of uniqueness).

Data tensor have a normal distribution under the following assumption:

**A 3.1.** Additive noise follows an array normal distribution with zero mean:  $\mathcal{N} \sim \mathcal{N}(\mathbf{0}, \mathbf{C})$ . It follows that  $\mathcal{X} \sim \mathcal{N}(\mathcal{M}, \mathbf{C})$ , where  $\mathcal{M}$  has a CPD structure.

The approximation problem of a tensor  $\mathcal{X} \in \mathbb{C}^{I \times J \times K}$  through a CPD with  $R$  components is given by

$$\min_{\hat{\mathcal{X}}} \|\mathcal{X} - \hat{\mathcal{X}}\| = \min_{\hat{\mathbf{A}}, \hat{\mathbf{B}}, \hat{\mathbf{C}}} \left\| \mathcal{X} - \sum_{r=1}^R \hat{\zeta}_r \hat{\mathbf{a}}_r \otimes \hat{\mathbf{b}}_r \otimes \hat{\mathbf{c}}_r \right\|_{\mathbf{C}}^2 \quad (3.44)$$

where  $\mathbf{C}$  indicates the covariance of tensor  $\mathcal{X}$ , after defining the weighted tensor norm  $\|\mathcal{X}\|_{\mathbf{C}} = \|\mathbf{C}^{-1/2} \bullet_1 \bullet_2 \bullet_3 \mathcal{X}\|$ .

The cost function (3.44) can be expressed via unfoldings  $\mathbf{X}_{(1)} \in \mathbb{C}^{I \times JK}$ ,  $\mathbf{X}_{(2)} \in \mathbb{C}^{J \times IK}$ , and  $\mathbf{X}_{(3)} \in \mathbb{C}^{K \times IJ}$ :

$$\begin{cases} \min_{\hat{\mathbf{X}}_{(1)}} \|\mathbf{X}_{(1)} - \hat{\mathbf{X}}_{(1)}\| = \min_{\hat{\mathbf{A}}, \hat{\mathbf{B}}, \hat{\mathbf{C}}} \left\| \mathbf{X}_{(1)} - \hat{\mathbf{A}} (\hat{\mathbf{C}} \odot \hat{\mathbf{B}})^\top \right\|_{\mathbf{C}_{(1)}}^2 = \\ \min_{\hat{\mathbf{X}}_{(2)}} \|\mathbf{X}_{(2)} - \hat{\mathbf{X}}_{(2)}\| = \min_{\hat{\mathbf{A}}, \hat{\mathbf{B}}, \hat{\mathbf{C}}} \left\| \mathbf{X}_{(2)} - \hat{\mathbf{B}} (\hat{\mathbf{C}} \odot \hat{\mathbf{A}})^\top \right\|_{\mathbf{C}_{(2)}}^2 = \\ \min_{\hat{\mathbf{X}}_{(3)}} \|\mathbf{X}_{(3)} - \hat{\mathbf{X}}_{(3)}\| = \min_{\hat{\mathbf{A}}, \hat{\mathbf{B}}, \hat{\mathbf{C}}} \left\| \mathbf{X}_{(3)} - \hat{\mathbf{C}} (\hat{\mathbf{B}} \odot \hat{\mathbf{A}})^\top \right\|_{\mathbf{C}_{(3)}}^2 \end{cases} \quad (3.45)$$

where  $\mathbf{C}_{(d)}$  represents the covariance of the mode- $d$  unfolding.

Alternatively, (3.44) can be expressed through vectorization  $\mathbf{x} = \text{vec}\{\mathcal{X}\}$ :

$$\min_{\hat{\mathbf{x}}} \|\mathbf{x} - \hat{\mathbf{x}}\| = \min_{\hat{\mathbf{A}}, \hat{\mathbf{B}}, \hat{\mathbf{C}}} \left\| \mathbf{x} - \sum_{r=1}^R \hat{\zeta}_r \hat{\mathbf{c}}_r \boxtimes \hat{\mathbf{b}}_r \boxtimes \hat{\mathbf{a}}_r \right\|_{\Sigma_{(1)}}^2 \quad (3.46)$$

where  $\Sigma_{(1)}$  represents the covariance of tensor vectorization  $\mathbf{x}$ . Analogously, we define the weighted matrix norm as  $\|\mathbf{X}\|_{\Sigma} = \sqrt{\text{trace}\{\mathbf{X}^H \Sigma^{-1} \mathbf{X}\}}$ .

In the remainder, unless otherwise specified, we will make the following assumption:

**A 3.2.** Additive noise is white Gaussian, *i.e.* its variance  $\mathbf{C}$  is diagonal:  $\mathbf{C} = \sigma^2 \mathcal{I}_{I \times J \times K}$ . It follows that the noise of tensor unfoldings and vectorization also have a diagonal covariance:  $\mathbf{C}_{(1)} = \sigma^2 \mathcal{I}_{I \times JK}$ ,  $\mathbf{C}_{(2)} = \sigma^2 \mathcal{I}_{J \times IK}$ , and  $\mathbf{C}_{(3)} = \sigma^2 \mathcal{I}_{K \times IJ}$ ;  $\Sigma_{(1)} = \sigma^2 \mathbf{I}_{IJK}$ .

Notice that, if Assumption A 3.2 is verified, the weighted norms  $\|\cdot\|_{\mathbf{C}}$  and  $\|\cdot\|_{\Sigma}$  reduce to simple Frobenius norms  $\|\mathcal{X}\| = \sqrt{\langle \mathcal{X}, \mathcal{X} \rangle}$  and  $\|\mathbf{X}\| = \sqrt{\text{trace}\{\mathbf{X}^H \mathbf{X}\}}$ .

The Cramér-Rao Bound (CRB) for the CPD approximation problem in additive i.i.d. complex circularly symmetric Gaussian noise was derived in [90, 149].

### 3.6.2. Existence and Degeneracies

For matrices, Eckart and Young [39] showed that a best rank- $k$  approximation, with  $k \leq R$ , is given by the first  $k$  leading singular vectors of the SVD  $\mathbf{X} = \sum_{r=1}^R \varsigma_r \mathbf{u}_r \otimes \mathbf{v}_r$ . This means that the rank- $k$  approximation  $\mathbf{A}$  minimizing  $\|\mathbf{X} - \mathbf{A}\|^2$  is given by

$$\mathbf{A} = \sum_{r=1}^k \varsigma_r \mathbf{u}_r \otimes \mathbf{v}_r \quad (3.47)$$

This result is not true for higher order tensors: the existence of the best rank- $k$  approximant is not guaranteed. As a consequence, all the factors of a rank- $k$  approximation must be found simultaneously [75]. This problem leads to the definition of *degeneracy*:

**Definition 3.22.** A tensor is said *degenerate* if it may be approximated arbitrarily well by a factorization of lower rank.

In the case of degeneracy, although reducing the approximation error, some rank-1 factors become close to proportional, and the magnitude of some terms goes to infinity, with opposite signs. The best rank- $k$  approximation is on the boundary of the space of rank- $k$  and rank- $k+1$  tensors. Since the space of rank- $k$  tensors is not closed, the sequence of arbitrarily better rank- $k$  approximant tensors can converge to a tensor of rank  $k+1$ . Hence, the infimum of the approximation problem in (3.44) may never be reached; we refer to [88, 27] for further details.

Imposing non negative constraints on the tensor model is a way to prevent degeneracy, as cancellation of opposite diverging rank-1 tensors cannot occur when tensors have positive entries only [87]. On the other hand, if tensor entries are free and  $R > 1$ , one might perform the minimization over a closed subset, or by adding a regularization term to the objective function in (3.44) (see [128] for an example).

Alternatively, one might also adopt a closed superset, such as the adherence of rank- $R$  tensors. In light of this fact, it is useful to define the concept of border rank:

**Definition 3.23.** The border rank of a tensor  $\mathcal{X}$  corresponds to the minimum number of rank-1 tensors that approximate  $\mathcal{X}$  with arbitrarily small nonzero error:

$$\widetilde{\text{rank}}\{\mathcal{X}\} = \min\{r : \forall \epsilon > 0 \exists \mathcal{E} \text{ s.t. } \|\mathcal{E}\| < \epsilon \text{ and } \text{rank}\{\mathcal{X} + \mathcal{E}\} = r\} \quad (3.48)$$

We always have:  $\widetilde{\text{rank}}\{\mathcal{X}\} \leq \text{rank}\{\mathcal{X}\}$ .

### 3.6.3. Algorithms for Tensor Approximation

All the algorithms proposed in the literature aim at minimizing the fitting error in (3.44). References can be found in [27]. Before resorting to tensor approximation algorithms, dimension reduction through HOSVD is often recommended, both for speed of convergence and computational complexity, provided that the tensor dimensions are not smaller than the rank  $R$  chosen for the decomposition [27]. In particular, since the core  $\mathcal{S}$  of HOSVD in (3.18) is all orthogonal, we can calculate the *truncated* HOSVD [32], which gives a good starting point for the Alternating Least Squares (ALS). The truncation discards the multilinear singular vectors and slices in the core tensors corresponding to the smallest multilinear singular values.

#### Gradient descent

We can express the cost function in (3.44) through parameter vectorization,  $\Upsilon = \Upsilon(\boldsymbol{\vartheta})$ , where  $\boldsymbol{\vartheta} = [\text{vec}\{\mathbf{A}\}, \text{vec}\{\mathbf{B}\}, \text{vec}\{\mathbf{C}\}]^\top$ . Hence, the iteration is given by

$$\boldsymbol{\vartheta}(k+1) = \boldsymbol{\vartheta}(k) - \mu(k) \nabla \Upsilon(\boldsymbol{\vartheta})|_{\boldsymbol{\vartheta}=\boldsymbol{\vartheta}(k)} \quad (3.49)$$

where  $\mu$  is the iteration dependent stepsize.

The gradient descent is the simplest algorithm, but with very poor convergence behaviour. However, it can be improved through *Enhanced Line Search* (ELS) or through the *Levenberg-Marquardt* algorithm [27]. ELS in particular is more robust to the presence of local minima and more efficient than simple gradient descent.

#### Alternating Least Squares

Alternating Least Squares (ALS) can be seen as an example of non linear LS problem, where variables separate [27]. We present the ALS method only for  $D = 3$  through unfoldings (3.23). However, it is easily generalized to any  $D$  through (3.22).

The idea is to obtain a quadratic function of one factor matrix, while keeping the other factor matrices fixed: for instance, for  $D = 3$ , we fix  $\mathbf{B}$  and  $\mathbf{C}$ , and we solve for  $\mathbf{A}$ , alternatively, until convergence of a given criterion. We have then the quadratic form

$$\min_{\hat{\mathbf{A}}} \|\mathbf{X}_{(1)} - \hat{\mathbf{A}}(\mathbf{C} \odot \mathbf{B})^\top\|^2 \quad (3.50)$$

where we store weights in  $\hat{\mathbf{A}} = \mathbf{A} \text{Diag}\{\boldsymbol{\varsigma}\}$ . The solution to (3.50) is given by

$$\begin{aligned} \hat{\mathbf{A}} &= \mathbf{X}_{(1)}[(\mathbf{C} \odot \mathbf{B})^\top]^\dagger = \\ & \mathbf{X}_{(1)}(\mathbf{C}^* \odot \mathbf{B}^*)(\mathbf{C}^\top \mathbf{C}^* \boxminus \mathbf{B}^\top \mathbf{B}^*)^{-1} \end{aligned} \quad (3.51)$$

Finally, we normalize the columns of  $\hat{\mathbf{A}}$  to get  $\mathbf{A}$ :  $\varsigma_r = \|\hat{\mathbf{a}}_r\|$  and  $\mathbf{a}_r = \hat{\mathbf{a}}_r/\varsigma_r$ . If  $(\mathbf{C} \odot \mathbf{B})^\top$  has full column rank, (3.51) is the LS solution of the over-determined linear system.

The ALS algorithm for generic  $D$  is described in Algorithm 3.1. The factor matrices can be initialized through the HOSVD:

$$\mathbf{A}^{(d)} \leftarrow R \text{ leading left singular vectors of } \mathbf{X}_{(d)} \quad (3.52)$$

ALS is very easy to implement, but can take many iterations and is not guaranteed to converge to a global minimum nor a stationary point. It may depend strongly on initialization [75]. It has a satisfactory performance for high SNR, and for well *separated* components (cf. Section 3.7 for a measure of separateness).

**Algorithm 3.1 CP ALS**

1: Inputs:

- Initialize with  $\mathbf{A}^{(d)} \in \mathbb{C}^{I_d \times R}$ ,  $1 \leq d \leq D$ .
- Data tensor  $\mathcal{X} \in \mathbb{C}^{I_1 \times \dots \times I_D}$ .

2: While convergence criterion not met, do  $k := k + 1$ 3: **for**  $d = 1, \dots, D$  **do**

4:

$$\begin{aligned} \mathbf{V} &\leftarrow \mathbf{A}^{(1)\top} \mathbf{A}^{(1)*} \square \dots \square \mathbf{A}^{(d-1)\top} \mathbf{A}^{(d-1)*} \square \mathbf{A}^{(d+1)\top} \mathbf{A}^{(d+1)*} \square \dots \square \mathbf{A}^{(D)\top} \mathbf{A}^{(D)*} \\ \mathbf{A}^{(d)} &= \mathbf{X}_{(d)} (\mathbf{A}^{(D)*} \odot \dots \odot \mathbf{A}^{(d+1)*} \odot \mathbf{A}^{(d-1)*} \odot \dots \odot \mathbf{A}^{(1)*}) \mathbf{V}^{-1} \end{aligned} \quad (3.53)$$

Normalize columns of  $\mathbf{A}^{(d)}$ , storing their norms in  $\varsigma$ 5: **end for**

6: Outputs:

- Factor matrices  $\mathbf{A}^{(d)}$ ,  $1 \leq d \leq D$ .
- Coefficient vector  $\varsigma$ .

7: End

**Other methods**

An interesting semi-algebraic solution for approximate CPD via simultaneous joint diagonalizations can be found in [121].

**3.7. Physical Diversity and Coherence**

As we will develop in Section 5.2, many physical phenomena can be modeled through two fundamental concepts: sparsity (sum of simpler constituents) and separability (separation of variables). The underlying model is then expressed through a  $D$ -partite target function  $f : \mathcal{S}_1 \times \dots \times \mathcal{S}_D \mapsto \mathbb{C}$ :

$$f(\mathbf{x}_1, \dots, \mathbf{x}_D) = \sum_{r=1}^R \varsigma_r \prod_{d=1}^D \phi_{rd}(\mathbf{x}_d), \quad \varsigma_r \in \mathbb{C}, \forall r \quad (3.54)$$

For  $D = 3$ , we have  $f : \mathcal{S}_1 \times \mathcal{S}_2 \times \mathcal{S}_3 \mapsto \mathbb{C}$ :

$$f(\mathbf{x}, \mathbf{y}, \mathbf{z}) = \sum_{r=1}^R \varsigma_r a_r(\mathbf{x}) b_r(\mathbf{y}) c_r(\mathbf{z}) \quad (3.55)$$

If we discretize (3.55), we obtain a tensor array:

$$\begin{cases} \mathcal{M} = \sum_{r=1}^R \varsigma_r \mathbf{a}_r \otimes \mathbf{b}_r \otimes \mathbf{c}_r \\ M_{ijk} = \sum_{r=1}^R \varsigma_r A_{ir} B_{jr} C_{kr} \end{cases} \quad (3.56)$$

with  $M_{ijk} = f(\mathbf{x}_i, \mathbf{y}_j, \dots, \mathbf{z}_k)$ ,  $A_{ir} = a_r(\mathbf{x}_i)$ ,  $B_{jr} = b_r(\mathbf{y}_j)$  and  $C_{kr} = c_r(\mathbf{z}_k)$ , and vectors  $\mathbf{a}_r = [A_{1r}, \dots, A_{I_r}]^\top$ ,  $\mathbf{b}_r = [B_{1r}, \dots, B_{J_r}]^\top$ , and  $\mathbf{c}_r = [C_{1r}, \dots, C_{K_r}]^\top$ . Notice that the

discretization of a sparse and separable function in (3.56) is equivalent to the CPD in (3.21). Namely, separability of a continuous function is equivalent to the discrete concept of rank-1 or decomposable tensor, when subsets  $\{\mathcal{S}_1, \dots, \mathcal{S}_D\}$  are finite sets.

In the continuous case, the domain  $\Omega$  of function  $f$  is generally constrained through differentiability or integrability ( $C^\infty(\Omega)$  or  $L^2(\Omega)$ ), whereas in the discrete case  $\Omega = \mathbb{C}^{I_1 \times \dots \times I_D}$ . The requirement  $D \geq 3$  for identifiability of CPD in (3.15) implies that our data must be at least a 3-way array in the discrete case as in (3.56), and that the underlying model must be a function of at least three variables in the continuous case, *i.e.* a  $D$ -partite or multipartite function, where the arguments are partitioned in  $D$  blocks of variables, as in (3.55). Therefore, we will refer to (3.55) and (3.56) as a rank- $R$  multilinear decomposition, *i.e.* the decomposition of a function into a linear combination of separable functions.

When the domain of a function  $f$  is a Hilbert space with scalar product  $\langle \cdot, \cdot \rangle$ , we can define an angular constraint that is going to ease the identification problem: the uniqueness of the decomposition of Section 3.5 and the existence of the best rank- $R$  approximant of Section 3.6.

**Definition 3.24.** Let  $\mathbb{H}$  be a Hilbert space with scalar product  $\langle \cdot, \cdot \rangle$ , and  $\Phi \subseteq \mathbb{H}$  be a set of elements  $\phi_i$  with unit norm. The coherence of  $\Phi$  is defined as

$$\mu(\Phi) = \sup_{i \neq j} |\langle \phi_i, \phi_j \rangle| \quad (3.57)$$

If  $\Phi$  is a finite set,  $\Phi = \{\phi_1, \dots, \phi_R\}$ , we can write

$$\mu(\Phi) = \max_{i \neq j} |\langle \phi_i, \phi_j \rangle| \quad (3.58)$$

The relative incoherence of subset  $\Phi$  is then defined as

$$\chi(\Phi) = \frac{1 - \mu(\Phi)}{\mu(\Phi)} \quad (3.59)$$

It is clear that  $0 \leq \mu(\Phi) \leq 1$  ( $0 \leq \chi(\Phi) \leq \infty$ ), and that  $\mu(\Phi) = 0$  ( $\chi(\Phi) = \infty$ ) *iif*  $\phi_1, \dots, \phi_R$  are orthonormal. Also,  $\mu(\Phi) = 1$  ( $\chi(\Phi) = \infty$ ) *iif* contains at least a pair of collinear elements, *i.e.*  $\exists p \neq q, \lambda \neq 0 : \phi_p = \lambda \phi_q$ .

*Remark.* When dealing with a  $D$ -partite function  $f$ , that can be modeled through (3.22), we can define  $D$  coherences for the  $D$  subsets  $\Phi_d = [\phi_{d1}, \dots, \phi_{dR}]$ :

$$\mu_d = \mu(\Phi_d) \quad (3.60)$$

For instance, when  $D = 3$ , we can define three coherences for the three subsets formed by the  $R$  columns of factor matrices in (3.56),  $\mathbf{A} = [\mathbf{a}_1, \dots, \mathbf{a}_R]$ ,  $\mathbf{B} = [\mathbf{b}_1, \dots, \mathbf{b}_R]$ , and  $\mathbf{C} = [\mathbf{c}_1, \dots, \mathbf{c}_R]$ , and we write  $\mu_A = \mu(\mathbf{A})$ ,  $\mu_B = \mu(\mathbf{B})$ , and  $\mu_C = \mu(\mathbf{C})$ :

$$\begin{cases} \mu_A = \max_{p \neq q} \frac{|\mathbf{a}_p^H \mathbf{a}_q|}{\|\mathbf{a}_p\| \|\mathbf{a}_q\|} \\ \mu_B = \max_{p \neq q} \frac{|\mathbf{b}_p^H \mathbf{b}_q|}{\|\mathbf{b}_p\| \|\mathbf{b}_q\|} \\ \mu_C = \max_{p \neq q} \frac{|\mathbf{c}_p^H \mathbf{c}_q|}{\|\mathbf{c}_p\| \|\mathbf{c}_q\|} \end{cases} \quad (3.61)$$

[88] derived two important results for the identifiability of the CPD problem, based on the definition of coherences  $\mu_d$  of factor matrices  $\mathbf{A}^{(d)} = [\mathbf{a}_1^{(d)}, \dots, \mathbf{a}_R^{(d)}]$ :

$$\mu_d = \max_{p \neq q} \frac{|\mathbf{a}_p^{(d)H} \mathbf{a}_q^{(d)}|}{\|\mathbf{a}_p^{(d)}\| \|\mathbf{a}_q^{(d)}\|} \quad (3.62)$$

The first result provides a sufficient condition for the uniqueness of the CPD [88]:

**Theorem 3.2.** CPD in (3.22) is essentially unique, if coherences satisfy

$$\sum_{d=1}^D \frac{1}{\mu_d} \geq 2R + D - 1 \quad (3.63)$$

The second result provides a sufficient condition for the existence and the uniqueness of the CPD approximation problem constrained through coherences [88]:

**Theorem 3.3.** If  $D \geq 3$ , and if coherences satisfy

$$\left( \prod_{d=1}^D \mu_d \right)^{1/D} \leq \frac{D}{2R + D - 1} \quad (3.64)$$

the coherence-bounded approximation problem

$$\min_{\hat{\mathbf{A}}^{(d)}} \left\| \boldsymbol{\mathcal{X}} - \sum_{r=1}^R \hat{\zeta}_r \hat{\mathbf{a}}_r^{(1)} \otimes \cdots \otimes \hat{\mathbf{a}}_r^{(D)} \right\|_{\mathcal{C}}^2 \quad \text{s.t.} \quad \mu \left( \hat{\mathbf{a}}_r^{(1)}, \dots, \hat{\mathbf{a}}_r^{(D)} \right) \leq \bar{\mu}_d \quad (3.65)$$

has an essentially unique solution.

These results have been used to derive a practical algorithm in [128].

The concept of coherence presents two main advantages compared to Kruskal rank:

1. Whereas Kruskal rank is NP-hard, coherences are trivial to compute. The Kruskal rank  $\kappa_d$  of a factor matrix  $\mathbf{A}^{(d)}$  can be checked in polynomial time only when its columns  $\mathbf{a}_r^{(d)}$  are linearly independent, in which case  $\kappa_d = \text{rank}\{\mathbf{A}^{(d)}\}$ .
2. As coherences of factor matrices has a straightforward physical meaning, they are more suitable as constraints to guarantee the existence of a solution to the approximation problem (3.44). In fact, other artificial constraints such as orthogonality would not often correspond to any physical reality. We will detail the physical meaning of coherences in the framework of sensor arrays in Sections 4.5, 5.3.6 and 5.4.2.



# 4. Tensor Array Processing with Multiple Rotational Invariances

## 4.1. Introduction

This chapter gathers concepts from all the previous ones, showing one of the main applications of tensor decompositions: joint localization and estimation of narrowband sources in the far field. At first, signal subspace methods described in Chapter 2 were extended to more than one dimension, as we briefly present in Section 4.2. Then, Section 4.3 introduces the deterministic approach of [136], applying the Canonical Polyadic Decomposition (CPD) directly to sensor arrays through multiple translations in space. The main results around the identifiability of the model are addressed in Section 4.4. A physical interpretation of coherences in the light of the present application to sensor arrays is discussed in Section 4.5. Sections 4.6 and 4.7 detail the estimation of Directions of Arrival (DoAs) and source signatures respectively. Finally, Section 4.8 summarizes the advantages of tensor array processing.

We use all the physical assumptions of Section 1.2.2: A 1.1 (far field), 1.3 (narrowband), A 1.4 (baseband), A 1.2 (band limited sources), A 1.5 (no dissipation), A 1.6 and A 1.7 (homogeneous, isotropic and non-dispersive medium).

## 4.2. Multidimensional Subspace Methods

When received signals are multidimensional or can be parameterized as a function of multidimensional parameters, several high resolution techniques have been adapted to tackle the increased complexity of the problem, such as 2D ESPRIT [164], *DD* ESPRIT [60], and *DD* MUSIC [151]. In these extensions, the *DD* signals are stacked into matrices, thus losing the multilinear structure that they often carry.

Low rank approximation through SVD has been extended to deal with multidimensional data for the harmonic retrieval problem in [61, 122, 73, 129], through HOSVD in (3.18). This approach can be used to improve the estimate of the signal subspace of any subspace based parameter estimation scheme, such as Multiple Signal Characterization (MUSIC) and Estimation of Signal Parameters via Rotational Invariance Techniques (ESPRIT), whenever a multidimensional structure can be exploited.

The ESPRIT algorithm as described in Section 2.6 and proposed by [126] takes advantage of only a single displacement invariance in the acquisition system. However, many configurations, such as ULAs or rectangular arrays, possess multiple such invariances. The questions of an optimal choice of subarrays and of a unique solution that exploits all possible invariances simultaneously are addressed in [142], as a natural extension of the TLS ESPRIT algorithm. This led to the algorithm Multiple Invariance ESPRIT (MI ESPRIT) with collinear displacements.

In a similar fashion, root-MUSIC of [5] was extended to multiple parallel ULAs in [109].

### 4.3. CPD through Multiple Invariances

The ESPRIT algorithm involves two identical arbitrary subarrays, displaced from each other: this structure induces a rotational invariance in the baseband data, that can be exploited to recover DoAs, with no need for subarray calibration (see Sections 2.6 and 4.6 for details). For multiple parameter estimation, however, one needs invariances in 2D, and ESPRIT must be applied separately to each dimension, so that the problem of pairing azimuth and elevation estimates remains [164]. The same is true for higher dimensions [60, 61].

[136] extended the shift invariance of the subarray to more than two displacements: suppose that the acquisition system contains  $M$  displaced identical subarrays of  $L$  sensors each. We denote  $\boldsymbol{\delta}_m \in \mathbb{R}^3$  the location of the  $m$ -th subarray within the acquisition system, as the subarray space shifts can be arbitrarily chosen, and not strictly collinear as in MI ESPRIT. In this formulation, ESPRIT corresponds to  $M = 2$  in Section 2.6. For instance, Figure 4.1 shows  $M = 3$  displaced identical subarrays of  $L = 4$  sensors each.

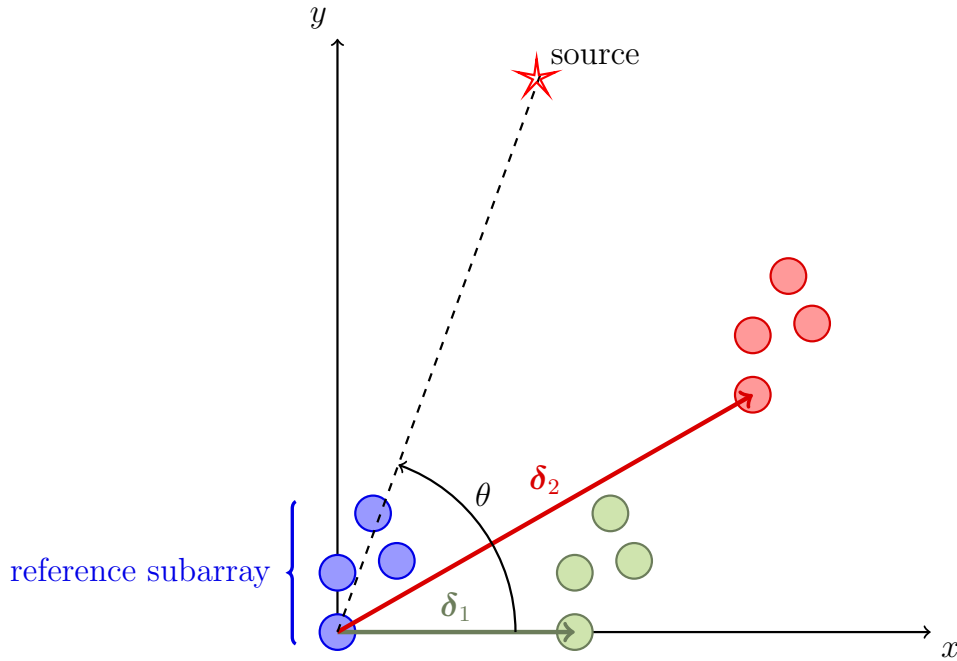


Figure 4.1.: Acquisition system for  $L = 4, M = 3$  - space shift diversity

If we stack slices corresponding to different subarray outputs, we obtain:

$$\begin{bmatrix} \mathbf{X}_1 \\ \mathbf{X}_2 \\ \vdots \\ \mathbf{X}_M \end{bmatrix} = \begin{bmatrix} \mathbf{J}_1 \\ \mathbf{J}_2 \\ \vdots \\ \mathbf{J}_M \end{bmatrix} \bar{\mathbf{A}} \mathbf{S}^T + \mathbf{N} = \begin{bmatrix} \mathbf{A} \Phi_1 \\ \mathbf{A} \Phi_2 \\ \vdots \\ \mathbf{A} \Phi_M \end{bmatrix} \mathbf{S}^T + \mathbf{N} \quad (4.1)$$

where  $\mathbf{S} = [\mathbf{s}_1, \dots, \mathbf{s}_R]$  is the  $T \times R$  source signature matrix as in (1.57), whereas  $\mathbf{A} = [\mathbf{a}(\theta_1), \dots, \mathbf{a}(\theta_R)]$  is the  $L \times R$  subarray steering matrix as in (1.11), and  $\mathbf{N}$  refers to additive noise. For more details, cf. Chapter 1 for notations and assumptions.  $\mathbf{J}_m$  is a  $L \times L_{tot}$  selection matrix that extracts  $L$  rows corresponding to the  $m$ -th subarray from the global steering matrix  $\bar{\mathbf{A}}$ , and  $\Phi_m$  is a diagonal  $R \times R$  matrix depending on source parameters:

$$\Phi_m = \text{Diag}\{e^{-j\omega \delta_m^T \mathbf{d}(\theta_1)/c}, \dots, e^{-j\omega \delta_m^T \mathbf{d}(\theta_R)/c}\} \quad (4.2)$$

As for MI ESPRIT, the total number of sensor  $L_{tot}$  is constrained by

$$L + M - 1 \leq L_{tot} \leq LM \quad (4.3)$$

which covers the overlapping case (with  $L - 1$  shared sensors) by the left equality and the non overlapping case by the right equality.

The inverse problem for array processing with multiple invariances becomes

**Problem 4.1.** Given noisy subarray slices  $\mathbf{X}_m$ , and the number of sources  $R$ , find steering matrix  $\mathbf{A}$ , space shift diagonal matrices  $\Phi_m$ , and source signatures matrix  $\mathbf{S}$ .

If  $\mathbf{B}$  is the  $M \times R$  matrix whose  $m$ -th row  $\mathbf{b}_m$  corresponds to the diagonal of  $\Phi_m$ , its elements are given by  $B_{mr} = e^{j\omega \delta_m^T \mathbf{d}(\theta_r)/c}$ . From (4.1), the  $m$ -th subarray output is then expressed as

$$\mathbf{X}_m = \mathbf{A} \mathbf{D}_m(\mathbf{b}_m) \mathbf{S}^T, \quad 1 \leq m \leq M \quad (4.4)$$

where  $\mathbf{D}_m(\mathbf{b}_m) = \text{Diag}\{\mathbf{b}_m\}$  has  $\mathbf{b}_m$  as its diagonal. Since (4.4) describes a trilinear model (cf. the slice representation (3.24) in Section 3.3.3), it is straightforward to express it through CPD, after staking all the subarray  $\mathbf{X}_m$  as lateral slices  $\mathbf{X}_{:m}$  of a  $L \times M \times T$  tensor  $\mathcal{X}$ :

$$\begin{cases} \mathcal{X} = \sum_{r=1}^R \mathbf{a}_r \otimes \mathbf{b}_r \otimes \mathbf{s}_r + \mathcal{N} \\ \mathcal{X}_{\ell mt} = \sum_{r=1}^R A_{\ell r} B_{mr} S_{tr} + \mathcal{N}_{\ell mt} \end{cases} \quad (4.5)$$

where rank- $R$  corresponds to the number of sources, supposed known, thanks to Assumption A 1.10, and  $\mathcal{N}$  refers to additive noise. The physical meaning of the three factor matrices is given through their elements:

$$\begin{cases} A_{\ell r} = \exp\{-j\omega \tau_\ell(\theta_r)\} \text{ refers to space diversity} \\ B_{mr} = \exp\{-j\omega \zeta_m(\theta_r)\} \text{ refers to space shift diversity} \\ S_{tr} = s_r(t) \text{ refers to time diversity} \end{cases} \quad (4.6)$$

where  $\tau_\ell(\theta_r) = \mathbf{p}_\ell^T \mathbf{d}(\theta_r)/c$  denotes the time delay at sensor  $\ell$  w.r.t. the reference sensor, and  $\zeta_m(\theta_r) = \delta_m^T \mathbf{d}(\theta_r)/c$  denotes the time delay at subarray  $m$  with respect to the reference subarray.

Thus, through CPD formulation, Problem 4.1 becomes

**Problem 4.2.** Given noisy tensor  $\mathcal{X}$ , and the number of sources  $R$ , find steering matrix  $\mathbf{A}$ , space shift matrix  $\mathbf{B}$ , and source signatures matrix  $\mathbf{S}$ .

In the remainder, we will make the following assumption around the deterministic nature of our model:

**A 4.1.** DoAs  $\theta_r \forall r$  as well as source complex envelopes  $s_r(t) \forall r$  are considered deterministic.

### 4.3.1. CPD Factors, Normalization and Scaling

After ensuring the essential uniqueness of the third order tensor, we need to fix  $(D - 1)R$  scale and permutation ambiguities, where  $D = 3$  (cf. Section 3.3.4 for the definition of essential uniqueness).

As for the scale indeterminacy, we need the following hypotheses:

**A 4.2.** The first sensor ( $\ell = 1$ ) is taken as origin, *i.e.*  $\mathbf{p}_1 = \mathbf{0}$  and  $A_{1r} = \exp\{-j\frac{2\pi}{\lambda}(\mathbf{p}_1^\top \mathbf{d}(\theta_r))\} = 1$ .

**A 4.3.** The sensor gains  $g_\ell(\theta)$  are supposed nonzero and known, and then compensated for (*calibration*)<sup>1</sup>, which is equivalent to the omnidirectional case  $g_\ell(\theta) = 1 \forall \ell$ . Section 5.4 will deal with generic gain sensors as a new form of physical diversity.

**A 4.4.** The first subarray ( $m = 1$ ) is taken as origin, *i.e.*  $\boldsymbol{\delta}_1 = \mathbf{0}$  and  $B_{1r} = \exp\{-j\frac{2\pi}{\lambda}(\boldsymbol{\delta}_1^\top \mathbf{d}(\theta_r))\} = 1$ .

For practical purposes and without restricting the generality, we have preferred to impose the first row of matrices  $\mathbf{A}$  and  $\mathbf{B}$  to be formed of ones (in fact, as justified in Assumptions A 4.2, 4.3 and A 4.4,  $\mathbf{p}_1 = \mathbf{0}$ ,  $\boldsymbol{\delta}_1 = \mathbf{0}$  and  $g_\ell(\theta) = 1 \forall \ell$ ), and to pull column-wise the remaining scaling coefficients,  $\{\varsigma_r A_{1r} B_{1r} \mathbf{s}_r, 1\}$ , into matrix  $\mathbf{S}$ . More precisely, we fix all scale indeterminacies through the following transformation:

$$(\hat{\mathbf{a}}_r, \hat{\mathbf{b}}_r, \hat{\mathbf{s}}_r, \varsigma_r) \leftarrow \left( \frac{\mathbf{a}_r}{A_{1r}}, \frac{\mathbf{b}_r}{B_{1r}}, \varsigma_r A_{1r} B_{1r} \mathbf{s}_r, 1 \right) \quad (4.7)$$

This choice permits to compute performance bounds on the retrieval of CPD factors in (4.5) more easily.

On the other hand, we will resolve the issue of permutation indeterminacies only for the assessment of performance in comparison with the ground truth for the case of computer simulations in the following chapters, using a greedy LS matching algorithm (cf. Section 3.3.4). For example, for matrix estimate  $\hat{\mathbf{A}}$ , we have

$$\hat{\boldsymbol{\Pi}} = \min_{\boldsymbol{\Pi}} (\hat{\mathbf{A}}\boldsymbol{\Pi} - \mathbf{A})^2 \text{ for any } R \times R \text{ permutation matrix of the columns of } \hat{\mathbf{A}}, \boldsymbol{\Pi} \quad (4.8)$$

and for DoA estimate  $\boldsymbol{\theta} = [\theta_1, \dots, \theta_R]$ , we have

$$\hat{\boldsymbol{\Pi}} = (\hat{\boldsymbol{\theta}}\boldsymbol{\Pi} - \boldsymbol{\theta})^2 \text{ for any } R \times R \text{ permutation matrix of the elements of } \hat{\boldsymbol{\theta}}, \boldsymbol{\Pi} \quad (4.9)$$

Note that after fixing the scaling indeterminacies, the number of remaining free parameters is now  $(L + M + K - 2)R$  [128] as stated in Section 3.3.4 for the general *DD* case, and not  $(L + M + K - 3)R$  as assumed in [136].

## 4.4. Identifiability of the CPD Model

For identifiability, we mean uniqueness of all spatial source parameters as well as temporal signatures, given a finite set of measurements in the absence of noise, up to trivial indeterminacies of permutations and scale (see Section 3.3.4). We will show that the uniqueness of the angular parameter estimates is closely related to that of the CPD factor matrices. Identifiability conditions on DoAs for ESPRIT and MI ESPRIT are illustrated and compared in [142].

[136] extended MI ESPRIT to arbitrary displacements, through tensor CPD, as we detailed in Section 4.3, and also stated the following identifiability condition, based on the sufficient condition for CPD uniqueness in (3.34):

<sup>1</sup>This operation may change the noise spatial distribution.

**Proposition 4.1.** If

$$\kappa_A + \kappa_B + \kappa_S \geq 2R + 2 \quad (4.10)$$

then the CP model in (4.5) identifiable, *i.e.* the factorization of the model into  $D = 3$  factor matrices is essentially unique.

The concept of Kruskal rank of steering matrices  $\mathbf{A}$  and  $\mathbf{B}$  is related to the concept of *rank ambiguity* [136]:

**Definition 4.1.** A manifold  $\mathcal{A}(\boldsymbol{\theta})$  is free of rank- $\nu$  ambiguities if every  $\nu + 1$  steering vectors corresponding to distinct DoAs drawn from the manifold are linearly independent.

As for the identifiability, we can state that

**Proposition 4.2.** Let  $\bar{\nu}$  be the maximum value satisfying (4.1). Then, the associated array can resolve up to  $\bar{\nu}$  uncorrelated sources.

From the definition (3.18) of Kruskal rank, we have  $\kappa_A \geq \nu_A + 1$  and  $\kappa_B \geq \nu_B + 1$ .

We will now address the question of identifiability in two distinct cases: uncorrelated and correlated sources.

#### 4.4.1. Incoherent Sources Scenario

Impinging sources are said incoherent if they are not fully correlated (see Section 1.3.1 for the definition of source correlation).

If  $\mathbf{S}$  is fat ( $T \geq R$ ) and full rank ( $R$ ), the sufficient condition (4.10) becomes

$$\kappa_A + \kappa_B \geq R + 2 \quad (4.11)$$

which is always satisfied if different sources have different DoAs, thanks to the assumption of manifold injectivity A 1.18. Thus, we obtain the following sufficient condition for identifiability:

$$\nu_A + \nu_B \geq R \quad (4.12)$$

that we call *subarray synthesis*, since the resolving powers of the reference subarray and of the displacement subarray add up.

In the case of  $R$  linearly independent sources,  $\kappa_S = \min\{R, T\}$ , and (4.10) becomes

$$\kappa_A + \kappa_B + \min\{R, T\} \geq 2R + 2 \quad (4.13)$$

Therefore,  $R$  sources can be identified with at least  $T = 2$  time samples, provided  $\mathbf{A}$  and  $\mathbf{B}$  are both tall ( $L, M \geq R$ ) and full rank ( $R$ ). This allows the tensor formulation to deal with very short data samples, as we will state in Section 4.8.

A necessary condition for identifiability when  $\mathbf{S}$  is full column rank is given by [90]:

**Proposition 4.3.** CPD is identifiable only if  $\mathbf{A} \odot \mathbf{B}$  has full column rank.

The following result ensuring the previous necessary identifiability condition is presented in [57]:

**Proposition 4.4.** If either  $\text{rank}\{\mathbf{A}\} + \kappa_B \geq R + 1$  or  $\text{rank}\{\mathbf{B}\} + \kappa_A \geq R + 1$ , then  $\mathbf{A} \odot \mathbf{B}$  has full column rank.

This shows that a full rank Khatri-Rao matrix can be generated with two rank-deficient matrices, thus offering a signal decorrelation of the same kind as spatial smoothing [132] or the polarization smoothing algorithm in [112] (see Section 5.3.5 for details). Through this result, [57] derived a more relaxed sufficient condition:

**Theorem 4.1.** If  $\mathbf{S}$  is full column rank, and  $\kappa_A, \kappa_B \geq 2$ , a sufficient condition for identifiability is given by

$$\text{rank}\{\mathbf{A}\} + \kappa_B \geq R + 2 \quad \text{or} \quad \text{rank}\{\mathbf{B}\} + \kappa_A \geq R + 2 \quad (4.14)$$

which reduces to Kruskal condition in (4.11) if  $\text{rank}\{\mathbf{A}\} = \kappa_A$  or  $\text{rank}\{\mathbf{B}\} = \kappa_B$ .

From theorem 4.1 we derive the condition for uniformly distributed subarrays, *i.e.* when matrix  $\mathbf{A}$  is Vandermonde with distinct non zero generators (given by  $R$  spatially distinct sources):

$$\min\{L, R\} + \kappa_B \geq R + 2 \quad (4.15)$$

Analogously, if the space-shifts are uniformly distributed, matrix  $\mathbf{B}$  is Vandermonde and

$$\kappa_A + \min\{M, R\} \geq R + 2 \quad (4.16)$$

#### 4.4.2. Coherent Source Scenario

When  $R_c \leq R$  sources are fully correlated or coherent (see Section 1.3.1 for the definition of source correlation), the source covariance matrix is singular. However, in the tensor framework, through Assumption 4.1, sources signatures are deterministic. Hence, we want to assess the link between this stochastic concept (coherent sources) and its deterministic and algebraic counterpart:

**Proposition 4.5.** Through the Cauchy-Schwarz inequality, the singularity of  $\mathbf{R}_S$  implies that with probability one the corresponding  $R_c$  columns of  $\mathbf{S}$  are collinear [4].

*Proof for  $R = 2$ .* If there are  $R = 2$  sources, covariance matrix  $\mathbf{R}_S$  is the expected value  $\mathbf{R}_S = \mathbb{E}[\check{\mathbf{R}}_S]$ :

$$\check{\mathbf{R}}_S = \mathbf{S}^H \mathbf{S} = \begin{bmatrix} \mathbf{s}_1^H \mathbf{s}_1 & \mathbf{s}_1^H \mathbf{s}_2 \\ \mathbf{s}_2^H \mathbf{s}_1 & \mathbf{s}_2^H \mathbf{s}_2 \end{bmatrix} \quad (4.17)$$

As a covariance matrix, it is semi-definite positive:  $\check{\mathbf{R}}_S \succeq 0 \iff |\check{\mathbf{R}}_S| = (\mathbf{s}_1^H \mathbf{s}_1)(\mathbf{s}_2^H \mathbf{s}_2) - (\mathbf{s}_1^H \mathbf{s}_2)^2 \geq 0$ , which coincides with the Cauchy-Schwarz inequality. If  $\check{\mathbf{R}}_S$  is singular, its determinant cancels and equality holds:

$$|\check{\mathbf{R}}_S| = (\mathbf{s}_1^H \mathbf{s}_1)(\mathbf{s}_2^H \mathbf{s}_2) - (\mathbf{s}_1^H \mathbf{s}_2)^2 = 0 \quad (4.18)$$

This holds if and only if source are collinear:  $\mathbf{s}_2 = \alpha \mathbf{s}_1$ .

On the other hand, if sources are not fully correlated, the covariance is positive definite:  $\check{\mathbf{R}}_S \succ 0 \iff |\check{\mathbf{R}}_S| > 0$ , and then the Cauchy-Schwarz result holds with strict inequality:  $(\mathbf{s}_1^H \mathbf{s}_2)^2 < (\mathbf{s}_1^H \mathbf{s}_1)(\mathbf{s}_2^H \mathbf{s}_2)$ .  $\square$

When dealing with tensors, we find this algebraic characterization of coherence more useful, as it is directly connected to Definition (3.18) of Kruskal rank and Definition (3.24) of coherence. In particular, the Kruskal rank of a matrix with  $R_c \geq 2$  collinear columns is always one. Hence, the sufficient condition for CPD identifiability in (4.10) is never verified, as  $\kappa_S = 1$ :

$$\kappa_A + \kappa_B + 1 \leq 2R + 1 \implies \kappa_A + \kappa_B + 1 < 2R + 2 \quad (4.19)$$

However, there exist solutions to the problem of coherent sources to restore the identifiability of tensor CPD:

1. More strict uniqueness conditions ensure identifiability when  $R_c$  sources are coherent, at the price of rotational indeterminacies affecting the corresponding columns of  $\mathbf{A}$  and  $\mathbf{B}$  [11].
2. If the tensor presents a particular structure, such as Vandermonde, along one or two modes, spatial smoothing techniques can be applied [137, 132] (cf. Section 2.9). If sensors have multiple components, as in vector sensor arrays, we refer to [112] for a polarization smoothing algorithm.

When sources are closely spaced or partially correlated, the coherence structure described in Section 3.7 is strongly affected, thus impairing the problem of the existence of a solution. In this case, if the SNR is low, working in the subspace domain with CPD can give better results [136]. This difference is analogous to that between deterministic and stochastic ML, to which Weighted Subspace Fitting is equivalent asymptotically for proper weights. Weights can also be applied to the data domain formulation, and a few initialization of the ALS can help dealing with local minima.

## 4.5. Physical Meaning of Coherences

In Section 3.7, we defined the concept of coherence of a factor matrix and linked it to the identifiability of CPD. For the CPD with space, space shift and time diversities of the current chapter, the coherences of factor matrices  $\mathbf{A}$  and  $\mathbf{B}$  have a very clear and interchangeable physical meaning. From (3.61) and (4.6), we express the coherence of factor matrix  $\mathbf{A}$ :

$$\mu_A = \max_{p \neq q} \frac{|\mathbf{a}_p^H \mathbf{a}_q|}{L} \quad (4.20)$$

[88] shows the link between this angular measure and the angular separation between DoAs, through the following theorem, based on Definition 1.1:

**Theorem 4.2.** If sensor position vectors  $\{\mathbf{p}_1, \dots, \mathbf{p}_L\}$  are resolvent with respect to three linearly independent directions, then  $\forall p, \forall q$

$$\|\mathbf{a}_p^H \mathbf{a}_q\| = 1 \iff \mathbf{d}(\theta_p) = \mathbf{d}(\theta_q) \quad (4.21)$$

The condition of resolvent sensors is not very restrictive, as sensor arrays usually have elements separated by less than half wavelength (see Section 1.2.3). Theorem 4.2 means that the uniqueness of factor matrix  $\mathbf{A} = [\mathbf{a}_1, \dots, \mathbf{a}_R]$  is equivalent to the identifiability of DoAs  $\{\mathbf{d}(\theta_1), \dots, \mathbf{d}(\theta_R)\}$ . Thus, the coherence of space factor matrix  $\mathbf{A}$  is a measure of the minimal angular separation between sources, viewed from the reference subarray.

Similarly, the coherence of space shift factor matrix  $\mathbf{B} = [\mathbf{b}_1, \dots, \mathbf{b}_R]$  is a measure of the minimal angular separation between sources, viewed from the subarray translations:

$$\mu_B = \max_{p \neq q} \frac{|\mathbf{b}_p^H \mathbf{b}_q|}{M} \quad (4.22)$$

The third coherence of source factor matrix  $\mathbf{S}$  is a measure of the maximal correlation coefficient between sources:

$$\mu_S = \max_{p \neq q} \frac{|\mathbf{s}_p^H \mathbf{s}_q|}{\|\mathbf{s}_p\| \|\mathbf{s}_q\|} \quad (4.23)$$

Thus, uniqueness and existence conditions in (3.63) and (3.64) of Section 3.7 can be interpreted in a physical sense. In particular, the best rank- $R$  approximation exists if sources are not too closely spaced, and their temporal signatures are not too correlated. Thus, we can separate sources with arbitrarily high correlation provided their DoAs are different enough [88].

As an example, coherence constraints of Theorem 3.3 ensuring the existence of a rank- $R$  approximation were implemented in [128], through a differentiable penalty in a descent algorithm. The role of coherences in problem conditioning is also pointed out in [28].

## 4.6. DoA Estimation

The DoA estimation can be performed according to a two-step procedure: at first, factor matrices  $\mathbf{A}$ ,  $\mathbf{B}$  and  $\mathbf{C}$  are estimated through one of the methods described in Section 3.6.3, such as the ALS; then, DoAs are estimated either from  $\mathbf{A}$ , or from  $\mathbf{B}$ , or from both. ALS can be initialized through the algebraic solution of [85] detailed in Section 3.5.1, or by a standard ESPRIT algorithm when possible, or randomly: in any case, the conditional updates of any given matrix in Algorithm 3.1 guarantees a monotonous convergence to an at least local minimum, but it cannot worsen the fit.

Our knowledge on the acquisition system can be of three kinds:

1. *Subarray manifold  $\mathcal{A}(\boldsymbol{\theta})$  unknown, displacement manifold  $\mathcal{B}(\boldsymbol{\theta})$  known.* As it is generally assumed in ESPRIT approaches [126, 142], the reference subarray is not calibrated, *i.e.* sensor positions  $\mathbf{p}_\ell, \ell \neq 1$  are unknown. However, space shifts  $\boldsymbol{\delta}_m \forall m$  are known. Hence, DoA estimation is derived from  $\mathbf{B}$ . In this case, at least one displacement must respect spatial sampling conditions: for instance, for linear displacements in 1D,  $\exists m : |\boldsymbol{\delta}_m| \leq \lambda/2$ .
2. *Subarray manifold  $\mathcal{A}(\boldsymbol{\theta})$  known, displacement manifold  $\mathcal{B}(\boldsymbol{\theta})$  unknown.* As it is assumed in [128], space shifts  $\boldsymbol{\delta}_m, m \neq 1$  are unknown. However, sensor positions within a subarray,  $\mathbf{p}_\ell \forall \ell$  are known. Hence, DoA estimation is derived from  $\mathbf{A}$ . In this case, we will suppose that the distance between successive sensors is less than or equal to  $\lambda/2$ .

An example of this scenario is given by sonar buoys freely floating on the surface, but equipped with a device that maintain their orientation towards North. In this case, the shape of each subarray is known but relative displacements are not known. Other examples include geophysical measurements in difficult conditions, such as on glaciers.

3. *Both subarray manifold  $\mathcal{A}(\boldsymbol{\theta})$  and displacement manifold  $\mathcal{B}(\boldsymbol{\theta})$  are known.* In this case, DoAs can be recovered jointly from  $\mathbf{A}$  and  $\mathbf{B}$ . The full knowledge of the whole acquisition system is also assumed by the MUSIC algorithm, although without the space shift invariance structure.

Cases 1) and 2) are actually interchangeable, as they draw their expression from similar kinds of space diversity, which translates into a very similar expression for matrices  $\mathbf{A}$  and  $\mathbf{B}$  in (4.6). For instance, the acquisition system in Figure 4.1 can be seen as the set of 3 displaced identical subarrays of 4 sensors, or as the set of 4 displaced identical subarrays of 3 sensors.

Alternatively, instead of an unconstrained ALS, one could impose some knowledge about the array configuration through parametric or non parametric constraints upon the columns (*i.e.* source-wise) of any of the three matrices ( $\mathbf{A}$ ,  $\mathbf{B}$ ,  $\mathbf{S}$ ). Another strategy might be to apply a gradient descent for a cost function, directly parameterized with respect to the DoA, and to initialize it with the ALS two steps algorithm. However, this is known to produce very little improvement and have a very high computational burden.

The unconstrained two-step approach that we adopt in this thesis, though suboptimal, is very simple to implement. Its computational cost is mainly due to ALS iterations in the first step, and, for more complex array geometries as in Section 4.6.1, to the exhaustive search on a grid of angles in the second step. In particular, we will detail case 2) (*i.e.* sensor positions known within a subarray, but space shifts unknown), as it can be generalized easily to cases 1) and 3). If we only know sensor positions  $\mathbf{p}_\ell$ , we will use matrix  $\hat{\mathbf{A}}$ , whereas if we only know subarray translations  $\boldsymbol{\delta}_m$ , we will use matrix  $\hat{\mathbf{B}}$  for DoA estimation. We will detail in particular the former case, as both cases are indeed interchangeable.

### 4.6.1. General 3D DoA Estimation

The array configuration in 3D is described by the  $L \times 3$  sensor position matrix  $\mathbf{P} = [\mathbf{p}_1, \dots, \mathbf{p}_L]^\top = [\mathbf{p}^x, \mathbf{p}^y, \mathbf{p}^z]$ , with rows  $\mathbf{p}_\ell = [p_\ell^x, p_\ell^y, p_\ell^z]$ . Analogously, the space shift structure is described by the  $M \times 3$  displacement matrix  $\boldsymbol{\Delta} = [\boldsymbol{\delta}_1, \dots, \boldsymbol{\delta}_M]^\top = [\boldsymbol{\delta}^x, \boldsymbol{\delta}^y, \boldsymbol{\delta}^z]$ , with rows  $\boldsymbol{\delta}_m = [\delta_m^x, \delta_m^y, \delta_m^z]$ . For scalar wavefields in 3D, the parameter vector to estimate includes the azimuth and the elevation:  $\boldsymbol{\vartheta} = [\boldsymbol{\theta}^\top, \boldsymbol{\psi}^\top]^\top = [\theta_1, \dots, \theta_R, \psi_1, \dots, \psi_R]^\top \in \mathbb{R}^{2R}$  (cf. Section 1.7). Once we recover factor matrices  $\mathbf{A}$  and/or  $\mathbf{B}$  through CPD, we estimate DoAs column-wise, *i.e.* source-wise,  $\forall r, 1 \leq r \leq R$ :

$$\begin{cases} (\hat{\theta}_r, \hat{\psi}_r) = \arg \min_{\theta, \psi} \left[ (\hat{\mathbf{a}}_r - \mathbf{a}_r(\theta, \psi))^H (\hat{\mathbf{a}}_r - \mathbf{a}_r(\theta, \psi)) \right] \\ (\hat{\theta}_r, \hat{\psi}_r) = \arg \min_{\theta, \psi} \left[ (\hat{\mathbf{b}}_r - \mathbf{b}_r(\theta, \psi))^H (\hat{\mathbf{b}}_r - \mathbf{b}_r(\theta, \psi)) \right] \\ (\hat{\theta}_r, \hat{\psi}_r) = \arg \min_{\theta, \psi} \left[ (\hat{\mathbf{a}}_r - \mathbf{a}_r(\theta, \psi))^H (\hat{\mathbf{a}}_r - \mathbf{a}_r(\theta, \psi)) \right] + \left[ (\hat{\mathbf{b}}_r - \mathbf{b}_r(\theta, \psi))^H (\hat{\mathbf{b}}_r - \mathbf{b}_r(\theta, \psi)) \right] \end{cases} \quad (4.24)$$

### 4.6.2. 2D DoA Estimation

In 2D, *i.e.* when sources and subarrays are coplanar, thanks to Assumption A 1.8,  $\mathbf{p}_\ell = [p_\ell^x, p_\ell^y]$  and  $\boldsymbol{\delta}_m = [\delta_m^x, \delta_m^y]$ : thus (4.6) becomes

$$\begin{cases} A_{\ell r} = \exp \left\{ -j \frac{\omega}{c} (p_\ell^x \cos \theta_r + p_\ell^y \sin \theta_r) \right\} \\ B_{mr} = \exp \left\{ -j \frac{\omega}{c} (\delta_m^x \cos \theta_r + \delta_m^y \sin \theta_r) \right\} \\ S_{tr} = s_r(t) \end{cases} \quad (4.25)$$

In order to avoid phase unwrapping issues, we form the quotient between two successive subarrays, as in [128]:

$$\frac{A_{\ell+1,r}}{A_{\ell,r}} = \exp \left\{ -j \frac{\omega}{c} [(p_{\ell+1}^x - p_\ell^x) \cos \theta_r + (p_{\ell+1}^y - p_\ell^y) \sin \theta_r] \right\} \quad (4.26)$$

Taking the log, we obtain:

$$(p_{\ell+1}^x - p_\ell^x) \cos \theta_r + (p_{\ell+1}^y - p_\ell^y) \sin \theta_r = j \frac{c}{\omega} \ln \left( \frac{A_{\ell+1,r}}{A_{\ell,r}} \right) \quad (4.27)$$

Hence, for each source  $r, 1 \leq r \leq R$ , we obtain a linear system:

$$\mathbf{M} \begin{bmatrix} \cos \theta_r \\ \sin \theta_r \end{bmatrix} = \mathbf{v}_r \quad (4.28)$$

with  $\mathbf{M} = [\mathbf{p}_{2:L} - \mathbf{p}_{1:L-1}]$  and  $\mathbf{v}_r = j \frac{c}{\omega} \ln(\mathbf{A}_{2:L,r} \boxtimes \mathbf{A}_{1:L-1,r})$ . If the LS solution of (4.28)  $\mathbf{w}_r = \mathbf{M}^\dagger \mathbf{v}_r$  has norm close to 1, *i.e.*  $\|\mathbf{w}_r\| \in [0.8, 1.2]$ , then the DoA estimation of the  $r$ -th source is given by

$$\begin{bmatrix} \cos \hat{\theta}_r \\ \sin \hat{\theta}_r \end{bmatrix} = \frac{\mathbf{w}_r}{\|\mathbf{w}_r\|} \quad (4.29)$$

However, if the norm  $\|\mathbf{w}_r\|$  is not close to 1, (4.29) has revealed to be inaccurate [128], and we must adopt an exhaustive search as in (4.24).

### 4.6.3. 1D DoA Estimation for ULAs

In 1D, *i.e.* when the array is linear and  $\mathbf{p}_\ell = p_\ell$ , the steering elements take the form

$$A_{\ell r} = \exp \left\{ -j \frac{\omega}{c} p_\ell \cos \theta_r \right\} \quad (4.30)$$

In particular, if the reference subarray is a ULA, this becomes

$$A_{\ell r} = \exp \left\{ -j \frac{\omega}{c} p_0 (\ell - 1) \cos \theta_r \right\} \quad (4.31)$$

Matrix  $\mathbf{A}$  can be considered as a *Vandermonde* matrix in the absence of noise if the antenna is ULA, with kernel  $u_r = \exp \left\{ -j \frac{\omega}{c} p_0 \cos \theta_r \right\}$ . Direction of arrival is then estimated through a LS solution or a more robust TLS solution.

Each  $r$ -th column of the Vandermonde matrix contains multiple information about the direction of arrival  $\theta_r$ . If two overlapping blocks are taken,  $\bar{\mathbf{a}} = (1 \ u_r \ \cdots \ u_r^{L-2})^\top$  and  $\underline{\mathbf{a}} = (u_r \ u_r^2 \ \cdots \ u_r^{L-1})^\top$ , the following relationship should hold in the absence of noise:

$$u_r \bar{\mathbf{a}} = \underline{\mathbf{a}} \quad (4.32)$$

The LS solution is given by

$$\hat{u}_r^{\text{LS}} = (\bar{\mathbf{a}}^H \bar{\mathbf{a}})^{-1} \bar{\mathbf{a}}^H \underline{\mathbf{a}} = \frac{\bar{\mathbf{a}}^H \underline{\mathbf{a}}}{\|\bar{\mathbf{a}}\|^2} \quad (4.33)$$

The TLS solution theoretically yields a better solution, especially for low SNR. It is given by the minimization problem

$$\hat{u}_r^{\text{TLS}} = \min_{\alpha, \beta} \|\alpha \underline{\mathbf{a}} - \beta \bar{\mathbf{a}}\|^2, \text{ s.t. } \|\alpha \beta\| = 1 \quad (4.34)$$

where  $\alpha \underline{\mathbf{a}} - \beta \bar{\mathbf{a}} = [\underline{\mathbf{a}} \mid -\bar{\mathbf{a}}] \begin{bmatrix} \alpha \\ \beta \end{bmatrix}$ . Thus,

$$\hat{u}_r^{\text{TLS}} = \min_{\alpha, \beta} [\alpha^* \ \beta^*] \begin{bmatrix} \|\underline{\mathbf{a}}\|^2 & -\underline{\mathbf{a}}^H \bar{\mathbf{a}} \\ -\bar{\mathbf{a}}^H \underline{\mathbf{a}} & \|\bar{\mathbf{a}}\|^2 \end{bmatrix} \begin{bmatrix} \alpha \\ \beta \end{bmatrix} \quad (4.35)$$

The corresponding solution is given by  $\hat{u}_r = -V_{12} V_{22}^{-1}$ , where matrix  $\mathbf{V}$  derives from the SVD of augmented matrix  $[\bar{\mathbf{a}} \mid \underline{\mathbf{a}}] = \mathbf{U} \mathbf{S} \mathbf{V}^\top$ .

Once  $\hat{u}_r$  is computed, another operation is necessary to estimate the  $r$ -th angle of arrival. The latter can be obtained as  $\hat{\theta}_r = \arccos \left[ -\frac{c}{\omega p_0} \text{angle}(\hat{u}_r) \right] = \arccos \left[ -\frac{\Omega}{\pi} \text{angle}(\hat{u}_r) \right]$ , where  $\Omega = \frac{\lambda}{2p_0} \geq 1$  denotes the oversampling factor, and  $\text{angle}(\cdot)$  is the phase angle determination in  $[-\pi, \pi]$ .

**Remark** If  $\hat{u}_r$  is badly estimated, it may happen that  $|\cos \hat{\theta}_r|$  is larger than 1. This occurs if  $\text{angle}(\hat{u}_r)$  falls outside the interval  $[-\pi/\Omega, \pi/\Omega]$ . Should this be the case, for large  $L$  it can be helpful to redefine  $\underline{\mathbf{a}}$  and  $\overline{\mathbf{a}}$  as:

$$\begin{aligned}\overline{\mathbf{a}} &= ( 1 \quad u_r \quad \cdots \quad u_r^{L-3} )^\top \\ \underline{\mathbf{a}} &= ( u_r^2 \quad u_r^3 \quad \cdots \quad u_r^{L-1} )^\top\end{aligned}$$

The relation between  $\hat{u}_r$  and  $\hat{\theta}_r$  then changes and  $\text{angle}(\hat{u}_r)$  just needs to belong to the interval  $[-2\pi/\Omega, 2\pi/\Omega]$ , and the value of  $|\cos \hat{\theta}_r|$  will be smaller than 1 as long as  $\Omega \leq 2$ , that is, as long as  $p_0 \geq \lambda/4$ .

**Remark** The algorithm proposed in [58], named *Structured Least Squares*, can also achieve a significant improvement of the estimation accuracy by preserving the invariance structure in (4.32).

## 4.7. Source Signature Extraction

As for source complex envelopes, we make the following assumption:

**A 4.5.** Signals  $\mathbf{s}_r, \forall r$  are considered as deterministic.

Tensor CPD also delivers source complex envelopes for free, without any further estimation step, through the third factor matrix  $\mathbf{S}$  of (4.6). After fixing scaling indeterminacies through transformation (4.7), the  $r$ -th source signature is given by

$$\hat{\mathbf{s}}_r = \varsigma_r A_{1r} B_{1r} \mathbf{s}_r \quad (4.36)$$

If signal copy is the main goal of the CPD, then we can fix the permutation ambiguity by using some a priori or embedded information, such as known DoAs or user ID bits in telecommunications, respectively [136].

## 4.8. Advantages of Tensor Decomposition for Sensor Arrays

We present a short list of the advantages of the tensor formalism for array processing:

1. Tensor methods do not require the estimation of the data covariance matrix. Thus, we can relax the assumption of stationarity over sufficiently long observation times. According to identifiability condition in (4.13), tensor CPD can handle very short data samples. In this context, it makes sense to consider source signatures as deterministic.
2. According to identifiability condition (4.11), tensor CPD can separate more sources than sensors in a subarray.
3. Unlike MUSIC, we can relax our knowledge on the sensor response and positions of the whole acquisition system: we can either not require the calibration information on each subarray, or on the space shift structure (see Section 4.6 for details).

4. Tensor methods jointly estimate steering matrices and source complex envelopes, without any need for further estimation or coupling step.

However, since the CPD model must be separable in space and space shift, it cannot handle subarrays of different size, nor subarrays rotated one from another.

## **Part II.**

**Contribution: Wideband Multiple  
Diversity Tensor Array Processing**



# 5. Multiple Diversity Array Processing

## 5.1. Contribution

This chapter proposes an adaptation of the tensor formalism to other physical diversities (in addition to space shift in Chapter 4), such as polarization and directivity gains. It is based on the ideas developed in two articles of ours: a French conference [115] for polarization diversity and an international journal [116] for gain pattern diversity.

Section 5.2 introduces the concept of physical diversity. Polarization diversity for tensor analysis is the subject of Section 5.3, whereas directivity gain diversity is presented in Section 5.4.

The tensor formalism has already been extended to describe vector sensor arrays in [57, 56]. This chapter proposes and evaluates a procedure for tensor estimation of polarized sources, and it compares related performance to the Cramér-Rao Bound (CRB) and to the MUSIC algorithm.

On the other hand, in Section 5.4 directivity gain patterns are treated as a physical diversity for tensor array processing, replacing space diversity, in addition to time and space shift diversities. We show that the tensor formulation allows to estimate Directions of Arrival (DoAs) under the assumption of unknown gain patterns, improving the performance of the omnidirectional case. We propose a trilinear model where one dimension of the multi-way data array is fully provided by gain patterns, allowing tensor approaches even when space diversity is missing due to sensor overlap.

As detailed in Chapter 4, the rotational invariance of [126] was extended to multiple space shift translations through a subspace fitting approach in [142] for collinear space shifts, and a deterministic tensor approach in [136] for arbitrary space shifts. In this scenario a reference subarray (representing space diversity through sensors located at different positions) is repeated through multiple translations (representing space shift diversity through displaced subarrays). In [136, 126, 142], gain patterns have not been exploited to improve the estimation performance. Indeed, although they may be unknown, gain patterns contain important spatial information about impinging sources and their inclusion into the model may help the underlying low rank approximation problem.

## 5.2. Physical Diversities

In many cases, the superposition principle applies in practical problems, provided the nonlinearity domain is not reached (turbulence, saturation, etc). This allows us to model physical phenomena as linear combinations of a few simpler ones. In this chapter, we are interested in the decomposition of a multivariate function into a sum of functions whose variables separate. In particular, this simplified model is relevant in narrow-band antenna array processing in the far-field, which we consider in the present framework, as in Chapter 4.

The tensor model is based on the concepts of parsimony and separability [88]:

1. Parsimony expresses a function  $g$  as a finite sum of simpler constituents:

$$g = \sum_{r=1}^R \varsigma_r h_r \quad (5.1)$$

2. Separability decouples a function  $h$  that depends on multiple factors into a product of simpler constituents  $\phi_d$ ,  $d = 1, \dots, D$ , each one depending only on one factor  $\mathbf{x}_d$ :

$$h(\mathbf{x}_1, \dots, \mathbf{x}_D) = \prod_{d=1}^D \phi_d(\mathbf{x}_d) \quad (5.2)$$

In the field of array processing for source separation and DoA estimation,  $R$  refers to the number of sources impinging on an array, and  $D$  to the tensor order, i.e. the dimension of multilinearity within the model:

$$g(\mathbf{x}_1, \dots, \mathbf{x}_D) = \sum_{r=1}^R \varsigma_r \prod_{d=1}^D \phi_{rd}(\mathbf{x}_d), \quad \varsigma_r \in \mathbb{C}, \forall r \quad (5.3)$$

Tensor decomposition derives from the need to solve the corresponding *inverse problem*, i.e., the identification of factors  $\phi_{rd}$  starting from noisy measurements of  $g : \mathcal{S}_1 \times \dots \times \mathcal{S}_D \mapsto \mathbb{C}$ : as it was illustrated in Section 4.6 through space and space shift diversities, the DoA can be extracted after the resolution of this problem. For this purpose, the measurements are stored in a multidimensional array and decomposed into a sum of *rank one* terms [26, 136].

The multidimensional character of tensor models requires the presence of at least  $D = 3$  types of diversity. We review below some diversities that may be available in antenna array processing.

1. *Time diversity*: Every base-band signal  $s$  is a function of time  $t$ . Moreover, it may be stationary or transient. Thus, recorded signal  $g^{(1)}$  is given by the sum of  $R$  simultaneous sources:

$$g(t) = \sum_{r=1}^R s_r(t) \iff g_t = \sum_{r=1}^R S_r[t], \quad (5.4)$$

The right equation represents a discretization of the left one, i.e.  $S_r[t]$  corresponds to impinging wave  $s_r(t)$  after sampling, at discrete instants  $t = 1, \dots, T$ , as recorded by a single sensor.

2. *Space diversity*. The basis of traditional array processing consists in performing a spatial sampling, in addition to the temporal sampling, through multiple sensors located at different positions (cf. Chapter 1). According to assumptions A 1.1, A 1.3 and A 4.2

$$\begin{aligned} g(\mathbf{p}, t) &= \sum_{r=1}^R \exp \left\{ -j \frac{2\pi}{\lambda} \mathbf{p}^\top \mathbf{d}_r \right\} s_r(t) \\ &\iff G_{\ell t} = \sum_{r=1}^R A_r(\mathbf{p}_\ell) S_r[t] \end{aligned} \quad (5.5)$$

where  $\ell = 1, \dots, L$  refers to the sensor cardinality with respect to the reference,  $\lambda$  is the observed narrowband wavelength,  $\mathbf{p} \in \mathbb{R}^3$  is the recording position within the acquisition system and  $\mathbf{d}_r$  is the unit vector pointing to the  $r$ -th source<sup>1</sup>.

3. *Space shift diversity* (refer to [126] for one rotational invariance and to [136] for multiple translations):

$$g(\mathbf{p}, \boldsymbol{\delta}, t) = \sum_{r=1}^R \exp \left\{ -j \frac{2\pi}{\lambda} \mathbf{p}^\top \mathbf{d}_r \right\} \exp \left\{ -j \frac{2\pi}{\lambda} \boldsymbol{\delta}^\top \mathbf{d}_r \right\} s_r(t) \quad (5.6)$$

$$\iff \mathcal{G}_{\ell mt} = \sum_{r=1}^R A_r(\mathbf{p}_\ell) B_r(\boldsymbol{\delta}_m) S_r[t]$$

where  $m = 1, \dots, M$  is the index of the translation with respect to the reference subarray, and  $\boldsymbol{\delta}$  is the translational invariant repeating the array configuration over space. ESPRIT may be seen as a particular case of this diversity, when translation vector  $\boldsymbol{\delta}$  relates  $M = 2$  identical subarrays, whereas the tensor model itself can be applied to  $M > 2$  identical configurations (cf. Chapter 4).

4. *Polarization diversity*. Expressions (5.4), (5.5) and (5.6) refer to one-component (1C) sensors, but can be generalized to three-component (3C) sensors as well (cf. Section 1.4). Moreover, in the latter case, one can take advantage of an additional diversity related to polarization, as introduced in Section 1.4:

$$\mathbf{g}(t) = \sum_{r=1}^R \mathbf{k}(\boldsymbol{\vartheta}_r) s_r(t) \iff G_{pt} = \sum_{r=1}^R K_p(\boldsymbol{\vartheta}_r) S_r[t] \quad (5.7)$$

where  $\mathbf{k}(\cdot)$  is the polarization response vector of the considered sensor and  $\boldsymbol{\vartheta}_r = [\theta_r, \psi_r, \alpha_r, \beta_r]^\top$  contains the polarization information of the  $r$ -th impinging wavefield with respect to the sensor position: the azimuth  $\theta$ , the elevation  $\psi$ , the orientation angle  $\alpha$  and the ellipticity angle  $\beta$ . In particular, the azimuth  $\theta$  refers to the DoA when assumption A 1.8 is made. Discrete index  $p \in \{1, 2, 3\}$  refers to one out of three components of the 3C sensor vector  $\mathbf{k}$ .

5. *Repetition diversity* is a possible extension of dimensionality whenever we deal with multiple events describing the same physical phenomenon. The additional assumption of a linear relation between events from the same cluster has to be made, so that multiple events describing the same physical phenomenon are related to each other by a complex coefficient:

$$g(j, t) = \sum_{r=1}^R e_r(j) s_r(t) \iff G_{jt} = \sum_{r=1}^R e_r(j) S_r[t] \quad (5.8)$$

where discrete index  $j = 1, \dots, J$  is the cardinality of the event of the cluster (1 being the first recorded occurrence and  $J$  the last one), and  $e_r(\cdot)$  a (generally unknown) complex coefficient. Repetition diversity has been already used in other contexts, in [97] for instance.

<sup>1</sup>We remind that, for sake of simplicity, we refer to both the proper direction of arrival  $\mathbf{d}_r$  and the angle of arrival  $\theta_r$  with the acronym DoA (see Section 1.7).

6. *Frequency diversity.* Denote by  $\mathcal{F}\{\cdot\}$  the Fourier Transform (FT) operator applied to received signals in the time window  $t \in [0, T]$ . Then, in frequency domain, we write

$$g(\omega) = \sum_{r=1}^R S_r(\omega) \iff g_q = \sum_{r=1}^R S_r(\omega_q), \quad (5.9)$$

where frequency  $0 < \omega_{min} \leq \omega_q \leq \omega_{max} < \pi$ , and  $1 \leq q \leq Q$  refer to the bins of the Discrete Fourier Transform (DFT).

Traditional 2D solutions only employ the concepts of *time diversity* and *space diversity*: base-band signals are stored in a data matrix  $\mathbf{Y}$  of size  $L \times T$ , where  $L$  is the number of sensors and  $T$  the number of time samples, as detailed in Chapter 1.

Other sources of diversity are given by the following elements:

- *scale* as in [93] via multi-scale tensor array processing;
- particular structures of the sensor array, as in [62], via nested tensor array processing for vector sensors;
- non stationarity in time or space [8, 6].

## 5.3. Tensor Decomposition of Polarized Waves

### 5.3.1. The Long Vector MUSIC

In Section 1.4 we introduced the concept of vector sensor array. After applying the vectorization operator to multi-component data, in (1.38) we derived the long vector

$$\mathbf{x}(t) = \sum_{r=1}^R \mathbf{e}_r s_r(t) + \mathbf{n}(t) \in \mathbb{C}^{LP} \quad (5.10)$$

where  $\mathbf{e}_r = \mathbf{k}_r \boxtimes \mathbf{a}_r$  is the 3C steering vector of the  $r$ -th source and  $\mathbf{n}(t) \sim \mathcal{N}(\mathbf{0}, \sigma^2 \mathbf{I}_{LP})$ . In the acoustic vector sensor model in [3], the steering vectors  $\mathbf{e} \in \mathbb{C}^{LP}$  are given by the Kronecker product

$$\mathbf{e}(\theta, \alpha, \beta) = \mathbf{k}(\theta, \alpha, \beta) \boxtimes \mathbf{a}(\theta) \quad (5.11)$$

where  $\theta$  refers to the DoA and  $\alpha$  and  $\beta$  to the orientation and ellipticity angles respectively. In the decoupled polarimetric model of [92, 44], steering vectors are given by the Kronecker product

$$\mathbf{e}(\theta, \boldsymbol{\rho}, \boldsymbol{\phi}) = \mathbf{k}(\boldsymbol{\rho}, \boldsymbol{\phi}) \boxtimes \mathbf{a}(\theta) \quad (5.12)$$

where DoA  $\theta$  and amplitude and phase polarization parameters  $\boldsymbol{\rho}, \boldsymbol{\phi}$  are decoupled.

The covariance matrix  $\mathbf{R}_X = \mathbb{E}[\mathbf{x}\mathbf{x}^H] \in \mathbb{C}^{LP \times LP}$  is estimated as

$$\hat{\mathbf{R}}_X = \frac{1}{T} \sum_{t=1}^T \mathbf{x}(t)\mathbf{x}(t)^H \in \mathbb{C}^{LP \times LP} \quad (5.13)$$

Through EVD of the covariance, or SVD of raw data, we extract the  $R$  leading singular vectors  $\mathbf{U}_S$  as a basis for signal subspace, and the  $LP - R$  last smallest singular vectors  $\mathbf{U}_N$  as a basis for noise subspace. Thus, we constitute the projector operator for the noise

subspace (see Section 1.3.2 for details) as  $\mathbf{\Pi}_N = \mathbf{U}_N \mathbf{U}_N^H$ . The cost function minimizing this projection is given by:

$$\Upsilon_{LV}(\theta, \alpha, \beta) = \|\mathbf{e}(\theta, \alpha, \beta)^H \mathbf{U}_N\|^2 = \text{trace}\{\mathbf{\Pi}_N \mathbf{e}(\theta, \alpha, \beta) \mathbf{e}(\theta, \alpha, \beta)^H\} \quad (5.14)$$

for the acoustic vector sensor model of Section 1.4.2, or by

$$\Upsilon_{LV}(\theta, \boldsymbol{\rho}, \phi) = \|\mathbf{e}(\theta, \boldsymbol{\rho}, \phi)^H \mathbf{U}_N\|^2 = \text{trace}\{\mathbf{\Pi}_N \mathbf{e}(\theta, \boldsymbol{\rho}, \phi) \mathbf{e}(\theta, \boldsymbol{\rho}, \phi)^H\} \quad (5.15)$$

for the polarimetric model of Section 1.4.3.

Notice that in both cases this is equivalent to maximizing the normalized MUSIC spectrum

$$P_{\text{MU}} = \frac{\|\mathbf{e}\|^2}{\|\mathbf{e}^H \mathbf{U}_N\|^2} \quad (5.16)$$

Long Vector MUSIC (LV MUSIC) does not fully exploit the multidimensional structure of the observations. Moreover, in order to yield accurate subspace estimate through the sample covariance, it needs more data samples, as the  $\text{vec}\{\cdot\}$  operation increases the size of the data.

### 5.3.2. Tensor MUSIC

Tensor MUSIC (T-MUSIC) proposed in [44] does not vectorize the array output, but directly consider matrix  $\mathbf{X}(t) \in \mathbb{C}^{L \times P}$  in (1.37):

$$\mathbf{X}(t) = \sum_{r=1}^R \mathbf{E}_r s_r(t) + \mathbf{N}(t) \quad (5.17)$$

where  $\text{vec}\{\mathbf{N}(t)\} \sim \mathcal{N}(\mathbf{0}, \sigma^2 \mathbf{I}_{LP})$ , and the steering matrix  $\mathbf{E}_r$  of the  $r$ -th source is given by the outer product

$$\mathbf{E}_r = \mathbf{a}_r \otimes \mathbf{k}_r = \text{reshape}(\mathbf{e}_r, L, P) \quad (5.18)$$

In the acoustic vector sensor model in [3], the steering matrices  $\mathbf{E} \in \mathbb{C}^{L \times P}$  are given by the outer product

$$\mathbf{E}(\theta, \alpha, \beta) = \mathbf{a}(\theta) \otimes \mathbf{k}(\theta, \alpha, \beta) = \mathbf{a}(\theta) \mathbf{k}(\theta, \alpha, \beta)^T \quad (5.19)$$

where  $\theta$  refers to the DoA and  $\alpha$  and  $\beta$  to the orientation and ellipticity angles respectively. In the decoupled polarimetric model of [92, 44], steering matrices are given by the outer product

$$\mathbf{E}(\theta, \boldsymbol{\rho}, \phi) = \mathbf{a}(\theta) \otimes \mathbf{k}(\boldsymbol{\rho}, \phi) = \mathbf{a}(\theta) \mathbf{k}(\boldsymbol{\rho}, \phi)^T \quad (5.20)$$

The covariance tensor  $\mathcal{R}_X = \mathbb{E}[\mathbf{X} \otimes \mathbf{X}^*] \in \mathbb{C}^{L \times P \times L \times P}$  is estimated as  $\hat{\mathcal{R}}_X = \frac{1}{T} \sum_{t=1}^T \mathbf{X}(t) \otimes \mathbf{X}^*(t)$ .

As we detailed in Section 4.2, the tensor subspace estimation relies on the HOSVD of the covariance tensor:

$$\mathcal{R} = \mathcal{S} \bullet_1 \mathbf{U}_1 \bullet_2 \mathbf{U}_2 \bullet_3 \mathbf{U}_1^H \bullet_4 \mathbf{U}_2^H \quad (5.21)$$

where the all-orthogonal core tensor  $\mathcal{S}$  has the same size as  $\mathcal{R}_X$ , and matrices  $\mathbf{U}_1 \in \mathbb{C}^{L \times L}$ ,  $\mathbf{U}_2 \in \mathbb{C}^{P \times P}$  are orthonormal. We then extract the  $R$  leading singular vectors of  $\mathbf{U}_1$  and  $\mathbf{U}_2$  as bases for the two signal subspaces, and the  $L-R$  and  $P-R$  last smallest singular vectors of  $\mathbf{U}_1$  and  $\mathbf{U}_2$  respectively as a basis for the two noise subspaces:  $\mathbf{U}_{1,N}$ ,  $\mathbf{U}_{2,N}$ . As

mentioned in Section 3.6.2, this low mode-rank approximation of a tensor is not optimal in the LS sense [106, 33], but is often a reasonable and easy approximation [61].

The cost function minimizing the projection of the array manifold on the noise subspaces is given by:

$$\Upsilon_T(\theta, \alpha, \beta) = \|\mathbf{E}(\theta, \alpha, \beta) \bullet_1 \mathbf{U}_{1,N}^H \bullet_2 \mathbf{U}_{2,N}^H\|_F^2 \quad (5.22)$$

for the acoustic vector sensor model of Section 1.4.2, or by

$$\Upsilon_T(\theta, \boldsymbol{\rho}, \phi) = \|\mathbf{E}(\theta, \boldsymbol{\rho}, \phi) \bullet_1 \mathbf{U}_{1,N}^H \bullet_2 \mathbf{U}_{2,N}^H\|_F^2 \quad (5.23)$$

for the polarimetric model of Section 1.4.3. Notice that in the latter case this is equivalent to a separable cost function:

$$\Upsilon_T(\theta, \boldsymbol{\rho}, \phi) = \text{trace}\{\mathbf{\Pi}_{1,N} \mathbf{a}(\theta) \mathbf{a}(\theta)^H\} \text{trace}\{\mathbf{\Pi}_{2,N} \mathbf{k}(\boldsymbol{\rho}, \phi) \mathbf{k}(\boldsymbol{\rho}, \phi)^H\} \quad (5.24)$$

Thus, for the polarimetric model of [92, 44] DoA and polarization parameters can be estimated independently.

[44] compared T-MUSIC with LV MUSIC of [92]. LV MUSIC can estimate jointly DoA and polarization, through the composite steering vector  $\mathbf{e}$ . Since closely spaced sources can have almost orthogonal steering vectors when their polarization parameters are different enough, LV MUSIC has better performance thanks to the joint estimation. On the other hand, T-MUSIC estimate DoA and polarization parameters separately.

The interest of T-MUSIC is that it needs fewer samples to estimate the subspace projectors, as the data size reduces from  $LP$  to  $L$  for DoA and to  $P$  for polarization. Moreover, it takes into account the separable structure of DoA and polarization steerings, unlike classical LV MUSIC. We would like to highlight that the main non negligible limitation of T-MUSIC is the number of resolvable sources: for instance, it cannot estimate  $R > 2$  sources with a 3C sensor array, since it needs to extract the  $R$  leading and the last  $P - R$  singular vectors from matrix  $\mathbf{U}_2 \in \mathbb{C}^{P \times P}$  as a basis for the signal and noise subspaces associated to polarization. This implies as a necessary condition that  $P > R$ . Now, for a 3C sensor array, we have  $P = 3$ .

### 5.3.3. Tensor CPD for Vector Sensor Arrays

In the remainder, we will adopt the acoustic polarization model of [3], that we detailed in Section 1.4. This choice is consistent with the electromagnetic polarization model of [96] mostly used in the literature. However, in our derivation, as in Section 1.4, we will only study elastic waves. [57] first used tensor Canonical Polyadic Decomposition (CPD) for vector sensor arrays, for electromagnetic waves. Moreover, polarization has revealed useful to disambiguate the DoA of closely spaced sources for tensor estimation in [56].

From Section 1.4.2, we know that the array output of a 3C vector sensor array at time  $t$  is given by the  $L \times 3$  matrix

$$\begin{aligned} \mathbf{X}(t) &= \sum_{r=1}^R \mathbf{a}_r \otimes \mathbf{k}_r s_r(t) + \mathbf{N}(t) = \\ &= \mathbf{A} \mathbf{S}(t) \mathbf{K}^T + \mathbf{N}(t) \end{aligned} \quad (5.25)$$

with steering vector  $\mathbf{a}_r = \mathbf{a}(\theta_r, \psi_r)$ , and polarization vector  $\mathbf{k}_r = \mathbf{k}(\theta_r, \psi_r, \alpha_r, \beta_r)$ . Moreover,  $\mathbf{S}(t) = \text{Diag}\{s_1(t), \dots, s_R(t)\}$ ,  $\mathbf{K} = [\mathbf{k}_1, \dots, \mathbf{k}_R]$  refers to the  $3 \times R$  sensor response matrix, and  $\mathbf{A} = [\mathbf{a}_1, \dots, \mathbf{a}_R]$  refers to the  $L \times R$  array steering matrix. Notice that

this expression follows a third order CPD model (discussed in Section 3.3.3): we can reformulate it through tensor slices

$$\mathbf{X}_{::t} = \mathbf{A} \mathbf{D}_t(\mathbf{s}_{t:}) \mathbf{K}^\top + \mathbf{N}_{::t} \text{ where } \mathbf{D}_t(\mathbf{s}_{t:}) = \text{Diag}\{\mathbf{s}_{t:}\} \quad (5.26)$$

Since (5.25) describes a trilinear model (cf. the slice representation (5.26)), it is straightforward to express it through CPD, after stacking all the time snapshots  $\mathbf{X}_t$  as frontal slices  $\mathbf{X}_{::t}$  of a  $L \times P \times T$  tensor  $\mathcal{X}$ :

$$\begin{cases} \mathcal{X} = \sum_{r=1}^R \mathbf{a}_r \otimes \mathbf{k}_r \otimes \mathbf{s}_r + \mathcal{N} \\ \mathcal{X}_{\ell pt} = \sum_{r=1}^R A_{\ell r} K_{pr} S_{tr} + \mathcal{N}_{\ell pt} \end{cases} \quad (5.27)$$

where rank- $R$  corresponds to the number of sources, supposed known, thanks to Assumption A 1.10, and  $\mathcal{N}$  refers to additive complex circular Gaussian noise. The physical meaning of the three factor matrices is given through

$$\begin{cases} A_{\ell r} = \exp\{-j\omega\tau_\ell(\theta_r)\} \text{ refers to space diversity} \\ \mathbf{k}_r = \mathbf{H}(\theta_r, \psi_r) \mathbf{W}(\alpha_r) \mathbf{w}(\beta_r) \text{ refers to polarization diversity} \\ S_{tr} = s_r(t) \text{ refers to time diversity} \end{cases} \quad (5.28)$$

where  $\tau_\ell(\theta_r) = \mathbf{p}_\ell^\top \mathbf{d}_r / c$  refers to the time delay at sensor  $\ell$  w.r.t. the reference sensor, and  $\mathbf{H}(\theta_r, \psi_r)$ ,  $\mathbf{W}(\alpha_r)$ ,  $\mathbf{w}(\beta_r)$  have been defined in Section 1.4.

Thanks to (5.27), space shift diversity is not mandatory anymore as the third mode of the data tensor, provided that the impinging waves are polarized and that their polarization is neither linear nor circular.

### 5.3.4. CPD Factors, Normalization and Scaling

From [144, 145], we know that the manifold  $\mathbf{k}(\theta, \alpha, \beta)$  of an electromagnetic vector sensor array is free of rank-2 ambiguities, *i.e.*  $\kappa_K \geq 3$ , but in general we have  $\kappa_K \geq 4$ . Moreover, a necessary condition of identifiability for an electromagnetic vector sensor array is that  $R \leq 3L$ .

For the CPD model of vector sensor arrays, the same uniqueness conditions of Section 4.4 holds, and space shift matrix  $\mathbf{B}$  is replaced by polarization matrix  $\mathbf{K}$  in every result. Scale indeterminacies are fixed as in Section 4.3.1, except for factor matrix  $\mathbf{K}$ . Thus, we impose the first row of matrix  $\mathbf{A}$  to be formed of ones (in fact, as justified in Assumption A 4.2,  $\mathbf{p}_1 = \mathbf{0}$ , and  $g_\ell(\theta) = 1 \forall \ell$ ), and columns of matrix  $\mathbf{K}$  to have unit norm:  $\|\mathbf{k}_r\| = 1 \forall r$ . Then we pull column-wise the remaining scaling coefficients,  $\{\varsigma_r A_{1r} \|\mathbf{k}_r\|\}$ , into matrix  $\mathbf{S}$ . More precisely, we fix all scale indeterminacies through the following transformation:

$$(\hat{\mathbf{a}}_r, \hat{\mathbf{k}}_r, \hat{\mathbf{s}}_r, \varsigma_r) \longleftarrow \left( \frac{\mathbf{a}_r}{A_{1r}}, \frac{\mathbf{k}_r}{\|\mathbf{k}_r\|}, \varsigma_r A_{1r} \|\mathbf{k}_r\| \mathbf{s}_r, 1 \right) \quad (5.29)$$

This choice permits to compute performance bounds on the retrieval of CPD factors in (5.27) more easily.

### 5.3.5. Coherent Sources

We showed in Section 4.4.2 that if sources are coherent, matrix  $\mathbf{S}$  is rank deficient, *i.e.*  $\text{rank}\{\mathbf{S}\} < R$  and  $\kappa_S = 1$ . A solution to tackle the problem of coherent sources is the polarization smoothing algorithm proposed by [112] and revisited by [57] through the tensor formalism: it forms a new signal matrix  $\bar{\mathbf{S}} \triangleq \mathbf{K} \odot \mathbf{S}$ , which is ensured to be full column rank thanks to Proposition 4.4. Thus, a sufficient identifiability condition becomes

$$R \leq \kappa_K + \text{rank}\{\mathbf{S}\} - 1 \quad (5.30)$$

The new data matrix  $\bar{\mathbf{Y}} = \mathbf{A}\bar{\mathbf{S}}^T$  can then be processed by another algorithm such as MUSIC, which also requires Assumption 1.13:  $L \geq R + 1$ . Combining this condition with (5.30), we obtain

$$R \leq \min\{L, \kappa_K + \text{rank}\{\mathbf{S}\}\} - 1 \quad (5.31)$$

We derived the CRB for the tensor CPD model of polarized waves in [115]. For details of the CRB of the general tensor CPD model of elastic waves, see Chapter 7.

### 5.3.6. Physical Meaning of Coherences

In Section 3.7, we defined the concept of coherence of a factor matrix and linked it to the identifiability of the CPD. We examined the physical meaning of coherences for space, space shift and time diversities in Section 4.5. We now describe the case of polarization diversity: from (3.61) and (5.28), we express the coherence of factor matrix  $\mathbf{K}$ :

$$\mu_K = \max_{p \neq q} |\mathbf{k}_p^H \mathbf{k}_q| \quad (5.32)$$

[88] shows the link between this angular measure and the polarization separation between sources, through the following theorem:

**Theorem 5.1.**  $\|\mathbf{k}_p^H \mathbf{k}_q\| \leq 1 \forall p, \forall q$ , with equality if and only if  $\alpha_p = \alpha_q + n\pi$ ,  $\beta_p = \beta_q$ ,  $\theta_p = \theta_q + n'\pi$  and  $\psi_p = \psi_q$ .

Thus, uniqueness and existence conditions of (3.63) and (3.64) of Section 3.7 can be interpreted in a physical sense. In particular, the best rank- $R$  approximation exists if sources are not too closely spaced, not too similarly polarized and their temporal signatures are not too correlated. Thus, we can separate sources with arbitrarily similar polarization, provided that their DoAs are different enough [88]. This result is consistent with [56], where polarization is used to disambiguate the DoAs of closely spaced sources.

### 5.3.7. Estimation of Source, DoAs and Polarization Angles

The tensor model in (5.27) can be expressed in vector form as

$$\mathbf{x} = \text{vec}\{\mathcal{X}\} = \sum_{r=1}^R \mathbf{s}_r \boxtimes \mathbf{k}_r \boxtimes \mathbf{a}_r + \mathbf{n} \quad (5.33)$$

where  $\boxtimes$  denotes the Kronecker product, as defined in [26, 75] (cf. (3.22) for generic tensor order  $D$ ). Since, thanks to Assumption A 1.11, the *measurement* noise vector,

$\mathbf{n} = \text{vec}\{\mathcal{N}\}$ , is circular white Gaussian and isotropic, *i.e.* with zero mean and covariance  $\Sigma = \sigma^2 \mathbf{I}$ , the log-likelihood takes the form:

$$\Upsilon(\boldsymbol{\vartheta}) = -(\mathbf{x} - \boldsymbol{\mu})^H \Sigma^{-1} (\mathbf{x} - \boldsymbol{\mu}) + \text{constant} \quad (5.34)$$

where  $\boldsymbol{\mu} = \sum_{r=1}^R \mathbf{s}_r \boxtimes \mathbf{k}_r \boxtimes \mathbf{a}_r$  is unknown and constrained by its parameterization  $\boldsymbol{\vartheta} = [\boldsymbol{\theta}, \boldsymbol{\alpha}, \boldsymbol{\beta}, \text{vec}\{\mathbf{S}\}]$ . For the CRB of the tensor DoA and polarization estimation, see Chapter 7, and in particular Section 7.3.4.

Although the optimal solution is given by the global maximum of  $\Upsilon(\boldsymbol{\vartheta})$ , we propose a suboptimal two-step procedure in the same spirit as [128], with smaller computational burden: first  $\Upsilon$  is maximized with respect to parameter  $\boldsymbol{\xi} = [\text{vec}\{\mathbf{A}\}, \text{vec}\{\mathbf{K}\}, \text{vec}\{\mathbf{S}\}]$  through a CPD routine, such as ALS [27]; then DoAs and polarization angles can be estimated as follows.

1. For one single polarization parameter  $\beta_r$ , we perform an exhaustive search over a 2D grid of DoA  $\theta \in [-\pi, \pi]$  and polarization angle  $\beta \in [-\pi/4, \pi/4]$ , by searching  $[-\pi, \pi] \cup [-\pi/4, \pi/4]$  for:

$$(\hat{\theta}_r, \hat{\beta}_r) = \arg \min_{\theta, \beta} \left\| \begin{pmatrix} \hat{\mathbf{a}}_r - \mathbf{a}_r(\theta) \\ \hat{\mathbf{k}}_r - \mathbf{k}_r(\theta, \beta) \end{pmatrix} \right\|^2 \quad (5.35)$$

2. For two polarization angles,  $\alpha_r$  and  $\beta_r$ , a suboptimal solution consists in first estimating DoAs  $\theta$  from factor matrix  $\mathbf{A}$ , and then estimating polarization angles  $\alpha \in (-\pi/2, \pi/2]$  and  $\beta \in [-\pi/4, \pi/4]$  separately from factor matrix  $\mathbf{K}$ :

$$\begin{cases} \hat{\theta}_r^A = \arg \min_{\theta} \|\hat{\mathbf{a}}_r - \mathbf{a}_r(\theta)\|^2 \\ (\hat{\alpha}_r, \hat{\beta}_r) = \arg \min_{\alpha, \beta} \|\hat{\mathbf{k}}_r - \mathbf{k}_r(\hat{\theta}_r^A, \alpha, \beta)\|^2 \end{cases} \quad (5.36)$$

Notice that there are in general better (*i.e.* less computationally expensive) ways than brute force exhaustive search to estimate  $\theta_r$  from  $\hat{\mathbf{a}}_r$ , as detailed in Section 4.6, in particular if the reference subarray has a specific structure.

*Remark:* the above mentioned minimization procedures are performed in a limited domain:  $\theta \in [-\pi, \pi], \alpha \in (-\pi/2, \pi/2], \beta \in [-\pi/4, \pi/4]$ . In order to prevent this search from becoming too costly, we apply an iterative progressive refinement of the grid, where each iteration is a zoomed version of the previous one.

This solution can then, if necessary, be refined by a local ascent of  $\Upsilon(\boldsymbol{\vartheta})$ . However, this improvement has revealed to be negligible in subsequent computer experiments.

### 5.3.8. Computer Results

Thanks to Assumption A 1.8, impinging sources are assumed coplanar with respect to the array: only azimuth is to be estimated, and not elevation, without any loss of generality, as described in Section 4.6.2. We simulated  $R = 2$  sources, at sampling frequency  $f_s = 1$  kHz, for an observation time of 64 ms and propagating at  $c = 1800$  m s<sup>-1</sup>, which is approximately the propagation speed of seismic S-waves through ice [117]. Hence,  $T = 64$  time samples are available. Sources in time domain are white Gaussian processes with unit variance. Impinging signals are supposed to be elliptically polarized seismic sources, recorded by one 3C sensor array, or vector-sensor array, as defined in Section 1.4.2.

We assume:

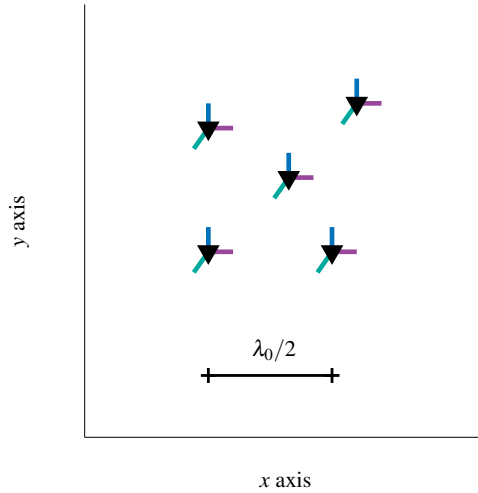


Figure 5.1.: 3C sensor position matrix - polarization diversity

1. an array of  $L = 5$  sensors, as in Figure 5.1;
2. the distance between two sensors is  $\approx \lambda_0/2$ ;
3.  $R = 2$  uncorrelated polarized sources arrive from angles  $\theta_1 = 30^\circ$  and  $\theta_2 = 60^\circ$ , respectively.
4. Rayleigh waves, *i.e.*  $\alpha = 0$ ,  $\psi = 0$  (coplanar with the array),  $\beta \neq 0$ . In particular,  $\beta_1 = -20^\circ$ ,  $\beta_2 = 10^\circ$ .

Estimation efficiency is also evaluated in comparison to the multilinear CRB derived in Section 7.2. The performance criterion is the relative total MSE of the DoA estimates and of the polarization ellipticity estimates:

$$\begin{cases} \text{MSE}(\boldsymbol{\theta}) = \frac{1}{\pi^2} \frac{1}{NR} \sum_{n=1}^N \sum_{r=1}^R (\hat{\theta}_{rn} - \theta_r)^2 \\ \text{MSE}(\boldsymbol{\beta}) = \frac{1}{\pi^2} \frac{1}{NR} \sum_{n=1}^N \sum_{r=1}^R (\hat{\beta}_{rn} - \beta_r)^2 \end{cases} \quad (5.37)$$

where  $\hat{\theta}_{rn}$  and  $\hat{\beta}_{rn}$  are the estimated DoA and ellipticity angle, respectively, of source  $r$  in the  $n$ -th MC trial,  $N = 2500$  being the number of trials. As in [90, 128], the SNR definition below is assumed:

$$\text{SNR} = 10 \log_{10} \frac{\mathbb{E} [\boldsymbol{\mu}^H \boldsymbol{\mu}]}{\mathbb{E} [\mathbf{n}^H \mathbf{n}]} = 10 \log_{10} \frac{\|\boldsymbol{\mu}\|^2}{LPT\sigma^2} \quad (5.38)$$

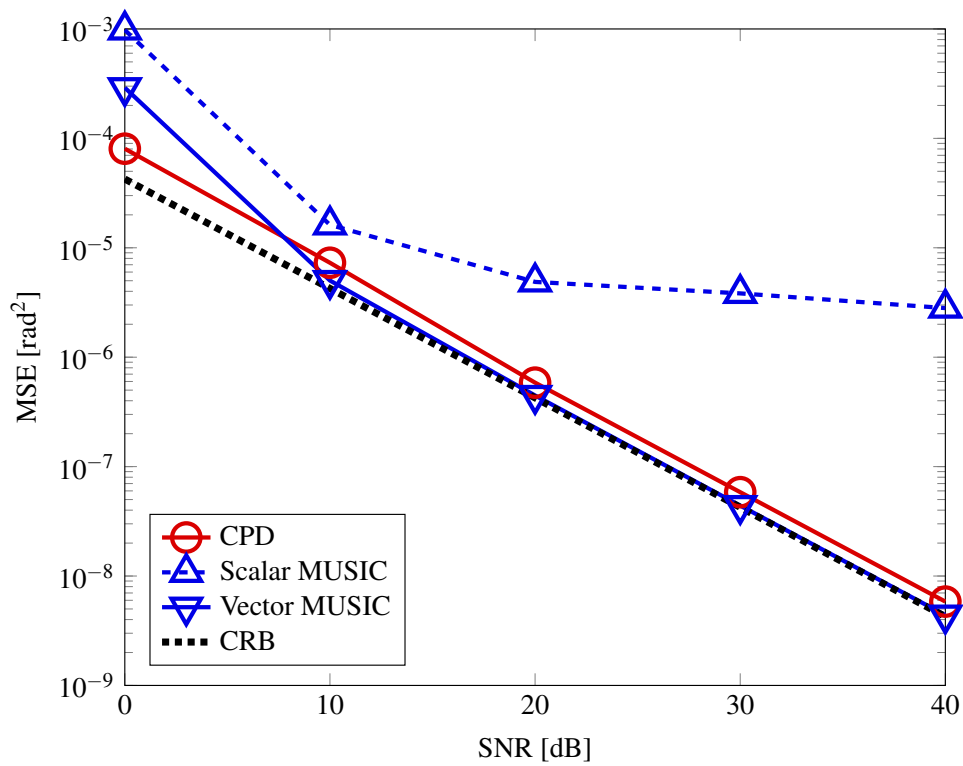
We compare the following estimation algorithms:

**CPD:** CPD model as detailed in Section 5.3.3 and parameter estimation using (5.35). The tensor CPD approximation is achieved via a randomly initialized ALS. In particular, initial estimates are drawn from unit variance complex Gaussian distributions.

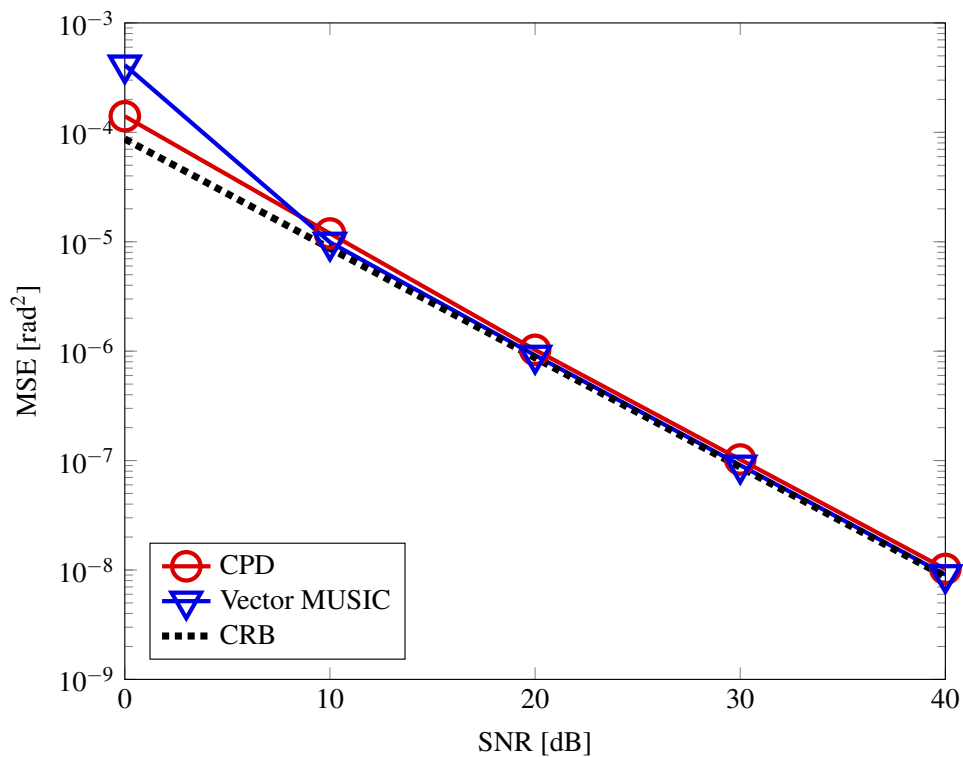
**Scalar MUSIC:** via an incoherent average of  $P$  covariances.

**Vector MUSIC** in Section 5.3.1, where the array manifold takes into account wave polarization parameters, via a long covariance matrix of size  $PL \times PL$ .

Figures 5.2a and 5.2b show the MSE with respect to the SNR for DoA estimation and for polarization estimation, respectively. Vector MUSIC slightly outperforms tensor estimation, both nearly overlapping each other in the proximity of the CRB. On the contrary, Scalar MUSIC presents a severe saturation.



(a) DoA estimation



(b) Polarization estimation

Figure 5.2.: MSE vs SNR - polarization diversity - seismic Rayleigh waves

## 5.4. Directivity Gain Pattern Diversity

In our article [116] we proposed a new type of physical feature as a dimension of the data tensor, by considering the diversity induced by anisotropic sensor gains. We refer to the latter as *gain pattern diversity*. Directional sensor arrays have been used in the context of smart antennas, through beamforming techniques [113] and null-steering (see [20, 72] for a list of examples). Several studies have investigated directional elements for DoA estimation, such as [107, 13], both with UCAs High resolution DoA estimation through the MUSIC algorithm [131] with known sensor gains has been further studied in [72], where the effects and advantages of different directivity patterns have been considered, as well as a realistic dipole array implementation. A derivation of the CRB for directional elements of a UCA can be found in [72].

If sensors are omnidirectional (as in most of the literature in array processing), only relative phase differences between sensors are needed to extract DoA information. However, if the antenna elements are directional, one may jointly exploit gain and phase differences in every direction of interest. Existing studies on DoA estimation in the presence of directional elements mostly cover the case of known directivity gains; on the contrary, our aim is to treat the case of DoA estimation using sensors with *unknown* gain patterns.

In fact, contrary to more standard approaches, *e.g.* MUSIC [79, 131], tensor approaches can handle unknown gains, as subsequently demonstrated. On the other hand, ESPRIT [12] can be seen as a particular tensor approach and can solve the localization problem if two identical translated subarrays are available. However, in [126], gain patterns have not been explicitly taken into account as a pure source of diversity (*i.e.* when all sensors are co-located within each subarray, and only differ in their directivity). The same observation applies to multidimensional extensions of ESPRIT [142, 136]. We show that even when directional sensors completely overlap within a subarray, thus canceling space diversity, their gain patterns allow a trilinear tensor model, fully replacing the space diversity of [136].

Hence, we propose a trilinear model, where one dimension of the multi-way data array is fully provided by gain patterns, allowing tensor approaches even when space diversity is missing due to sensor overlap. Computer results are reported as a function of SNR, sensor directivity, and sensor overlap, in comparison to CRBs. The effect of directivity patterns is also studied with respect to the equivalent omnidirectional case. We think that sensor gain patterns have considerable potential in the context of small electronic devices with limited space available.

### 5.4.1. CPD Factors, Normalization and Scaling

In the present section we introduce the gain pattern into the tensor model, thus allowing to exploit directional elements even when their gain patterns are not known. For this purpose, we relax Assumption A 4.3, in order to include gain patterns as a further source of diversity into the model. We then make this alternative assumption:

- A 5.1.**
- a) Sensors within a subarray have different gain patterns.
  - b) Sensor gains  $g_\ell(\theta)$ ,  $\ell > 1$ , are unknown, real (which is actually equivalent to assuming that their phase is known) and frequency-flat.
  - c) The first sensor ( $\ell = 1$ ) is taken as origin, *i.e.*,  $\mathbf{p}_1 = \mathbf{0}$ , and has unit gain in all directions, *i.e.*  $g_1(\theta) = 1, \forall \theta$ .

**A 5.2.** Space shifts  $\mathbf{\Delta} = [\boldsymbol{\delta}_1, \dots, \boldsymbol{\delta}_M]^\top$  are known, whereas sensor positions  $\mathbf{P} = [\mathbf{p}_2, \dots, \mathbf{p}_L]^\top$  are unknown.<sup>2</sup>

Moreover, Assumptions A 4.4 and A 1.12 are still valid, so that scaling indeterminacies are fixed through (4.7). Notice that Assumptions 5.1 b) and 5.1 c) are not restrictive, and permit to fix the scale indeterminacies in model (5.39), as pointed out in Section 5.4.2. Assumption 5.1 b) means that  $L$  continuous real functions are unknown. However, they appear in the model only at values  $\theta_r$ , so that we may consider only the  $(L - 1) \times R$  matrix,  $\mathbf{G}$ , with  $G_{\ell r} = g_{\ell+1}(\theta_r)$ ,  $1 \leq \ell \leq L - 1$ , as unknown.

Now, following the configuration in Section 4.3 of multiple translations, assume we have at our disposal a set of  $M$  subarrays, each containing  $L$  directional sensors, and deducible from each other by a translation (see Figure 5.3). The delay of arrival of the  $r$ -th source to reach sensor  $\ell$  of subarray  $m$  is then  $\tau_\ell(\theta_r) + \zeta_m(\theta_r)$ , where  $\tau_\ell(\theta_r) = \mathbf{p}_\ell^\top \mathbf{d}(\theta_r)/c$  and  $\zeta_m(\theta_r) = \boldsymbol{\delta}_m^\top \mathbf{d}(\theta_r)/c$ . Then, we slightly generalize the tensor formulation in (4.6) so as to include gain patterns into factor matrix  $\mathbf{A}$ .

### 5.4.2. Diversity of Space Shift and Gain Pattern

Thus, at fixed radial frequency  $\omega_0$ , the complex envelope of the signals received at the  $\ell$ -th sensor of the  $m$ -th subarray can be written as  $\mathcal{X}_{\ell mt} = \mathcal{M}_{\ell mt}^{\text{full}} + \mathcal{N}_{\ell mt}$ , where

$$\mathcal{M}_{\ell mt}^{\text{full}} = \sum_{r=1}^R A_{\ell r}^{\text{full}} B_{mr} S_{tr} \in \mathbb{C}^{L \times M \times T} \quad (5.39)$$

$$\text{with} \quad \begin{cases} A_{\ell r}^{\text{full}} &= g_\ell(\theta_r) e^{-j\omega_0 \tau_\ell(\theta_r)} \\ B_{mr} &= e^{-j\omega_0 \zeta_m(\theta_r)} \\ S_{tr} &= s_r(t) \end{cases}$$

Notice that if sensors within a sub-array do not overlap,  $\mathbf{p}_\ell = 0 \iff \ell = 1$  and we obtain the *full* model in (5.39). In any case, scale indeterminacies of the CPD model are fixed as in Section 4.3.1 with the addition of A 5.1. See Section 4.3.1 for more details on fixing the scaling indeterminacies.

Again, if the acquisition system is composed of  $M = 2$  subarrays, deduced from each other by a single translation  $\boldsymbol{\delta} = \boldsymbol{\delta}_2$ , the tensor approach based on model (5.39) reduces to ESPRIT [126]:

$$\begin{cases} \mathbf{x}_1(t) = \mathbf{A} \mathbf{s}(t) + \mathbf{n}_1(t) \\ \mathbf{x}_2(t) = \mathbf{\Phi} \mathbf{A} \mathbf{s}(t) + \mathbf{n}_2(t) \end{cases} \quad (5.40)$$

where  $\mathbf{\Phi} = \text{Diag}\{e^{-j\omega_0 \zeta(\theta_1)}, \dots, e^{-j\omega_0 \zeta(\theta_R)}\}$  is a unitary operator that relates both subarrays, and  $\zeta(\theta_r) = \boldsymbol{\delta}^\top \mathbf{d}(\theta_r)/c$ .<sup>3</sup>

#### Diversity of Gain Pattern Only

On the other hand, if sensors within a subarray do overlap, *i.e.* are located at the same place, and differ only through their directivity, then  $\mathbf{p}_\ell = 0, \forall \ell$ , and matrix  $\mathbf{A}$  only contains information about gain patterns:  $A_{\ell r} = g_\ell(\theta_r)$ . Therefore, in this degenerate

<sup>2</sup>This is the standard assumption of ESPRIT approaches [79, 126, 142, 136], *i.e.* uncalibrated subarrays.

However, with unknown space shifts and known sensor positions, the mathematical problem is the same [128]. See Section 4.6 for details.

<sup>3</sup>If  $M = 2$ , we also need to fix a rotation ambiguity with respect to the translation axis.

case, the approaches of [142, 136] do not apply and the only space information is carried by space-shift matrix  $\mathbf{B}$ :

$$\mathcal{M}_{\ell mt}^{\text{gain}} = \sum_{r=1}^R A_{\ell r}^{\text{gain}} B_{mr} S_{tr} \in \mathbb{C}^{L \times M \times T} \quad (5.41)$$

with  $\begin{cases} A_{\ell r}^{\text{gain}} &= g_{\ell}(\theta_r) \\ B_{mr} &= e^{-j\omega_0 \zeta_m(\theta_r)} \\ S_{tr} &= s_r(t) \end{cases}$

Notice that in this way we managed to decouple space information (that we know through shifts  $\delta_m$ ) from gain pattern information (that we do not know). Model (5.41) is the starting point of our contribution.

### Diversity of Space Shift Only

In this case,  $g_{\ell}(\theta) = 1 \forall \theta, \forall \ell$ , and we end up with the classic omnidirectional model described in [136]:  $A_{\ell r}^{\text{shift}} = e^{-j\omega_0 \tau_{\ell}(\theta_r)}$  (see Section 4.3 for details).

### 5.4.3. Physical Meaning of Coherences

In Section 3.7, we defined the concept of coherence of a factor matrix and linked it to the identifiability of CPD, with angular conditions easy to compute and interpret. We examined the physical meaning of coherences for space, space shift and time diversities in Section 4.5. We recall that for space shift  $\mathbf{B}$ , coherence  $\mu_B$  is a measure of the angular separation between sources, similarly to  $\mathbf{A}^{\text{shift}}$ , whereas the coherence  $\mu_S$  of signal matrix  $\mathbf{S}$  is the largest correlation coefficient between sources. We now describe the case of gain pattern diversity: from (3.61) and (5.41), we express the coherence of factor matrix  $\mathbf{A}^{\text{gain}}$  as

$$\mu_A^{\text{gain}} = \max_{p \neq q} \frac{|\mathbf{a}_p^{\top} \mathbf{a}_q|}{\|\mathbf{a}_p\| \|\mathbf{a}_q\|} \quad (5.42)$$

For pure gain pattern diversity embedded in  $\mathbf{A}^{\text{gain}}$  of (5.41), coherence  $\mu_A^{\text{gain}}$  is a measure of similarity among pattern responses to impinging sources.

Since  $\mathbf{a}_p^{\top} \mathbf{a}_q = \sum_{\ell=1}^L g_{\ell}(\theta_p) g_{\ell}(\theta_q)$ ,  $\frac{|\mathbf{a}_p^{\top} \mathbf{a}_q|}{\|\mathbf{a}_p\| \|\mathbf{a}_q\|} \leq 1$ , with equality if and only if  $g_{\ell}(\theta_p) = g_{\ell}(\theta_q) \forall \ell$ .

Thus, uniqueness and existence conditions in (3.63) and (3.64) of Section 3.7 can be interpreted in a physical sense. The tensor model of (5.41) is unique if sources are not too closely spaced, if their directivity response is not too similar, and if their time signatures are not too correlated.

### 5.4.4. Estimation of Sources and DoA

The tensor model in (3.21) can be expressed in vector form as

$$\mathbf{x} = \text{vec}\{\mathcal{X}\} = \sum_{r=1}^R \mathbf{s}_r \boxtimes \mathbf{b}_r \boxtimes \mathbf{a}_r + \mathbf{n} \quad (5.43)$$

where  $\boxtimes$  denotes the Kronecker product, as defined in [26, 75] (cf. (3.22) for generic tensor order  $D$ ). Since the *measurement* noise vector,  $\mathbf{n} = \text{vec}\{\mathcal{N}\}$ , is circular white Gaussian

and isotropic, *i.e.* with zero mean and covariance  $\Sigma = \sigma^2 \mathbf{I}$ , the log-likelihood takes the form:

$$\Upsilon(\boldsymbol{\vartheta}) = -(\mathbf{x} - \boldsymbol{\mu})^H \Sigma^{-1} (\mathbf{x} - \boldsymbol{\mu}) + \text{constant} \quad (5.44)$$

where  $\boldsymbol{\mu} = \sum_{r=1}^R \mathbf{s}_r \boxtimes \mathbf{b}_r \boxtimes \mathbf{a}_r$  is unknown and constrained by its actual parameterization  $\boldsymbol{\vartheta} = [\boldsymbol{\theta}, \text{vec}\{\mathbf{G}\}, \text{vec}\{\mathbf{P}\}, \text{vec}\{\mathbf{S}\}]$ . Similarly to [128], the CRB is computed assuming that  $\mathbf{a}_r$  and  $\mathbf{s}_r$  are nuisance parameters, *i.e.* with parameter vector  $\boldsymbol{\chi}$  composed of DoAs and factor matrices:  $\boldsymbol{\chi} = [\boldsymbol{\theta}, \text{vec}\{\mathbf{A}\}, \text{vec}\{\mathbf{S}\}]$ . For the CRB of the tensor DoA estimation, see Chapter 7, and in particular Section 7.3.3.

Although the optimal solution is given by the global maximum of  $\Upsilon(\boldsymbol{\vartheta})$ , we propose a suboptimal two-step procedure in the same spirit as [128], with smaller computational burden: first  $\Upsilon$  is maximized with respect to parameter  $\boldsymbol{\xi} = [\text{vec}\{\mathbf{A}\}, \text{vec}\{\mathbf{B}\}, \text{vec}\{\mathbf{S}\}]$  through a CPD routine, such as ALS [27]; then DoAs can be estimated by

$$\hat{\theta}_r = \arg \min_{\theta \in \Theta} \left[ (\hat{\mathbf{b}}_r - \mathbf{b}_r(\theta))^H (\hat{\mathbf{b}}_r - \mathbf{b}_r(\theta)) \right]. \quad (5.45)$$

This solution can then, if necessary, be refined by a local ascent of  $\Upsilon(\boldsymbol{\vartheta})$ . However, this improvement has revealed to be negligible in subsequent computer experiments. Notice that there are in general better (*i.e.* less computationally expensive) ways than brute force exhaustive search to estimate  $\theta_r$  from  $\hat{\mathbf{b}}_r$ , as detailed in Section 4.6, in particular if the subarray translations  $\boldsymbol{\delta}_m$  have a specific structure.

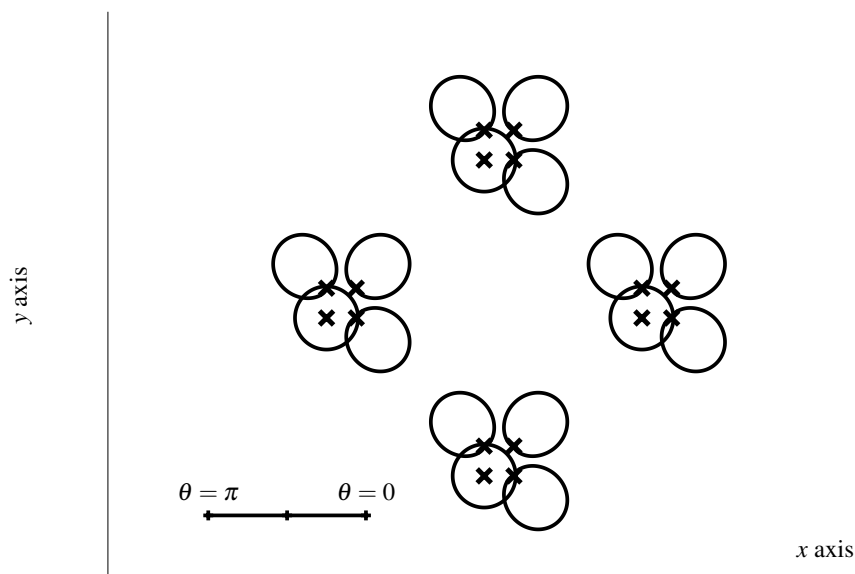


Figure 5.3.: Acquisition system for  $L = M = 4$ ,  $\rho_A > 0$  - gain pattern diversity

### 5.4.5. Computer Results

For the sake of simplicity, sources and the acquisition system are assumed to be coplanar, thanks to Assumption A 1.8. Sensor and subarray positions then become  $\mathbf{p}_\ell = [p_\ell^x, p_\ell^y]$ ,  $1 \leq \ell \leq L$  and  $\boldsymbol{\delta}_m = [\delta_m^x, \delta_m^y]$ ,  $1 \leq m \leq M$ , and delays become  $\tau_\ell(\theta_r) = [p_\ell^x \cos(\theta_r) + p_\ell^y \sin(\theta_r)]/c$  and  $\zeta_m(\theta_r) = [\delta_m^x \cos(\theta_r) + \delta_m^y \sin(\theta_r)]/c$ , both functions of azimuth only. This amounts to considering elevation  $\psi_r = 0 \forall r$ . We work with UCAs of radius  $\rho$ , with  $p_\ell^x = \rho \cos(2\pi\ell/L)$  and  $p_\ell^y = \rho \sin(2\pi\ell/L)$ , as in [72]. We choose a directivity pattern  $g(\cdot)$  with maximum gain in the radial directions from the center of the array,  $2\pi\ell/L$ . Hence,

the response of sensor  $\ell$  to source  $r$  amounts to  $g_\ell(\theta_r) = g(\theta_r - 2\pi\ell/L)$ . Function  $g(\theta)$  is chosen to be a simple nonnegative, smooth and  $2\pi$ -periodical function, with

$$g(\theta)^2 = \frac{\mathcal{D}(\gamma)}{2^\gamma} (1 + \cos(\theta))^\gamma \quad (5.46)$$

and parameter  $\gamma$  controls directivity  $\mathcal{D}(\gamma) = \frac{2^\gamma 2\pi}{\int_0^{2\pi} (1 + \cos(\theta))^\gamma d\theta}$  exponentially.

We simulated  $R = 4$  uncorrelated narrowband sources arriving from  $\theta_1 = 25^\circ$ ,  $\theta_2 = 65^\circ$ ,  $\theta_3 = 105^\circ$ , and  $\theta_4 = 345^\circ$ , with  $T = 64$  time samples. Each subarray is a UCA of radius  $\rho_A = \lambda/(20\sqrt{2})$  with  $L = 4$  sensors, whereas gain patterns have  $\mathcal{D}(\gamma) = 4$  (*i.e.*  $\gamma = 5$ ).  $M = 4$  subarrays with the aforementioned structure are located around a UCA of radius  $\rho_B = \lambda/(2\sqrt{2})$  (see Figure 5.3). As in [90, 128], SNR is defined as:

$$\text{SNR} = 10 \log_{10} \frac{\mathbb{E} [\boldsymbol{\mu}^H \boldsymbol{\mu}]}{\mathbb{E} [\mathbf{n}^H \mathbf{n}]} = 10 \log_{10} \frac{\|\boldsymbol{\mu}\|_2^2}{LMT\sigma^2} \quad (5.47)$$

and estimated MSE is defined as

$$\text{MSE}(\boldsymbol{\theta}) = \frac{1}{\pi^2} \frac{1}{NR} \sum_{n=1}^N \sum_{r=1}^R (\hat{\theta}_{rn} - \theta_r)^2 \quad (5.48)$$

Results are obtained by averaging over  $N = 200$  noise realizations.

The three approaches compared in Figures 5.4, 5.5, 5.6 refer to tensor DoA estimation, with the same equivalent SNR:

**ALS Full** refers to tensor  $\mathcal{M}^{\text{full}}$  in (5.39), when sensors are non overlapping ( $\rho_A > 0$ ) and directional:  $A_{\ell r}^{\text{full}} = g_\ell(\theta_r) e^{-j\omega_0\tau_\ell(\theta_r)}$  and  $\sigma^2_{full} = \frac{\|\boldsymbol{\mu}^{\text{full}}\|_2^2}{LMT} 10^{-SNR/10}$ .

**ALS Gain** refers to tensor  $\mathcal{M}^{\text{gain}}$  in (5.41), when sensors are overlapping ( $\rho_A = 0$ ) and directional:  $A_{\ell r}^{\text{gain}} = g_\ell(\theta_r)$  and  $\sigma^2_{gain} = \frac{\|\boldsymbol{\mu}^{\text{gain}}\|_2^2}{LMT} 10^{-SNR/10}$ .

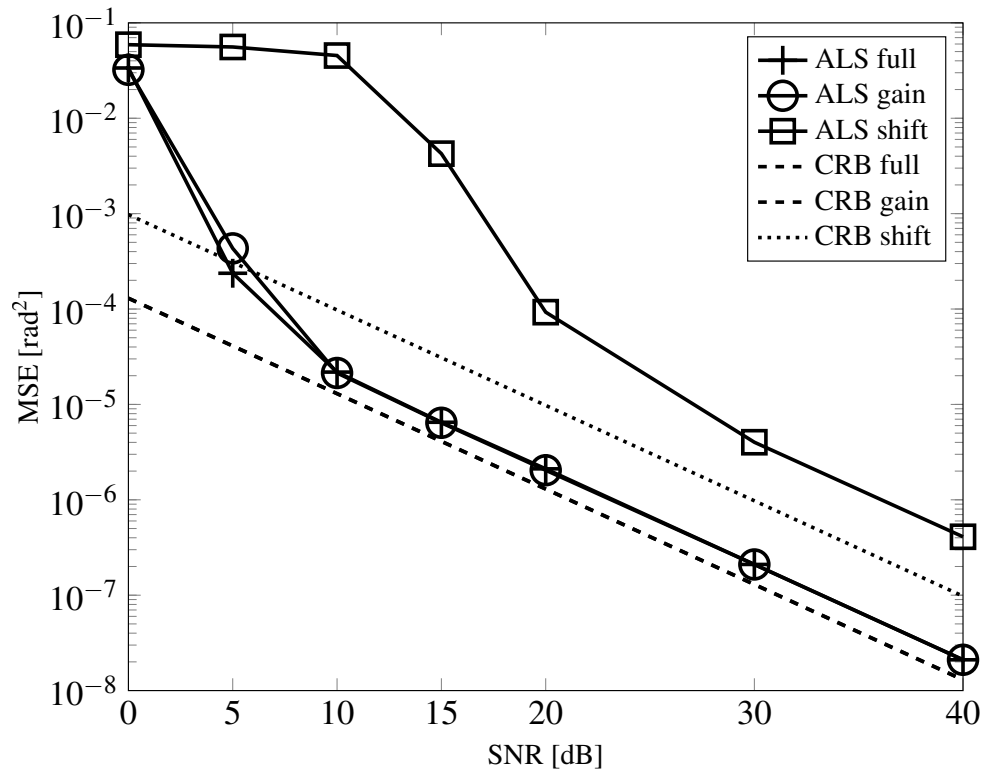
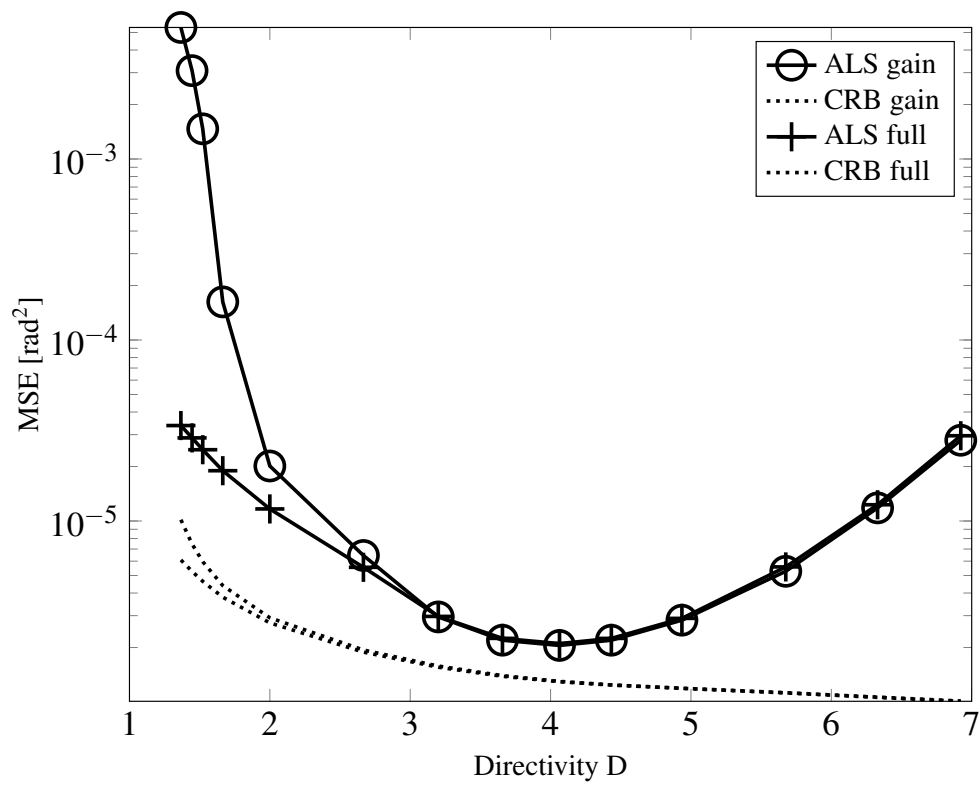
**ALS Shift** refers to tensor  $\mathcal{M}^{\text{shift}}$  as in [136], when sensors are non overlapping and omnidirectional:  $A_{\ell r}^{\text{shift}} = e^{-j\omega_0\tau_\ell(\theta_r)}$  and  $\sigma^2_{shift} = \frac{\|\boldsymbol{\mu}^{\text{shift}}\|_2^2}{LMT} 10^{-SNR/10}$ .

The tensor CPD approximation is achieved via a randomly initialized ALS. In particular, initial estimates are drawn from unit variance complex Gaussian distributions.

Figure 5.4 shows MSE as a function of SNR: when sensor positions within the reference subarray are not known, the introduction of unknown directional elements improves the estimation (ALS Full), even when sensors overlap (ALS Gain).

Figure 5.5 illustrates the dependence of the MSE on sensor directivity  $\mathcal{D}$ , showing an optimum at  $\mathcal{D} \approx 4$  (*i.e.*  $\gamma \approx 5$ ) for the present configuration. The large value of the MSE for small and large directivity is due to bad conditioning of factor matrix  $\mathbf{A}^{\text{gain}}$ . Indeed as  $\mathcal{D}$  grows, gain patterns  $g_\ell(\theta_r)$  become elongated along one direction, thus attenuating all the others. In this configuration, pattern coherence  $\mu_A$  approaches 1.

Figure 5.6 shows the dependence of the MSE on the inter-sensor distance within the reference subarray, for ALS Shift (omnidirectional non overlapping sensors,  $\rho_A > 0$ ) in comparison with ALS Gain (directional overlapping sensors, null inter-sensor distance,  $\rho_A = 0$ ). The former is a decreasing function of inter-sensor distance, hence intersecting the latter at a critical distance where the presence of directional elements is not essential for tensor modeling.

Figure 5.4.: MSE vs SNR,  $\mathcal{D} = 4$ Figure 5.5.: MSE vs  $D$ , SNR = 20dB

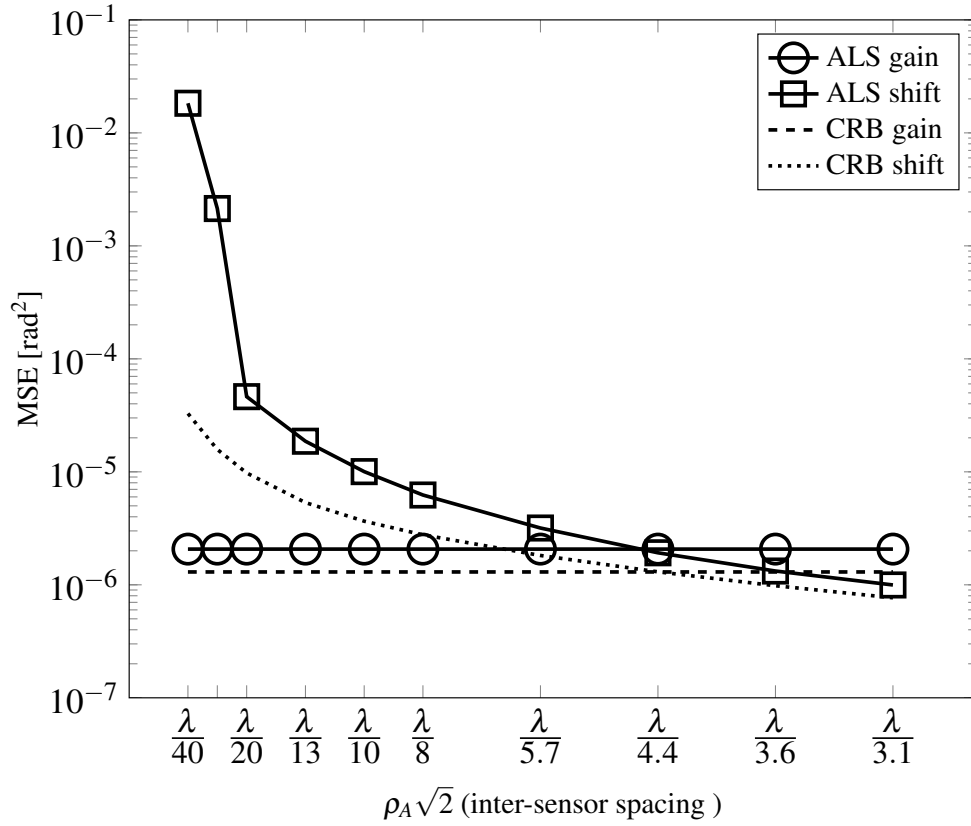


Figure 5.6.: MSE vs  $\rho_A \sqrt{2}$  (inter-sensor distance), SNR = 20dB,  $\mathcal{D} = 4$

We already knew from [136] that space, time, and translation in space induced exploitable diversities, when omnidirectional sensors are used. This remains true if sensors have known nonzero gain patterns, because they can be compensated. But the question of whether sensor gain patterns could induce a diversity of their own was still open. We showed that it can indeed be the case, even when sensors are co-located within each sub-array. In this case, there is no space diversity anymore, but tensor approaches, which need at least three diversities, can still be applied thanks to gain pattern diversity.

# 6. Wideband Tensor DoA Estimation

## 6.1. Contribution

In traditional matrix approaches described in Chapter 2, space and time/frequency diversities have been taken into account. Yet, DoA estimation can be significantly improved if other modalities are considered, such as space shift, polarization and gain patterns, thanks to the tensor formalism, as discussed in Chapter 4 and Chapter 5.

A major contribution of our work relies on the extension of the tensor formalism to wideband DoA estimation, *i.e.* when the signals of interest are wideband (see Section 1.5.1 for the definition of wideband sources).

MUSIC in Section 2.5, ESPRIT in Section 2.6, and CPD tensor decompositions for array processing in Chapter 4 and Chapter 5 originally addressed the narrowband case. In fact, in wideband, signal subspace and steering matrices vary with frequency, thus requiring a focusing operation on the same reference subspace. This approach, named Coherent Signal Subspace (CSS), described in Section 2.8, may require an approximate prior estimate of DoAs to form focusing matrices [157, 102], or virtual arrays obtained by spatial interpolation [23, 80]. The latter proposes a wideband formulation of the MUSIC algorithm for ULAs. To our knowledge, only recently coherent tensor analysis was extended to process wideband waves for ULAs in our contribution [119], where a spatial interpolation technique was adopted.

The present chapter aims at establishing a tensor model for high resolution wideband array processing with multiple antenna diversities (space, space shift, polarization and gain patterns), under the assumption of plane waves in the far field. The multilinear coherent subspace preprocessing, required in the wideband case, introduces a correlation into the noise structure. An algorithm for tensor decomposition taking into account the noise covariance is proposed, and the performance is evaluated via the Cramér-Rao Bound (CRB).

For the sake of clarity, Table 6.1 illustrates the state of the art and our contributions: rows refer to different theoretical approaches along with their corresponding references, whereas columns indicate the physical diversities jointly taken into account in each approach. Approaches related to wideband (frequency diversity) are indicated by WB, whereas contributions using statistics by averaging the covariance matrix through multiple snapshots are indicated by *s*.

This chapter is organized as follows: Section 6.2 illustrates the main antenna diversities that can be exploited in tensor processing of wideband waves; Section 6.3 explains the effect of wideband coherent processing on the tensor formulation; tensor decomposition problems are treated in Section 6.4; Section 6.5 addresses algorithmic issues; Section 6.6 reports computer results for the particular case of space shift and polarization diversities, in comparison with wideband MUSIC and with the multilinear CRB.

Our work was published by IEEE Transactions on Signal Processing [114].

Table 6.1.: Diversities that can be taken into account in array processing;  
 $\times$  = what exists in the literature;  $\otimes$  = our contribution;  
 $s$  = estimation of spatial covariance is required

Diversity	Time	Space	Freq.	Space Shift	Polar.	Gain Patterns
MUSIC [131, 140]	$s, \times$	$\times$				
Vector Sensor MUSIC [131, 95, 96]	$s, \times$	$\times$			$\times$	
WB MUSIC [46, 157, 68, 23, 80, 36]	$s$	$\times$	$\times$			
WB Vector Sensor MUSIC [16]	$s$	$\times$	$\times$		$\times$	
ESPRIT ( $M = 2$ ) [126]	$s, \times$	$\times$		$\times$		
WB ESPRIT [102, 69]	$s$	$\times$	$\times$	$\times$		
NB Tensor CP [136, 90, 128]	$\times$	$\times$		$\times$		
Vector Sensor CP [57, 56, 115]	$\times$	$\times$			$\times$	
WB Tensor CP [119]		$\otimes$	$\otimes$	$\otimes$		
Gain Pattern CP [116]	$\otimes$		$\otimes$	$\otimes$		$\otimes$
WB Vector Sensor CP		$\otimes$	$\otimes$		$\otimes$	

## 6.2. Tensor Model for Wideband Waves

In this section, a multi-way formulation including multiple diversities is presented: Section 6.2.1 introduces space shift diversity, Section 6.2.2 polarization diversity, and Section 6.2.3 combines them together.

### 6.2.1. Space Shift and Gain Pattern Diversity in Wideband

Space shift diversity was initially exploited by the ESPRIT algorithm for two subarrays deduced from each other by a translation [126], as detailed in Section 2.6. It has been extended to more than two subarrays in [136], giving rise to a third order tensor decomposition for array processing, detailed in Chapter 4. The diversities involved are space, time, and space shift. It is also possible to consider diversity induced by anisotropic sensor gains, as proposed in Section 5.4 for the narrowband case. We refer to Section 5.4 for further details about gain pattern diversity.

In this chapter, we make use of the following models, introduced in the previous chapters, that we merge into a new tensor wideband formulation:

- Section 1.5.1: the wideband matrix formulation for scalar wavefields, expressed by (1.46);
- Section 1.5.2: the wideband matrix formulation for polarized wavefields, expressed by (1.49);
- Section 4.3: the narrowband tensor model with space shift diversity, expressed by (4.5).
- Section 5.3.3: the narrowband tensor model with polarization diversity, expressed by (5.27).

Denote by  $\mathcal{F}\{\cdot\}$  the Fourier Transform (FT) operator applied to received signals  $X_{\ell m}(t)$  in the time window  $t \in [0, T]$ . Then, in the presence of additive noise  $\mathbf{N}(\omega)$ , the narrowband formulation of (5.39) is replaced by its wideband counterpart:

$$\begin{aligned} X_{\ell m}(\omega) &= M_{\ell m}(\omega) + N_{\ell m}(\omega) \\ M_{\ell m}(\omega) &= \sum_{r=1}^R A_{\ell r}(\omega) B_{mr}(\omega) s_r(\omega) \end{aligned} \quad (6.1)$$

$$\text{with} \quad \begin{cases} X_{\ell m}(\omega) &= \mathcal{F}\{X_{\ell m}(t)\} \\ A_{\ell r}(\omega) &= g_{\ell}(\theta_r) e^{-j\omega\tau_{\ell}(\theta_r)} \\ B_{mr}(\omega) &= e^{-j\omega\zeta_m(\theta_r)} \\ s_r(\omega) &= \mathcal{F}\{s_r(t)\}. \end{cases} \quad (6.2)$$

where  $\tau_{\ell}(\theta) + \zeta_m(\theta) = \mathbf{p}_{\ell}^T \mathbf{d}(\theta)/c + \boldsymbol{\delta}_m^T \mathbf{d}(\theta)/c$  is the delay of arrival on sensor  $\ell$  of subarray  $m$ , with  $\mathbf{p}_{\ell}$  the location of the  $\ell$ -th sensor and  $\boldsymbol{\delta}_m$  the location of the  $m$ -th subarray, as in (4.6).

In the remainder, since received signals  $X_{\ell m}(t)$  are real, we consider only positive frequencies (without any loss of information). After discretization, we have

$$X_{\ell m}(\omega_q) = \sum_{r=1}^R A_{\ell r}(\omega_q) B_{mr}(\omega_q) S_{qr} + N_{\ell m}(\omega_q) \quad (6.3)$$

where frequency  $0 < \omega_{min} \leq \omega_q \leq \omega_{max} < \pi$ ,  $1 \leq q \leq Q$ , and  $S_{qr} = s_r(\omega_q)$ . In the remainder of this chapter, we will assume omnidirectional sensors, *i.e.* we resort again to Assumption A 4.3: gain patterns are known with  $g_{\ell}(\theta) = 1, \forall \theta, \forall \ell$ .

However, the derivation of the CRB in Chapter 7 also addresses the case of unknown gain patterns. The presence of anisotropic gain patterns is therein treated as a nuisance, but could be exploited as a plain diversity as shown in Section 5.4.

## 6.2.2. Polarization Diversity in Wideband

It is also possible to consider diversities induced by polarized sensors, as we discussed in Section 5.3 for the narrowband case. If we have at our disposal a single antenna ( $M = 1$ ) array of polarized elements, or 3-components (3C) sensors, each capable of recording 3 orthogonal components<sup>1</sup>, the observation model is similar to (6.1). If we omit measurement noise, it takes the form:

$$M_{\ell p}(\omega_q) = \sum_{r=1}^R A_{\ell r}(\omega_q) K_{pr} S_{qr}, \quad 1 \leq p \leq P = 3 \quad (6.4)$$

where the  $R$  columns of the  $3 \times R$  factor matrix  $\mathbf{K}$  are detailed in [3, 88]:

$$\mathbf{k}_r = \mathbf{H}(\theta_r) \mathbf{W}(\alpha_r) \mathbf{w}(\beta_r) \quad (6.5)$$

Both angles  $\alpha_r \in (-\pi/2, \pi/2]$  and  $\beta_r \in [-\pi/4, \pi/4]$  characterize the polarization of the  $r$ -th source; see [3, 96] for general expressions of  $\mathbf{H}(\theta)$ ,  $\mathbf{W}(\alpha)$  and  $\mathbf{w}(\beta)$ . For instance,

<sup>1</sup>For electromagnetic waves, two 3-component sensors can be used, leading to an observation of dimension 6 [57].

Rayleigh waves considered in Section 6.6 belong to the model characterized by

$$\mathbf{H}(\theta_r) = \begin{bmatrix} \cos \phi_r \cos \psi_r & -\cos \phi_r \sin \psi_r \\ \sin \phi_r \cos \psi_r & -\sin \phi_r \sin \psi_r \\ \sin \psi_r & \cos \psi_r \end{bmatrix} \quad (6.6)$$

$$\mathbf{W}(\alpha_r) = \begin{bmatrix} \cos \alpha_r & \sin \alpha_r \\ -\sin \alpha_r & \cos \alpha_r \end{bmatrix} \quad (6.7)$$

$$\mathbf{w}(\beta_r) = \begin{bmatrix} \cos \beta_r \\ j \sin \beta_r \end{bmatrix} \quad (6.8)$$

where it is reminded that in 3D the DoA  $\theta_r = (\phi_r, \psi_r)$  is formed by a pair of angles: azimuth  $\phi_r \in (-\pi, \pi]$  and elevation  $\psi_r \in [-\pi/2, \pi/2]$ . Without restricting too much the generality, we assume that polarization does not depend on  $\omega$  over the bandwidth of interest, thanks to Assumption A 1.20. The main difference between (6.3) and (6.4) is that the second factor matrix,  $\mathbf{K}$ , now depends on extraneous unknown angular parameters  $(\alpha_r, \beta_r)$ , instead of the subarray space shifts  $\delta_m$ .

### 6.2.3. Multiple Diversity in Wideband

It is clear that the aforementioned diversities (space shift in Section 6.2.1 and polarization in Section 6.2.2) can be modeled all together, at the price of an increased notational complexity. If frequency, space, space shift, and polarization diversities are considered simultaneously, the data measurements depend on 4 variables, the data array is of size  $L \times M \times P \times Q$ , with  $P = 3$ . Therefore, discretizing and merging models (6.3) and (6.4) yields

$$\mathcal{X}_{\ell mp}(\omega_q) = \sum_{r=1}^R A_{\ell r}(\omega_q) B_{mr}(\omega_q) K_{pr} S_{qr} + \mathcal{N}_{\ell mp}(\omega_q) \quad (6.9)$$

Traditional subspace processing usually breaks the multidimensionality of the multiple diversity model through a vectorization of the entire array manifold (including space, polarization and/or space shift) [131].

The tensor approach through Canonical Polyadic Decomposition (CPD) fully takes advantage of the multilinearity of a model with at least three diversities [88]. However, in order to have a totally multilinear model in (6.9), we need to remove the dependency on  $\omega_q$  from factor matrices  $\mathbf{A}$  and  $\mathbf{B}$ , *e.g.* through a bilinear interpolation. This matter will be addressed in Section 6.3, whereas tensor model and notations will be discussed in Section 6.4.

## 6.3. Tensor Wideband Processing

Equation (6.3), as a matrix equation for a given frequency, cannot yield a unique factorization if  $\mathbf{A}(\omega_q)$  and  $\mathbf{B}(\omega_q)$  have not a particular structure that can be taken into account. Hence, such equations need to be treated simultaneously for all frequencies, through the tensor formalism. The bilinear interpolation we propose is precisely a means to coherently combine them in a manner that has a physical meaning. In this section, we aim at jointly exploiting models (6.3), (6.4) and (6.9) for several angular frequencies. As mentioned in Section 6.2.3, the difficulty comes from the fact that these models are obviously not multilinear w.r.t.  $\omega_q$ , because exponentials in  $\mathbf{A}(\omega_q)$  and  $\mathbf{B}(\omega_q)$  are a function of frequency.

Section 6.3.1 extends the definition of virtual arrays to the rotational invariant structure of space shift diversity, whereas Sections 6.3.2 and 6.3.3 propose a bilinear interpolation to be applied to two tensor modes separately. The effect of this preprocessing on the noise structure is studied in Section 6.3.4, whereas bilinear interpolation in the presence of polarization diversity is addressed in Section 6.3.5.

### 6.3.1. Virtual Subarrays

The idea is to build virtual arrays, as described in (2.49) of Section 2.8.1; but we have now a second condition to satisfy, in addition to (2.46):

$$[\omega_q \tilde{\boldsymbol{\delta}}_m(\omega_q) - \omega_0 \boldsymbol{\delta}_m]^\top \mathbf{d}(\theta) \equiv 0, \text{ mod } 2\pi c \quad (6.10)$$

It is clear that it is sufficient to define the locations of virtual sensors and virtual subarrays by:

$$\tilde{\mathbf{p}}_\ell(\omega_q) = \frac{\omega_0}{\omega_q} \mathbf{p}_\ell, \quad \tilde{\boldsymbol{\delta}}_m(\omega_q) = \frac{\omega_0}{\omega_q} \boldsymbol{\delta}_m \quad (6.11)$$

to satisfy both (2.46) and (6.10). An illustration of virtual subarrays is provided in Figure 6.1. With these virtual arrays, one can associate time delays  $\tilde{\tau}_\ell(\omega_q, \theta) = \tilde{\mathbf{p}}_\ell(\omega_q)^\top \mathbf{d}(\theta)$  and  $\tilde{\zeta}_m(\omega_q, \theta) = \tilde{\boldsymbol{\delta}}_m(\omega_q)^\top \mathbf{d}(\theta)$ , and corresponding steering vectors  $\tilde{\mathbf{a}}(\omega_q, \theta) = \exp\{-j\omega_q \tilde{\tau}(\omega_q, \theta)\}$  and  $\tilde{\mathbf{b}}(\omega_q, \theta) = \exp\{-j\omega_q \tilde{\zeta}(\omega_q, \theta)\}$ . Once virtual arrays are defined, it is necessary to compute the virtual data these array would receive, and this is done by interpolation as explained in the next two sections.

### 6.3.2. Bilinear Transform

This section extends the linear transform of (2.49) in Section 2.8.2 to two dimensions (the former at the sensor level and the latter at the subarray level). Space is first partitioned into  $K$  angular sectors of limited extent,  $\Theta_k$ ,  $1 \leq k \leq K$ . Then each sector is discretized into  $I$  angular values:  $\Theta_k = \{\theta_{k1}, \dots, \theta_{kI}\}$ . In each sector  $\Theta_k$  and for every discretized frequency  $\omega_q$ , we define matrices  $\mathbb{A}$  and  $\mathbb{B}$  of size  $L \times I$  and  $M \times I$ , respectively:

$$\begin{aligned} \mathbb{A}(\omega_q, \Theta_k) &= [\mathbf{a}(\omega_q, \theta_{k1}), \dots, \mathbf{a}(\omega_q, \theta_{kI})] \\ \mathbb{B}(\omega_q, \Theta_k) &= [\mathbf{b}(\omega_q, \theta_{k1}), \dots, \mathbf{b}(\omega_q, \theta_{kI})] \end{aligned}$$

We also build  $\tilde{\mathbb{A}}$  and  $\tilde{\mathbb{B}}$  in the same manner with vectors  $\tilde{\mathbf{a}}(\omega_q, \theta_{ki})$  and  $\tilde{\mathbf{b}}(\omega_q, \theta_{ki})$ , respectively. For a fixed reference frequency  $\omega_0$  (generally chosen to be inside of the band of interest [80]), two focusing matrix families can then be defined, by solving for square matrices  $\mathbf{U} \in \mathbb{C}^{L \times L}$  and  $\mathbf{V} \in \mathbb{C}^{M \times M}$  the linear systems below in the LS sense:

$$\mathbf{U}(\omega_q, \omega_0, \Theta_k) \mathbb{A}(\omega_q, \Theta_k) \approx \tilde{\mathbb{A}}(\omega_0, \Theta_k) \quad (6.12)$$

$$\mathbf{V}(\omega_q, \omega_0, \Theta_k) \mathbb{B}(\omega_q, \Theta_k) \approx \tilde{\mathbb{B}}(\omega_0, \Theta_k) \quad (6.13)$$

for every angular sector  $\Theta_k$  and every frequency  $\omega_q$ . In what follows we only consider one angular sector  $\Theta$ , and we hence refer to  $\mathbf{U}(\omega_q, \omega_0, \Theta)$  and  $\mathbf{V}(\omega_q, \omega_0, \Theta)$  with  $\mathbf{U}_q$  and  $\mathbf{V}_q$ , respectively. As for the detection of the most relevant sectors  $\Theta_k$ , the angular field of view of the array can be scanned and sectors of largest power can be detected through a simple optimum beamforming technique [152, 89].



Figure 6.1.: Illustration of virtual subarrays

### 6.3.3. Bilinear Interpolation

Measurements recorded on actual arrays with sensors located at  $\mathbf{p}_\ell + \boldsymbol{\delta}_m$  at frequency  $\omega_q$  are interpolated to yield virtual measurements recorded by sensors located at  $\tilde{\mathbf{p}}_\ell(\omega_q) + \tilde{\boldsymbol{\delta}}_m(\omega_q)$ , as defined in (6.11). More precisely, applying the bilinear interpolation (6.12-6.13) to model (6.3) leads to

$$\tilde{\mathcal{M}}_{\ell m q} \approx \sum_{r=1}^R \tilde{A}_{\ell r}(\omega_q) \tilde{B}_{mr}(\omega_q) S_{qr} \quad (6.14)$$

where the slice  $\tilde{\mathbf{M}}_q$  of tensor  $\tilde{\mathcal{M}}$  is obtained through the bilinear transformation of slice  $\mathbf{M}_q$ :

$$\begin{aligned} \tilde{\mathbf{M}}_q &= \mathbf{M}_q \bullet_1 \mathbf{U}_q \bullet_2 \mathbf{V}_q \\ &= \mathbf{U}_q \mathbf{M}_q \mathbf{V}_q^\top \end{aligned} \quad (6.15)$$

Now,  $\tilde{\mathcal{M}}$  may be seen as a tensor of order 3, since frequency  $\omega_q$  only affects the third mode, and (6.14) is actually a CPD model.

However, a new difficulty appears, due to the fact that the bilinear transformation in (6.15) affects the color of the noise. This must be taken into account into the CPD identification algorithm (cf. Section 6.5) and the computation of the performance bounds (cf. Chapter 7).

### 6.3.4. Noise Correlation Induced by Interpolation

The observation model (6.14) can be expressed through  $Q$  matrix slices,  $1 \leq q \leq Q$ :

$$\tilde{\mathbf{X}}_q = \tilde{\mathbf{M}}_q + \tilde{\mathbf{N}}_q \quad (6.16)$$

where  $\tilde{\mathbf{N}}_q$  is colored by the transform:

$$\tilde{\mathbf{N}}_q = \mathbf{U}_q \mathbf{N}_q \mathbf{V}_q^\top \quad (6.17)$$

Yet from [10], we have  $\text{vec}\{\mathbf{U}\mathbf{N}\mathbf{V}^\top\} = (\mathbf{V} \boxtimes \mathbf{U}) \text{vec}\{\mathbf{N}\}$ . This leads to the following noise vectorization:

$$\text{vec}\{\tilde{\mathbf{N}}_q\} = (\mathbf{V}_q \boxtimes \mathbf{U}_q) \text{vec}\{\mathbf{N}_q\} \quad (6.18)$$

Hence, for every frequency  $\omega_q$ , the noise vector  $\text{vec}\{\tilde{\mathbf{N}}_q\}$  is circular complex Gaussian with covariance

$$\boldsymbol{\Sigma}_q = \sigma^2 \mathbf{V}_q \mathbf{V}_q^\text{H} \boxtimes \mathbf{U}_q \mathbf{U}_q^\text{H} \quad (6.19)$$

If we stack all vectors  $\text{vec}\{\tilde{\mathbf{N}}_q\}$  in a single vector  $\tilde{\mathbf{n}}$ , then the latter has a covariance  $\boldsymbol{\Sigma}_{(1)}$  that is block-diagonal<sup>2</sup> with diagonal blocks  $\boldsymbol{\Sigma}_q$  in (6.19):

$$\boldsymbol{\Sigma}_{(1)} = \begin{bmatrix} \boldsymbol{\Sigma}_1 & \mathbf{0} & \mathbf{0} \\ \mathbf{0} & \ddots & \mathbf{0} \\ \mathbf{0} & \mathbf{0} & \boldsymbol{\Sigma}_Q \end{bmatrix} \quad (6.20)$$

This change in covariance structure will be taken into account for calculating the Fisher Information Matrix (FIM) in Chapter 7, and in the CPD identification algorithm in Section 6.5.

<sup>2</sup>Notice that  $\boldsymbol{\Sigma}_{(1)}$  also corresponds to the covariance matrix of the vectorization of the mode-1 tensor unfolding of  $\mathcal{N}$ ,  $\text{vec}\{\mathbf{N}_{(1)}\}$ . See (3.9) in Definition 3.7 for more details.

### 6.3.5. Interpolation in the Presence of Polarization

Instead of space shift, if we consider polarization as the second diversity as in (6.4), the bilinear transformation (6.15) becomes

$$\tilde{\mathbf{M}}_q = \mathbf{U}_q \mathbf{M}_q \mathbf{I}_P^\top, \quad (6.21)$$

as polarization matrix  $\mathbf{K}$  does not depend on frequency by assumption:

$$\tilde{\mathcal{M}}_{\ell pq} \approx \sum_{r=1}^R \tilde{A}_{\ell r}(\omega_0) K_{pr} S_{qr} \quad (6.22)$$

Moreover, the diagonal blocks of the vectorized noise covariance  $\Sigma_{(1)}$  are simplified to

$$\Sigma_q = \sigma^2 \mathbf{I}_P \boxtimes \mathbf{U}_q \mathbf{U}_q^\text{H} \quad (6.23)$$

If we now include all the diversities as in model (6.9), then interpolation is given by the following multilinear transformation:

$$\tilde{\mathcal{M}}_q = \mathcal{M}_q \bullet_1 \mathbf{U}_q \bullet_2 \mathbf{V}_q \bullet_3 \mathbf{I}_P \quad (6.24)$$

where index  $q$  may be seen as denoting the  $q$ -th slice of a fourth order tensor. The mode- $d$  product indicated as  $\bullet_d$  refers to the multiplication of a tensor and a matrix along its  $d$ -th mode (see Section 3.2.3 for details on this contraction product)<sup>3</sup>. This yields to interpolated elements

$$\tilde{\mathcal{M}}_{\ell mpq} \approx \sum_{r=1}^R \tilde{A}_{\ell r}(\omega_0) \tilde{B}_{mr}(\omega_0) K_{pr} S_{qr} \quad (6.25)$$

Similarly, the noise covariance of the  $q$ -th vectorized slice  $\text{vec}\{\tilde{\mathbf{N}}_q\}$  becomes

$$\Sigma_q = \sigma^2 \mathbf{I}_P \boxtimes \mathbf{V}_q \mathbf{V}_q^\text{H} \boxtimes \mathbf{U}_q \mathbf{U}_q^\text{H} \quad (6.26)$$

## 6.4. CPD Factors, Normalisation and Scaling

Consider the case of a tensor of order  $D = 4$ , which is sufficient for our purposes. Once the bases of the linear spaces involved are fixed, a fourth order tensor  $\mathcal{M}$  is defined by its coordinates, denoted  $\mathcal{M}_{\ell mpq}$ . If its dimensions are  $L \times M \times P \times Q$ , then the CPD (3.22) becomes

$$\mathcal{M} = \sum_{r=1}^R \varsigma_r \mathbf{a}_r \otimes \mathbf{b}_r \otimes \mathbf{k}_r \otimes \mathbf{s}_r \quad (6.27)$$

and can be rewritten in terms of array of coordinates:

$$\mathcal{M}_{\ell mpq} = \sum_{r=1}^R \varsigma_r A_{\ell r} B_{mr} K_{pr} S_{qr} \quad (6.28)$$

where matrices  $\mathbf{A}$ ,  $\mathbf{B}$ ,  $\mathbf{K}$  and  $\mathbf{S}$ , are of dimensions  $L \times R$ ,  $M \times R$ ,  $P \times R$  and  $Q \times R$ , respectively. For practical purposes and without restricting the generality, we have preferred to impose the following constraints:

<sup>3</sup>Notice that for matrices  $\mathbf{X} \bullet_1 \mathbf{A} \bullet_2 \mathbf{B} = \mathbf{A} \mathbf{X} \mathbf{B}^\text{T}$ , as in (6.15) and (6.21)

- the first row of matrices  $\mathbf{A}$  and  $\mathbf{B}$  to be formed of ones (in fact, as assumed in A 4.2, A 4.4, and A 5.1 b),  $\mathbf{p}_1 = \mathbf{0}$ ,  $\boldsymbol{\delta}_1 = \mathbf{0}$  and  $g_1(\theta) = 1, \forall \theta$ ); cf. Section 4.3.1 for the narrowband case.
- unit norm columns in matrix  $\mathbf{K}$ ; cf. Section 5.3.4 for the narrowband case.
- and to pull the remaining  $R \times R$  scaling matrix,  $\text{Diag}\{\varsigma_r A_{1r} B_{1r} \|\mathbf{k}_r\|\}$ , into matrix  $\mathbf{S}$ .

Thus, we fix all scale indeterminacies through the following transformation (see (4.7) and (5.29) for its narrowband counterpart):

$$(\hat{\mathbf{a}}_r, \hat{\mathbf{b}}_r, \hat{\mathbf{k}}_r, \hat{\mathbf{s}}_r, \varsigma_r) \leftarrow \left( \frac{\mathbf{a}_r}{A_{1r}}, \frac{\mathbf{b}_r}{B_{1r}}, \frac{\mathbf{k}_r}{\|\mathbf{k}_r\|}, \varsigma_r A_{1r} B_{1r} \|\mathbf{k}_r\| \mathbf{s}_r, 1 \right) \quad (6.29)$$

This choice permits to compute performance bounds on the retrieval of CPD factors in (6.27) more easily. To conclude, in the rest of the chapter, we shall use a CPD model of the form:

$$\begin{cases} \mathcal{X} = \sum_{r=1}^R \mathbf{a}_r \otimes \mathbf{b}_r \otimes \mathbf{k}_r \otimes \mathbf{s}_r + \mathcal{N} \\ \mathcal{X}_{\ell mpq} = \sum_{r=1}^R A_{\ell r} B_{mr} K_{pr} S_{qr} + \mathcal{N}_{\ell mpq} \end{cases} \quad (6.30)$$

with the normalizations mentioned above.

Note that after fixing the scaling indeterminacies, the number of remaining free parameters is now given by  $R(L + M + P + Q - 3)$ , as stated in Section 3.3.4 for the general DD case.

As introduced in Section 3.3.5, there exist sufficient conditions ensuring uniqueness of the exact CPD [136], establishing the maximum number of sources that can be estimated. Again, less stringent conditions guaranteeing almost surely a unique solution can be found in [88, 19]:

$$R(L + M + P + Q - 3) < LMPQ \quad (6.31)$$

This holds true when data are not corrupted by noise. As explained in Section 3.7, in the presence of noise, the existence of a best approximant to the low-rank problem can be inferred through physical quantities named *coherences*, related to the maximum degree of correlation between any two sources along each mode [88]. For the physical interpretation of coherences, see Section 4.5 for space, time, and space shift diversities; Section 5.3.6 for polarization diversity; Section 5.4.2 for pattern diversity.

## 6.5. Algorithms

The goal of the two remaining sections is to illustrate the performance of tensor wideband processing and to compare it to the CRB. The ALSCOLOR algorithm described in this section is meant to take into account the noise covariance structure.

Tensor wideband processing will be executed in two stages: we first recover factor matrices through CPD model fitting (assuming they are uncoupled), and then estimate the DoAs or polarization parameters from the estimated factor matrices. A refinement could also be executed as a post-processing, *e.g.* by a local ascent maximizing the log-likelihood in (7.2), but it generally brings negligible improvement. We first describe both steps of this procedure, in their respective order: retrieval of the CPD factors taking into account the noise correlation structure in Section 6.5.1, and the estimation of DoAs and polarization parameters in Section 6.5.2.

Notice that interpolated slices  $\mathbf{x}_q$  have now a separable covariance structure, as in Definition 3.20. A multidimensional noise  $\mathcal{N} \in \mathbb{C}^{I_1 \times I_2 \times \dots \times I_D}$  is said to be a Kronecker colored noise if it has a separable covariance structure:

$$\text{Cov}[\mathcal{N}] = \Sigma_1 \otimes \Sigma_2 \otimes \dots \otimes \Sigma_D \quad (6.32)$$

or, equivalently, thanks to Proposition 3.4, if its vectorization  $\mathbf{n} = \text{vec}\{\mathcal{N}\} \in \mathbb{C}^{I_1 I_2 \dots I_D}$  has a Kronecker covariance structure

$$\text{Cov}[\mathbf{n}] = \Sigma_1 \boxtimes \Sigma_2 \boxtimes \dots \boxtimes \Sigma_D \quad (6.33)$$

A deterministic prewhitening for tensor data in additive noise with Kronecker structure was proposed in [29]. However, if we directly applied this kind of deterministic prewhitening to our interpolated data  $\tilde{\mathbf{x}}_q$ , this would result not only in a whitening of the noise  $\tilde{\mathcal{N}}$ , but also in a cancellation of the previous interpolation:

$$\begin{aligned} \tilde{\mathbf{x}}_q &= \tilde{\mathcal{M}}_q + \tilde{\mathcal{N}}_q = \\ &= \mathbf{x}_q \bullet_1 \mathbf{U}_q \bullet_2 \mathbf{V}_q + \mathcal{N}_q \bullet_1 \mathbf{U}_q \bullet_2 \mathbf{V}_q \end{aligned} \quad (6.34)$$

In fact, prewhitening as in [29] would give

$$\hat{\mathbf{x}}_q = \tilde{\mathbf{x}}_q \bullet_1 \hat{\mathbf{U}}_q^{-1} \bullet_2 \hat{\mathbf{V}}_q^{-1} \approx \mathbf{x}_q \quad (6.35)$$

which is equal to the data before the interpolation step. Hence, we are required to deal with the Kronecker structure in (6.19), (6.23), and (6.26) not as a preprocessing step, but directly within the very estimation of factor matrices. Section 6.5.1 develops this particular problem.

### 6.5.1. Estimation of Factor Matrices

CPD fitting corresponds to minimizing the tensor approximation error for model (6.14). Notice that similar considerations can be made for models (6.22) and (6.25). Supposing that the interpolation error is negligible compared to the error introduced by measurement noise, we are interested in minimizing the following cost function with respect to  $\tilde{\mathbf{a}}_r$ ,  $\tilde{\mathbf{b}}_r$  and  $\mathbf{s}_r$ :

$$\begin{aligned} \Upsilon &= \left\| \text{vec}\{\tilde{\mathbf{X}}_{(1)}\} - \sum_{r=1}^R \mathbf{s}_r \boxtimes \tilde{\mathbf{b}}_r \boxtimes \tilde{\mathbf{a}}_r \right\|_{\Sigma_{(1)}}^2 = \\ &= \left\| \text{vec}\{\tilde{\mathbf{X}}_{(2)}\} - \sum_{r=1}^R \mathbf{s}_r \boxtimes \tilde{\mathbf{a}}_r \boxtimes \tilde{\mathbf{b}}_r \right\|_{\mathbf{P}_{12}\Sigma_{(1)}\mathbf{P}_{12}^\top}^2 = \\ &= \left\| \text{vec}\{\tilde{\mathbf{X}}_{(3)}\} - \sum_{r=1}^R \tilde{\mathbf{b}}_r \boxtimes \tilde{\mathbf{a}}_r \boxtimes \mathbf{s}_r \right\|_{\mathbf{P}_{13}\Sigma_{(1)}\mathbf{P}_{13}^\top}^2 \end{aligned} \quad (6.36)$$

where we define the weighted matrix norm  $\|\mathbf{X}\|_{\Sigma}^2 = \text{trace}\{\mathbf{X}^\text{H}\Sigma^{-1}\mathbf{X}\}$ . Expression  $\mathbf{X}_{(d)}$  refers to the mode- $d$  unfolding of tensor  $\mathbf{X}$  (see Definition 3.5 for the definition of tensor unfolding). Notice that  $\Sigma_{(1)}$  is the covariance matrix of  $\tilde{\mathbf{x}}$ , the vectorization of the first unfolding  $\tilde{\mathbf{X}}_{(1)}$ , and permutation matrix  $\mathbf{P}_{ij}$  denotes the transfer matrix from the covariance of the mode- $i$  unfolding to that of the mode- $j$  unfolding.

**Algorithm 6.1 ALSCOLOR** : ALS for correlated noise

- 
- 1: Inputs:  $\hat{\mathbf{A}}^0, \hat{\mathbf{B}}^0, \hat{\mathbf{S}}^0$ , the covariance matrix  $\Sigma_{(1)}$  given by (6.20), the interpolated data tensor  $\tilde{\mathbf{X}}$ .
  - 2: Initialize with  $\hat{\mathbf{A}}^0, \hat{\mathbf{B}}^0, \hat{\mathbf{S}}^0$ . Denote for all  $i$ :  
 $\hat{\mathbf{a}}^i = \text{vec}\{\hat{\mathbf{A}}^i\}, \hat{\mathbf{b}}^i = \text{vec}\{\hat{\mathbf{B}}^i\}, \hat{\mathbf{s}}^i = \text{vec}\{\hat{\mathbf{S}}^i\}$ .
  - 3: While convergence criterion not met, do  $i := i + 1$

$$\begin{cases} \mathbf{Z} = (\hat{\mathbf{S}}^i \odot \hat{\mathbf{B}}^i) \boxtimes \mathbf{I}_L \\ \hat{\mathbf{a}}^i = (\mathbf{Z}^H \Sigma_{(1)}^{-1} \mathbf{Z})^{-1} \mathbf{Z}^H \Sigma_{(1)}^{-1} \text{vec}\{\tilde{\mathbf{X}}_{(1)}\} \end{cases} \quad (6.37)$$

Proceed similarly for  $\hat{\mathbf{b}}^i$  and  $\hat{\mathbf{s}}^i$ , with  $\Sigma_{(2)} = \mathbf{P}_{12} \Sigma_{(1)} \mathbf{P}_{12}^\top$  and  $\Sigma_{(3)} = \mathbf{P}_{13} \Sigma_{(1)} \mathbf{P}_{13}^\top$ , respectively.

- 4: Unvectorize estimates:  $\hat{\mathbf{A}}^i = \text{unvec}\{\hat{\mathbf{a}}^i\}, \hat{\mathbf{B}}^i = \text{unvec}\{\hat{\mathbf{b}}^i\}$  and  $\hat{\mathbf{S}}^i = \text{unvec}\{\hat{\mathbf{s}}^i\}$ ; normalize columns of  $\hat{\mathbf{A}}^i$  and  $\hat{\mathbf{B}}^i$  by their first element:

$$\begin{cases} \hat{\mathbf{a}}_r^i := \hat{\mathbf{a}}_r^i / \hat{A}_{1r}^i \\ \hat{\mathbf{b}}_r^i := \hat{\mathbf{b}}_r^i / \hat{B}_{1r}^i \end{cases} \quad (6.38)$$

and normalize  $\hat{\mathbf{S}}^i$  accordingly:  $\hat{\mathbf{s}}_r^i := \hat{A}_{1r}^i \hat{B}_{1r}^i \hat{\mathbf{s}}_r^i$ .

**NB:** When dealing with model (6.22), where the third diversity is given by polarization instead of space-shift,  $\mathbf{B}^i$  is replaced by  $\mathbf{K}^i$  in the steps above, and normalization is achieved as:

$$\begin{cases} \hat{\mathbf{a}}_r^i := \hat{\mathbf{a}}_r^i / \hat{A}_{1r}^i \\ \hat{\mathbf{k}}_r^i := \hat{\mathbf{k}}_r^i / \|\hat{\mathbf{k}}_r^i\| \\ \hat{\mathbf{s}}_r^i := \hat{A}_{1r}^i \|\hat{\mathbf{k}}_r^i\| \hat{\mathbf{s}}_r^i \end{cases} \quad (6.39)$$

5: End

---

The above mentioned minimization corresponds to maximum likelihood estimation and can be performed in several ways: gradient descent, conjugate gradient, Newton methods and coordinate descent methods [27]. For ease of implementation, we choose to minimize (6.36) using block coordinate descent, with blocks corresponding to factor matrices themselves. This is commonly known as ALS [27], as each block coordinate update corresponds to the solution of a LS problem (cf. Section 3.6.3). Initializations for the ALS are randomly drawn from complex normal distributions with unit variance. The proposed algorithm, which we name ALSCOLOR, is detailed in Algorithm 6.1.

### 6.5.2. Estimation of Signal Parameters

Once column vectors  $\hat{\mathbf{a}}_r, \hat{\mathbf{b}}_r$  and/or  $\hat{\mathbf{k}}_r$  are recovered from the tensor approximation algorithm, we can estimate DoA  $\theta_r$  through an exhaustive search within the considered angular sector  $\Theta$  and/or polarization parameters  $\beta_r$  and/or  $\alpha_r$ .

### Space Shift Diversity

If there are space, space shift and frequency diversities (cf. Section 6.6.1), DoAs are estimated by minimizing a weighted LS criterion of the form:

$$\hat{\theta}_r^{\mathbf{D}} = \arg \min_{\theta \in \Theta_i} \left\| \begin{pmatrix} \hat{\mathbf{a}}_r - \tilde{\mathbf{a}}_r(\theta) \\ \hat{\mathbf{b}}_r - \tilde{\mathbf{b}}_r(\theta) \end{pmatrix} \right\|_{\mathbf{D}}^2 \quad (6.40)$$

where  $\mathbf{D}$  is a positive definite matrix and  $\|\mathbf{u}\|_{\mathbf{D}}^2 = \mathbf{u}^H \mathbf{D}^{-1} \mathbf{u}$ . We have experimented several choices for  $\mathbf{D}^{-1}$ : (i) the FIM<sup>4</sup>  $\mathbf{F}_r$  related to vector  $[\mathbf{a}_r^T, \mathbf{b}_r^T]^T$  computed at  $[\hat{\mathbf{a}}_r, \hat{\mathbf{b}}_r, \hat{\mathbf{s}}_r]$ , (ii) its approximation by its two main diagonal blocks, (iii)  $\mathbf{D} = \mathbf{I}$ . The two diagonal blocks are not diagonal, so that the parameter estimation  $\hat{\theta}_r^{\mathbf{I}}$  assuming that all components of  $\hat{\mathbf{a}}_r$  and  $\hat{\mathbf{b}}_r$  have the same variance is less accurate. On the other hand, since the correlation between  $\hat{\mathbf{a}}_r$  and  $\hat{\mathbf{b}}_r$  has revealed to be small, estimates obtained with (i) and (ii) are very similar, and will be both denoted by  $\hat{\theta}_r^{\mathbf{F}}$ .

Objective (6.40) is arbitrary and suboptimal, but permits to find an acceptable solution, as will be demonstrated in Section 6.6. In fact, a refinement by gradient ascent does not bring any significant improvement.

### Polarization Diversity

If there are space, polarization and frequency diversities (cf Section 6.6.2), we can also estimate polarization parameters. For one single polarization parameter  $\beta_r$ , we perform an exhaustive search over a 2D grid of DoA  $\theta \in \Theta$  and polarization angle  $\beta \in [-\pi/4, \pi/4]$ . We proceed analogously, by searching  $\Theta \cup [-\pi/4, \pi/4]$  for:

$$(\hat{\theta}_r^{\mathbf{D}}, \hat{\beta}_r^{\mathbf{D}}) = \arg \min_{\theta, \beta} \left\| \begin{pmatrix} \hat{\mathbf{a}}_r - \tilde{\mathbf{a}}_r(\theta) \\ \hat{\mathbf{k}}_r - \mathbf{k}_r(\theta, \beta) \end{pmatrix} \right\|_{\mathbf{D}}^2 \quad (6.41)$$

The same choices of matrix  $\mathbf{D}$  have been experimented (see Section 6.6).

*Remark:* the above mentioned minimization procedures are performed in a limited domain:  $\theta \in \Theta, \beta \in [-\pi/4, \pi/4]$ . In order to prevent this search from becoming too costly, we apply an iterative progressive refinement of the grid, where each iteration is a zoomed version of the previous one.

## 6.6. Computer Results

This section is meant to illustrate the advantage of wideband tensor processing for the problem of DoA and/or polarization estimation.

MC simulations make use of multiple diversities, throughout the section (in addition to space and frequency):

1. Section 6.6.2: space shifts of a reference subarray, as described in Section 6.2.1.
2. Section 6.6.2: polarization diversity, as described in Section 6.2.2.

<sup>4</sup>See Chapter 7, and references [128, 90] for further details on the computation of CRB for factor matrices.

Thanks to Assumption A 1.8, impinging sources are assumed coplanar with respect to the array: only azimuth is to be estimated, and not elevation, without any loss of generality, as described in Section 4.6.2. We simulated  $R = 2$  sources, at sampling frequency  $f_s = 1$  kHz, for an observation time of 64 ms and propagating at  $c = 1800$  m s<sup>-1</sup>, which is approximately the propagation speed of seismic S-waves through ice [117]. Hence,  $T = 64$  time samples are available. Sources in time domain are white Gaussian processes with unit variance. The number of working frequency bins is  $Q = 14$  (within the selected frequency range from  $f_{min} = 0.25 f_s$  to  $f_{max} = 0.45 f_s$ ). As for the distance  $d_{ij}$  between two neighboring sensors ( $\ell = i$  and  $\ell = j$ ) of the same subarray, we set  $d_{ij} \leq \lambda_0/2$ , where  $\lambda_0$  is the reference wavelength,  $\lambda_0 = 2\pi c/\omega_0$ . The reference frequency  $f_0 = \omega_0/2\pi$  is chosen to be the central bin  $f_0 = (f_{min} + f_{max})/2 = 0.35 f_s$ . Correlation between sources, when present, is  $\rho = 0.9$ .

Wideband processing is performed in a single sector  $\Theta$ , assuming interesting sectors (*i.e.* sectors containing most of the signal power) have been previously detected through a former low resolution beamforming technique. Former detection of relevant sectors is beyond the scope of this chapter and can be found in the literature [89, 152]. Interpolation is then performed within the angular sector  $\Theta = [0, 25^\circ]$ , with a discretization of  $0.1^\circ$ .

In order to understand the relevance of tensor wideband processing, we also present a narrowband alternative for comparison (referred to as NB-ALS): received signals are filtered around central frequency  $f_0 = \omega_0/2\pi$  with narrowband filter bandwidth  $BW = 0.015 f_s$ , and then directly processed through tensor CPD approximation [136, 128], as in Chapter 4. Estimation efficiency is also evaluated in comparison to the wideband MUSIC approach [157], and to the wideband multilinear CRB derived in Section 7.2. The performance criterion is the relative total MSE of the DoA estimates and, whenever present, of the polarization ellipticity estimates:

$$\begin{cases} \text{MSE}(\boldsymbol{\theta}) = \frac{1}{\pi^2} \frac{1}{NR} \sum_{n=1}^N \sum_{r=1}^R (\hat{\theta}_{rn} - \theta_r)^2 \\ \text{MSE}(\boldsymbol{\beta}) = \frac{1}{\pi^2} \frac{1}{NR} \sum_{n=1}^N \sum_{r=1}^R (\hat{\beta}_{rn} - \beta_r)^2 \end{cases} \quad (6.42)$$

where  $\hat{\theta}_{rn}$  and  $\hat{\beta}_{rn}$  are the estimated DoA and ellipticity angle, respectively, of source  $r$  in the  $n$ -th MC trial,  $N = 2500$  being the number of trials. As in [90, 128], the SNR definition below is assumed:

$$\text{SNR} = 10 \log_{10} \frac{\mathbb{E} [\boldsymbol{\mu}^H \boldsymbol{\mu}]}{\mathbb{E} [\mathbf{n}^H \mathbf{n}]} = 10 \log_{10} \frac{\|\boldsymbol{\mu}\|^2}{LMPQ\sigma^2} \quad (6.43)$$

We compare the following estimation algorithms:

**NB-ALS:** standard narrowband ALS in time domain as in Chapter 4, after narrowband filtering around  $f_0$ , and simple parameter estimation: parameters are estimated by taking the identity matrix for  $\mathbf{D}$  in (6.40) and (6.41).

**WB-ALS:** Wideband (WB) preprocessing and standard ALS in frequency domain not taking into account the correlation structure of noise, and simple DoA estimation taking  $\mathbf{D} = \mathbf{I}$  in (6.40) and (6.41).

**WB-ALSCOLOR:** WB preprocessing and ALS Algorithm 6.1 for correlated noise, and simple DoA estimation taking  $\mathbf{D} = \mathbf{I}$  in (6.40) and (6.41).

**WB-W-ALSCOLOR:** WB preprocessing and ALS Algorithm 6.1 for correlated noise and weighted DoA estimation: parameters are estimated through (6.40) and (6.41) with FIM weighting  $\mathbf{D} = \mathbf{F}_r$ .

**WB-MUSIC** with covariance matrix expressed in (2.51) and, for polarized sensors, **WB Vector MUSIC** in Section 5.3.1, where the array manifold takes into account wave polarization parameters.

Notice that WB preprocessing refers to the multilinear interpolation described in Section 6.3.

### 6.6.1. Space Shift in Wideband

As described in Section 6.2.1, the same sub-array is repeated in space through  $M$  translations (cf. Figure 6.2):

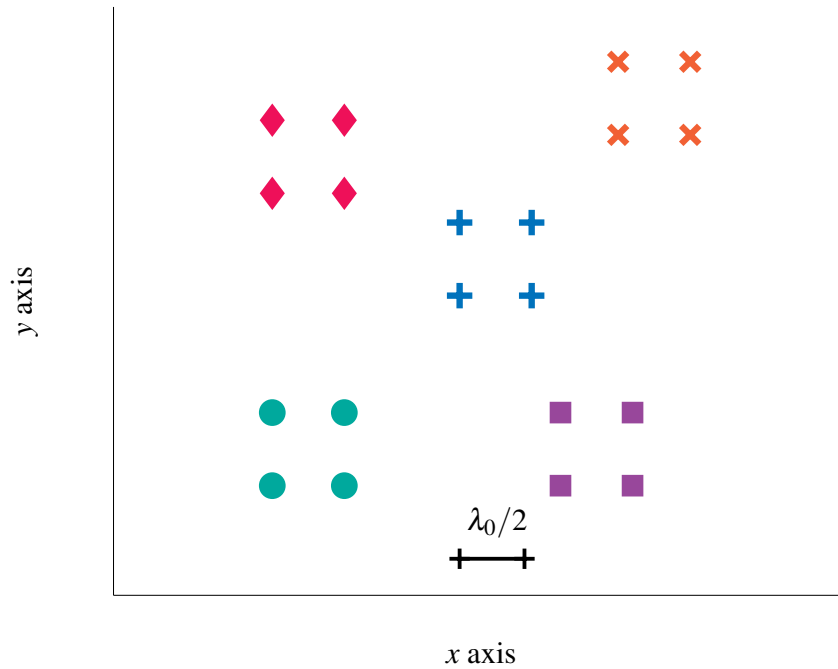


Figure 6.2.: Sensor position matrix - space shift diversity

1.  $M = 5$  sub-arrays;
2. each sub-array is a square 2D array of  $L = 4$  sensors;
3. the distance between two neighboring sensors is  $\lambda_0/2$ ;
4. the distance between two neighboring sub-arrays is  $\approx 4 * \lambda_0/2$ .

Interpolation of the data tensor is bilinear, which means it is performed for matrices  $\mathbf{A}$  and  $\mathbf{B}$  separately, as described in Section 6.3.3. Therefore, both sensor positions in  $\mathbf{P} = [\mathbf{p}_1, \dots, \mathbf{p}_L]^\top$  and space shifts in  $\mathbf{\Delta} = [\boldsymbol{\delta}_1, \dots, \boldsymbol{\delta}_M]^\top$  need to be known, and DoA can be estimated from both  $\mathbf{A}$  and  $\mathbf{B}$ , as explained in Section 4.6. On the other hand, the linear interpolation of wideband MUSIC is performed on the global  $LM \times 2$  matrix  $\mathbf{P}_{tot} = [\mathbf{p}_1 + \boldsymbol{\delta}_1, \dots, \mathbf{p}_L + \boldsymbol{\delta}_1, \dots, \mathbf{p}_1 + \boldsymbol{\delta}_M, \dots, \mathbf{p}_L + \boldsymbol{\delta}_M]^\top$  of the whole acquisition system (cf. Figure 6.2), without taking into account the bilinearity of the tensor model.

Figure 6.3 shows the dependence of the narrowband tensor CPD method, NB-ALS, on the number of available time samples,  $T$ : the MSE drastically drops for increasing data

samples, because a larger data window allows a narrowband filtering of higher quality. In what follows, we fix the number of time samples to  $T = 64$ : we expect then that narrowband tensor CPD, NB ALS, will show a saturation starting from a certain SNR.

Figure 6.4a shows the MSE on DoA estimation with respect to the SNR when  $R = 2$  uncorrelated sources arrive from angles  $\theta_1 = 5^\circ$  and  $\theta_2 = 20^\circ$ , respectively; Figure 6.4b refers to a correlation coefficient of  $\rho = 0.9$  between sources. Notice that values of correlation coefficient  $\rho$  around 0.9 are very high for wideband sources, because dissipation is different at various frequencies. In addition, this decorrelation effect is even accentuated in actual propagation media because of dispersion. Proposed ALS algorithm for correlated noise (ALSCOLOR) (*i.e.* Algorithm 6.1) significantly improves the standard ALS, since it takes into account the noise correlation structure introduced by interpolation. The reliability information contained in the FIM weighting  $\mathbf{D} = \mathbf{F}_r$  on factor vectors in (6.40) also helps the estimation performance. In the present experimental conditions, wideband tensor methods outperform both MUSIC and narrowband CPD. If the sources are correlated, the performance of all the algorithms slightly deteriorates correspondingly, and the gap w.r.t. the CRB increases (*cf.* Figure 6.4b). Further simulations showed this gap to be a monotonically increasing function of the source correlation coefficient  $\rho$ .

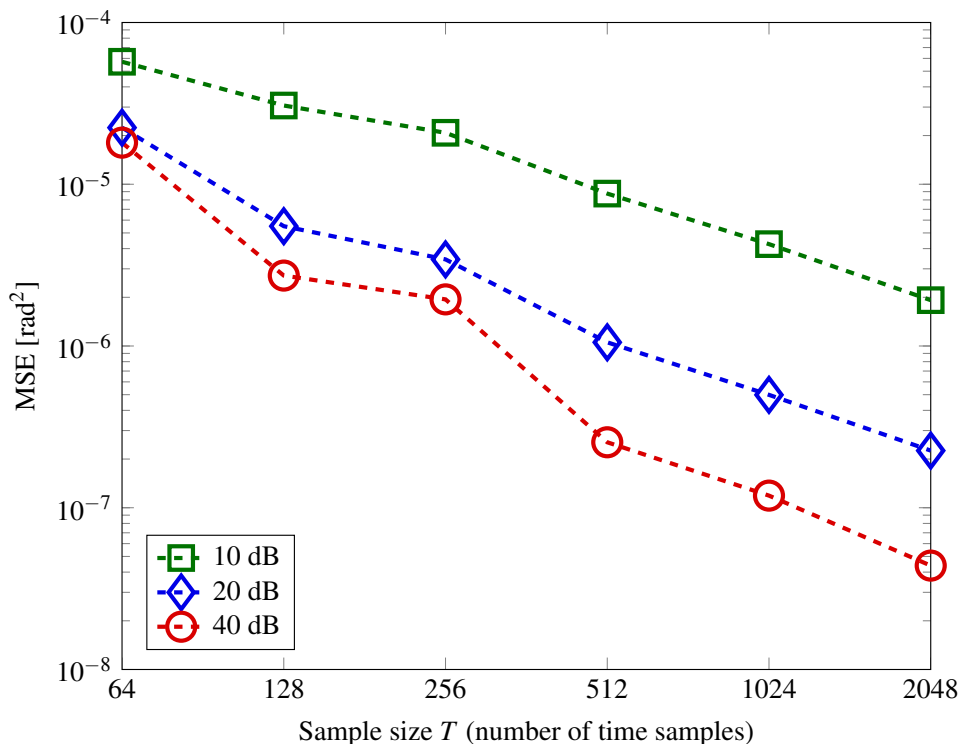
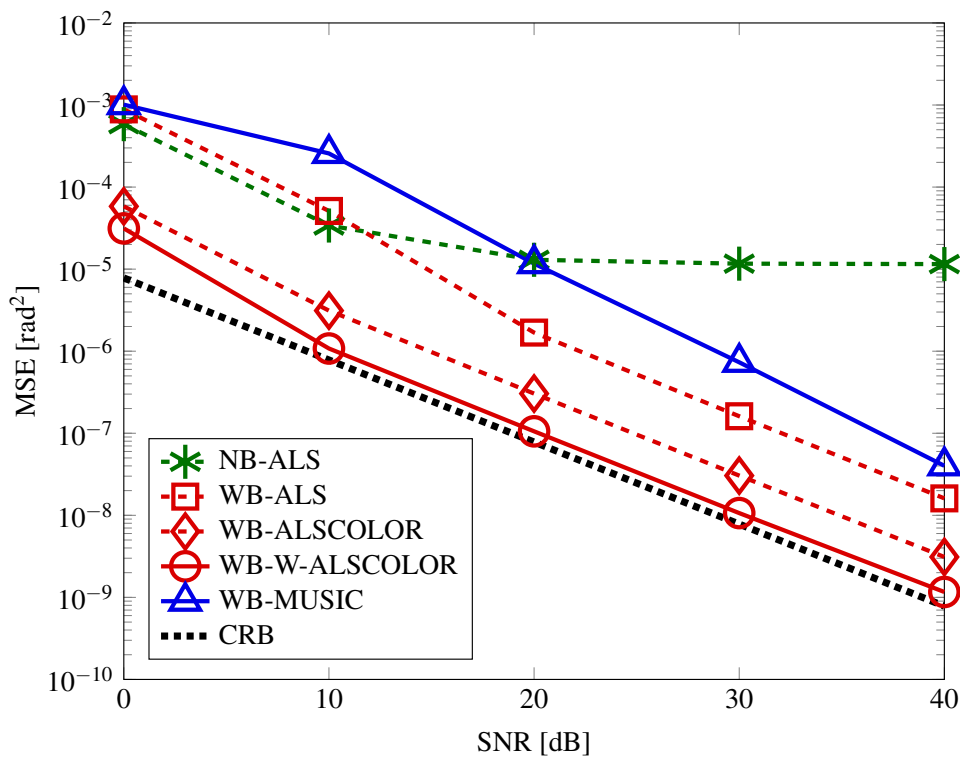


Figure 6.3.: MSE vs  $T$  - NB ALS - narrowband Tensor CP

Figure 6.5 qualitatively shows the effect that the bilinear interpolation has on the noise covariance in the present numerical experiment,  $\mathbf{\Sigma}_{(1)}$ , as described in Section 6.3.4. In particular, one can easily observe the diagonal blocks  $\mathbf{\Sigma}_q = \sigma^2 \mathbf{V}_q \mathbf{V}_q^H \boxtimes \mathbf{U}_q \mathbf{U}_q^H$ ,  $1 \leq q \leq Q = 14$ , of size  $LM = 20$  each. We can quantify the deviation of this new covariance structure from the original diagonal matrix as follows:

$$\varepsilon_{\Sigma} = \frac{\|\mathbf{\Sigma}_{(1)} - \sigma^2 \mathbf{I}_{LMQ}\|^2}{LMQ\sigma^2} = \frac{1}{Q} \sum_{q=1}^Q \frac{\|\mathbf{\Sigma}_q - \sigma^2 \mathbf{I}_{LM}\|^2}{LM\sigma^2} \quad (6.44)$$



(a) DoA estimation - Uncorrelated sources

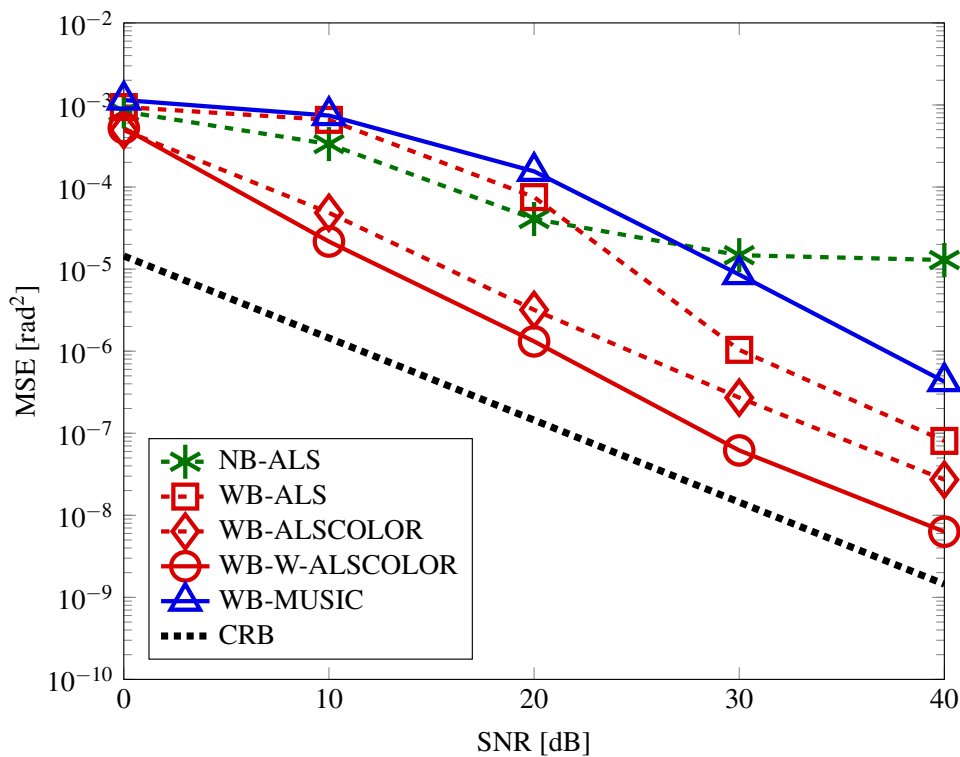
(b) DoA estimation - Correlated sources:  $\rho = 0.9$ 

Figure 6.4.: MSE vs SNR - space shift diversity

We find  $\varepsilon_{\Sigma} = 1.1121$ .

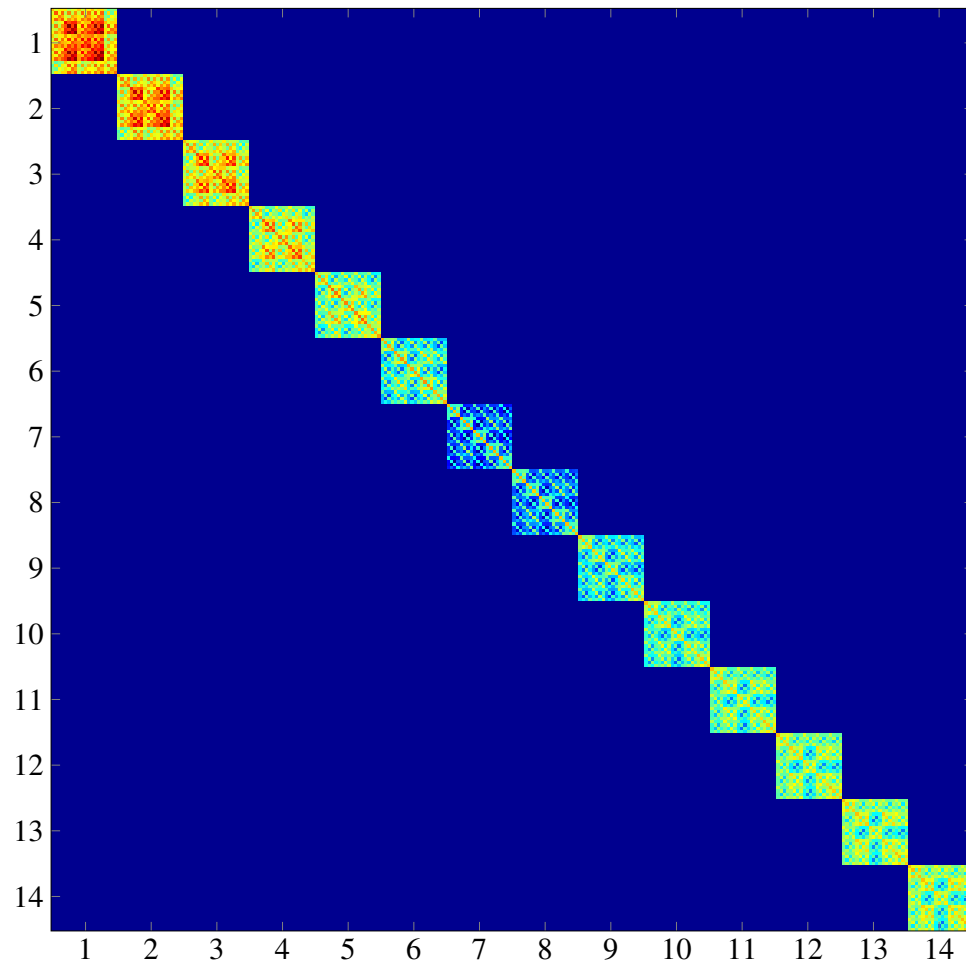


Figure 6.5.: Structure of the noise covariance matrix  $\Sigma_{(1)}$  after interpolation

### 6.6.2. Polarization in Wideband

Impinging signals are supposed to be elliptically polarized seismic sources, recorded by one 3C sensor array, or vector-sensor array, as defined in Section 1.4.2 (cf. Figure 6.6).

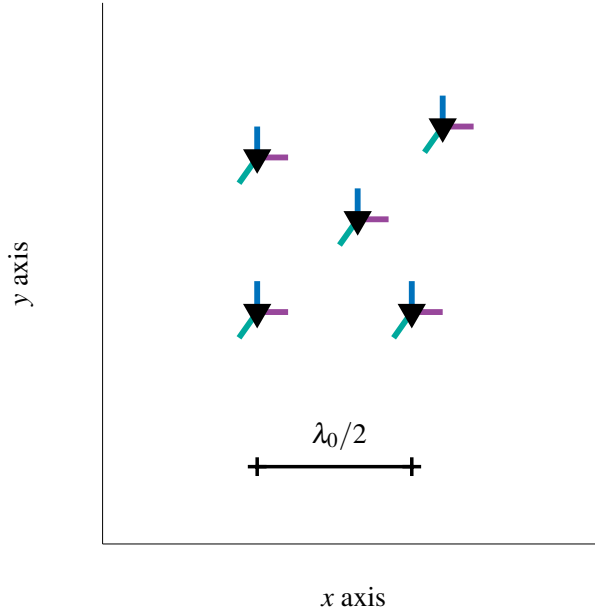


Figure 6.6.: 3C sensor position matrix - polarization diversity

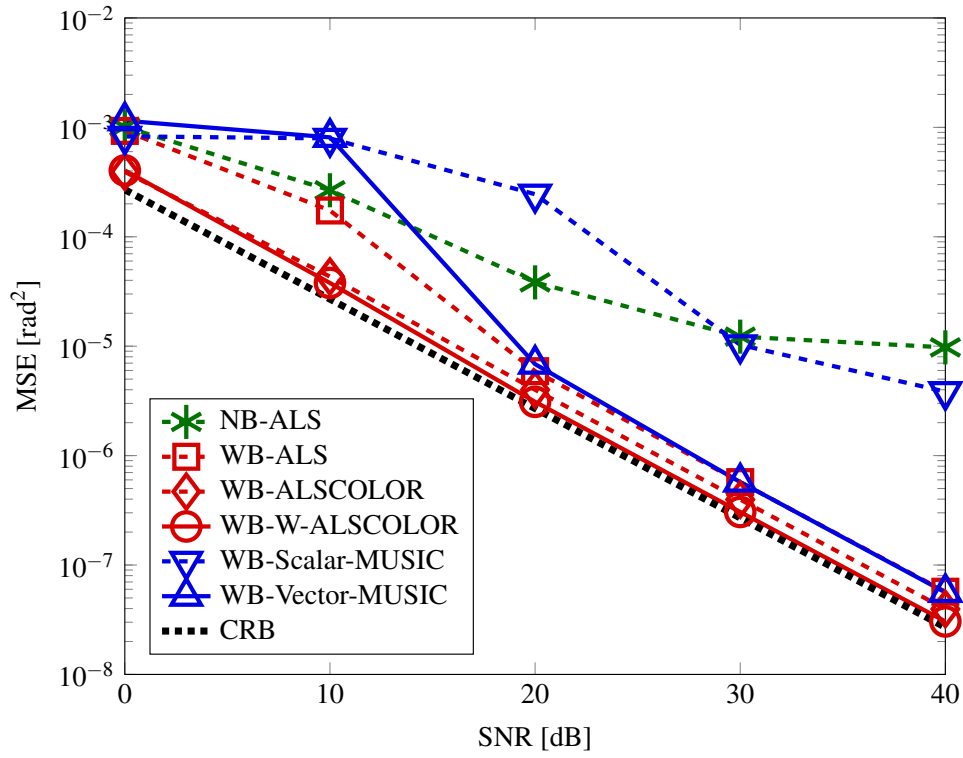
We assume:

1. an array of  $L = 5$  sensors;
2. the distance between two sensors is  $\approx \lambda_0/2$ ;
3.  $R = 2$  uncorrelated polarized sources arrive from angles  $\theta_1 = 5^\circ$  and  $\theta_2 = 20^\circ$ , respectively.
4. Rayleigh waves, *i.e.*  $\alpha = 0$ ,  $\psi = 0$  (coplanar with the array),  $\beta \neq 0$ . In particular,  $\beta_1 = -20^\circ$ ,  $\beta_2 = 10^\circ$ .

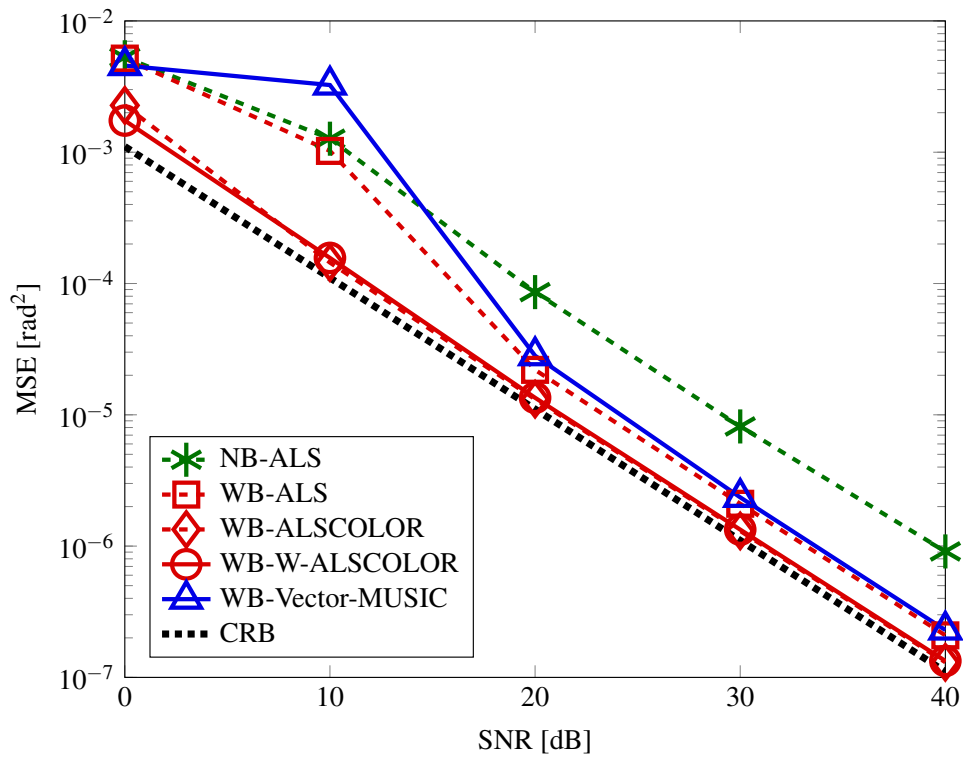
Interpolation is linear, *i.e.* only for matrix  $\mathbf{A}$ , because polarization factor matrix  $\mathbf{K}$  is independent of frequency, as described in Section 6.3.5. We compare tensor methods with **WB Scalar MUSIC**, via an incoherent average of  $P$  covariances, and **WB Vector MUSIC**, via a coherently averaged covariance matrix of size  $PL \times PL$ . Figures 6.7a and 6.7b show the MSE with respect to the SNR for DoA estimation and for polarization estimation, respectively. The overall performance of the compared algorithms is similar to the space-shift case of Section 6.6.1. However, the gain granted by FIM weighting  $\mathbf{D} = \mathbf{F}_r$  is less significant, especially for  $\beta$ .

Figure 6.8 qualitatively shows the effect that the bilinear interpolation has on the noise covariance in the present numerical experiment,  $\Sigma_{(1)}$ , as described in Section 6.3.5. In particular, one can easily observe the diagonal blocks  $\Sigma_q = \sigma^2 \mathbf{I}_P \boxtimes \mathbf{U}_q \mathbf{U}_q^H$ ,  $1 \leq q \leq Q = 14$ , of size  $LP = 15$  each. We can quantify the deviation of this new covariance structure from the original diagonal matrix as follows:

$$\varepsilon_\Sigma = \frac{\|\Sigma_{(1)} - \sigma^2 \mathbf{I}_{LPQ}\|^2}{LPQ\sigma^2} = \frac{1}{Q} \sum_{q=1}^Q \frac{\|\Sigma_q - \sigma^2 \mathbf{I}_{LP}\|^2}{LP\sigma^2} \quad (6.45)$$



(a) DoA estimation



(b) Polarization estimation

Figure 6.7.: MSE vs SNR - polarization diversity - seismic Rayleigh waves

We find  $\varepsilon_{\Sigma} = 0.2376$ .

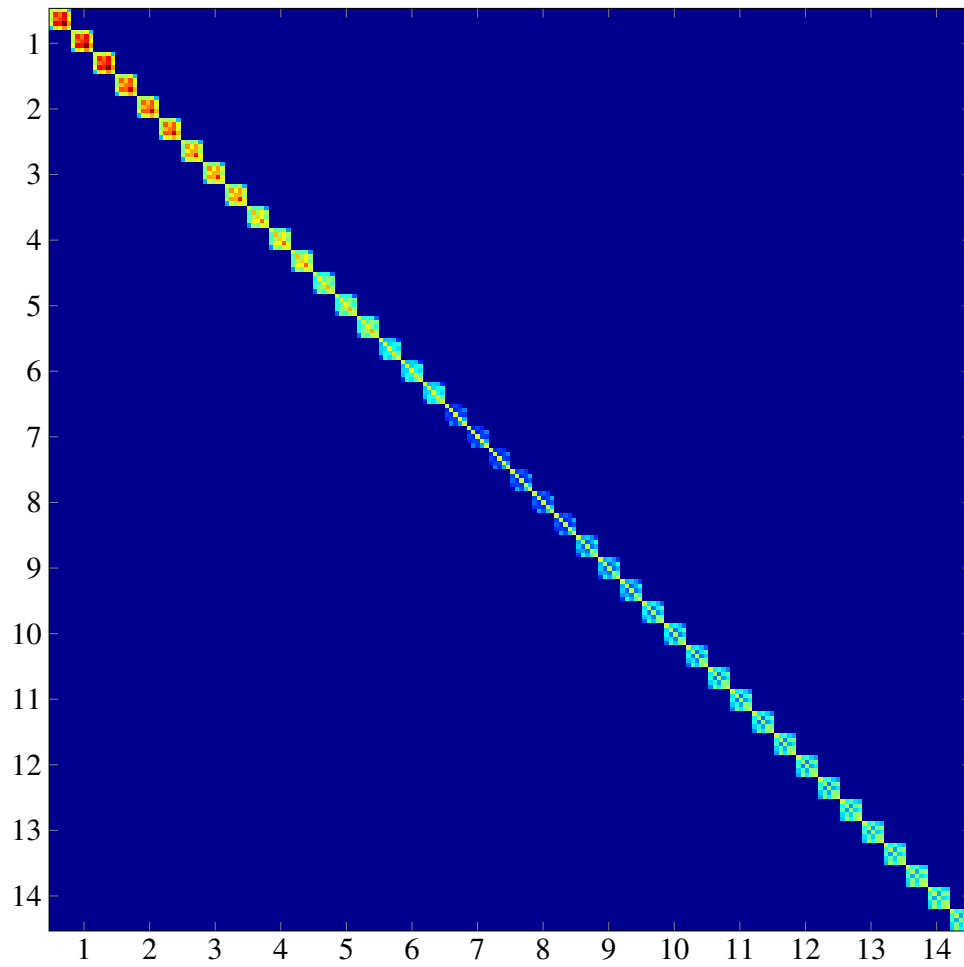


Figure 6.8.: Structure of the noise covariance matrix  $\Sigma_{(1)}$  after interpolation

## 6.7. Conclusion

The crucial difficulty of the tensor wideband approach for source estimation and localization stems from the need to focus every frequency contribution on the same subspace. We show that multilinear interpolation can solve this issue: it allows to have a multilinear model and thus to apply tensor decomposition techniques to wideband data. An important side effect is that the latter interpolation correlates the noise, which needs to be taken into account in the optimization process. In simulations, both with space shift diversity and polarization diversity, the proposed approach improves narrowband tensor processing and outperforms traditional subspace methods such as wideband MUSIC of Section 2.8. We also show that, in addition to space and frequency, polarization can be used instead of space shift diversity, even in the wideband case.



# 7. Cramér-Rao Bound for Source Estimation and Localization

## 7.1. Contribution

This chapter addresses the derivation of the Cramér-Rao Bound (CRB) for tensor DoA and polarization estimation. It refers to the general fourth order tensor model in (6.30) with multiple diversities, *i.e.* time or frequency, space and/or gain patterns, space shift and polarization. For further details about tensor CRB on factor matrices, see [149]; for details about the general CRB for multidimensional sensor arrays with space shift diversity, we refer to [90], and, for white non circular complex noise, to [128].

Our work was presented at a French conference [115] and accepted for publication with minor revisions by IEEE Transactions on Signal Processing [114].

## 7.2. Cramér-Rao Bounds

In order to assess the performance of the approaches proposed in Chapter 5 and Chapter 6, we can compare obtained estimation errors with the CRB, *e.g.* for DoA and polarization parameters. The CRB, which is the lower bound on the covariance  $\mathbf{\Gamma}$  of any unbiased estimator, is given by the inverse of the Fisher Information Matrix (FIM); in other words<sup>1</sup>,  $\mathbf{\Gamma} \succeq \mathbf{F}^{-1}$  (cf. Section 2.2 for the general definition).

The evaluation of the FIM requires the partial derivatives of the log-likelihood w.r.t. the unknown parameters,  $\boldsymbol{\vartheta}$ , given the tensor models previously described. We state the general expression of the log-likelihood in Section 7.2.1, whereas we compute its derivatives and the general expression of the FIM in Section 7.2.2.

The derivation of the CRB addresses both cases of unknown and known gain patterns. The presence of unknown anisotropic gain patterns is herein treated as a nuisance, but could be exploited as a plain diversity as shown in Section 5.4. Alternatively, if gain patterns are known, they are no longer nuisance parameters. Up to a calibration operation, this case is equivalent to assuming  $g_\ell(\theta) = 1, \forall \theta, \forall \ell$ , as in Assumption A 1.16.

### 7.2.1. Log-Likelihood

The general tensor model in additive noise for multiple diversities is given in (6.30). First, the multidimensional  $L \times M \times P \times Q$  array  $\mathcal{X}$  is stored in a vector  $\mathbf{x}$  of size  $LMPQ$ , following the bijective map:  $\mathbf{x} = \text{vec}\{\mathcal{X}\}$  of Definition 3.7. We remind that we adopt the usual definition [10] where the  $\text{vec}\{\cdot\}$  operation takes indices in lexicographical order.

---

<sup>1</sup>This inequality means that matrix  $\mathbf{\Gamma} - \mathbf{F}^{-1}$  is semi-definite positive.

Thus, applying the  $\text{vec}\{\cdot\}$  operator to equation (6.30), thanks to identity (3.10), leads to

$$\mathbf{x} = \sum_{r=1}^R \mathbf{s}_r \boxtimes \mathbf{k}_r \boxtimes \mathbf{b}_r \boxtimes \mathbf{a}_r + \mathbf{n} \quad (7.1)$$

with  $\mathbf{x} = \text{vec}\{\mathcal{X}\}$  and  $\mathbf{n} = \text{vec}\{\mathcal{N}\}$ . In narrowband, the column  $\mathbf{s}_r$  contains the time samples of the  $r$ -th source complex envelope, whereas in wideband  $\mathbf{s}_r$  refers to the Fourier coefficients of the  $r$ -th source. In both cases, we assume in this chapter that  $\mathbf{S} \in \mathbb{C}^{Q \times R}$ .

Now since the noise vector  $\mathbf{n}$  is circular Gaussian, with zero mean and covariance  $\Sigma$ , the log-likelihood then takes the form, up to a constant additive term:

$$\Upsilon(\boldsymbol{\vartheta}) = -(\mathbf{x} - \boldsymbol{\mu})^H \Sigma^{-1} (\mathbf{x} - \boldsymbol{\mu}) \quad (7.2)$$

where  $\boldsymbol{\mu} = \sum_{r=1}^R \mathbf{s}_r \boxtimes \mathbf{k}_r \boxtimes \mathbf{b}_r \boxtimes \mathbf{a}_r$ . We shall assume an isotropic *measurement* noise. However, in wideband, as we explained in Section 6.3, the noise covariance is affected by wideband interpolation so that  $\Sigma \neq \sigma^2 \mathbf{I}$ . The circularity Assumption A 1.12 could be relaxed to the price of an increased notational complexity, as in [128].

### 7.2.2. Fisher Information Matrix (FIM)

Two cases need to be distinguished, namely known and unknown gain patterns:

- 1) If gains  $g_\ell(\theta_r)$  are unknown, the  $(L-1)R$  entries  $G_{\ell r} = g_\ell(\theta_r)$ ,  $2 \leq \ell \leq L$ , are real nuisance parameters related to gain patterns in Section 5.4. For every  $r$ , we store them in a vector  $\bar{\mathbf{g}}_r$  of size  $L-1$  (as stated in Assumption A 5.1,  $g_1(\theta_r) = 1, \forall r$ ). In turn, we stack all these vectors  $\bar{\mathbf{g}}_r$  in a  $(L-1)R$ -dimensional vector denoted by  $\boldsymbol{\gamma}$ . Define then  $\mathbf{v} = [\boldsymbol{\theta}^\top, \boldsymbol{\alpha}^\top, \boldsymbol{\beta}^\top, \boldsymbol{\gamma}^\top]^\top$ , a real parameter vector of size  $R(L+2)$ .
- 2) If gains  $g_\ell(\theta_r)$  are known, define  $\mathbf{v} = [\boldsymbol{\theta}^\top, \boldsymbol{\alpha}^\top, \boldsymbol{\beta}^\top]^\top$ , a real parameter vector of size  $3R$ .

Next, define  $\boldsymbol{\xi} = [\mathbf{s}_1^\top, \dots, \mathbf{s}_R^\top]^\top$ , a complex parameter vector of size  $RQ$ . Notice that, thanks to Assumption A 4.5, source vector  $\boldsymbol{\xi}$  is deterministic. Consequently, for each source, there are three real parameters,  $\theta_r$ ,  $\alpha_r$  and  $\beta_r$ , and two complex parameters,  $\mathbf{s}_r$  and  $\mathbf{s}_r^*$ ; if gain patterns are unknown, there are  $L-1$  additional real parameters  $\bar{g}_{\ell r}$ .

When computing the FIM with respect to complex parameters, it is also necessary to include the complex conjugate parameter, in order to avoid a loss in information [65]. This means just appending  $\partial \mathbf{f} / \partial \mathbf{z}^*$ , which is nothing else but  $(\partial \mathbf{f} / \partial \mathbf{z})^*$ . Now, following [65], real and complex parameters must be treated differently. From (7.2), the FIM contains nine blocks [128]:

$$\mathbf{F} = \begin{bmatrix} 2\Re\{\mathbf{G}_{11}\} & \mathbf{G}_{12} & \mathbf{G}_{12}^* \\ \mathbf{G}_{12}^H & \mathbf{G}_{22} & \mathbf{0} \\ \mathbf{G}_{12}^\top & \mathbf{0} & \mathbf{G}_{22}^* \end{bmatrix}, \quad (7.3)$$

where  $\mathbf{G}_{11}$  is related to the real parameters, and  $\mathbf{G}_{22}$  is related to the complex ones. More precisely, blocks  $\mathbf{G}_{ij}$  are defined by:

$$\begin{aligned} \mathbf{G}_{11} &= \left( \frac{\partial \boldsymbol{\mu}}{\partial \mathbf{v}} \right)^H \Sigma^{-1} \left( \frac{\partial \boldsymbol{\mu}}{\partial \mathbf{v}} \right) \\ \mathbf{G}_{22} &= \left( \frac{\partial \boldsymbol{\mu}}{\partial \boldsymbol{\xi}} \right)^H \Sigma^{-1} \left( \frac{\partial \boldsymbol{\mu}}{\partial \boldsymbol{\xi}} \right) \\ \mathbf{G}_{12} &= \left( \frac{\partial \boldsymbol{\mu}}{\partial \mathbf{v}} \right)^H \Sigma^{-1} \left( \frac{\partial \boldsymbol{\mu}}{\partial \boldsymbol{\xi}} \right), \end{aligned}$$

where  $\Sigma$  is the covariance of noise  $\mathbf{n}$ . If all diversities are present, the total dimensions of the FIM  $\mathbf{F}$  are hence  $R(L + 2 + 2Q)$  if gain patterns are treated as nuisances, and  $R(3 + 2Q)$  if gain patterns are known. With these definitions, the covariance matrix  $\Gamma$  of any unbiased estimator of  $\boldsymbol{\vartheta} = [\mathbf{v}^\top, \boldsymbol{\xi}^\top, \boldsymbol{\xi}^H]^\top$  satisfies  $\Gamma \succeq \mathbf{F}^{-1}$ .

Note that in  $\mathbf{G}_{11}$ , we obtain the derivative w.r.t. the DoAs using the chain rule below:

$$\frac{\partial \boldsymbol{\mu}}{\partial \theta_r} = \frac{\partial \boldsymbol{\mu}}{\partial \bar{\mathbf{a}}_r} \frac{\partial \bar{\mathbf{a}}_r}{\partial \theta_r} + \frac{\partial \boldsymbol{\mu}}{\partial \bar{\mathbf{b}}_r} \frac{\partial \bar{\mathbf{b}}_r}{\partial \theta_r} + \frac{\partial \boldsymbol{\mu}}{\partial \mathbf{k}_r} \frac{\partial \mathbf{k}_r}{\partial \theta_r}. \quad (7.4)$$

The scalar factor 2 in (7.3) is justified by (7.6), because chain rules used to calculate  $\mathbf{G}_{11}$  involve complex variables when computing real derivatives. The derivatives required to evaluate (7.3) and (7.4) are given in Section 7.3.

## 7.3. Derivatives Required for the FIM

In order to evaluate the derivatives required for the computation of the FIM, and consequently of the CRB, we have to introduce the concept of complex derivatives.

### 7.3.1. Complex Derivatives

A real function of a complex variable is never holomorphic, unless it is constant [25]. It is hence necessary to specify which convention is assumed. Even if a convention has been proposed much earlier in [25], we assume the definition proposed in [65], as it is now more widely used. Let  $\mathbf{f}(\mathbf{z})$  be a real function from  $\mathbb{C}^P$  to  $\mathbb{R}^N$ . Its complex derivative with respect to  $\mathbf{z} \in \mathbb{C}^P$  is defined by

$$\frac{\partial \mathbf{f}}{\partial \mathbf{z}} = \frac{1}{2} \frac{\partial \mathbf{f}}{\partial \mathbf{x}} - \frac{j}{2} \frac{\partial \mathbf{f}}{\partial \mathbf{y}} \quad (7.5)$$

where  $\mathbf{x}$  and  $\mathbf{y}$  denote the real and imaginary parts of  $\mathbf{z}$ , respectively. This definition is consistent with [65, 128, 90]. This derivative is stored in a complex  $N \times P$  matrix, regardless of the fact that  $\mathbf{f}$  and  $\mathbf{z}$  are row or column vectors, which allows easy-writing chain rules of the form:  $\frac{\partial \mathbf{f}}{\partial \mathbf{z}} = \frac{\partial \mathbf{f}}{\partial \mathbf{a}} \frac{\partial \mathbf{a}}{\partial \mathbf{z}}$ , with compatible matrix sizes.

Next, it is often convenient to compute some derivatives by the chain rule, which means that derivatives of a complex quantity w.r.t. a complex variable are needed. It turns out that quantities involved are holomorphic, so that this differential is meant in the usual sense of complex analysis.

If a real function  $\mathbf{f}$  is to be derived w.r.t. a real variable  $\boldsymbol{\theta}$ , but using a chain rule involving a complex variable  $\mathbf{z}$ , then for consistency with (7.5) the following relation must apply [65, 128, 115]:

$$\frac{\partial \mathbf{f}}{\partial \boldsymbol{\theta}} = 2\Re \left\{ \frac{\partial \mathbf{f}}{\partial \mathbf{z}} \frac{\partial \mathbf{z}}{\partial \boldsymbol{\theta}} \right\} \quad (7.6)$$

In what follows, we calculate the derivatives required for the evaluation of the FIM in (7.3) and (7.4).

### 7.3.2. Derivatives w.r.t. $\mathbf{S}$

The matrices  $\mathbf{A}$  and  $\mathbf{B}$  depend on the DoAs  $\theta_r$ , whereas  $\mathbf{K}$  depends on angles<sup>2</sup>  $(\theta_r, \alpha_r, \beta_r)$ ,  $1 \leq r \leq R$ . Let us start with matrix  $\mathbf{S}$ , which is unconstrained. Thanks to Assumption A 4.5, the source signals are indeed treated as deterministic parameters, which allows to extract them. The derivative w.r.t  $\mathbf{s}_r$  is given by

$$\frac{\partial \boldsymbol{\mu}}{\partial \mathbf{s}_r} = \mathbf{I}_Q \boxtimes \mathbf{k}_r \boxtimes \mathbf{b}_r \boxtimes \mathbf{a}_r \in \mathbb{C}^{LMPQ \times Q} \quad (7.7)$$

### 7.3.3. Derivatives w.r.t. $\mathbf{A}$ and $\mathbf{B}$ , and their Parameters

Since the first row of  $\mathbf{A}$  and  $\mathbf{B}$  contains only ones, only the remaining rows need to be estimated. The submatrices formed of the remaining rows are denoted by  $\bar{\mathbf{A}}$  and  $\bar{\mathbf{B}}$ , and their columns by  $\bar{\mathbf{a}}_r$  and  $\bar{\mathbf{b}}_r$ , respectively. In other words,  $\bar{\mathbf{A}} = \mathbf{J}_L \mathbf{A}$ , where  $\mathbf{J}_L$  is the  $L-1 \times L$  line-selection matrix  $\mathbf{J}_L = [\mathbf{0}, \mathbf{I}_{L-1}]$ . This is necessary to reduce the size of the FIM (otherwise it would be always rank deficient).

For space steering vectors, we have

$$\frac{\partial \boldsymbol{\mu}}{\partial \bar{\mathbf{a}}_r} = \mathbf{s}_r \boxtimes \mathbf{k}_r \boxtimes \mathbf{b}_r \boxtimes \mathbf{J}_L^\top \in \mathbb{C}^{LMPQ \times L-1} \quad (7.8)$$

As in Section 7.2.2, we distinguish between two cases: unknown and known gain patterns.

#### Unknown Gain Patterns

Since functions  $g_\ell(\theta)$  are unknown, but needed only at  $R$  points  $\theta_r$ ,  $G_{\ell r} = g_\ell(\theta_r)$  are treated as extraneous fixed nuisance (unknown) parameters; this approach avoids the need for derivatives  $\partial g_\ell(\theta)/\partial \theta$ . For convenience, we denote by  $\mathbf{g}_r$  the  $L$ -dimensional vector with entries  $g_\ell(\theta_r)$ ,  $1 \leq \ell \leq L$ , and  $\bar{\mathbf{g}}_r$  the vector obtained by removing the first entry of  $\mathbf{g}_r$  (which is equal to 1 by definition, thanks to Assumption A 5.1). The following derivative can be readily obtained:

$$\frac{\partial \bar{\mathbf{a}}_r}{\partial \bar{\mathbf{g}}_r} = \mathbf{J}_L \exp\{-j\omega \boldsymbol{\tau}_r\} \mathbf{J}_L^\top \in \mathbb{C}^{L-1 \times L-1} \quad (7.9)$$

where  $\boldsymbol{\tau}_r \in \mathbb{C}^L$  is the vector containing entries  $\tau_\ell(\theta_r)$ .

#### Known Gain Patterns

In this case (7.9) is not used, as gain patterns are not nuisance parameters anymore.

In both cases, the derivative of the steering vectors with respect to DoAs is readily obtained:

$$\frac{\partial \bar{\mathbf{a}}_r}{\partial \theta_r} = -\frac{j\omega}{c} \mathbf{J}_L \left( \mathbf{g}_r \boxtimes \mathbf{P} \dot{\mathbf{d}}(\theta_r) \boxtimes \exp\{-j\omega \boldsymbol{\tau}_r\} \right) \in \mathbb{C}^{L-1} \quad (7.10)$$

where the exponential is taken entry-wise, and  $\mathbf{P}$  is the  $L \times 2$  sensor position matrix with rows  $\mathbf{p}_\ell$ . The case of known omnidirectional gain patterns is equivalent to assuming  $g_\ell(\theta) = 1, \forall \theta, \forall \ell$ .

<sup>2</sup>In a 3D space,  $\theta_r = (\phi_r, \psi_r)$ , as two angles are necessary. In a 2D space, we shall just use notation  $\theta_r$ , thanks to Assumption A 1.8.

Similarly, for space shift steering vectors we have

$$\frac{\partial \boldsymbol{\mu}}{\partial \bar{\mathbf{b}}_r} = \mathbf{s}_r \boxtimes \mathbf{k}_r \boxtimes \mathbf{J}_M^\top \boxtimes \mathbf{a}_r \in \mathbb{C}^{LMPQ \times M-1} \quad (7.11)$$

The following derivative is readily obtained:

$$\frac{\partial \bar{\mathbf{b}}_r}{\partial \theta_r} = -\frac{j\omega}{c} \mathbf{J}_M \left( \boldsymbol{\Delta} \dot{\mathbf{d}}(\theta_r) \boxtimes \exp\{-j\omega \boldsymbol{\zeta}_r\} \right) \in \mathbb{C}^{M-1} \quad (7.12)$$

where  $\boldsymbol{\zeta}_r \in \mathbb{C}^M$  is the vector containing entries  $\zeta_m(\theta_r)$ , and  $\boldsymbol{\Delta}$  is the  $M \times 2$  subarray position matrix with rows  $\boldsymbol{\delta}_m$ .

### The Case of Pattern Diversity

If time, space shift and gain pattern diversities are available, as in Section 5.4, but not space and polarization, then expressions are simpler. It is worth detailing this scenario because it has not been reported in the literature. In this case, matrix  $\mathbf{A}$  only contains gains  $G_{\ell_r}$  and matrix  $\mathbf{B}$  only contains delays  $\zeta_m(\theta_r)$ , and one can prove that

$$\begin{aligned} \left( \frac{\partial \boldsymbol{\mu}}{\partial \mathbf{s}_r} \right)^\text{H} \left( \frac{\partial \boldsymbol{\mu}}{\partial \mathbf{s}_k} \right) &= (\mathbf{b}_r^\text{H} \mathbf{b}_k) (\mathbf{a}_r^\text{H} \mathbf{a}_k) \mathbf{I}_Q \\ \left( \frac{\partial \boldsymbol{\mu}}{\partial \mathbf{a}_r} \right)^\text{H} \left( \frac{\partial \boldsymbol{\mu}}{\partial \mathbf{a}_k} \right) &= (\mathbf{s}_r^\text{H} \mathbf{s}_k) (\mathbf{b}_r^\text{H} \mathbf{b}_k) \mathbf{I}_L \\ \left( \frac{\partial \boldsymbol{\mu}}{\partial \theta_r} \right)^\text{H} \left( \frac{\partial \boldsymbol{\mu}}{\partial \theta_k} \right) &= \omega^2 (\mathbf{s}_r^\text{H} \mathbf{s}_k) (\mathbf{a}_r^\text{H} \mathbf{a}_k) (\mathbf{b}_r^* \boxtimes \mathbf{b}_k)^\text{T} (\dot{\boldsymbol{\zeta}}_r \boxtimes \dot{\boldsymbol{\zeta}}_k) \end{aligned} \quad (7.13)$$

The effects of anisotropic gain patterns was addressed in more detail in Section 5.4.

#### 7.3.4. Derivatives w.r.t. $\mathbf{K}$ and its Parameters

From (7.1) and (6.7), we have [115]

$$\begin{aligned} \frac{\partial \boldsymbol{\mu}}{\partial \mathbf{k}_r} &= \mathbf{s}_r \boxtimes \mathbf{I}_3 \boxtimes \mathbf{b}_r \boxtimes \mathbf{a}_r \\ \frac{\partial \boldsymbol{\mu}}{\partial \alpha_r} &= \mathbf{s}_r \boxtimes \frac{\partial \mathbf{k}_r}{\partial \alpha_r} \boxtimes \mathbf{b}_r \boxtimes \mathbf{a}_r \\ \frac{\partial \boldsymbol{\mu}}{\partial \beta_r} &= \mathbf{s}_r \boxtimes \frac{\partial \mathbf{k}_r}{\partial \beta_r} \boxtimes \mathbf{b}_r \boxtimes \mathbf{a}_r \end{aligned} \quad (7.14)$$

### TGR Waves

For Tilted Generalized Rayleigh (TGR) waves (cf. (1.35) in Section 1.4), partial derivatives are given by

$$\begin{aligned}\frac{\partial \mathbf{k}_r}{\partial \theta_r} &= \begin{bmatrix} -\sin \theta_r \cos \psi_r & \sin \theta_r \sin \psi_r \\ \cos \theta_r \cos \psi_r & -\cos \theta_r \sin \psi_r \\ 0 & 0 \end{bmatrix} \mathbf{W}(\alpha_r) \mathbf{w}(\beta_r) \\ \frac{\partial \mathbf{k}_r}{\partial \psi_r} &= \begin{bmatrix} -\cos \theta_r \sin \psi_r & -\cos \theta_r \cos \psi_r \\ -\sin \theta_r \sin \psi_r & -\sin \theta_r \cos \psi_r \\ \cos \psi_r & -\sin \psi_r \end{bmatrix} \mathbf{W}(\alpha_r) \mathbf{w}(\beta_r) \\ \frac{\partial \mathbf{k}_r}{\partial \alpha_r} &= \mathbf{H}_{TGR}(\theta_r) \begin{bmatrix} -\sin \alpha_r & \cos \alpha_r \\ -\cos \alpha_r & -\sin \alpha_r \end{bmatrix} \mathbf{w}(\beta_r) \\ \frac{\partial \mathbf{k}_r}{\partial \beta_r} &= \mathbf{H}_{TGR}(\theta_r) \mathbf{W}(\alpha_r) \begin{bmatrix} -\sin \beta_r \\ j \cos \beta_r \end{bmatrix}\end{aligned}$$

In the 2D case when elevation  $\psi = 0$ , we have

$$\frac{\partial \mathbf{k}_r}{\partial \theta_r} = \begin{bmatrix} -\sin \theta_r & 0 \\ \cos \theta_r & 0 \\ 0 & 0 \end{bmatrix} \mathbf{W}(\alpha_r) \mathbf{w}(\beta_r) \quad (7.15)$$

### TR Waves

For Transverse (TR) waves (cf. (1.34) in Section 1.4), partial derivatives are given by

$$\begin{aligned}\frac{\partial \mathbf{k}_r}{\partial \theta_r} &= \begin{bmatrix} \cos \theta_r & \sin \theta_r \sin \psi_r \\ -\sin \theta_r & -\cos \theta_r \sin \psi_r \\ 0 & 0 \end{bmatrix} \mathbf{W}(\alpha_r) \mathbf{w}(\beta_r) \\ \frac{\partial \mathbf{k}_r}{\partial \psi_r} &= \begin{bmatrix} 0 & -\cos \theta_r \cos \psi_r \\ 0 & -\sin \theta_r \cos \psi_r \\ 0 & -\sin \psi_r \end{bmatrix} \mathbf{W}(\alpha_r) \mathbf{w}(\beta_r) \\ \frac{\partial \mathbf{k}_r}{\partial \alpha_r} &= \mathbf{H}_{TR}(\theta_r) \begin{bmatrix} -\sin \alpha_r & \cos \alpha_r \\ -\cos \alpha_r & -\sin \alpha_r \end{bmatrix} \mathbf{w}(\beta_r) \\ \frac{\partial \mathbf{k}_r}{\partial \beta_r} &= \mathbf{H}_{TR}(\theta_r) \mathbf{W}(\alpha_r) \begin{bmatrix} -\sin \beta_r \\ j \cos \beta_r \end{bmatrix}\end{aligned}$$

In the 2D case when elevation  $\psi = 0$ , we have

$$\frac{\partial \mathbf{k}_r}{\partial \theta_r} = \begin{bmatrix} \cos \theta_r & 0 \\ -\sin \theta_r & 0 \\ 0 & 0 \end{bmatrix} \mathbf{W}(\alpha_r) \mathbf{w}(\beta_r) \quad (7.16)$$

## 7.4. Interpolation errors

Notice that as for the wideband model in frequency domain, the CRBs derived in this chapter refer to the interpolated model in (6.25) and (6.27). These bounds then represent a good approximation if the interpolation bias and errors are negligible compared to additive measurement noise.

However, if this is not the case, the interpolation bias and errors should be taken into account, in the same spirit as [70, 71]. Alternatively, the CRB of the original model in (6.9) before interpolation should be derived. Model (6.9) can be rewritten in tensor form as

$$\mathcal{M}(\omega_q) = \sum_{r=1}^R \mathbf{a}_r(\omega_q) \otimes \mathbf{b}_r(\omega_q) \otimes \mathbf{k}_r S_{qr}, \quad 1 \leq q \leq Q \quad (7.17)$$

or in vector form as  $\boldsymbol{\mu}(\omega_q) = \text{vec}\{\mathcal{M}(\omega_q)\}$ :

$$\boldsymbol{\mu}(\omega_q) = \sum_{r=1}^R \mathbf{k}_r \boxtimes \mathbf{b}_r(\omega_q) \boxtimes \mathbf{a}_r(\omega_q) S_{qr}, \quad 1 \leq q \leq Q \quad (7.18)$$

Hence, since the frequency slices are independent from one another, the resulting log-likelihood is the sum of  $Q$  individual contributions (up to an additive constant):

$$\Upsilon(\boldsymbol{\vartheta}) = - \sum_{q=1}^Q [\mathbf{x}(\omega_q) - \boldsymbol{\mu}(\omega_q)]^H \boldsymbol{\Sigma}^{-1} [\mathbf{x}(\omega_q) - \boldsymbol{\mu}(\omega_q)] \quad (7.19)$$

where  $\mathbf{x}(\omega_q) = \text{vec}\{\mathcal{X}(\omega_q)\}$ ,  $1 \leq q \leq Q$ , are the vectorized frontal slices of the data tensor.



# 8. Tensor Wideband Estimation through Spatial Resampling

## 8.1. Contribution

This chapter aims at achieving a tensor method for wideband source estimation and localization through spatial resampling.

The core of Chapter 6 lay in the combination of several elements: introduction of the frequency diversity into the tensor model, a coherent preprocessing through focusing matrices of each narrow band so as to align (focus) their respective contributions, and finally a joint tensor processing leading to the estimation of DoA and polarization angles. However, this approach needs a prior knowledge of relevant angular sectors, through a former BF technique (as explained in Sections 2.8.2 and 6.3.2).

We saw in Section 2.8.3 that, when the array has a regular structure such as a ULA, spatial interpolation can replace the linear transformations of Section 2.8.2, with no need for a division of the angular range into sectors. Similarly, this chapter intends to solve the focusing operation for wideband tensor processing through spatial interpolation of regular arrays, such as ULAs and rectangular arrays, which are widespread in many applications [151].

Similarly to Chapter 6, space shift and polarization diversities are the subjects of Sections 8.2 and 8.3, respectively. The bilinear interpolation of the data tensor in Section 6.3.2 is replaced by a spatial resampling, thus allowing us to simultaneously scan the whole angular range, with no need for its division into angular sectors. Section 8.4 describes the estimation of signal parameters, whereas Section 8.5 presents results based on computer simulations.

This chapter further develops the main idea of our 2016 ICASSP paper [119], which was also source of inspiration for another 2017 ICASSP paper on MIMO radars and telecommunications [163].

## 8.2. Space Shift Diversity in Wideband

We rewrite the model in (6.1) for space and space shift in frequency domain with omnidirectional sensors:

$$M_{\ell m}(\omega) = \sum_{r=1}^R A_{\ell r}(\omega) B_{mr}(\omega) s_r(\omega)$$

with

$$\begin{cases} X_{\ell m}(\omega) &= \mathcal{F}\{X_{\ell m}(t)\} \\ A_{\ell r}(\omega) &= e^{-j\omega\tau_{\ell}(\theta_r)} \\ B_{mr}(\omega) &= e^{-j\omega\zeta_m(\theta_r)} \\ s_r(\omega) &= \mathcal{F}\{s_r(t)\} \end{cases} \quad (8.1)$$

where  $\tau_\ell(\theta) + \zeta_m(\theta) = \mathbf{p}_\ell^\top \mathbf{d}(\theta)/c + \boldsymbol{\delta}_m^\top \mathbf{d}(\theta)/c$  is the delay of arrival on sensor  $\ell$  of subarray  $m$ , with  $\mathbf{p}_\ell$  the location of the  $\ell$ -th sensor and  $\boldsymbol{\delta}_m$  the location of the  $m$ -th subarray (cf. (4.6)). In Section 6.3.1, the wideband preprocessing operation consists in interpolating received data at virtual positions corresponding to virtual sensors and subarrays:

$$\tilde{\mathbf{p}}_\ell(\omega_q) = \frac{\omega_0}{\omega_q} \mathbf{p}_\ell, \quad \tilde{\boldsymbol{\delta}}_m(\omega_q) = \frac{\omega_0}{\omega_q} \boldsymbol{\delta}_m \quad (8.2)$$

We refer to Section 2.8.3 for spatial resampling for wideband DoA estimation using the MUSIC and ESPRIT algorithms, whereas we refer to Section 1.2.3 for generalities on the array geometry. We shall now extend Section 2.8.3 to separable array configurations (embodying space shift diversity), and to 3C sensors (embodying polarization diversity), for regular linear and planar array geometries.

### 8.2.1. Linear Arrays

If the array is linear as in Figure 8.1, the delay at one of its elements becomes

$$\tau_\ell(\theta) + \zeta_m(\theta) = p_\ell \cos \theta / c + \delta_m \cos \theta / c \quad (8.3)$$

From (8.2), we deduce that spatial interpolation involves the following virtual positions:

$$(\tilde{p}_\ell + \tilde{\delta}_m)(\omega) = \frac{\omega_0}{\omega} (p_\ell + \delta_m) \quad (8.4)$$



Figure 8.1.: Example of linear acquisition system

In this case, we can perform a unique 1D spatial interpolation on the whole linear array of  $LM$  sensors, from nominal positions  $\mathbf{p}_{tot}$  to virtual positions  $\tilde{\mathbf{p}}_{tot}(\omega)$ :

$$\begin{cases} \mathbf{p}_{tot} = [p_1 + \delta_1, \dots, p_L + \delta_1, \dots, p_1 + \delta_M, \dots, p_L + \delta_M]^\top \\ \tilde{\mathbf{p}}_{tot}(\omega) = [(\tilde{p}_1 + \tilde{\delta}_1)(\omega), \dots, (\tilde{p}_L + \tilde{\delta}_1)(\omega), \dots, (\tilde{p}_1 + \tilde{\delta}_M)(\omega), \dots, (\tilde{p}_L + \tilde{\delta}_M)(\omega)]^\top \end{cases} \quad (8.5)$$

Since, in general, the linear structure of this array is non uniform, we should rely on non uniform interpolation techniques. However, we shall just detail two common cases, which only require a simple uniform interpolation.

#### Uniform Sensor and Subarray Spacing

If the separable structure of the acquisition system is uniform at the sensor level and at the subarray level, as in Figure 8.2, we can apply a uniform interpolation to both scales independently.



Figure 8.2.: Example of uniform linear acquisition system

In this case, nominal positions are given by  $p_\ell = (\ell - 1)p_0$  and  $\delta_m = (m - 1)\delta_0$ , whereas virtual positions can be derived independently through two 1D uniform interpolators:

$$\begin{cases} \tilde{p}_\ell(\omega) = (\ell - 1)\tilde{p}_0(\omega), & \text{with } \tilde{p}_0(\omega) = \frac{\omega_0}{\omega} p_0 \\ \tilde{\delta}_m(\omega) = (m - 1)\tilde{\delta}_0(\omega), & \text{with } \tilde{\delta}_0(\omega) = \frac{\omega_0}{\omega} \delta_0 \end{cases} \quad (8.6)$$

### Long ULA

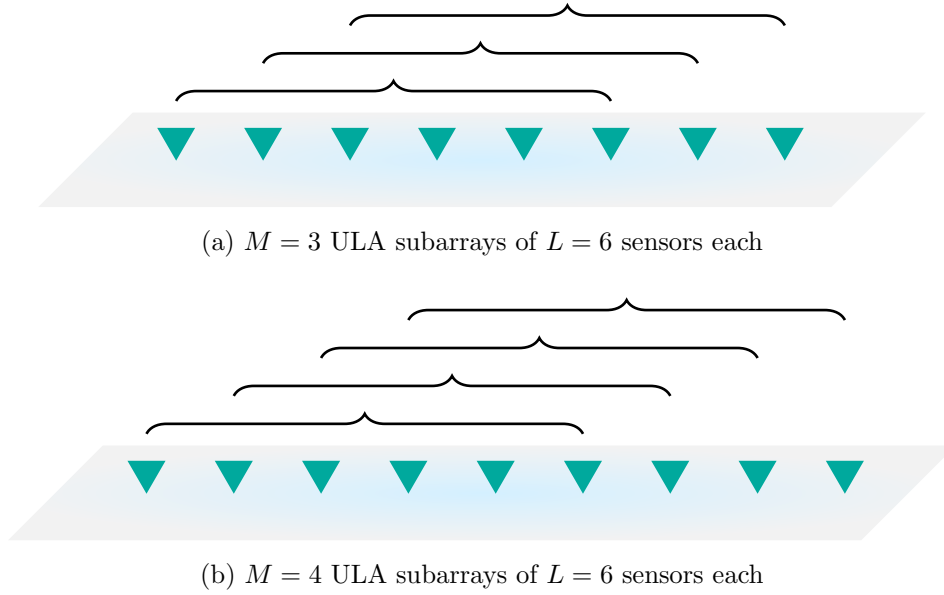


Figure 8.3.: Example of Long ULA

If the global array is a ULA, as in Figures 8.3a and 8.3b, global positions are given by  $p_\ell = (\ell - 1)p_0$ ,  $1 \leq \ell \leq L_{tot}$ , whereas 1D virtual positions become

$$\tilde{p}_\ell(\omega) = (\ell - 1)\tilde{p}_0(\omega), \quad 1 \leq \ell \leq L_{tot}, \quad \text{with} \quad \tilde{p}_0(\omega) = \frac{\omega_0}{\omega} p_0 \quad (8.7)$$

We can then achieve a global uniform interpolation of the long array  $\mathbf{p}_{tot}$ . In our simulations in Section 8.5, we shall choose this global ULA configuration. Indeed, if the long array is a ULA of  $L_{tot} = L + M - 1$  sensors, it can be considered as the combination of  $M$  displaced subarrays of  $L$  sensors each. Similarly to Section 2.8.3, we need to state one spatial sampling condition on inter-sensor spacing,  $p_0 \leq \lambda_0/2$ , and another on inter-subarray spacing,  $\delta_0 \leq \lambda_0/2$ .

#### 8.2.2. Planar Arrays

If the array is planar, as in Figure 8.4, thanks to Assumption A 1.8, the delay at one of its elements becomes

$$\tau_\ell(\theta) + \zeta_m(\theta) = p_\ell^x \cos \theta / c + p_\ell^y \sin \theta / c + \delta_m^x \cos \theta / c + \delta_m^y \sin \theta / c \quad (8.8)$$

From (8.2) we derive

$$\begin{cases} (\tilde{p}_\ell^x + \tilde{\delta}_m^x)(\omega) = \frac{\omega_0}{\omega} (p_\ell^x + \delta_m^x) \\ (\tilde{p}_\ell^y + \tilde{\delta}_m^y)(\omega) = \frac{\omega_0}{\omega} (p_\ell^y + \delta_m^y) \end{cases} \quad (8.9)$$

Thus, in order to perform the alignment of a planar array, a  $2D$  non uniform spatial interpolation is required. This can be achieved through two independent non uniform 1D interpolators.

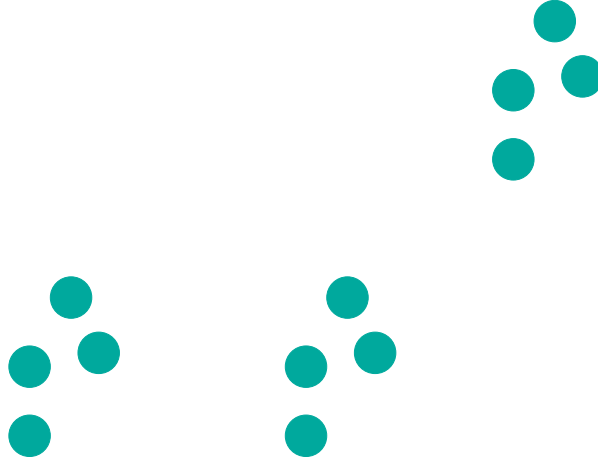


Figure 8.4.: Example of planar acquisition system

### Long URA

If the global array is a URA, as in Figure 8.5, nominal positions are given by  $p_\ell^x = (\ell^x - 1)p_0^x$ ,  $1 \leq \ell^x \leq L_{tot}^x$  and  $p_\ell^y = (\ell^y - 1)p_0^y$ ,  $1 \leq \ell^y \leq L_{tot}^y$ , whereas virtual positions can be derived independently through two uniform interpolators:

$$\begin{cases} \tilde{p}_\ell^x(\omega) = (\ell^x - 1)\tilde{p}_0^x(\omega), & 1 \leq \ell^x \leq L_{tot}^x, & \text{with } \tilde{p}_0^x(\omega) = \frac{\omega_0}{\omega} p_0^x \\ \tilde{p}_\ell^y(\omega) = (\ell^y - 1)\tilde{p}_0^y(\omega), & 1 \leq \ell^y \leq L_{tot}^y, & \text{with } \tilde{p}_0^y(\omega) = \frac{\omega_0}{\omega} p_0^y \end{cases} \quad (8.10)$$

In this case, the global array of  $L_{tot}^x \times L_{tot}^y = (L^x + M^x - 1) \times (L^y + M^y - 1)$  sensors can be seen as the combination of  $M^x + M^y$  subarrays of  $L^x \times L^y$  sensors each. Similarly to Section 2.8.3, we need to impose two spatial sampling conditions on inter-sensor spacing:  $p_0^x \leq \frac{\lambda_0}{2}$  and  $p_0^y \leq \frac{\lambda_0}{2}$ .

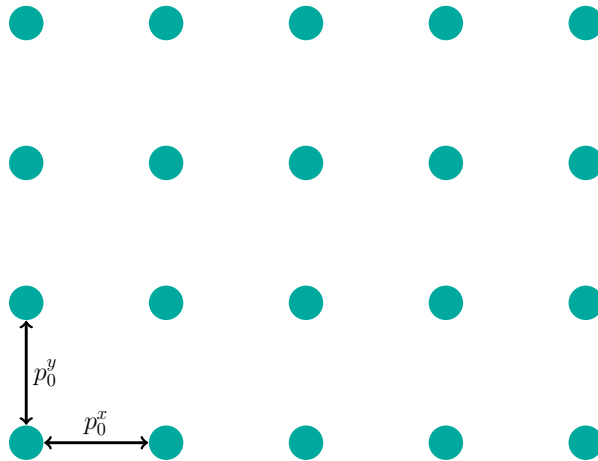


Figure 8.5.: Example of Long URA

### 8.2.3. Tensor Resampling

After discretization, model (8.1) becomes

$$M_{\ell m}(\omega_q) = \sum_{r=1}^R A_{\ell r}(\omega_q) B_{mr}(\omega_q) S_{qr}, \quad 1 \leq q \leq Q \quad (8.11)$$

For each  $q$ -th frequency bin, we need to interpolate the  $q$ -th row of the mode-3 unfolding of the data tensor  $\mathcal{X}$ ,

$$\mathbf{X}_{(3)q} = \mathbf{s}_q: [\mathbf{B}(\omega_q) \odot \mathbf{A}(\omega_q)]^\top + \mathbf{N}_{(3)q} \in \mathbb{C}^{1 \times LM} \quad (8.12)$$

at positions  $\tilde{\mathbf{p}}_{tot}(\omega_q) = \mathbf{p}_{tot} \frac{\omega_0}{\omega_q}$ . Thanks to (8.2), interpolated slices write

$$\tilde{\mathbf{X}}_{(3)q} \approx \mathbf{s}_q: [\tilde{\mathbf{B}}(\omega_0) \odot \tilde{\mathbf{A}}(\omega_0)]^\top + \tilde{\mathbf{N}}_{(3)q} \in \mathbb{C}^{1 \times LM} \quad (8.13)$$

We then recompose the interpolated tensor unfolding  $\tilde{\mathbf{X}}_{(3)}$ , by stacking all the interpolated rows  $\tilde{\mathbf{X}}_{(3)q}$ . This unfolding corresponds to a tensor

$$\begin{cases} \tilde{\mathcal{M}} \approx \sum_{r=1}^R \tilde{\mathbf{a}}_r(\omega_0) \otimes \tilde{\mathbf{b}}_r(\omega_0) \otimes \mathbf{s}_r \\ \mathcal{M}_{\ell m q} \approx \sum_{r=1}^R \tilde{A}_{\ell r}(\omega_0) \tilde{B}_{mr}(\omega_0) S_{qr} \end{cases} \quad (8.14)$$

We choose to study the simplest configuration of a ULA of  $L$  sensors, with  $M$  linear translations, as in Section 8.2.1. However, all that follows can be generalized to the planar arrays through 2D spatial interpolation.

After 1D sinc spatial interpolation as described in Section 8.2.1, the factor matrices of resulting tensor  $\mathcal{X}$  are given by

1.  $\tilde{A}_{\ell r} = \exp \left\{ -j \frac{1}{c} \omega_0 p_0 (\ell - 1) \cos(\theta_r) \right\}$  is the steering element of the  $\ell$ -th sensor.
2.  $\tilde{B}_{mr} = \exp \left\{ -j \frac{1}{c} \omega_0 p_0 (m - 1) \cos(\theta_r) \right\}$  is the steering element of the  $m$ -th subarray.
3.  $S_{qr} = s_r(\omega_q)$  is the  $q$ -th Fourier Transform (FT) coefficient of the  $r$ -th signal.

We remind that the distance  $p_0$  between two successive sensors must be less than or equal to  $\lambda_0/2$ , so as to avoid spatial aliasing.

## 8.3. Polarization Diversity in Wideband

On the other hand, we rewrite the model (6.4) for polarization diversity:

$$M_{\ell p}(\omega) = \sum_{r=1}^R A_{\ell r}(\omega) K_{pr} s_r(\omega), \quad 1 \leq p \leq P = 3 \quad (8.15)$$

where polarization vectors  $\mathbf{k}_r$  are defined in (6.5). In this case, as described in Section 6.3.5, since polarization matrix  $\mathbf{K}$  does not depend on frequency  $\omega$ , only space matrix  $\mathbf{A}(\omega)$  needs to be interpolated at sensor positions

$$\tilde{\mathbf{p}}_\ell(\omega_q) = \frac{\omega_0}{\omega_q} \mathbf{p}_\ell \quad (8.16)$$

Thus, for regular configurations, the required interpolation is simpler:

1. For a linear array of  $L$  sensors located at  $p_\ell$ , (8.16) becomes

$$\tilde{p}_\ell(\omega) = \frac{\omega_0}{\omega} p_\ell \quad (8.17)$$

Spatial resampling can then be achieved through a 1D non uniform interpolator.

2. For a ULA of  $L$  sensors located at  $p_\ell = (\ell - 1)p_0$ , (8.16) becomes

$$\tilde{p}_\ell(\omega) = (\ell - 1)\tilde{p}_0(\omega), \quad \text{with} \quad \tilde{p}_0(\omega) = \frac{\omega_0}{\omega} p_0 \quad (8.18)$$

as described in Section 2.8.3. Spatial resampling can then be achieved through a 1D uniform interpolator.

3. For a planar array of  $L$  sensors located at  $(p_\ell^x, p_\ell^y)$ , (8.16) becomes

$$\begin{cases} \tilde{p}_\ell^x(\omega_q) = \frac{\omega_0}{\omega_q} p_\ell^x \\ \tilde{p}_\ell^y(\omega_q) = \frac{\omega_0}{\omega_q} p_\ell^y \end{cases} \quad (8.19)$$

Spatial resampling can then be achieved through two independent 1D non uniform interpolators.

4. For a URA of  $L_x \times L_y$  sensors, with nominal positions given by  $p_\ell^x = (\ell^x - 1)p_0^x$  and  $p_\ell^y = (\ell^y - 1)p_0^y$ , (8.16) becomes

$$\begin{cases} \tilde{p}_\ell^x(\omega) = (\ell^x - 1)\tilde{p}_0^x(\omega), & \text{with} \quad \tilde{p}_0^x(\omega) = \frac{\omega_0}{\omega} p_0^x \\ \tilde{p}_\ell^y(\omega) = (\ell^y - 1)\tilde{p}_0^y(\omega), & \text{with} \quad \tilde{p}_0^y(\omega) = \frac{\omega_0}{\omega} p_0^y \end{cases} \quad (8.20)$$

Spatial resampling can then be achieved through two independent 1D uniform interpolators.

### 8.3.1. Tensor Resampling

After discretization, model (8.15) becomes

$$M_{\ell p}(\omega_q) = \sum_{r=1}^R A_{\ell r}(\omega_q) K_{pr} S_{qr}, \quad 1 \leq q \leq Q \quad (8.21)$$

For each  $q$ -th frequency bin, we need to interpolate all the  $P = 3$  fibers of data tensor  $\mathcal{X}$ :

$$\mathbf{x}_{:pq} = \mathbf{A} \mathbf{D}_k(\mathbf{s}_q) \mathbf{k}_p^\top + \mathbf{n}_{:pq} \in \mathbb{C}^L, \quad p = 1, \dots, 3 \quad (8.22)$$

at positions  $\tilde{\mathbf{p}}(\omega_q) = \mathbf{p} \frac{\omega_0}{\omega_q}$ , given by (8.16). Then, interpolated fibers write

$$\tilde{\mathbf{x}}_{:pq} = \tilde{\mathbf{A}}(\omega_0) \mathbf{D}_k(\mathbf{s}_q) \mathbf{k}_p^\top + \tilde{\mathbf{n}}_{:pq} \in \mathbb{C}^L, \quad p = 1, \dots, 3 \quad (8.23)$$

We then recompose the interpolated tensor  $\tilde{\mathcal{X}}$ , by stacking all the interpolated fibers  $\tilde{\mathbf{x}}_{:pq}$ , leading to the trilinear model

$$\begin{cases} \tilde{\mathcal{M}} \approx \sum_{r=1}^R \tilde{\mathbf{a}}_r(\omega_0) \otimes \mathbf{k}_r \otimes \mathbf{s}_r \\ \mathcal{M}_{\ell pq} \approx \sum_{r=1}^R \tilde{A}_{\ell r}(\omega_0) K_{pr} S_{qr}, \quad p = 1, \dots, 3 \end{cases} \quad (8.24)$$

For a ULA of  $L$  sensors, after 1D spatial interpolation of tensor fibers  $\mathbf{x}_{:pq}$  as described in Section 2.8.3, the factor matrices of resulting tensor  $\tilde{\mathcal{X}}$  are given by

1.  $\tilde{A}_{\ell r} = \exp \{-j_c^1 \omega_0 p_0 (\ell - 1) \cos(\theta_r)\}$  is the steering element of the  $\ell$ -th sensor.
2.  $\mathbf{k}_r = \mathbf{H}(\theta_r) \mathbf{W}(\alpha_r) \mathbf{w}(\beta_r)$  is the vector sensor response.
3.  $S_{qr} = s_r(\omega_q)$  is the  $q$ -th FT coefficient of the  $r$ -th signal.

As pointed out in Section 2.8.3, the distance  $p_0$  between two successive sensors must be less than or equal to  $\lambda_0/2$ , so as to avoid spatial aliasing.

## 8.4. Estimation of Signal Parameters

The factor matrices of the two Canonical Polyadic Decompositions (CPDs) in (8.14) and (8.24),  $\mathbf{A} \in \mathbb{C}^{L \times R}$ ,  $\mathbf{S} \in \mathbb{C}^{Q \times R}$ , and  $\mathbf{B} \in \mathbb{C}^{M \times R}$  or  $\mathbf{K} \in \mathbb{C}^{3 \times R}$ , are extracted through an ALS (see Section 3.6.3 for details on tensor approximation algorithms). Initial estimates are here given by the tensor decomposition technique [85] detailed in Section 3.5. However, unlike in Section 6.5, the noise correlation structure induced by spatial resampling is herein not taken into account.

Once column vectors  $\hat{\mathbf{a}}_r$ ,  $\hat{\mathbf{b}}_r$  and/or  $\hat{\mathbf{k}}_r$  are extracted from ALS estimates  $\hat{\mathbf{A}}$ ,  $\hat{\mathbf{B}}$ , and/or  $\hat{\mathbf{K}}$ , we can estimate DoA  $\theta_r$  and polarization angle  $\beta_r$  as follows.

1. DoAs  $\theta_r$  can be estimated through a TLS algorithm<sup>1</sup>, thanks to the Vandermonde structure of the factor vector  $\mathbf{a}_r$ , as in Section 4.6.3. We refer to these estimates as

$$\hat{\theta}_r^{\text{TLS}} = \text{TLS estimate of } \theta_r \text{ as in Section 4.6.3} \quad (8.25)$$

2. Polarization angle  $\beta_r$  can be estimated through a 1D exhaustive search:

$$\hat{\beta}_r^{\text{TLS}} = \arg \min_{\beta} \|\hat{\mathbf{k}}_r - \mathbf{k}_r(\hat{\theta}_r^{\text{TLS}}, \beta)\|^2 \quad (8.26)$$

If there are two polarization angles,  $\alpha_r$  and  $\beta_r$ , they can be estimated through a 2D exhaustive search:

$$(\hat{\alpha}_r^{\text{TLS}}, \hat{\beta}_r^{\text{TLS}}) = \arg \min_{\alpha, \beta} \|\hat{\mathbf{k}}_r - \mathbf{k}_r(\hat{\theta}_r^{\text{TLS}}, \alpha, \beta)\|^2 \quad (8.27)$$

3. Alternatively, or as a refinement step, both DoA and polarization angles can be recovered through a joint 2D exhaustive search, as in Section 6.5.2:

$$\hat{\theta}_r^{\text{joint}} = \arg \min_{\theta} \left\| \begin{pmatrix} \hat{\mathbf{a}}_r - \tilde{\mathbf{a}}_r(\theta) \\ \hat{\mathbf{b}}_r - \tilde{\mathbf{b}}_r(\theta) \end{pmatrix} \right\|^2 \quad (8.28)$$

for space shift diversity, and

$$(\hat{\theta}_r^{\text{joint}}, \hat{\beta}_r^{\text{joint}}) = \arg \min_{\theta, \beta} \left\| \begin{pmatrix} \hat{\mathbf{a}}_r - \tilde{\mathbf{a}}_r(\theta) \\ \hat{\mathbf{k}}_r - \mathbf{k}_r(\theta, \beta) \end{pmatrix} \right\|^2 \quad (8.29)$$

for polarization diversity.

However, (8.25) and (8.26), though suboptimal, have a smaller computational burden, compared to both exhaustive searches (8.28) and (8.29). Moreover, if there are two polarization angles,  $\alpha_r$  and  $\beta_r$ , (8.27) allows us to estimate them through a 2D search, whereas the MUSIC algorithm would need a 3D search over the parameter space  $(\theta, \alpha, \beta)$ . Notice that the estimation of the DoA  $\theta_r$  could be further improved using both  $\mathbf{a}_r$  and  $\mathbf{b}_r$  in (8.25).

<sup>1</sup>The TLS could also be replaced by the Structured Least Squares of [58] for further improvement.

## 8.5. Computer results

Experimental conditions are very similar to those of Section 6.6. We simulated  $R = 2$  white Gaussian unit-variance sources, at the sampling frequency  $f_S = 1$  kHz, during an observation time of 64 ms and propagating at  $c = 1800$  ms<sup>-1</sup>, which is approximately the propagation speed of seismic S-waves through ice [117]. The number of frequency bins is  $Q = 17$  (from  $f_{min} = 0.2 f_S$  to  $f_{max} = 0.5 f_S$ ), whereas Spatial Nyquist condition is ensured by  $d_0 = \lambda_{min}/4$ , where  $\lambda_{min} = c/f_{max}$  (cf. Section 2.8.3). For every frequency bin  $\omega_q$  within the band  $[\omega_1, \omega_Q] = [2\pi f_{min}, 2\pi f_{max}]$ , tensor interpolation of Sections 8.2.3 and 8.3.1 is performed using the sinc function, as detailed in Section 8.A.

The reference frequency is chosen to be  $\omega_0 = 2\pi f_{min}$ , such that  $d(\omega_q) \leq d_0, \forall q$  (*i.e.* the virtual subarrays are a shrunk version of the nominal reference subarray). The estimation accuracy of the proposed tensor method is evaluated in comparison to wideband MUSIC and to the multilinear Cramér-Rao Bound (CRB), as in Chapter 6. The performance criterion is the relative total MSE of the DoA estimates and, whenever present, of the polarization ellipticity estimates:

$$\begin{cases} \text{MSE}(\boldsymbol{\theta}) = \frac{1}{\pi^2} \frac{1}{NR} \sum_{n=1}^N \sum_{r=1}^R (\hat{\theta}_{rn} - \theta_r)^2 \\ \text{MSE}(\boldsymbol{\beta}) = \frac{1}{\pi^2} \frac{1}{NR} \sum_{n=1}^N \sum_{r=1}^R (\hat{\beta}_{rn} - \beta_r)^2 \end{cases} \quad (8.30)$$

where  $\hat{\theta}_{rn}$  and  $\hat{\beta}_{rn}$  are the estimated DoA and ellipticity angle, respectively, of source  $r$  in the  $n$ -th MC trial,  $N = 2500$  being the number of trials. The SNR definition below is assumed:

$$\text{SNR} = 10 \log_{10} \frac{\|\boldsymbol{\mathcal{X}}\|_F^2}{LMPQ\sigma^2} \quad (8.31)$$

### 8.5.1. Space Shift in Wideband

The two impinging sources arrive from the broadside:  $\theta_1 = 80^\circ$  and  $\theta_2 = 100^\circ$ . The acquisition system is given by a ULA of  $L$  sensors, where the following space invariances are considered:

**NB CP 3:** CPD with  $M = 3$  ULA subarrays of  $L - 2$  sensors each: standard narrowband CPD (4.5) in time domain as in Chapter 4, after narrowband filtering around  $f_0$ .

**WB CP 2:** WB preprocessing and CPD (8.14) with  $M = 2$  ULA subarrays of  $L - 1$  sensors each.

**WB CP 3:** WB preprocessing and CPD (8.14) with  $M = 3$  ULA subarrays of  $L - 2$  sensors each.

**WB CP 4:** WB preprocessing and CPD (8.14) with  $M = 4$  ULA subarrays of  $L - 3$  sensors each.

The **CRB**, calculated as in Chapter 7, refers to the model in WB CP 3.

Notice that WB preprocessing refers to the tensor spatial interpolation described in Section 8.2, in particular in Section 8.2.1. Source DoAs were estimated using (8.25), implying a negligible computational complexity, compared to the exhaustive search of the MUSIC algorithm.

In particular, as for the MUSIC algorithm,

**WB MUSIC** refers to the wideband MUSIC algorithm with covariance matrix expressed in (2.51).

The label **WB MUSIC SS** specifies that spatial smoothing (2.62) has been performed with  $M = 3$ .

Figures 8.6a and 8.6b show the MSE as a function of SNR, for uncorrelated and correlated sources, respectively, received by a ULA of  $L = 20$  sensors.

Figures 8.7a and 8.7b show the MSE as a function of the angular separation between  $R = 2$  sources, for uncorrelated and correlated sources, respectively, received by a ULA of  $L = 20$  sensors. In this case, DoAs are given by  $\theta_1 = 90^\circ - \Delta\theta/2$  and  $\theta_2 = 90^\circ + \Delta\theta/2$ .

Similarly, Figures 8.8a and 8.8b show the MSE as a function of the number of sensors,  $L$ , for uncorrelated and correlated sources, respectively, at a SNR of 20 dB.

The tensor decomposition with  $M \in \{3, 4\}$  space shifts yields better results when the number of sensors or the SNR increase. The WB preprocessing significantly improves the performance of the narrowband tensor estimation, NB CP 3. Moreover, tensor-based wideband DoA estimation appears to outperform the wideband MUSIC algorithm, in the present experimental conditions.

In Figures 8.6b and especially 8.6a at high SNR, we notice a saturation of the MSE, due to the interpolation error, resulting in a progressively significant gap from the CRB.

A slight saturation or deterioration of the performance of the DoA algorithms takes place when the two sources move away from the broadside ( $\theta_r \approx 0^\circ$ ), as demonstrated in Figures 8.7a and 8.7b.

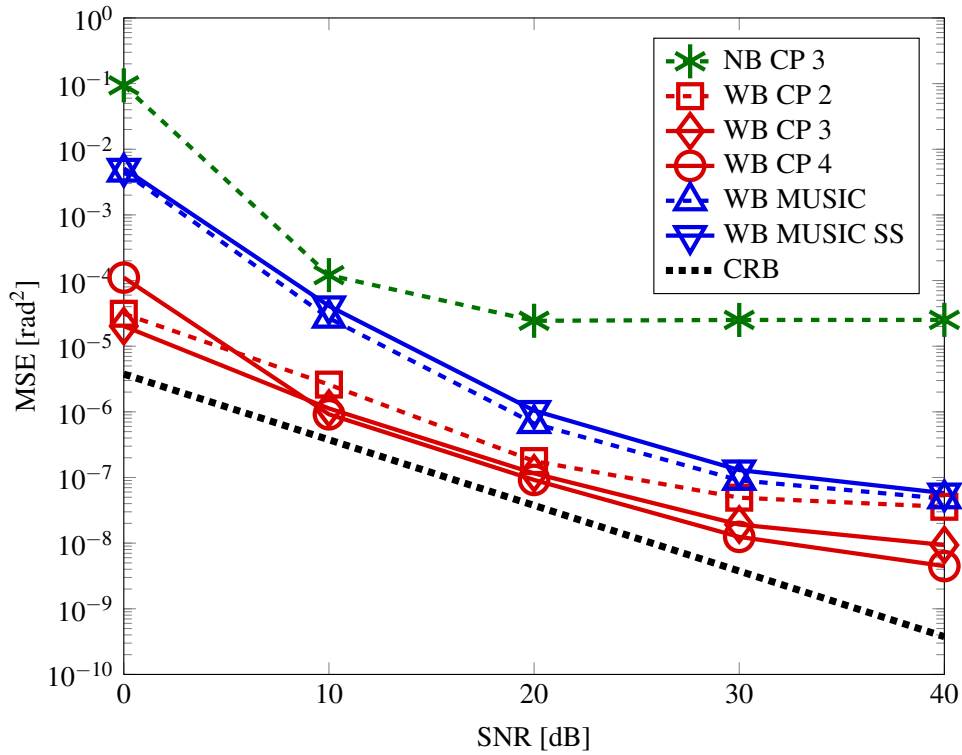
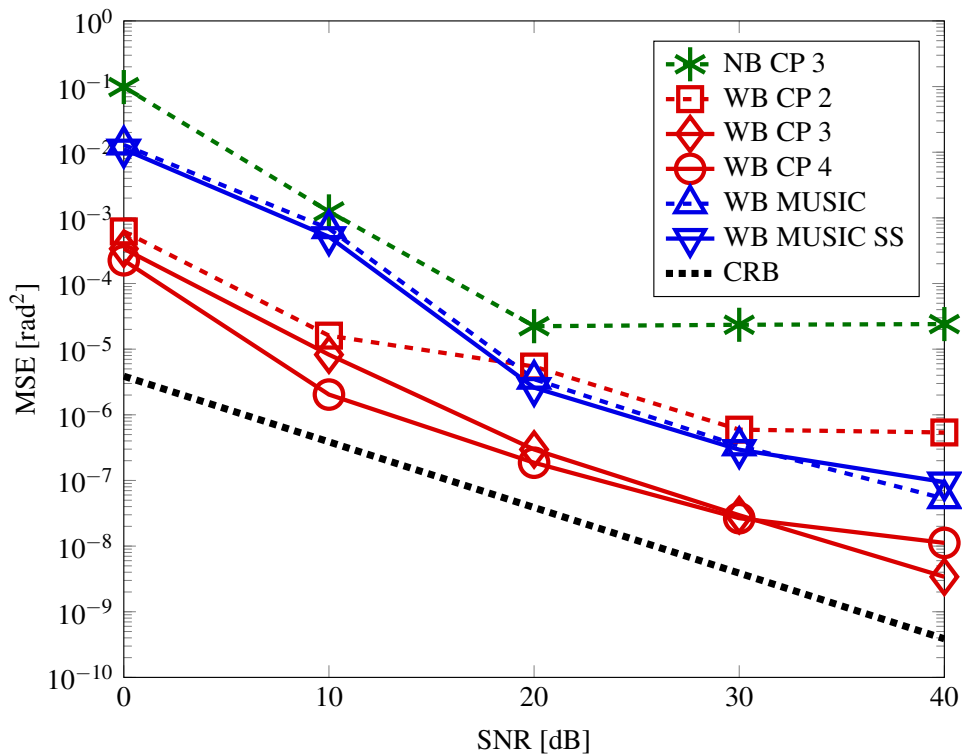
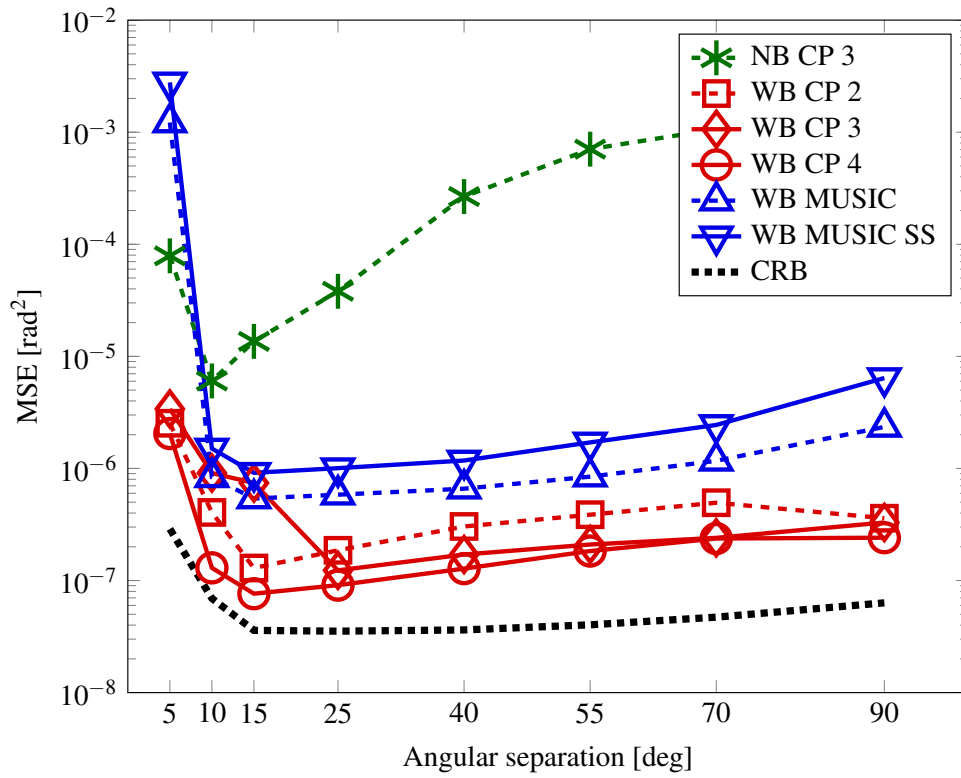
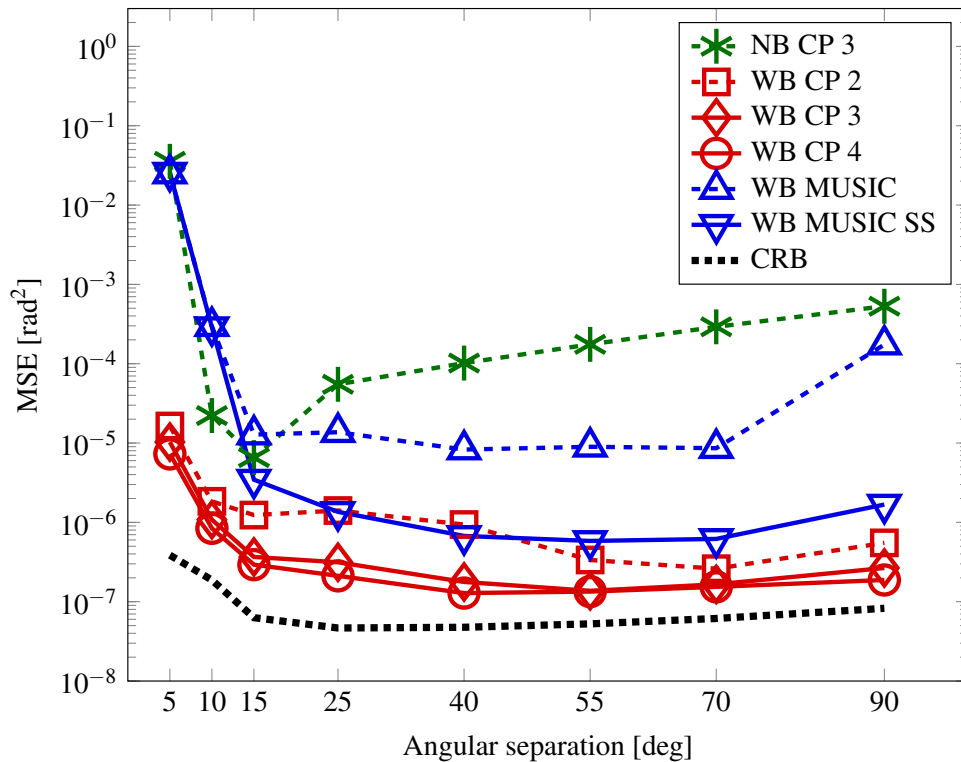
(a) DoA estimation - Uncorrelated sources,  $L = 20$  sensors(b) DoA estimation - Correlated sources:  $\rho = 0.9$ ,  $L = 20$  sensors

Figure 8.6.: MSE vs SNR - space shift diversity

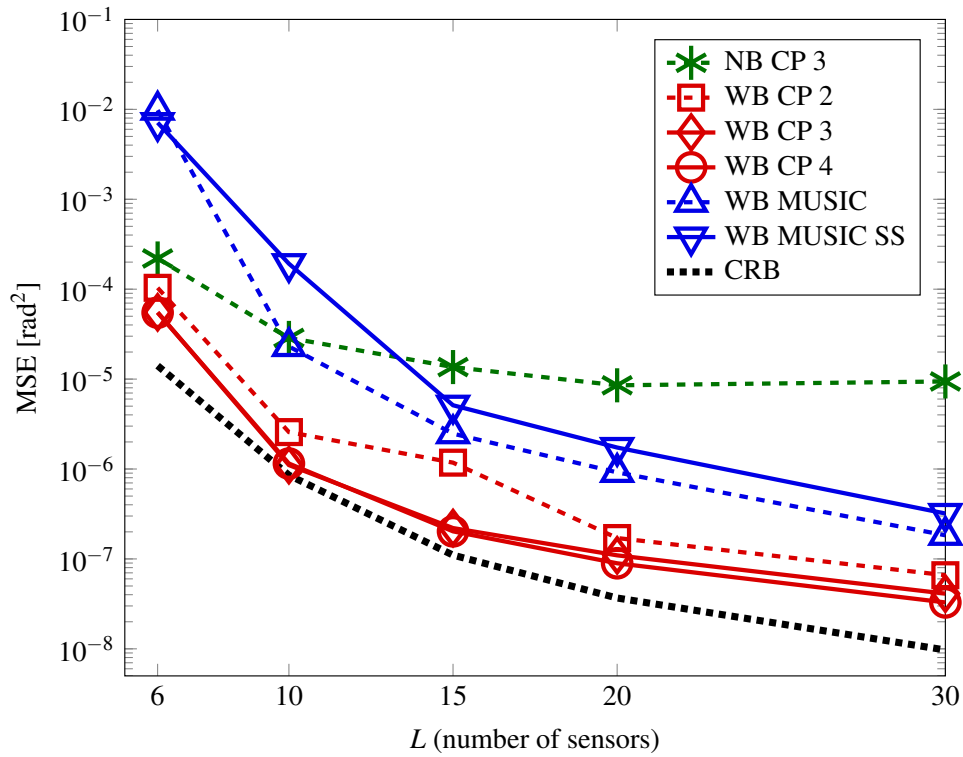


(a) DoA estimation - Uncorrelated sources,  $L = 20$  sensors



(b) DoA estimation - Correlated sources:  $\rho = 0.9$ ,  $L = 20$  sensors

Figure 8.7.: MSE vs angular separation - space shift diversity



(a) DoA estimation - Uncorrelated sources, SNR = 20 dB

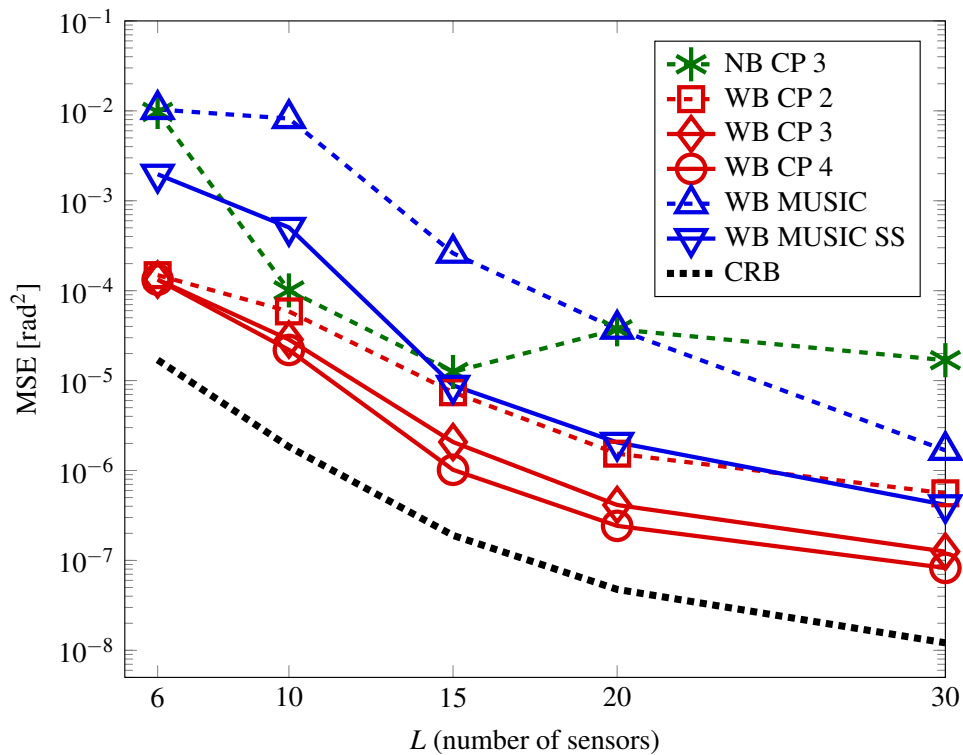
(b) DoA estimation - Correlated sources:  $\rho = 0.9$ , SNR = 20 dB

Figure 8.8.: MSE vs L - space shift diversity

### 8.5.2. Polarization in Wideband

We now replace space shift diversity of Section 8.5.1 with polarization diversity, as in Section 8.3. The two impinging sources are Rayleigh waves, *i.e.*  $\alpha = 0$ ,  $\psi = 0$  (coplanar with the array), arriving from the broadside:  $\theta_1 = 80^\circ$  and  $\theta_2 = 100^\circ$ , and differently polarized:  $\beta_1 = -20^\circ$  and  $\beta_2 = 10^\circ$ . This configuration is similar to that of Section 6.6.2. The acquisition system is given by a ULA of  $L = 20$  sensors, with  $P = 3$  polarization components. Hereafter, we compare the following methods:

**NB CP TLS:** standard narrowband CPD (5.27) in time domain as in Section 5.3, after narrowband filtering around  $f_0$ . Signal parameters are estimated using (8.25) and (8.26).

**WB CP TLS:** WB preprocessing is applied and, after CPD (8.24), signal parameters are estimated using (8.25) and (8.26).

**WB CP Joint:** WB preprocessing is applied and, after CPD (8.24), signal parameters are estimated using (8.29).

**WB Scalar MUSIC,** via an incoherent average of  $P$  covariances.

**WB Vector MUSIC** in Section 5.3.1, where the array manifold takes into account wave polarization parameters, via a coherently averaged covariance matrix of size  $PL \times PL$ .

Notice that WB preprocessing refers to the spatial interpolation described in Section 8.3.

Figures 8.9a and 8.9b show the MSE as a function of SNR, for DoA and polarization estimation, respectively. As for space shift diversity in Section 8.5.1, the proposed wideband tensor method significantly improve its narrowband counterpart, and outperform the WB Vector MUSIC algorithm, as for both DoA and polarization estimation. We notice that WB CP Joint is slightly better than WB CP TLS, as it achieves a joint estimation from factor matrices  $\mathbf{A}$  and  $\mathbf{K}$ .

However, the advantage of WB CP TLS lies in its lightest computational cost, as a TLS followed by a 1D search are less demanding than a 2D search. Finally, in Figure 8.9a we can observe an estimation bias of the DoA estimates of all the wideband methods for high SNR, due to the interpolation error. A similar bias also affects the WB MUSIC polarization estimation in Figure 8.9b.

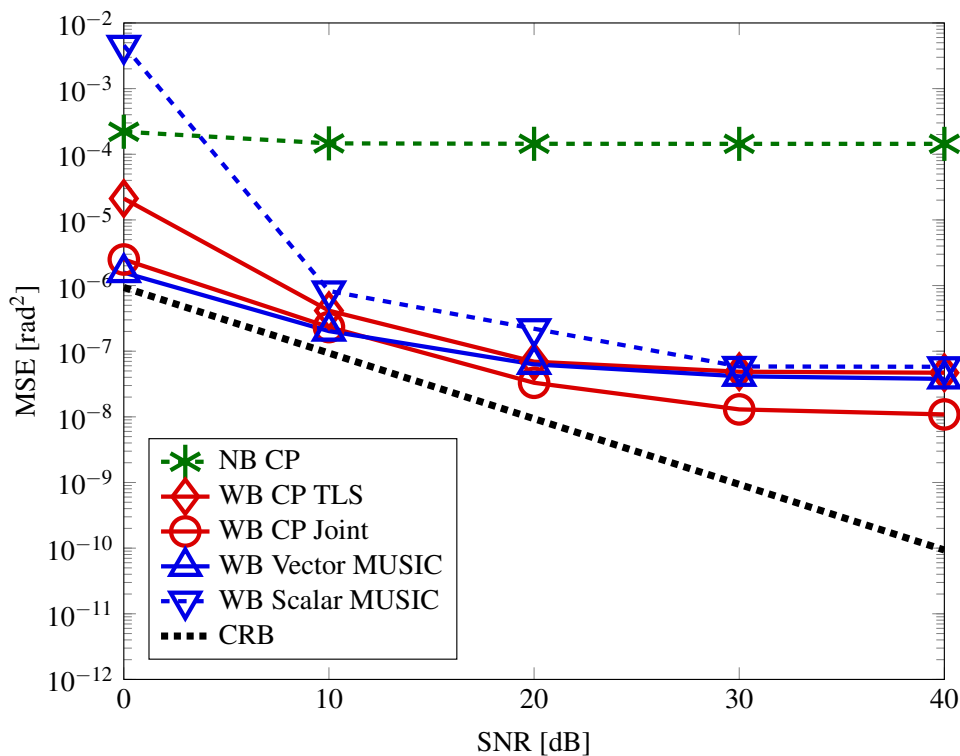
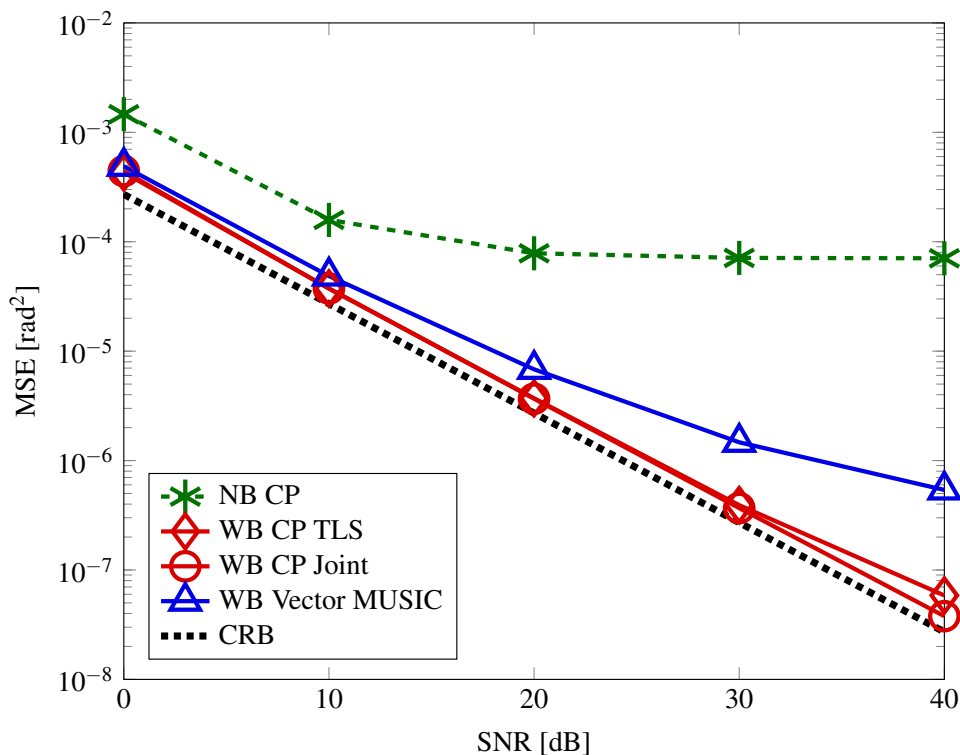
(a) DoA estimation - Uncorrelated sources -  $L = 20$  sensors(b) Polarization estimation - Uncorrelated sources -  $L = 20$  sensors

Figure 8.9.: MSE vs SNR - polarization diversity

## 8.6. Conclusions and Perspectives

Space and frequency smoothing have been realized in a deterministic framework, and we showed that polarization can replace space shift diversity in the tensor formulation, as in Chapter 6.

In this chapter, we extended the spatial interpolation technique of Section 2.8.3 to wideband tensor-based algorithms. This development can be seen as an alternative to the multilinear interpolation of Chapter 6, whenever the acquisition system has a regular structure, such as the ULA structure. In this case, the division into angular sectors is no longer necessary.

However, we studied so far only the ULA configuration, as spatial interpolation is easier to handle. The interest of the ULA configuration is also related to the large number of applications that resort to such arrays. For instance, in multidimensional harmonic retrieval, data tensors have a Vandermonde structure in multiple dimensions. In this case, multiple interpolations can be applied independently, as a generalization of (8.6) and (8.10). This was the object of [163], who extended our idea in [119] to MIMO radars, through multiple subsequent linear interpolations. In particular, [163] showed that linear interpolation performed better for their purpose, compared to the *sinc* interpolation.

Similarly, as a perspective, the results in the last two chapters could be extended to the design of wideband preprocessing routines for 2D ESRPIT [164] and *DD* ESPRIT [60], as well as for multidimensional harmonic retrieval [61], as in [163].

The wideband tensor estimation through spatial resampling could also be improved if the noise covariance structure induced by interpolation were taken into account within the tensor CPD approximation, as in Section 6.5.

In the end of next chapter, the proposed method is applied to real seismic data recorded by a ULA for DoA estimation.

# Appendix

## 8.A. Array 1D Interpolation

### 8.A.1. Sinc Interpolation

Interpolation is related to signal resampling as follows:

1. Thanks to the Shannon sampling theorem [100], the continuous signal  $x(t)$  can be reconstructed from its samples  $x(nT_s)$ :

$$\tilde{x}(t) = \sum_{k=-\infty}^{+\infty} x(kT_s) g(t - kT_s) \quad (8.32)$$

2. Only once the interpolating process has been expressed, the signal can be resampled at a new rate  $T'_s$  as follows:

$$\tilde{x}(t)|_{t=nT'_s} = \sum_{k=-\infty}^{+\infty} x(kT_s) g(nT'_s - kT_s) \quad (8.33)$$

The most common interpolating function is generally the sinc function:

$$g(t - kT_s) = \text{sinc}\left(\frac{t - kT_s}{T_s}\right) \quad (8.34)$$

leading to

$$\tilde{x}(t) = \left[ \sum_{k=-\infty}^{+\infty} x(kT_s) \delta(t - kT_s) \right] * \text{sinc}\left(\frac{t}{T_s}\right) \quad (8.35)$$

Since in practice only a finite number of samples is available, it is advisable to truncate the sinc function with a window of length  $\Delta T$  enhancing the central samples and related to the signal frequency behavior. This action is named *apodization*. As for our implementation, we chose a rectangular window  $W$  with a support of  $\Delta T = 5$  time samples:

$$\text{sinc}_W(t) = \frac{\sin(\pi t \bar{f})}{\pi t \bar{f}} \mathbb{1}_W(t) \quad (8.36)$$

where  $\mathbb{1}_W(t)$  is the indicator function of the window  $W$ . The parameter  $\bar{f}$  that we fixed to 0.4 controls the smoothness of the sinc interpolation.

### 8.A.2. Spatial Interpolation

Analogously, we define a spatial interpolator to reconstruct the signal at frequency  $\omega_q$  at any point  $p$  in space,  $x(\omega_q, p)$ , from its samples at nominal sensor positions  $p_\ell = \ell p_0$ :

$$\tilde{x}(\omega_q, p) = \sum_{\ell=-\infty}^{+\infty} x(\omega_q, \ell p_0) g(p - \ell p_0) \quad (8.37)$$

# 9. Tensor Decomposition of Seismic Volume Waves

## 9.1. Contribution

In this chapter, we consider the problem of DoA estimation of seismic plane waves impinging on an array of sensors from a new deterministic perspective using tensor decomposition techniques. In addition to temporal and spatial sampling of Chapter 1, we take into account further information, based on the different propagation speeds of body waves (P and S) through solid media. We evaluate performance through simulated data in terms of the Cramér-Rao Bound (CRB) and in comparison with other reference methods such as ESPRIT and MUSIC, in the presence of additive Gaussian circular noise (Assumption A 1.12). We then apply the proposed approach to real seismic data recorded at the Argentière glacier, occurring at the interface between the ice mass and the underlying bedrock. Information about propagation speed diversity is not taken into account by existing models in array processing. The discovered advantage in terms of the average error in estimating the direction of arrival of body waves is noteworthy, especially for a low number of sensors, and in separating closely located sources. Additionally, we observe an improvement of precision in processing real seismic data.

Our work was published in the journal article [117], and was source of inspiration for the more general development of the wideband tensor DoA estimation described in Chapter 6 and Chapter 8. Our work was cited by a review article on cryoseismology [111] and by a journal article on non-negative tensor decompositions for large datasets [154].

## 9.2. Context

In the context of seismic monitoring, seismology aims at studying waves generated by rupture phenomena taking place within a volume of interest (rock, ice, etc.). Although the most interesting events take place at a certain depth - mostly unknown - within the analyzed volume, acquisition systems and sensor arrays are most often located close to the surface. The main quantity to be measured is ground displacement (in the form of its derivative - velocity - or its second derivative - acceleration), produced by impinging elastic waves. The localization of the sources forms the first requirement of data analysis, in order to prevent damage provoked by seismic events, and to monitor the activity of complex structures such as glaciers or volcanoes. Seismic arrays, after being introduced in the 1960s, have made essential contributions to this problem. These arrays consist of numerous seismometers placed at discrete points in space in a well-defined configuration [123]: apart from an improvement of SNR by combining individual sensor recordings, they have been used to refine models of the Earth's interior, through classical tools such as beamforming, slant stacking techniques and frequency-wave number analysis.

This chapter exploits another type of diversity, in addition to spatial and temporal sampling traditionally employed in array processing (cf. Section 5.2 for a detailed explanation of the concept of diversity): the propagation speed diversity<sup>1</sup> of body waves through solids, namely pressure (P) and shear (S) waves. Current array processing methods like [131, 126] only focus on information conveyed by a single body wave, like the P wave, whereas the contents delivered by the other is somehow wasted. Our approach intends to exploit this information as a whole, whereas translational invariance used in [136] and detailed in Chapter 4 is no longer necessary.

This chapter is organized as follows. Section 9.3 presents the physical model and some assumptions. Our tensor deterministic method for DoA estimation, exploiting the propagation speed diversity of body waves, is presented in Section 9.4. Simulated data and real seismic data are treated in Sections 9.5 and 9.6 respectively. Computer results in Sections 9.5 are compared with 2D subspace methods of Chapter 2 and with the CRB of Chapter 7. An application to icequakes recorded at the Argentière glacier in 2012 is the object of Section 9.7.

### 9.3. Physical model and assumptions

When one wants to estimate and localize seismic events originating at depth, one has to deal with a double arrival of elastic body waves: P waves and S waves, which are detailed in Section 1.6. For the physical model of wave propagation, the following properties are assumed, in addition to all the assumptions of Sections 1.2.2 and 1.6:

**A 9.1.** The impulse responses of particle motion is the only source of variability between impinging P and S waves.

and in order to allow the multilinearity and separability of the final model:

**A 9.2.** We filter P and S signals in a narrow-band around  $f_1 = \omega_1/2\pi$  and  $f_2 = \omega_2/2\pi$ , respectively, such that  $\frac{v_1}{f_1} = \frac{v_2}{f_2} = \lambda$  is constant, where  $\lambda$  refers to the wavelength of impinging waves.

**A 9.3.** Base-band P and S signals propagating from the same source event and received in two different narrow bands around  $f_1$  and  $f_2$  are proportional:

$$w_{bf}^{\{2\}}(t) = \alpha(f_1, f_2) w_{bf}^{\{1\}}(t) \quad (9.1)$$

See (9.38) in Section 9.A for more details.

Furthermore, we state the following notation, which will be subsequently used:

**A 9.4.** In order to avoid scale indeterminacies in tensor decomposition, the P wave  $w_{bf}^{\{1\}}(t)$  is fixed up to a scale factor (see Section 9.A for more details).

---

<sup>1</sup>Since the focus is on narrow-band processing, the distinction between group and phase propagation velocities is irrelevant.

## 9.4. Speed diversity in tensor format

The advantage of the tensor formalism lies in its ability to restore the identifiability of signal parameters: impinging sources, their directions of arrival, and the related connection between P and S waves.

*Propagation speed diversity* may be seen as equivalent to a frequency diversity between P and S waves, under Assumption A 1.3 and properties A 1.21, A 9.2 and A 9.3. The proposed model for propagation speed diversity will be subsequently developed on the basis of the linear relation below:

$$g(t, f) = \sum_{r=1}^R w_r(t) \alpha_r(f) \iff G_{tk} = \sum_{r=1}^R S_r[t] C_r(f_k) \quad (9.2)$$

where the latter equation represents the discretization of the former.  $f_k$  denotes the working frequency for P and S waves ( $k = 1$  for the P wave and  $k = 2$  for the S wave), as defined in A 9.2; it is chosen by the user as a function of propagation speed  $v_k$ ;  $\alpha_r(\cdot)$  is a complex unknown coefficient.

The focus of our work consists in integrating at the same time the spatial, temporal and speed diversities, respectively embodied by matrices  $\mathbf{A} \in \mathbb{C}^{L \times R}$ ,  $\mathbf{S} \in \mathbb{C}^{T \times R}$  and  $\mathbf{C} \in \mathbb{C}^{2 \times R}$ .

P and S waves are generated by the same physical source but propagate at two different velocities,  $v_1$  and  $v_2$  respectively, and correspond to different propagation modalities (compression and shear waves respectively). Thus, P and S signals received at position  $\mathbf{p}$  and at time  $t$  are respectively given by

$$\begin{cases} y^P(\mathbf{p}, t) = \sum_{r=1}^R w_r^P(t - \tau_r^P(\mathbf{p})) + n^P(t, \mathbf{p}) \\ y^S(\mathbf{p}, t) = \sum_{r=1}^R w_r^S(t - \tau_r^S(\mathbf{p})) + n^S(t, \mathbf{p}) \end{cases} \quad (9.3)$$

where  $\{\tau_r^P, \tau_r^S\}$  express the respective delays for P and S signals recorded at position  $\mathbf{p}$ . The signal received at a point  $\mathbf{p}$  in space contains  $R$  sources of interest plus an additive noise: under assumptions A 1.1 and A 1.3, the time delays of P and S waves correspond to the phase shifts  $\exp\{-j\varpi_r^P(\mathbf{p})\}$  and  $\exp\{-j\varpi_r^S(\mathbf{p})\}$  respectively, with  $\varpi_r^P(\mathbf{p}) = \frac{\omega_1}{v_1} \mathbf{p}^\top \mathbf{d}(\theta_r)$ ,  $\varpi_r^S(\mathbf{p}) = \frac{\omega_2}{v_2} \mathbf{p}^\top \mathbf{d}(\theta_r)$ .

With properties A 9.2, A 9.3 and A 9.4, records produced by the  $r$ -th source contain two delayed narrowband waves propagating at frequencies  $f_1, f_2$  at velocities  $v_1$  and  $v_2$ , yielding two resulting waves with the same wavelength  $\lambda$ . After windowing, filtering and aligning the two waves (cf Section 9.6 for details), we can model them as a separable function of 3 variables:

$$x(\mathbf{p}, t, f) = \sum_{r=1}^R \exp\{-j\varpi_r(\mathbf{p})\} w_r(t) \alpha_r(f) + n(\mathbf{p}, t, f) \quad (9.4)$$

where coefficient  $\alpha_r(f)$  is the same as in (9.2) and  $\varpi_r(\mathbf{p}) = \frac{2\pi}{\lambda} \mathbf{p}^\top \mathbf{d}(\theta_r)$ . Thus, in the absence of noise  $n(\mathbf{p}, t, f)$ , function  $x(\mathbf{p}, t, f)$  decomposes into a sum of  $R$  functions whose variables separate. Discretization of (9.4) corresponds to a 3-way array of finite dimensions  $L \times T \times 2$  ( $L$  sensors located at  $\mathbf{p}_\ell$ ,  $T$  time samples and  $K = 2$  propagation velocities  $v_k$ ):

$$\mathcal{X}_{\ell tk} = \sum_{r=1}^R \exp\{-j\varpi_r(\mathbf{p}_\ell)\} w_r(t) \alpha_r(f_k) + \mathcal{N}_{\ell tk} \quad (9.5)$$

where frequency  $f_k$ ,  $k = 1, 2$  is fixed according to property A 9.2 ( $\lambda = \frac{v_1}{f_1} = \frac{v_2}{f_2}$ ). Notice that, thanks to convention A 9.4, the complex envelopes of the P and S waves are expressed in (9.5) as

$$\begin{cases} w_{bf}^{\{1\}}(t) = w(t) & \text{P wave complex envelope} \\ w_{bf}^{\{2\}}(t) = \alpha(f_2) w(t) & \text{S wave complex envelope} \end{cases} \quad (9.6)$$

Thus, the tensor Canonical Polyadic Decomposition (CPD) model  $\mathcal{X} = \mathcal{M} + \mathcal{N}$  is the result of stacking the two matrix slices  $\mathbf{M}_{::1}$  and  $\mathbf{M}_{::2}$ , corresponding to P and S waves respectively, as in Figure 9.1:

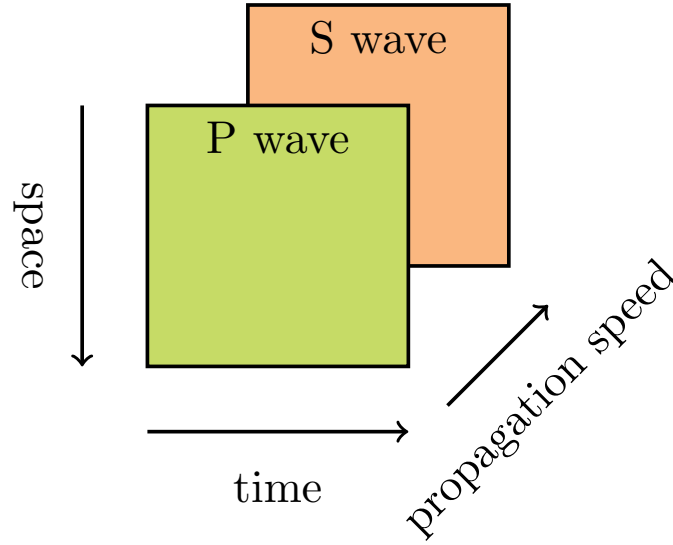


Figure 9.1.: P and S slices,  $\mathbf{M}_{::1}$  and  $\mathbf{M}_{::2}$

$$\begin{cases} \mathcal{X} = \sum_{r=1}^R \mathbf{a}_r \otimes \mathbf{s}_r \otimes \mathbf{c}_r + \mathcal{N} \\ X_{\ell tk} = \sum_r A_{\ell r} S_{tr} C_{kr} + N_{\ell tk} \end{cases} \quad (9.7)$$

where rank- $R$  corresponds to the number of sources, supposed known, thanks to Assumption A 1.10, and  $\mathcal{N}$  refers to additive noise. The physical meaning of the three factor matrices is as follows:

$$\begin{cases} A_{\ell r} = \exp\{-j\omega\tau_{\ell}(\theta_r)\} \text{ refers to space diversity} \\ S_{tr} = w_r(t) \text{ refers to time diversity} \\ C_{kr} = \alpha_r(f_k) \text{ refers to speed diversity} \end{cases} \quad (9.8)$$

where  $\tau_{\ell}(\theta_r) = \mathbf{p}_{\ell}^{\top} \mathbf{d}(\theta_r)/c$  refers to the time delay at sensor  $\ell$  w.r.t. the reference sensor.

Therefore, as in Section 4.3.1, we fix  $2R$  parameters without restricting the generality. More precisely, based on properties described in Section 9.3, we assume the following:

1. From property A 4.2 we refer to the first sensor by index 1, with  $\mathbf{p}_1 = \mathbf{0}$ :

$$A_{1r} = \exp\{-j\omega\tau_{1r}\} = \exp\left\{-j\frac{2\pi}{\lambda} \mathbf{p}_1^{\top} \mathbf{d}(\theta_r)\right\} = 1 \quad \forall r \quad (9.9)$$

2. From property A 9.3 we refer to the P wave by index 1:

$$\alpha_r(f_1) = 1, \forall r \implies C_{1r} = 1, \forall r \quad (9.10)$$

Thus, we impose the first rows of matrices  $\mathbf{A}$  and  $\mathbf{C}$  to be formed of ones. Then we pull column-wise the remaining scaling coefficients,  $\{\varsigma_r A_{1r} C_{1r}\}$ , into matrix  $\mathbf{S}$ . More precisely, we fix all scale indeterminacies through the following transformation:

$$(\hat{\mathbf{a}}_r, \hat{\mathbf{s}}_r, \hat{\mathbf{c}}_r, \varsigma_r) \longleftarrow \left( \frac{\mathbf{a}_r}{A_{1r}}, \varsigma_r A_{1r} C_{1r} \mathbf{s}_r, \frac{\mathbf{c}_r}{C_{1r}}, 1 \right) \quad (9.11)$$

This choice permits to compute performance bounds on the retrieval of CPD factors in (9.7) more easily.

In the present chapter, we deal with simpler examples when  $R = 1$  as for glacier data (Section 9.6) and  $R = 2$  relative to simulated data (cf. Section 9.5), so that essential uniqueness of a decomposition is always guaranteed (see Section 3.3.5 for details).

### 9.4.1. Estimation of Signal Parameters

The tensor model in (9.7) can be expressed in vector form as

$$\mathbf{x} = \text{vec}\{\mathcal{X}\} = \sum_{r=1}^R \mathbf{c}_r \boxtimes \mathbf{s}_r \boxtimes \mathbf{a}_r + \mathbf{n} \quad (9.12)$$

where  $\boxtimes$  denotes the Kronecker product, as defined in [26, 75] (cf. (3.22) for generic tensor order  $D$ ). Since, thanks to Assumption A 1.11, the *measurement* noise vector,  $\mathbf{n} = \text{vec}\{\mathcal{N}\}$ , is circular white Gaussian and isotropic, *i.e.* with zero mean and covariance  $\Sigma = \sigma^2 \mathbf{I}$ , the log-likelihood takes the form:

$$\Upsilon(\boldsymbol{\vartheta}) = -(\mathbf{x} - \boldsymbol{\mu})^H \Sigma^{-1} (\mathbf{x} - \boldsymbol{\mu}) + \text{constant} \quad (9.13)$$

where  $\boldsymbol{\mu} = \sum_{r=1}^R \mathbf{c}_r \boxtimes \mathbf{s}_r \boxtimes \mathbf{a}_r$  is unknown and constrained by its parameterization  $\boldsymbol{\vartheta} = [\boldsymbol{\theta}, \text{vec}\{\mathbf{S}\}, \text{vec}\{\mathbf{C}\}]$ . For the CRB of the tensor DoA estimation, see Chapter 7.

Although the optimal solution is given by the global maximum of  $\Upsilon(\boldsymbol{\vartheta})$ , we propose a suboptimal two-step procedure in the same spirit as [128], with smaller computational burden: first  $\Upsilon$  is maximized with respect to parameter  $\boldsymbol{\xi} = [\text{vec}\{\mathbf{A}\}, \text{vec}\{\mathbf{S}\}, \text{vec}\{\mathbf{C}\}]$  through the decomposition algorithm of [85] detailed in Section 3.5; then DoAs and the other signal parameters can be estimated as follows.

1. Direction of arrival  $\theta_r$  of the  $r$ -th source impinging on the array is calculated from  $A_{\ell r} = \exp\{-j\frac{2\pi}{\lambda} \mathbf{p}_\ell^T \mathbf{d}(\theta_r)\}$  as in Section 4.6, and, for ULAs, in Section 4.6.3.
2. The signal  $s_r(t)$  of the  $r$ -th source is extracted up to a scaling factor directly from matrix  $\mathbf{S}$ , as in Section 4.7.

$$\hat{w}_r(t) \propto S_{tr}, \quad t = 1, \dots, T \quad (9.14)$$

3. The complex multiplicative coefficient  $\alpha_r(f_k)$  is extracted directly from matrix  $\mathbf{C}$ :

$$\hat{\alpha}_r(f_k) = C_{kr} \quad (9.15)$$

## 9.5. Numerical simulations

Signals were simulated according to sampling conditions, that are typically those selected for experiments at Argentière (cf. [63, 64]) and emulate the normal seismic activity of a glacier. Estimation efficiency was evaluated in comparison with two other narrowband algorithms, **ESPRIT** [126] and **MUSIC** [131, 140], and with deterministic CRB as a benchmark. In the following figures, **CRB-2D** indicates the CRB of the MUSIC algorithm [140], whereas **CRB-3D** indicates the CRB of the tensor **CPD**.

The performance criterion is the Root Mean Square Error (RMSE) on the DoA:

$$\text{RMSE}(\boldsymbol{\theta}) = \sqrt{\frac{1}{NR} \sum_{n=1}^N \sum_{r=1}^R (\hat{\theta}_{rn} - \theta_r)^2}, \quad (9.16)$$

where  $\hat{\theta}_{rn}$  is the estimated DoA of source  $r$  in the  $n$ -th MC trial,  $N$  being the number of trials. The number of simultaneous sources was chosen to be  $R = 2$ . The SNR definition for P wave was:

$$\text{SNR} = 10 \log_{10} \frac{\|\boldsymbol{\mu}^P\|^2}{LT\sigma_n^2} \quad (9.17)$$

where  $\boldsymbol{\mu}^P = \text{vec}\{\mathbf{M}_{\cdot:1}\}$  refers to the P wave. This is consistent with previous works, where the S wave data is traditionally thrown away even if received. In fact, in our simulations we applied MUSIC and ESPRIT on the P wave only.

We have the following values:

1. We use values for P and S wave velocities through ice, as in [63, 150]:  $v_1 = 3600 \text{ m s}^{-1}$  and  $v_2 = 1610 \text{ m s}^{-1}$ .
2.  $\frac{v_1}{v_2} = \frac{f_1}{f_2} \approx 2.24$ .
3.  $f_1 = 193 \text{ Hz}$ ,  $f_2 = 86 \text{ Hz}$ .
4. Time duration of simulated records: 201 ms.
5. Configuration of the array: ULA with inter-sensor distance  $p_0 = 10 \text{ m}$ . Three arrays were simulated, each with a different number of sensors:  $L \in \{3, 10, 30\}$ .
6. Simulated directions of arrivals:

$$\left\{ \begin{array}{l} \text{Figure 1: endfire } \theta_1 = 30^\circ, \theta_2 = 50^\circ \\ \text{Figure 2: broadside } \theta_1 = 80^\circ, \theta_2 = 100^\circ \\ \text{Figure 3a: endfire } \theta_1 = 45^\circ - \Delta\theta/2, \theta_2 = 45^\circ + \Delta\theta/2 \\ \text{Figure 3b: broadside } \theta_1 = 90^\circ - \Delta\theta/2, \theta_2 = 90^\circ + \Delta\theta/2 \end{array} \right. \quad (9.18)$$

where  $\Delta\theta$  refers to the  $x$ -axis of Figure 9.5 (the overall angular separation between the two sources).

A simple source was simulated as approximately narrowband: a signal carried by a sinusoid modulated by a Kaiser window of envelope  $a_r(t)$ :

$$s_{kr}(t) = a_{kr}(t) \exp\{j\phi_{kr}(t)\} \exp\{j\omega_k t\} \quad (9.19)$$

where  $\phi_{kr}(t)$  are independently drawn in  $[0, 2\pi)$  for every  $t$ . Since narrowband  $\omega_k$  is known for P and S waves, simulated signal  $s_{kr}(t)$  is brought to the baseband through demodulation:

$$s_{kr}(t) = a_{kr}(t) \exp\{j\phi_{kr}(t)\} \quad (9.20)$$

MC simulations ( $N = 200$  trials) show a superior performance of the CPD with respect to MUSIC and ESPRIT algorithms, in the sense of the RMSE defined in (8.30), especially for a low number of sensors composing the array. For larger number of sensors, the performance of MUSIC and CPD becomes comparable. In particular, Figures 9.2 and 9.3 illustrate computer simulations for a variable number of sensors,  $L \in \{3, 10, 30\}$ , composing the array and for different configurations of sources impinging from a *broadside* (perpendicular to the array) or *endfire* (laterally to the array) perspective.

The following observations can be made.

- For low SNR values, the RMSE does not increase anymore at some point, as SNR decreases. This can be observed in particular for  $L = 3$  in Figures 9.2a and 9.3a. This is a known saturation phenomenon [151], which is due to the fact that estimated angles are bounded. For such low values of SNR, the CRB becomes meaningless.
- For larger numbers of sensors, e.g.  $L = 10$  or  $L = 30$ , the latter saturation phenomenon is not yet observed at  $\text{SNR} = 5$  dB, and one can observe a take-off of the RMSEs from their CRBs. This threshold effect is well known and expected at low SNR values [15].
- The performance of CPD and ESPRIT methods does not reach the CRB for  $L = 10$  or  $L = 30$ . This loss can be explained by the 2-step nature of the estimation process, which consists of estimating first steering vectors, and then corresponding DoAs in a second stage (cf. Section 4.6).
- For  $L = 10$  and  $L = 30$ , MUSIC seems to perform better than ESPRIT. This is due to the fact that MUSIC finds the DoA by executing an exhaustive search, which is hence a one-stage procedure.

Figures 9.4 and 9.5 represent the evolution of the RMSE (obtained with  $N = 300$  trials) with respect to the angular separation of the two simultaneous sources, for a fixed SNR of 20 dB: the tendency is an evident predominance in the performance of the CPD algorithm, especially for closely spaced sources.

To conclude, the advantage of CPD over ESPRIT is always present, whereas CPD outperforms MUSIC substantially when the number of sensors remains limited or when sources are close to each other (less than 15 degrees).

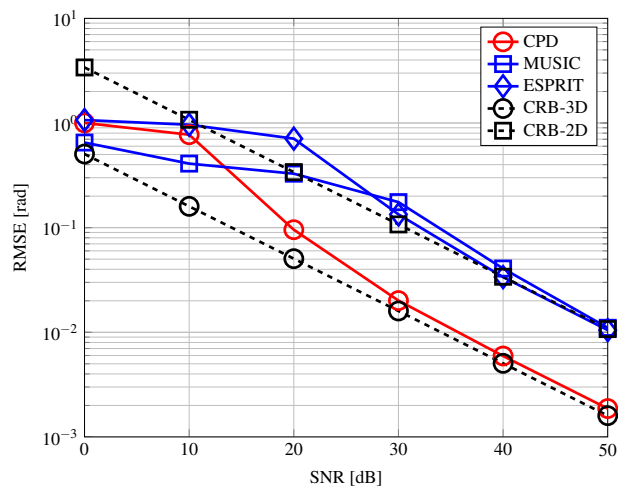
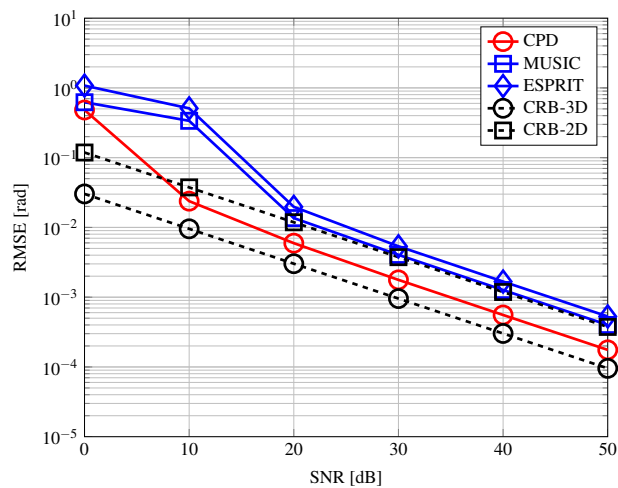
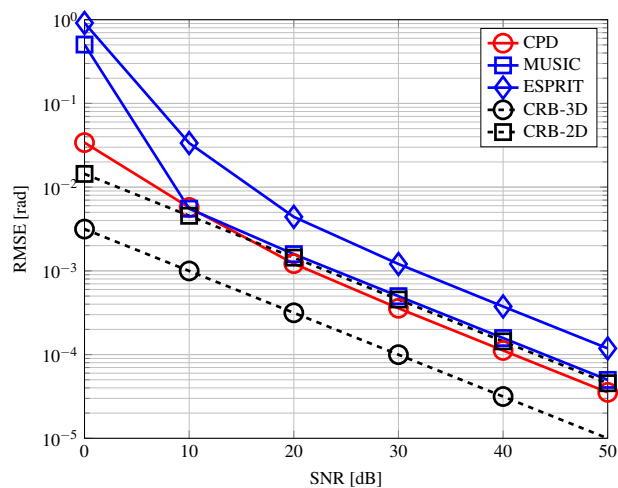
(a) array of  $L = 3$  sensors(b) array of  $L = 10$  sensors(c) array of  $L = 30$  sensors

Figure 9.2.: DoA RMSE [rad] vs SNR [dB] for various numbers of sensors and  $T = 20$  time samples. Broadside perspective: DoAs =  $[80^\circ, 100^\circ]$ .

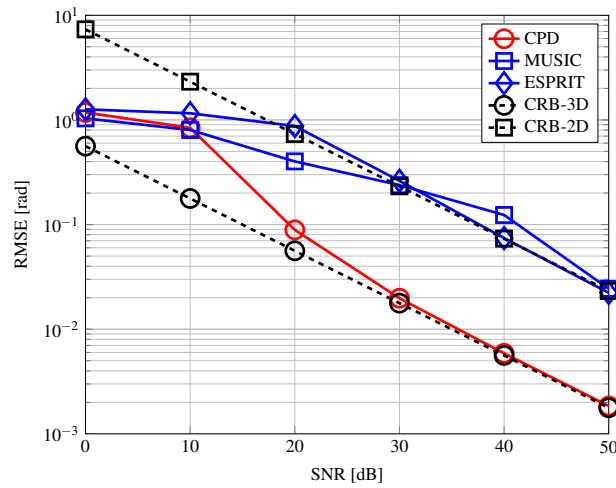
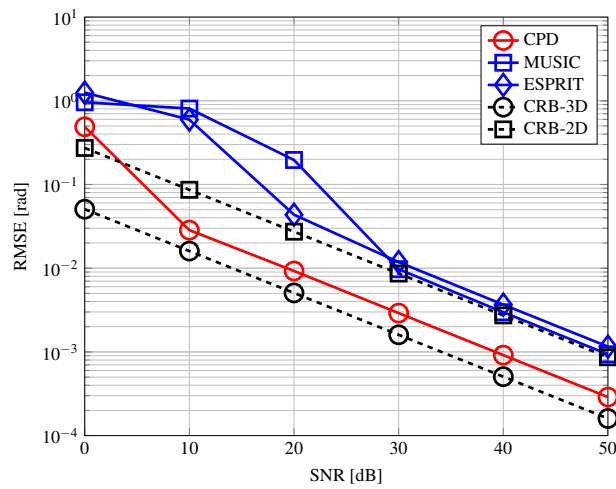
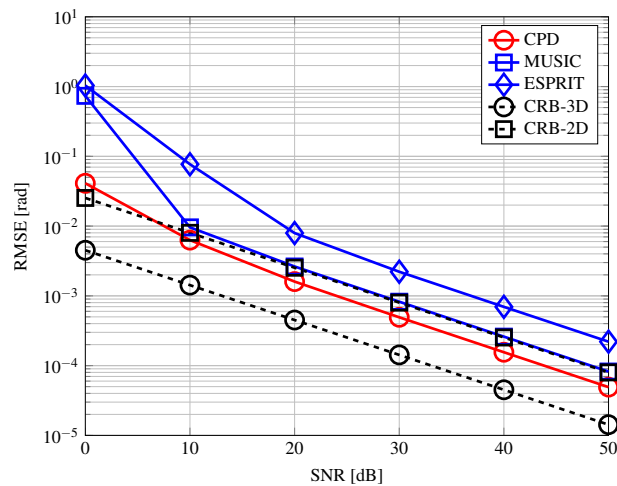
(a) Array of  $L = 3$  sensors(b) Array of  $L = 10$  sensors(c) Array of  $L = 30$  sensors

Figure 9.3.: DoA RMSE [rad] vs SNR [dB] for various numbers of sensors and  $T = 20$  time samples. Endfire perspective: DoAs =  $[30^\circ, 50^\circ]$ .

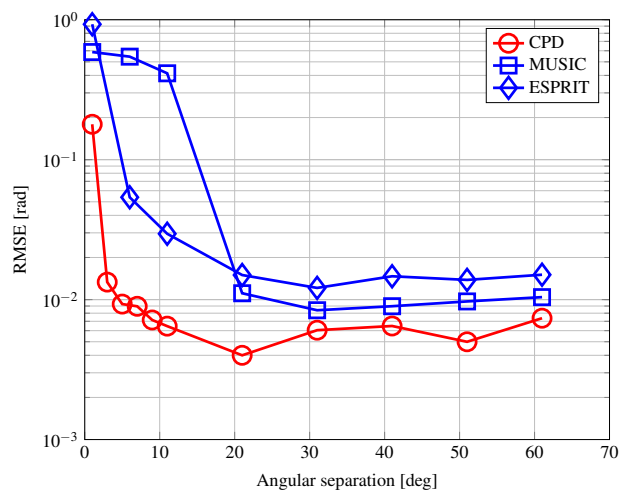


Figure 9.4.: RMSE [rad] vs angular separation [deg] - broadside perspective

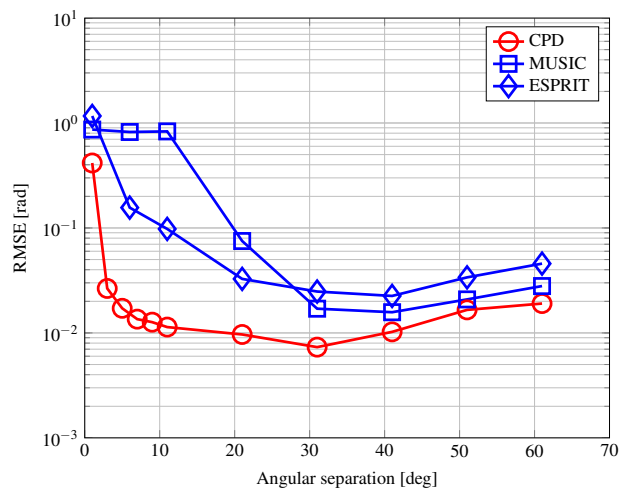


Figure 9.5.: RMSE [rad] vs angular separation [deg] - endfire perspective

## 9.6. Application to Real Seismic Data

We propose a procedure for real seismic data, according to the following order:

1. Detection of an event.
2. Windowing of P and S waves.
3. Alignment of P and S waves.
4. Choice of working frequencies  $f_1$  and  $f_2$ , satisfying assumption A 9.2 and respecting the signal spectral content.
5. Narrowband filtering of P waves around  $f_1$  and of S waves around  $f_2$ .
6. Constitution of the data tensor  $\mathcal{X}$  from the two slices  $\mathbf{X}_{:,1} = \mathbf{X}^{\{P\}}$  and  $\mathbf{X}_{:,2} = \mathbf{X}^{\{S\}}$ .
7. Tensor decomposition of  $\mathcal{X}$ , according to CPD model in (9.7).

Points 1) – 5) constitute a preprocessing stage. Points 6) – 7) are at the core of the tensor approach proposed in Section 9.4. In the present section, we detail some preprocessing steps: windowing, alignment, choice of the working frequencies and filtering.

### 9.6.1. Windowing and Alignment

Since recorded P and S waves are usually consecutive and distinct in time, they need to be selected and cropped, so as to form two  $T \times L$  slices, where  $T$  is the number of time samples, and  $L$  the number of sensors:  $\mathbf{X}_{:,1}$  and  $\mathbf{X}_{:,2}$ . The additive model consists in a deterministic component and random noise:

$$\begin{cases} x^{\{P\}}(t - t_\ell^{\{P\}}) = w_P(t - t_\ell^{\{P\}}) + n_\ell(t - t_\ell^{\{P\}}) \\ x^{\{S\}}(t - t_\ell^{\{S\}} + \xi_{PS}) = w_S(t - t_\ell^{\{S\}} + \xi_{PS}) + n_\ell(t - t_\ell^{\{S\}} + \xi_{PS}) \end{cases} \quad (9.21)$$

where  $\ell = 1, \dots, L$ , and  $\xi_{PS}$  is the alignment error between P and S slices. The narrowband approximation A 1.3 at a given ostensible wavelength  $\lambda = \frac{v_1}{f_1} = \frac{v_2}{f_2}$  gives

$$\begin{cases} x^{\{P\}}(t - t_\ell^{\{P\}}) \simeq \alpha_P w(t) \exp\{-j\varpi_\ell\} + n_\ell(t - t_\ell^{\{P\}}) \\ x^{\{S\}}(t - t_\ell^{\{S\}} + \xi_{PS}) \simeq \alpha_S w(t + \xi_{PS}) \exp\{-j\varpi_\ell\} + n_\ell(t - t_\ell^{\{S\}} + \xi_{PS}) \end{cases} \quad (9.22)$$

where  $\varpi_\ell = \frac{2\pi}{\lambda} \mathbf{p}_\ell^T \mathbf{d}(\theta)$ , and coefficients  $\alpha_P$  and  $\alpha_S$  directly derive from property A 9.3.

Alignment is pursued through cross-correlation between P and S narrowband complex envelopes after the detection process, which is theoretically justified provided signals are jointly stationary and uncorrelated to noise  $n_\ell(t)$  (Assumption A 1.14):

$$\begin{aligned} R_\ell^{PS}(\tau, \xi_{PS}) &= R_\ell^{PS}(\tau + \xi_{PS}) = \\ &= \mathbb{E}\{x^{\{P\}}(t - t_\ell^{\{P\}}) x^{\{S\}}(t - t_\ell^{\{S\}} + \tau + \xi_{PS})\} = \\ &= \alpha_P \alpha_S \exp\{-j2\varpi_\ell\} R^{ww}(\tau + \xi_{PS}) \end{aligned} \quad (9.23)$$

where  $R^{ww}(\tau + \xi_{PS}) = \mathbb{E}\{w(t)w^*(t + \tau + \xi_{PS})\}$ .

If the alignment is fulfilled on the reference sensor ( $\ell = 1$ ), we seek to maximize

$$R_1^{PS}(\tau + \xi_{PS}) = \alpha_P \alpha_S R^{ww}(\tau + \xi_{PS}) \quad (9.24)$$

which attains its maximum for  $\tau_{max} = -\xi_{PS}$ . Once  $\tau_{max}$  is determined, P and S waves can be aligned.

### 9.6.2. Working Frequencies and Filtering

In order to maintain a constant wavelength  $\lambda$ , which is necessary for the separability of the multilinear model in (9.7), a compromise needs to be reached in extracting the dominant frequencies, so as to match the ideal condition  $\lambda = \frac{v_1}{f_1} = \frac{v_2}{f_2}$  in property A 9.2. Within the set of four parameters determining the wavelength  $\lambda$ ,  $\{v_1, v_2, f_1, f_2\}$ , one only needs 3 degrees of freedom to determine optimal working conditions. P and S wave propagation velocities  $v_1$  and  $v_2$  are given by geophysical active analysis of known waves reflecting from the surface to the glacier bed [63], [156]. The only parameter subject to optimization is then P or S wave frequency  $f_1$  or  $f_2$ . If  $f_1$  is chosen as the free parameter and optimized, then  $f_2$  directly derives from property A 9.2

$$f_2 = \frac{v_2}{v_1} f_1 = \frac{v_2}{\lambda} \quad (9.25)$$

The optimization for  $f_1$  is fulfilled by minimizing the square norm of the CPD tensor decomposition error:

$$\hat{f}_1 = \arg \min_{f_1} \left\| \mathbf{x}^{(f_1)} - \sum_{r=1}^R \varsigma_r \hat{\mathbf{a}}_r^{(f_1)} \boxtimes \hat{\mathbf{s}}_r^{(f_1)} \boxtimes \hat{\mathbf{c}}_r^{(f_1)} \right\|^2 \quad (9.26)$$

where  $\mathbf{x}^{(f_1)} = \text{vec}\{\mathcal{X}^{(f_1)}\}$  refers to the data array after narrowband filtering around  $f_1 \in (0, f_S/2)$ , given sampling frequency  $f_S$ ; see (3.46) for the definition of tensor approximation. Then, from Equation (9.25), we have  $\hat{f}_2 = \frac{v_2}{v_1} \hat{f}_1$ .

Recorded P and S waves have to be filtered around  $\hat{f}_1$  and  $\hat{f}_2$  respectively, in order to satisfy the narrowband assumption A 1.3. Moreover, a tradeoff has to be sought with respect to the signal spectral content, in case the ratio of the dominant frequencies does not reflect the ratio of the velocities of P and S waves, according to property A 9.2.

## 9.7. Application to the Argentière Glacier

The Argentière glacier is a 10 km long glacier located in the French side of the Mont Blanc massif, covering a 19 km<sup>2</sup> surface (see pictures in Figure 9.6).



Figure 9.6.: Pictures of the Argentière glacier

It is characterized by high seismic activity, as stated in [124, 125]. Temperate Alpine glaciers are characterized by ice remaining at melting point, deformed by two main mechanisms: plastic deformation of ice and basal sliding. The underneath flow of water plays an important role in basal sliding, because it modifies the water pressure. Furthermore, brittle behavior of ice is the reason of the sudden openings of crevasses and falls of seracs on the surface of a glacier, with indirect effects on glacial hydrology by means of water transfer from the surface to greater depth zones.

An array composed of 9 velocimeters (model is Sismob IHR1C in Figure 9.7, 1 component, 2 Hz eigenfrequency, 1 kHz sampling frequency) pointing in the direction perpendicular to the glacier motion was placed on the glacier surface at 2400 m above sea level (see Figure 9.8).



Figure 9.7.: Pictures of the geophone used for our experiment

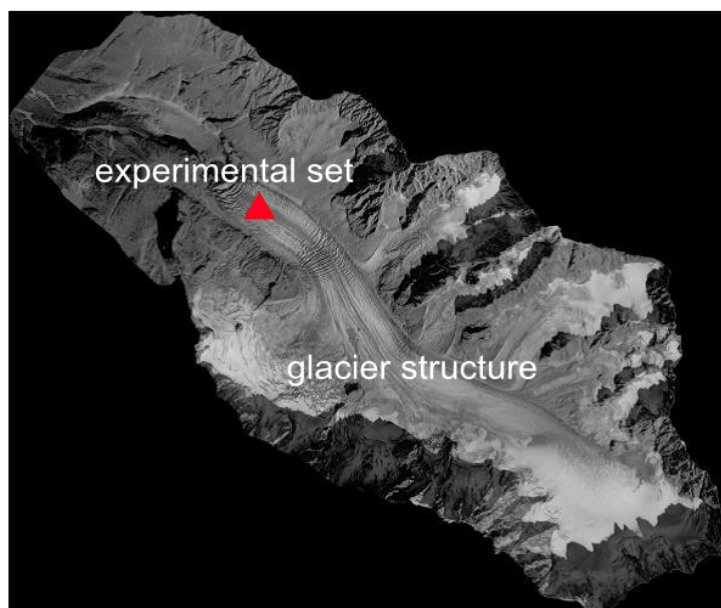


Figure 9.8.: Glacier structure and experimental set

The sensors within the array were spaced out at 10 m intervals, and the thickness of the glacier under the array is about 190 m [63, 155]. Deep events of interest took place at 450 m from the array, at a depth of about 190 m from the surface [63]. The general case involves  $R$  far field sources impinging on the array, at a large unknown distance [63], in the presence of noise, thus allowing us to use the plane wave approximation A 1.1.

Real data from the glacier are processed via speed diversity in Section 9.7.1, repetition diversity in Section 9.7.2, and through the proposed wideband tensor approach in Section 9.7.3.

### 9.7.1. Speed Diversity - Narrowband

The tensor DoA estimation via speed diversity proposed in Section 9.4 was applied to the 27 deep events recorded by the array during November 2012. These events were associated with the same cluster of deep events [63], on the basis of their waveform similarities, through cross-correlation. We use values for P and S wave velocities through ice, as in [150, 63]:  $v_1 = 3600 \text{ m s}^{-1}$  and  $v_2 = 1610 \text{ m s}^{-1}$ , according to Property A 1.21. An example of one deep event recorded by the 9 sensors with distinct P and S waves is provided in Figure 9.9.

The frequency optimization (*i.e.* the choice of the working frequencies  $f_1$  and  $f_2$ ) was achieved throughout the dataset from the same cluster of events, after preprocessing of recorded signals (see Section 9.6.2 for details). Results are shown in Figure 9.10.

The median dominant frequency  $\bar{f}_1$  of the P wave was then calculated. Thus, all the P waves from the cluster are filtered around  $\bar{f}_1 = 229 \text{ Hz}$ , whereas all the S waves are filtered around  $\bar{f}_2 = \frac{v_2}{v_1} \bar{f}_1 = 102 \text{ Hz}$ . Then, tensor CPD estimation in Section 9.4.1 was applied. The narrowband filter bandwidth was  $\text{BW} = 0.015 f_s$ . The derivation of  $\bar{f}_1$  and  $\bar{f}_2$  is coherent with the spectral content of P and S waves, as shown in Figure 9.13.

Beside filtering, we did not deconvolve the signals from any instrument response, because the frequency content of the icequakes is much higher than the resonance frequency of the velocimeters (2 Hz). We thus consider that the instrument response is flat.

DoA estimation is performed over the dataset with the following methods:

**MUSIC** over P and S waves separately.

**ESPRIT** over P and S waves separately.

**CP PS**: joint tensor CPD with speed diversity.

Results are shown in Figure 9.11: the dispersion of the DoA estimates through the joint CPD of P and S waves (CP PS) is smaller than that of MUSIC and ESPRIT for P and S waves separately. ESPRIT yields better results than MUSIC, perhaps because it is more robust to array imperfections, as stated in Section 2.6.2. However, ESPRIT requires two identical subarrays deducible from each other via a translation, whereas the proposed tensor method has no such requirement.

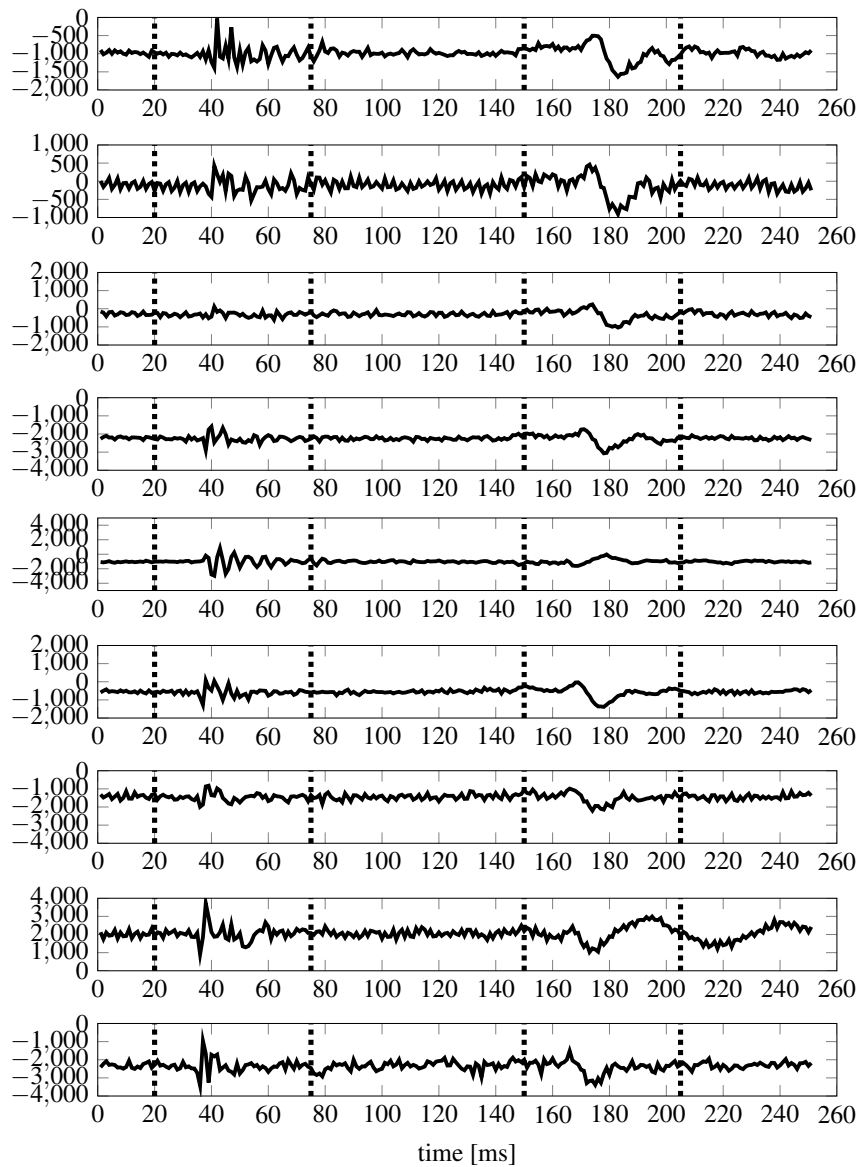


Figure 9.9.: Example of an event at the Argentière glacier - November 2012  
Record from the array with distinct P and S waves - vertical component

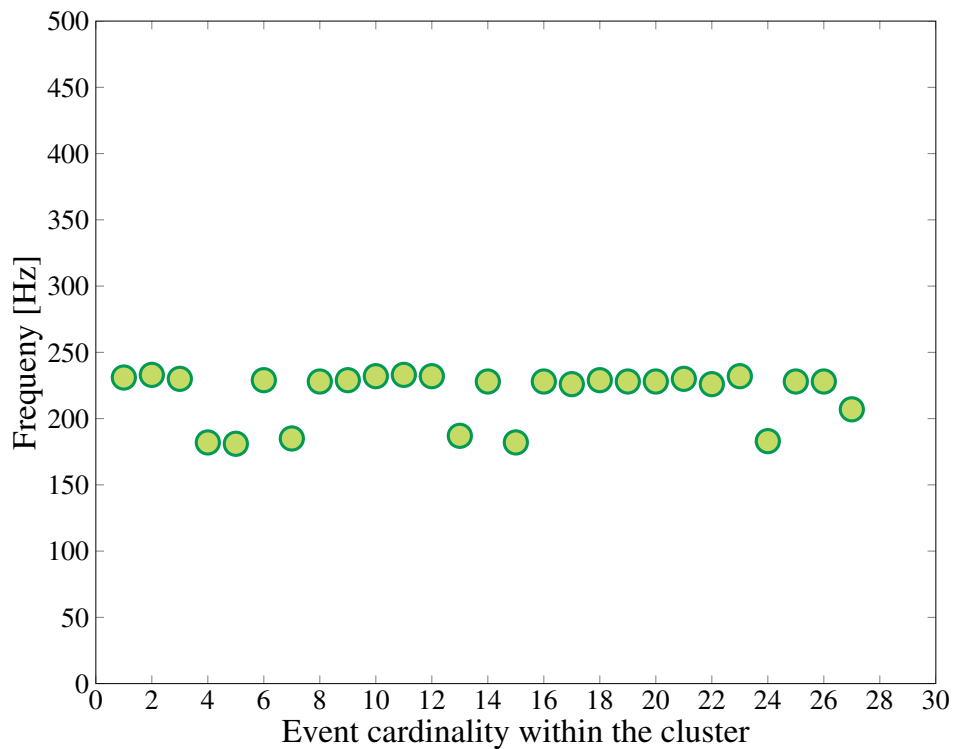
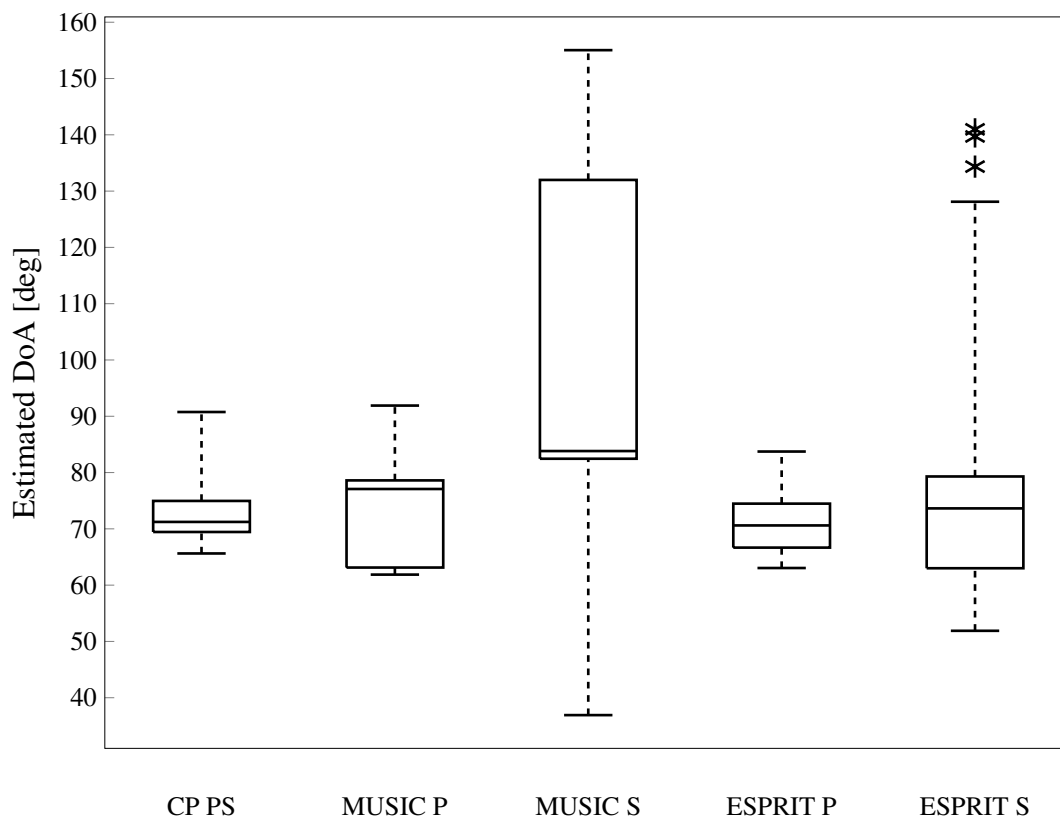
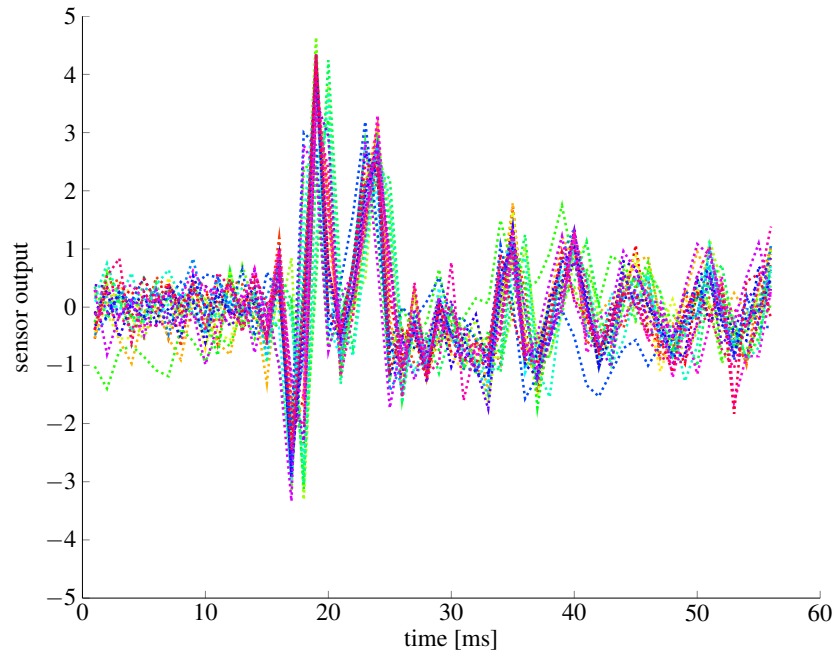
Figure 9.10.: Optimized working frequency for P wave,  $f_1$ 

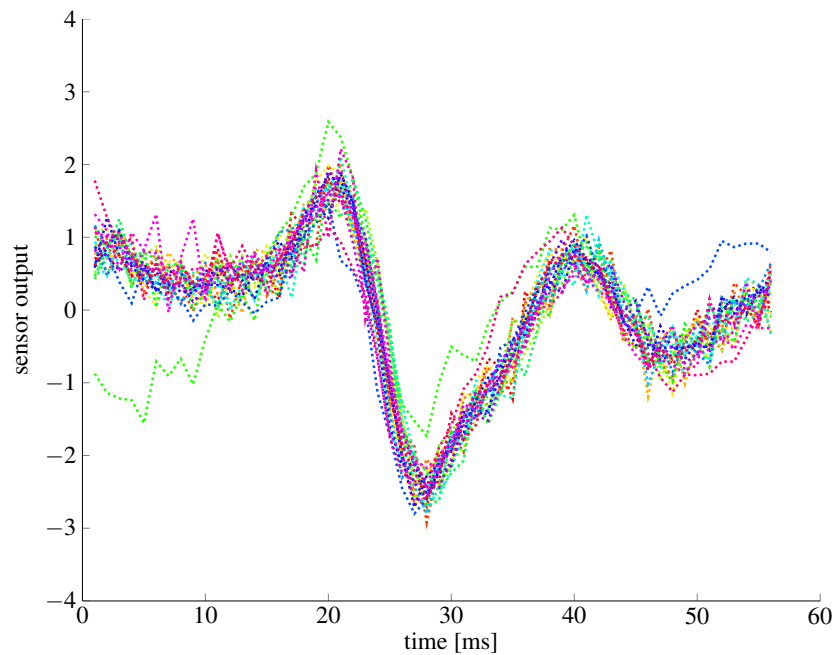
Figure 9.11.: DoA estimation throughout the cluster of deep events - propagation speed

### 9.7.2. Repetition Diversity

Since we deal with multiple events from the same seismic cluster in the depths of the glacier, we can also make use of repetition diversity, as explained in (5.8). Notice that after detection all the events have been previously centered around zero, divided by their standard deviation, and aligned through cross-correlation (see Figure 9.12 for received signals and Figure 9.13 for the estimate of their power spectral density).

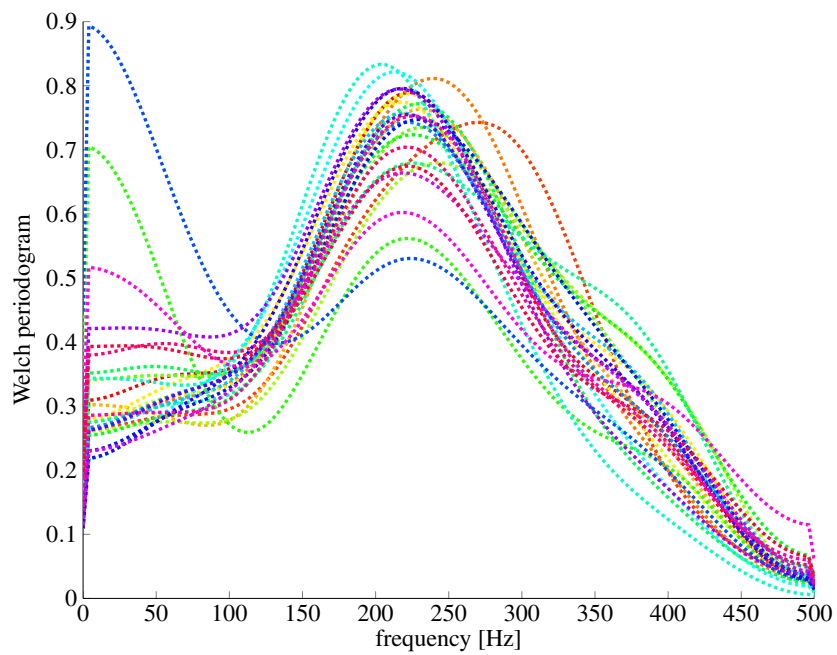


(a) P waves

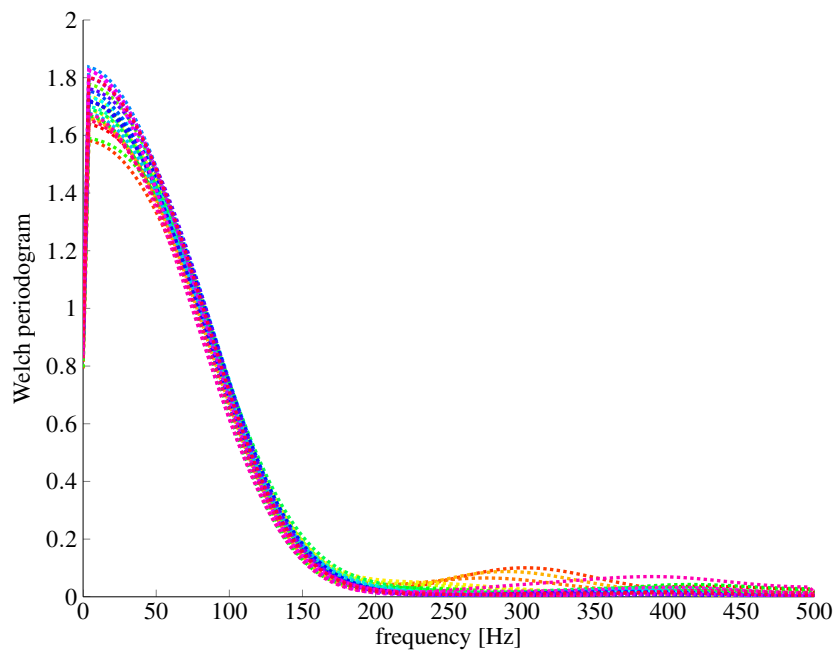


(b) S waves

Figure 9.12.: P and S waves from the same seismic cluster - sensor  $\ell = 6$



(a) P waves



(b) S waves

Figure 9.13.: Welch periodogram of P and S waves from the same seismic cluster - sensor  $\ell = 6$

After filtering P waves around  $f_1 = 229$  Hz and S waves around  $f_2 = 102$  Hz, as in Section 9.7.1, the corresponding narrowband tensor model is the following:

$$g(\mathbf{p}, j, t) = \sum_{r=1}^R \exp \left\{ -j \frac{2\pi}{\lambda} \mathbf{p}^\top \mathbf{d}_r \right\} e_r(j) s_r(t) \quad (9.27)$$

where  $e_r(j)$  is a complex coefficient relying all the events to one another,  $j = 1, \dots, J$  being the cardinality of each event within its cluster. The resulting tensor model writes

$$\begin{cases} \mathcal{X} = \sum_{r=1}^R \mathbf{a}_r \otimes \mathbf{e}_r \otimes \mathbf{s}_r + \mathcal{N} \\ \mathcal{X}_{\ell jt} = \sum_{r=1}^R A_{\ell r} E_{jr} S_{tr} + \mathcal{N}_{\ell jt} \end{cases} \quad (9.28)$$

where

$$\begin{cases} A_{\ell r} = \exp\{-j\omega\tau_\ell(\theta_r)\} \text{ refers to space diversity} \\ E_{jr} = e_r(j) \text{ refers to repetition diversity} \\ S_{tr} = s_r(t) \text{ refers to time diversity} \end{cases} \quad (9.29)$$

In order to fix scaling indeterminacies, in addition to (9.9), we need another condition:

$$e_r(1) = 1, \forall r \implies E_{1r} = 1, \forall r \quad (9.30)$$

This means that we take the first occurrence of each cluster as the reference event equal to  $s_r(t)$ .

Thus, we impose the first rows of matrices  $\mathbf{A}$  and  $\mathbf{E}$  to be formed of ones. Then we pull column-wise the remaining scaling coefficients,  $\{\varsigma_r A_{1r} E_{1r}\}$ , into matrix  $\mathbf{S}$ . More precisely, we fix all scale indeterminacies through the following transformation:

$$(\hat{\mathbf{a}}_r, \hat{\mathbf{e}}_r, \hat{\mathbf{s}}_r, \varsigma_r) \longleftarrow \left( \frac{\mathbf{a}_r}{A_{1r}}, \frac{\mathbf{e}_r}{E_{1r}}, \varsigma_r A_{1r} E_{1r} \mathbf{s}_r, 1 \right) \quad (9.31)$$

This choice permits to compute performance bounds on the retrieval of CPD factors in (9.28) more easily.

Since the sources recorded at the glacier are sequential, i.e they are not simultaneous, and they arise from the same deep cluster, we have  $R = 1$ . Notice that since P and S waves originate from the same deep source, their DoAs should coincide, *i.e.*  $\theta^P \equiv \theta^S$ .

After tensor DoA estimation, we found the following overall DoAs:

- P wave:  $\hat{\theta}^P = 70^\circ$ ;
- S wave:  $\hat{\theta}^S = 76^\circ$ ;

These results are consistent with those in Figure 9.11 of Section 9.7.1.

### 9.7.3. Space Shift Diversity - Wideband

The wideband tensor DoA estimation through spatial resampling proposed in Section 8.2.3 was also applied to the same cluster of deep events. P and S waves were processed separately. The frequency range for P wave was  $[f_1, f_Q] = [50 \text{ Hz}, 350 \text{ Hz}]$ , whereas the frequency range for S waves was  $[f_1, f_Q] = [50 \text{ Hz}, 150 \text{ Hz}]$  (cf. Figure 9.13).

We compare the following techniques:

**BF**: narrowband time domain beamforming, as described in Section 2.4.

**BF TDL**: wideband TDL beamforming in time domain, as described in Section 2.4.

**WB MUSIC**: the wideband MUSIC algorithm with covariance matrix expressed in (2.51).

**NB CP 3**: CPD with  $M = 3$  ULA subarrays of  $L - 2 = 7$  sensors each: standard narrowband CPD (4.5) in time domain as in Chapter 4, after narrowband filtering around  $\bar{f}_1 = 229 \text{ Hz}$  for P waves and  $\bar{f}_2 = 102 \text{ Hz}$  for S waves, as in Section 9.7.1.

**WB CP 2**: WB preprocessing and CPD (8.14) with  $M = 2$  ULA subarrays of  $L - 1 = 8$  sensors each.

**WB CP 3**: WB preprocessing and CPD (8.14) with  $M = 3$  ULA subarrays of  $L - 2 = 7$  sensors each.

**WB CP 4**: WB preprocessing and CPD (8.14) with  $M = 4$  ULA subarrays of  $L - 3 = 6$  sensors each.

Aside from the excellent focalization of beamforming for both P and S waves, let us analyze high resolution methods of Figures 9.14a and 9.14b.

Narrowband tensor estimation of P and S waves separately (NB CP) has a lesser focalization strength compared to the joint narrowband processing (CP PS) of Section 9.7.1 via the diversity of propagation speed in Figure 9.11.

Tensor wideband (WB CP) methods are all equivalent and outperform the wideband MUSIC algorithm as well as tensor narrowband estimation (NB CP). This is probably due to the small size of the P and S events, lasting only few milliseconds ( $T = 56$  time samples), leading to a bad estimate of the covariance matrix.

Finally, tensor wideband estimation (WB CP) outperforms all the other high resolution methods, even tensor narrowband estimation via propagation speed (CP PS). However, WB CP requires quite a regular array geometry, compared to CP PS with propagation speed, which has no such requirement.

Notice that as we do not know the ground truth, we can only evaluate different methods on the basis of the dispersion of their estimates within a cluster. This does not correspond to any actual error on the corresponding estimates, nor does this consider any estimation bias.

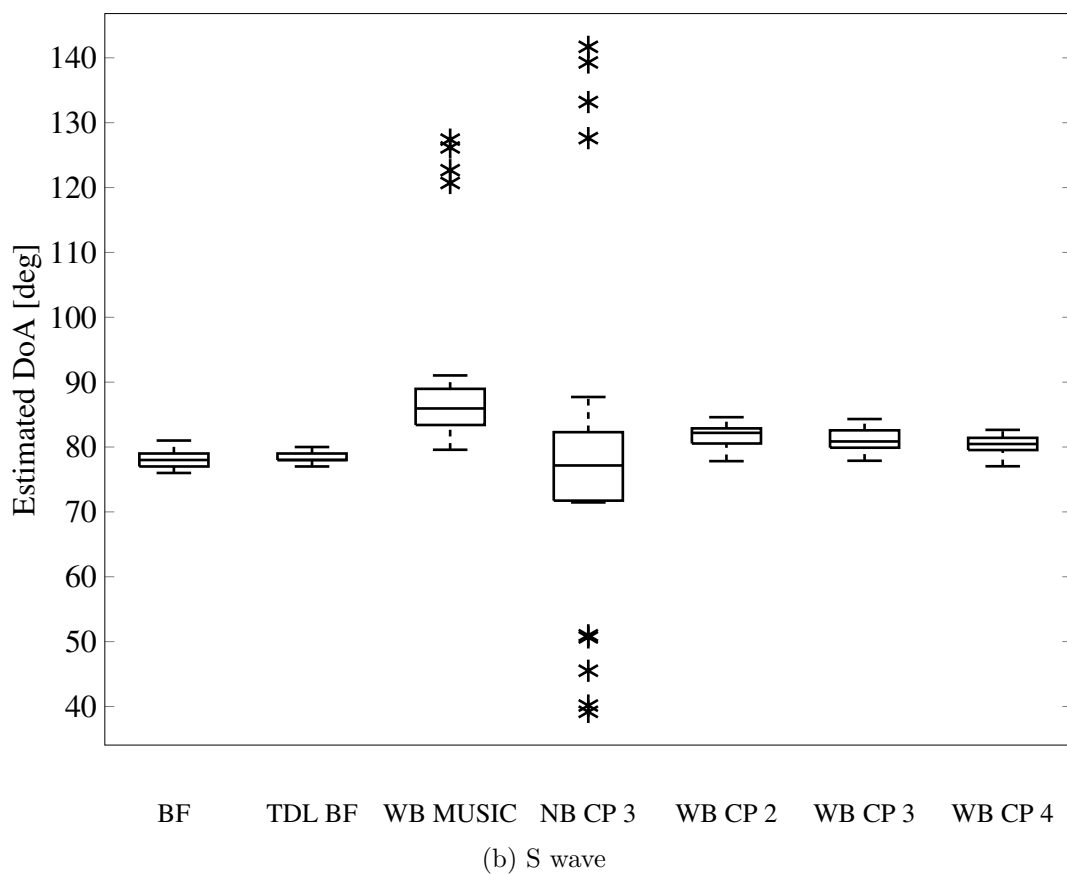
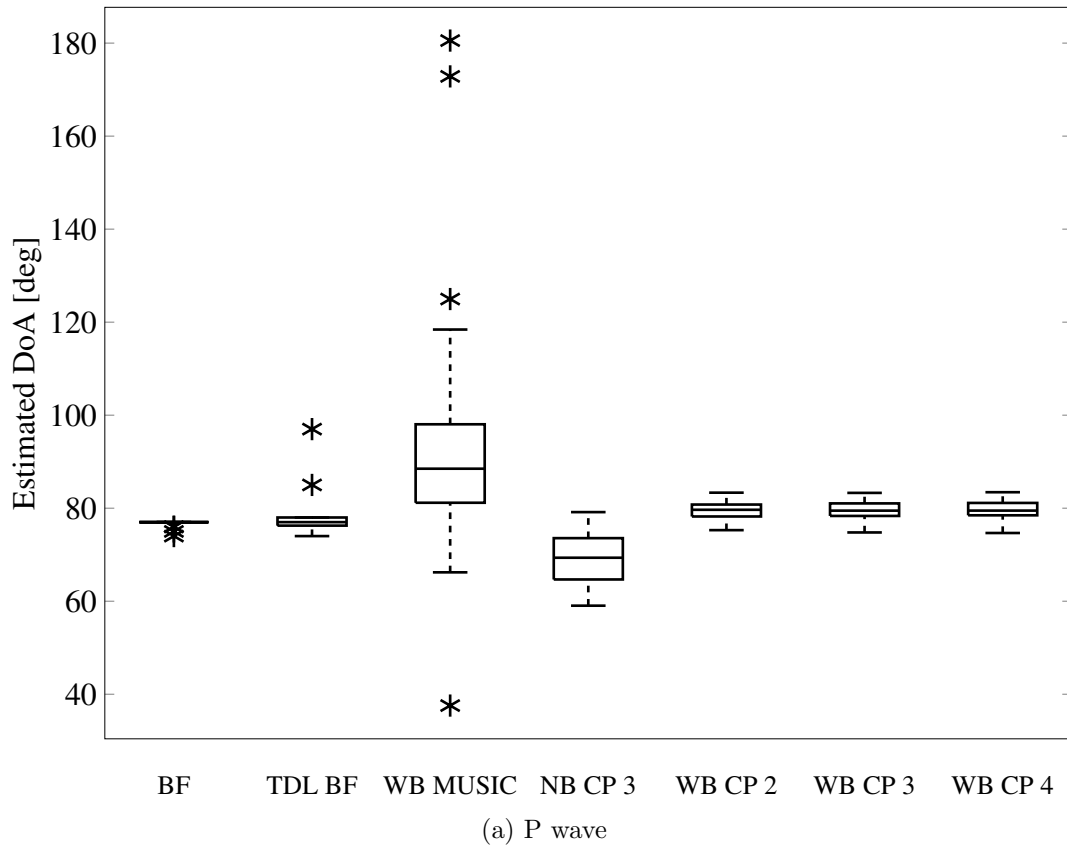


Figure 9.14.: DoA estimation throughout the cluster of deep events - wideband

## 9.8. Conclusion and perspectives

In this chapter, we developed a tensor decomposition model for seismic data exploiting propagation speed diversity of P and S waves. A physical model was traced, followed by simulations and statistical comparisons with ESPRIT and MUSIC, and theoretical CRBs. Our approach was also tested on real data from the seismic activity of an Alpine glacier, and different techniques were compared in terms of localization efficacy.

The strength of our method lies in the integration of the double information conveyed by P and S waves of distant events, impinging in succession on the array: to the traditional dimensions of array processing (recording samples for time and sensor locations for space), we added the dual content transmitted by the P and S waves, temporally distinct by virtue of the diversity of propagation speed. The effect of adding a way to the data array is evident in terms of estimation performance, especially for short data samples and for arrays composed of a small number of sensors. It also increases the localization precision of a cluster of real events originating from the same source.

In the matter of adaptation to real data, since assumption A 1.7 may become, unfortunately, unrealistic, a phase velocity heterogeneity among sensors may be another factor hindering the performance of practical applications.

High resolution methods become essential when the array receives more than one source, especially for closely spaced sources. In this case, beamforming methods are no more suitable. It would be of great interest to evaluate the effectiveness of the proposed methods in this more general scenario.

Another interesting perspective would consist in joining speed diversity at a particular narrow-band with wideband diversity over the whole frequency range of interest. Also, we could possibly extend repetition diversity to the wideband case, and include it into the overall model.

# Appendix

## 9.A. Justification of Assumption A 9.3

The signal propagating from a given source  $r$  and impinging on a given sensor of the array is composed of two contributions before addition to background and instrument noise: the P phenomenon, generally followed by the S phenomenon. If the source is deep enough, these two records are temporally separated (see Section 1.6 for details). The additional assumption A 9.1 identifies the impulse responses of particle motion as the only source of variability between received P and S waves:

$$\begin{aligned} w^{\{1\}}(t) &\approx h^{\{1\}}(t) * w(t) m(t) \\ w^{\{2\}}(t) &\approx h^{\{2\}}(t) * w(t) m(t) \end{aligned}$$

where  $h^{\{1\}}(t)$  is the impulse response of the given medium to the P wave and  $h^{\{2\}}(t)$  to the S wave. The symbol  $*$  indicates convolution. In particular, notice that the source signal can be decomposed into a product of a low-frequency part (the source complex envelope  $w(t)$ ) and a high-frequency contribution  $m(t)$ :

$$w^{\{i\}}(t) \approx h^{\{i\}}(t) * w(t) m(t) \quad (9.32)$$

This corresponds to the base-band complex signal

$$w_b^{\{i\}}(t) \approx h_b^{\{i\}}(t) * w(t) M_+ \exp \{-j 2\pi \Delta_{f_i} t\} \quad (9.33)$$

where  $\exp \{-j 2\pi \Delta_{f_i} t\}$  is a frequency shift due to different demodulation for P and S waves from working frequency  $f_1$  and  $f_2$  respectively, and  $M_+$  is the complex amplitude of  $m(t)$ . In the frequency domain, we have then

$$W_b^{\{i\}}(f) = \mathcal{F}\{w_b^{\{i\}}(t)\}(f) = H_b^{\{i\}}(f) M_+ \left( W(f) * \delta_{\Delta_{f_i}}(f) \right) \quad (9.34)$$

For a generally low-pass transfer function,  $H_b^{\{i\}}(f)$  can be considered as a constant  $H_b^{\{i\}}$  in the band of interest,

$$W_b^{\{i\}}(f) = H_b^{\{i\}} M_+ W(f - \Delta_{f_i}) \quad (9.35)$$

Since band-pass filtering around frequency  $f_i$  and a joint base-band translation are equivalent to a base-band translation from frequency  $f_i$  followed by a low-pass filtering with window  $\Pi(f)$ , we have

$$W_{bf}^{\{i\}}(f) \approx \Pi(f) H_b^{\{i\}} M_+ W(f - \Delta_{f_i}) \quad (9.36)$$

Then we have in time domain, for ideal low-pass filtering  $\Pi(f) \approx \Pi$  in the low-pass support of interest  $[-f_c, +f_c]$

$$w_{bf}^{\{i\}}(t) \propto \left( \Pi H_b^{\{i\}} M_+ \right) [w(t) * 2f_c \text{sinc}(2f_c t)] \quad (9.37)$$

provided that the source complex envelope has a smooth spectrum (almost constant in the narrow band of interest), *i.e.*  $W(f - \Delta_{f_1}) \propto W(f - \Delta_{f_2}) \propto W(f)$ .

Finally, resulting P wave and S wave complex envelopes, after base-band translation and filtering, are related by a proportionality relationship:

$$w_{bf}^{\{2\}}(t) \propto \frac{H_b^{\{2\}}}{H_b^{\{1\}}} w_{bf}^{\{1\}}(t) \quad (9.38)$$

## **Part III.**

# **Contribution: Multidimensional Spectral Factorization**



# 10. Multidimensional Factorization of Seismic Waves

## 10.1. Contribution

The first part of this thesis deal with multilinear decompositions for array processing of wideband elastic waves. Chapter 9 in particular involved the tensor decomposition of seismic waves, with an application to the estimation and localization of icequakes within a glacier.

On the other hand, this chapter moves to the subject of multidimensional spectral factorization of seismic images, illustrating an application to the estimation of the impulse response of the Sun.

Wavefield processing has been applied to several fields of physical sciences. Inverse problems include the estimation of the impulse response of a physical system, such as the earth response to an ideal impulse-like seismic source. On the other hand, seismic migration consists in inferring the signal that would be measured at any depth, starting from data recorded on the surface [48]. More generally, multidimensional digital filters are extensively used in remote sensing, image processing, medical imaging and geophysics. In array processing, multidimensional filters have been used to separate seismic waves based on their polarization or propagation velocity differences [35].

Physical filters are mostly ruled by Partial Differential Equations (PDEs) that can be studied, in some cases, as linear operators through Fourier Transform (FT). Wavefield propagation through an homogeneous medium can be represented by a linear PDE with constant coefficients, and hence the inverse problem is reduced to a  $dD$  deconvolution (and then, to multidimensional linear filtering). If we assume a minimum phase impulse response, and if the source is white in all its dimensions, blind deconvolution is equivalent to spectral factorization [120], which can be tackled through homomorphic deconvolution [146, 147]. This approach has been extended to parametric autoregressive processes through linear prediction (*predictive deconvolution*) [143], and cepstral analysis [130, 74].

In particular, spectral factorization consists in separating causal and anti-causal components in physical systems through decomposition of spectral density functions as the product of minimum phase and maximum phase terms [38]. Cepstrum analysis eases the design of causal filters [101, 99]. The latter have been extended to two dimensions [38, 40, 14, 162, 105], and generalized to the multidimensional case [54], through the definition of  $dD$  *semi-causality*. When dealing with  $dD$  spectral factorization with  $d \geq 2$ , problems arise from the lack of a unique definition of  $dD$  minimum phase, leading to the existence of multiple possible solutions [40]. Mersereau and Dudgeon [91] propose an alternative approach to describe 2D signals, based on a transformation of 2D sequences into 1D vectors, such that linear convolution becomes *helical* (cf. Section 10.2). Helical coordinates were applied later in [120] to blind deconvolution in helioseismology, through spectral factorization, and to other problems in geophysics [43].

The purpose of this chapter is to prove that helical mapping and spectral factorization

are asymptotically equivalent. We will show that the 1D causal solution after helical mapping is not only recursively computable and stable, but asymptotically convergent to the *semi-causal*  $dD$  solution, after inverse remapping.

Sections 10.2 and 10.3 introduce helical mapping, and spectral factorization, respectively. Section 10.4 proves the asymptotic equivalence of helical spectral factorization with its  $dD$  counterpart, whereas Section 10.5 shows how it applies to the case of wave-field propagation. Finally, Section 10.6 presents an example of causal physical filters (the anti-causal component representing the reversed time solution in propagating systems), and an application to helioseismology.

Our work was published in a journal article by Signal Processing, Elsevier [118].

## 10.2. The Helical Coordinate System

Physical fields are generally sampled through space (in a domain  $\Omega \subset \mathbb{R}^3$ ) and time (in a domain  $U \subset \mathbb{R}^+$ ), resulting in a  $dD$  data cube, where  $d \leq 4$ . Under certain conditions (translational invariance through homogeneous and linear media), the underlying processes of propagation can be modeled as Linear Shift Invariant (LSI) filters (including Linear Time Invariant (LTI) and space invariant systems). Moreover, thanks to multilinearity, the measured data cube can be represented as a tensor.

Let us remind some generalities of the tensor formalism that we will employ throughout this chapter. We refer the reader to Chapter 3 for more details. A tensor of order  $d$  is an element of the outer product of vector spaces  $\mathcal{S}_1 \otimes \cdots \otimes \mathcal{S}_d$ , and can be represented by a multi-way array (or multidimensional matrix), once bases of spaces  $\mathcal{S}_i$  have been fixed. The order  $d$  of a tensor corresponds to the number of dimensions of the physical system. The *mode- $i$  fiber* of a tensor is a vector obtained when all indices are fixed except the  $i$ -th. It is often useful to represent a tensor in matrix form [26]: the *mode- $i$  unfolding* of a tensor  $\mathcal{Y} \in \mathbb{R}^{I_1 \times I_2 \times \cdots \times I_d}$  reorders its elements, through arranging the mode- $i$  fibers into columns of a matrix denoted  $\mathbf{Y}_{(i)}$ . Furthermore, it is convenient to represent tensors as vectors: the vectorization of a tensor  $\mathcal{Y}$  is generally defined as a vectorization of the associated mode-1 unfolding matrix, that stacks the columns of  $\mathbf{Y}_{(1)}$  into a vector  $\mathbf{y} \in \mathbb{R}^{I_1 I_2 \cdots I_d}$ . Unfolding and then vectorizing a tensor are equivalent to gradually reducing its order: for instance, a 3D data cube is at first transformed into a matrix and then into a vector. It is clear that there exist potentially multiple ways of unfolding and vectorizing tensors, thus reducing their order, all related to the definition of a particular ordering relation.

Since causality of a LTI filter is related to the implicit order of the computation in convolution,  $dD$  causality is associated with the existence of an ordering relation organizing the elements of the multidimensional data cube. For 1D systems, there is only the natural (or reversed) ordering (*i.e. fully ordered* computation of a linear transformation such as convolution). For  $dD$  systems, the computation is only *partially ordered*, as there are multiple possible ordering relations [38]. In order to implement any  $dD$  linear transformation ( $dD$  convolution,  $dD$  filtering, etc.), there is a need to define an ordering map  $p = I(n_1, n_2, \dots, n_d)$ . Thus, if  $p' = I(n'_1, n'_2, \dots, n'_d)$ ,  $p < p'$  implies that the output at  $(n_1, n_2, \dots, n_d)$  will be computed before the output at  $(n'_1, n'_2, \dots, n'_d)$ .

One of the simplest ordering relations is the helical transformation of a tensor  $\mathcal{Y}$ , that stacks all the elements of any mode- $i$  unfolding, either row-wise or column-wise. Thus, the *helix* is a form of vectorization. Therefore, there exist several possible helical transforms of a tensor, corresponding to a progressive reduction of the order. For instance, the helical transform of a 2D sequence  $f(m, n)$ ,  $m \in \mathbb{N}$ ,  $0 \leq n \leq N - 1$  can be represented as a

row-wise invertible mapping:

$$\phi_1 : \mathbb{N} \times [0 : N - 1] \longrightarrow \mathbb{N}, (m, n) \longmapsto p = Nm + n \quad (10.1)$$

which corresponds to concatenating the rows of the matrix  $f(m, n)$ , with condition of invertibility  $N < \infty$ . Alternatively, the column-wise invertible mapping of a sequence  $f(m, n)$ ,  $0 \leq m \leq M - 1$ ,  $n \in \mathbb{N}$  can be written as

$$\phi_2 : [0 : M - 1] \times \mathbb{N} \longrightarrow \mathbb{N}, (m, n) \longmapsto p = m + Mn \quad (10.2)$$

which corresponds to concatenating the columns of matrix  $f(m, n)$ , with condition of invertibility  $M < \infty$ . Equivalently, one 3D helical mapping of a data cube  $f(\ell, m, n)$  for  $0 \leq \ell \leq L - 1$ ,  $0 \leq m \leq M - 1$ ,  $n \in \mathbb{N}$  is given by

$$\begin{aligned} \phi_3 : [0 : L - 1] \times [0 : M - 1] \times \mathbb{N} &\longrightarrow \mathbb{N} \\ (\ell, m, n) &\longmapsto p = L(Mn + m) + \ell \end{aligned} \quad (10.3)$$

with condition of invertibility  $L, M < \infty$ . In the seventies, Mersereau and Dudgeon [91] defined a helical convolution that transforms 2D convolution through helical periodicity, showing that helical convolution is numerically equal to its 2D counterpart.

## 10.3. Cepstral Factorization

**One-dimensional case** A 1D sequence  $s(n)$  is *causal* if  $s(n) = 0$ , for  $n < 0$ , and *minimum phase* if all the poles and zeros of the Z-transform  $S(z) = \mathcal{Z}\{s(n)\}$  are inside the unit circle  $\{|z| < 1\}$ . If a sequence is minimum phase, it is also causal. Moreover, minimum phase sequences are also *minimum-delay* (all their energy is concentrated close to time origin  $n = 0$ ), they are absolutely summable, and their inverses are both causal and absolutely summable [38].

A means to investigate the question of causality and minimum phase in relation to spectral factorization is homomorphic analysis. The homomorphic transform  $\mathcal{H} = \mathcal{Z}^{-1} \circ \log \circ \mathcal{Z}$  (*i.e.* the inverse Z-transform of the complex logarithm of the Z-transform), with inverse  $\mathcal{H}^{-1} = \mathcal{Z}^{-1} \circ \exp \circ \mathcal{Z}$ , has the advantage of converting convolutions into sums:  $\mathcal{H}\{s_1 * s_2\} = \mathcal{H}\{s_1\} + \mathcal{H}\{s_2\}$ .

The stability condition for a system with impulse response  $s$  is that its transfer function  $S$  converges on a region containing the unit circle  $\{z = e^{i\omega}\}$ , or, equivalently, its domain of convergence includes the locus  $\{|z| = 1\}$ . In this case, the FT,  $\mathcal{F}\{\cdot\}$ , of a sequence can be defined as the restriction of its Z-transform on the unit circle.  $\mathcal{H}$  is then defined as the Inverse Fourier Transform (IFT) of the complex logarithm of its FT,  $\mathcal{H} = \mathcal{F}^{-1} \circ \log \circ \mathcal{F}$ , after phase unwrapping of the complex logarithm [37]. The complex cepstrum of a limited sequence  $s(n)$ ,  $0 \leq n \leq N$ , can be calculated through the Discrete Fourier Transform (DFT), as an aliased version of the true cepstrum [101].

If  $s(n)$  is the autocorrelation of a sequence  $x(n)$  assumed stationary, its homomorphic transform  $\hat{s} = \mathcal{H}\{s\}$  is called *complex cepstrum* and corresponds to the IFT of the logarithm of the spectrum,  $\hat{s} = \mathcal{F}^{-1}\{\log(|X(\omega)|^2)\}$ . In what follows we will refer to positive definite or autocorrelation sequences  $s(n)$ . The complex cepstrum is useful to characterize causality: a sequence  $s(n)$  is minimum phase if its cepstrum is causal [139, 104]:  $\hat{s}(n) = 0$  for  $n < 0$ .

Inversely, maximum phase sequences can be defined as minimum phase sequences reversed in time<sup>1</sup>, and any absolutely summable signal, if conveniently shifted in time, can be expressed as the convolution between minimum and maximum phase parts [38]. As a result, its complex cepstrum is the sum of causal and anti-causal parts, and it is absolutely summable:  $s(n) = s_+(n) * s_-(n)$  corresponds to a product in the frequency domain  $S(\omega) = S_+(\omega)S_-(\omega)$ , and to a sum in the cepstrum domain  $\hat{s}(n) = \hat{s}_+(n) + \hat{s}_-(n)$ . In particular, the poles  $z_i$  of  $S(z)$  such that  $|z_i| < 1$  are associated with the causal part of the cepstrum, whereas the poles such that  $|z_i| > 1$  correspond to the anti-causal part of the cepstrum [139]. The 1D factorization problem consists in decomposing a real (or zero-phase) sequence (such as a power spectral density) into minimum and maximum phase terms.

**Higher-dimensional case** The concept of minimum phase solutions of the spectral factorization problem was extended to 2D signals in [40]. However, the derivation of the concepts of 2D causality and minimum phase from the 1D equivalent is not straightforward, due to the existence of several ordering relations in the  $(x, y)$  plane. From the 2D Z-transform

$$S(z_1, z_2) = \sum_{m=-\infty}^{\infty} \sum_{n=-\infty}^{\infty} s(n_1, n_2) z_1^{-n_1} z_2^{-n_2}, \quad (10.4)$$

the stability condition for a system with impulse response  $s$  is that its transfer function  $S$  converges on a region containing the unit bicircle ( $z_1 = e^{i\omega_1}$ ,  $z_2 = e^{i\omega_2}$ ), or, equivalently, its domain of convergence includes the locus  $\{|z_1|=1, |z_2|=1\}$ . Thus, the 2D FT,  $\mathcal{F}\{\cdot\}$ , of a 2D sequence is defined as the restriction of its Z-transform on the unit bicircle. In what follows, we shall consider spectral density functions  $S(z_1, z_2)$  as the 2D Z-transform of autocorrelations  $s(n_1, n_2)$ . The *2D spectral factorization* is a decomposition of the 2D Z-transform  $S(z_1, z_2)$  into factors that are free of poles and zeros in certain regions of  $\mathbb{C}^2$ . In particular, a sequence  $s(n_1, n_2)$  is said to be *min-min* phase, if none of the poles and zeros of  $S(z_1, z_2)$  lie in the closed domain  $\{|z_1| \geq 1, |z_2| \geq 1\}$ ; *min-mix* phase if none of its poles or zeros lie in  $\{|z_1| \geq 1, |z_2| = 1\}$ . See [40] for further details. We refer to the min-min phase as a *strict* 2D minimum phase.

Analogously, in the 3D case, a sequence  $s(n_1, n_2, n_3)$  is defined as *min-min-min* phase if poles and zeros of its Z-transform  $F(z_1, z_2, z_3)$  do not lie in  $\{|z_1| \geq 1, |z_2| \geq 1, |z_3| \geq 1\}$ .

2D causality can be studied through the 2D complex cepstrum [38], which is defined through 2D homomorphic transform  $\mathcal{H} = \mathcal{Z}^{-1} \circ \log \circ \mathcal{Z}$ :

$$\hat{s}(n_1, n_2) = -\frac{1}{4\pi^2} \oint_{|z_1|=1} \oint_{|z_2|=1} \log[S(z_1, z_2)] \cdot z_1^{n_1-1} z_2^{n_2-1} dz_1 dz_2 \quad (10.5)$$

Then, provided that the unit bicircle is confined in the definition domain of the 2D Z-transform  $S(z_1, z_2)$ , that  $|S(e^{i\omega_1}, e^{i\omega_2})| \neq 0$  for  $-\pi \leq \omega_1, \omega_2 \leq \pi$  and that the phase of the signal has been adjusted to be continuous and periodic in both frequency variables  $\omega_1$  and  $\omega_2$  (*i.e.* 2D phase unwrapping), we can write<sup>2</sup>

$$\hat{s}(n_1, n_2) = \frac{1}{4\pi^2} \int_{-\pi}^{\pi} \int_{-\pi}^{\pi} \log[S(e^{i\omega_1}, e^{i\omega_2})] \cdot e^{i\omega_1 n_1 + i\omega_2 n_2} d\omega_1 d\omega_2 \quad (10.6)$$

<sup>1</sup> A *maximum phase* sequence is anticausal with an anticausal inverse and anticausal complex cepstrum:  $\hat{s}(n) = 0$  for  $n > 0$ .

<sup>2</sup>The complex cepstrum of a time limited sequence  $s(n_1, n_2)$ ,  $0 \leq n_1 \leq N_1, 0 \leq n_2 \leq N_2$  can then be calculated through the 2D DFT [37], as a spatially aliased version of the cepstrum [38].

Based on the definition of Non-Symmetric Half Plane (NSHP) as a region of the form  $\{n_1 \geq 0, n_2 \geq 0\} \cup \{n_1 > 0, n_2 < 0\}$  or  $\{n_1 \geq 0, n_2 \leq 0\} \cup \{n_1 > 0, n_2 > 0\}$  or their rotations, an *admissible region* is the Cartesian product of a sector<sup>3</sup> and a NSHP. Before introducing the subject of multidimensional spectral factorization, we must restate some preliminary results from [40].

**Definition 10.1.** Given a sequence  $x(n_1, n_2)$ , a *projector operator*  $P$  is defined as the multiplication by a window  $w_P(n_1, n_2)$  with support  $\mathcal{R}_w \subset \mathbb{R}^2$ .

**Proposition 10.1.** Let  $s(n_1, n_2)$  be an autocorrelation, or a non negative definite sequence, and its Z-transform be the spectral function  $S(z_1, z_2)$ . The *2D spectral factorization* of  $s$  results in a decomposition of the range of its cepstrum  $\hat{s}$  into admissible regions, through a set of projections operators  $P_k$  whose sum is the identity ( $\prod_k w_k = 0, \sum_k w_k = 1$ ).

Proposition 10.1 is based on a result stated by the theorem below, whose proof can be found in [40]:

**Theorem 10.1.** Let  $\hat{s}$  be the cepstrum of a sequence  $s$  (assuming  $s$  is absolutely summable), and let  $P(\hat{s})$  be its projection on an admissible region, then  $s_P = \mathcal{H}^{-1}\{P(\hat{s})\}$  is recursively computable and stable.

In particular, a sequence  $s(n_1, n_2)$  is *min-min phase* if its cepstrum is causal, *i.e.* with support  $\mathcal{S}_{\hat{s}}$  included in the first quadrant:  $\mathcal{S}_{\hat{s}} \subset \mathcal{R}_{++}$ , with  $\mathcal{R}_{++} := \{n_1 \geq 0, n_2 \geq 0\}$ ; and *semi-minimum phase* if its cepstrum is semi-causal, *i.e.* with support included in the upper NSHP:  $\mathcal{S}_{\hat{s}} \subset \mathcal{R}_{\oplus+}$ , with  $\mathcal{R}_{\oplus+} := \{n_1 \geq 0, n_2 \geq 0\} \cup \{n_1 < 0, n_2 > 0\}$ . In the latter case,  $s(n_1, n_2)$  is minimum-phase only with respect to the variable  $n_2$ , as depicted in Figure 10.1.

Recursive computability is equivalent to the existence of an ordering relation. If the admissible regions coincide with the 4 quadrants, the four projections of the cepstrum on  $\mathbb{R}_{++}, \mathbb{R}_{+-}, \mathbb{R}_{-+}, \mathbb{R}_{--}$  give a four factor decomposition and involve a strong definition of 2D causality (cf. Figure 10.1a). If the admissible regions coincide with the upper and the lower NSHPs, the two projections of the cepstrum on  $\mathbb{R}_{\oplus+}, \mathbb{R}_{\ominus-}$  yield a two factor decomposition and involve a weaker definition of 2D semi-causality (cf. Figure 10.1b) [40]<sup>4</sup>. Through the projection on  $\mathcal{R}_{\oplus+}$  and  $\mathcal{R}_{\ominus-}$ , the cepstrum of the autocorrelation is decomposed into  $\hat{s} = \hat{s}_{\oplus+} + \hat{s}_{\ominus-}$  corresponding, after inverse homomorphic transform, to  $s = \mathcal{H}^{-1}(\hat{s}) = s_{\oplus+} * s_{\ominus-}$ . The two-factor decomposition, based on the definition of NSHPs, is less restrictive than the four factor decomposition, as it can describe the general class of positive definite magnitude functions. A magnitude function, such as the power spectral density in the spectral factorization problem, can be expressed by a limited number of factors, omitting those with conjugate symmetry. Then, for the two factor decomposition we have  $|s(m, n)|^2 = |s_{\oplus+}(m, n)|^2$ .

Spectral factorization was extended in [54] to multiple dimensions so as to process data cubes. It is based on multidimensional homomorphic transform, and on the definition of *dD Non-Symmetric Half Spaces (NSHSs)*, such as the 3D upper NSHS  $\mathcal{R}_{\oplus\oplus+}$ . Thus, all the results presented in this section are easily generalized to the *dD* case.

<sup>3</sup>A *sector*  $S(\alpha, \beta)$  is defined in polar form as  $S(\alpha, \beta) = \{(r, \theta) | r > 0, \alpha < \theta < \beta\}$ .

<sup>4</sup> with  $\mathcal{R}_{+-} := \{n_1 \geq 0, n_2 \leq 0\}$ ,  $\mathcal{R}_{-+} := \{n_1 \leq 0, n_2 \geq 0\}$ ,  $\mathcal{R}_{--} := \{n_1 \leq 0, n_2 \leq 0\}$ , and  $\mathcal{R}_{\ominus-} := \{n_1 \leq 0, n_2 \leq 0\} \cup \{n_1 > 0, n_2 < 0\}$ .

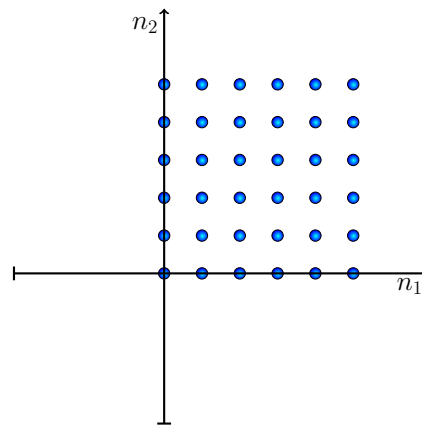
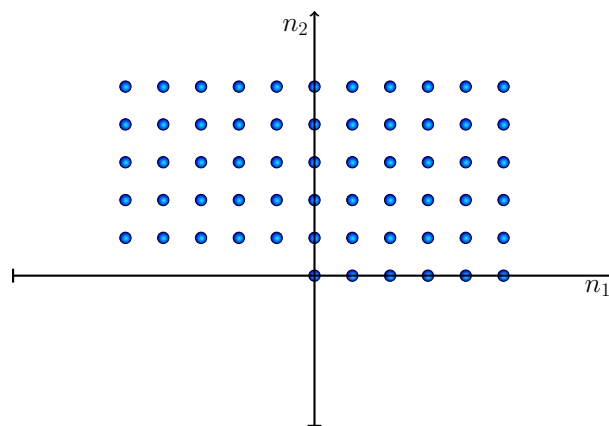
(a)  $\mathcal{R}_{++}$  - 2D causality(b)  $\mathcal{R}_{\oplus+}$  - 2D semi-causality

Figure 10.1.: Examples of admissible regions related to 2D causality

## 10.4. The Effect of the Helical Transform on the Multidimensional Factorization Problem

This section investigates the effects of the helical ordering relation on the multidimensional homomorphic analysis. We can initially state the following fact, which can be easily generalized to  $dD$  systems:

**Proposition 10.2.** Let  $f(m, n)$  define an absolutely summable 2D sequence, from which we want to extract the 2D semi-minimum phase component. Let  $f^{(1)}(p)$  be the helical transform of  $f(m, n)$ , after column-wise mapping  $p = m + Mn$ , and  $f_+^{(1)}(p)$  its 1D minimum phase projection, corresponding to causal cepstrum  $\hat{f}_+^{(1)}(p)$ . Then, after inverse helical mapping of  $f_+^{(1)}(p)$ , the solution  $f_+^{hel}(m, n)$  is recursively computable and stable, and it tends to be, for large  $M$ , the semi-minimum phase solution corresponding to semi-causal cepstrum  $\hat{f}_+(m, n)$  described in Section 10.3.

*Proof.* If we consider the discrete variable  $m$  bounded by  $M < \infty$  and we allow the variable  $n$  to be unbounded ( $n \in \mathbb{N}$ ), the helical transformation of the dataset  $f(m, n)$ ,  $f^{(1)}(p)$ , is equivalent to a periodization of  $f(m, n)$  with respect to the bounded variable  $m$ . After helical transform, the causal component of the 1D cepstrum  $\hat{f}^{(1)}(p)$  is given by the contribution for positive  $p$ . Through the projection operator in Proposition 10.1, the 1D complex cepstrum  $\hat{f}^{(1)} = \hat{f}_+^{(1)} + \hat{f}_-^{(1)}$  is decomposed into its causal and anti-causal components, so that  $f^{(1)} = f_+^{(1)} * f_-^{(1)}$  and  $\hat{f}_+^{(1)}(p) \neq 0$  for  $p \geq 0$ . Now,  $p \geq 0$  is equivalent to  $m + Mn \geq 0$  after helical transform, and then to the NSHP  $n > -m/M$  on the 2D plane  $(m, n)$ :

$$\hat{f}_+^{hel}(m, n) \neq 0 \text{ for } n > -m/M \quad (10.7)$$

Thus, the helical transformation fixes one particular instance among all the possible canonical factorizations. This means that after inverse mapping of the helical minimum phase solution, the support of the 2D cepstrum becomes an upper NSHP rotated of an angle  $\theta = \arctan(-1/M)$ . Since any rotated NSHP is an admissible region, according to Theorem 10.1, the resulting 2D filter  $f_+^{hel}(m, n) = \mathcal{H}^{-1}\{\hat{f}_+^{hel}(m, n)\}$  is recursively computable and stable. If  $M \rightarrow \infty$ , the rotation becomes irrelevant (as  $\theta \rightarrow 0$ ), and the support of the solution  $f_+^{hel}(m, n)$  and of its cepstrum coincides with the upper NSHP  $\mathcal{R}_{\oplus+}$  defined in Section 10.3 (cf. Figure 10.2).  $\square$

Moreover, we can state the following corollary:

**Corollary 10.1.** Since the two factor decomposition of [40] leads to a semi-minimum phase term which is minimum phase only in one variable,  $M \rightarrow \infty$  implies that the helical solution  $f_+^{hel}(m, n)$  is minimum phase with respect to the variable  $n$ .

Separable functions have noteworthy properties. We can state the following proposition for 2D functions (we choose to describe the 2D case for sake of simplicity, without restricting the generality):

**Proposition 10.3.** If the 2D function  $f(m, n)$  is separable, *i.e.* if  $f(m, n) = u(m)v(n)$ , the following two facts hold:

1. The 2D cepstrum of a separable function is given by  $\hat{f}(m, n) = \hat{u}(m)\delta(n) + \hat{v}(n)\delta(m)$ , that is non zero only on the axes of the  $(m, n)$  plane. Therefore, 2D semi-causality of the cepstrum  $\hat{f}$  is equivalent to strict 2D causality (*i.e.* the half-plane support reduces to two lines in the plane  $(m, n)$ ): cf. Figure 10.3.

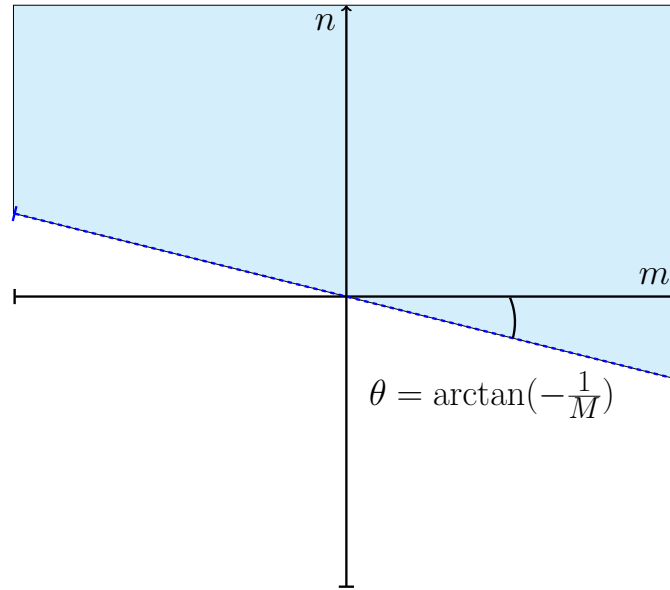


Figure 10.2.: Semi-causal cepstrum after inverse helix transform

2. The 1D cepstrum of the vectorized data  $f^{(1)}(p)$  is given by  $\hat{f}^{(1)}(p) = \hat{u}(p) + \frac{1}{M} \hat{v}\left(\frac{p}{M}\right)$ . Helical cepstrum  $\hat{f}^{(1)}$  is then causal if and only if 1D cepstra  $\hat{u}$  and  $\hat{v}$  are both causal, and thus, from 1) if and only if 2D cepstrum  $\hat{f}$  is strictly causal. Therefore, the equivalence between strict 2D minimum phase of  $f$  and 1D minimum phase of its helix  $f^{(1)}$  is always verified, not only asymptotically.

*Proof.* Let us define a function  $f(m, n)$ ,  $0 \leq m \leq M - 1$ ,  $n \in \mathbb{N}$ , that is separable with respect to its two variables:

$$f(m, n) = u(m) v(n) \quad (10.8)$$

Then, its Z-transform is also separable in the frequency domain:

$$\begin{aligned} F(z_1, z_2) &= \sum_{m=0}^{M-1} \sum_{n=0}^{\infty} f(m, n) z_1^{-m} z_2^{-n} = \\ &= \sum_{m=0}^{M-1} \sum_{n=0}^{\infty} u(m) v(n) z_1^{-m} z_2^{-n} = \\ &= U(z_1) V(z_2) \end{aligned} \quad (10.9)$$

Since  $\log[F(z_1, z_2)] = \log U(z_1) + \log V(z_2)$ , the cepstrum becomes

$$\begin{aligned}
 \hat{f}(m, n) &= -\frac{1}{4\pi^2} \oint_{|z_1|=1} \oint_{|z_2|=1} \log[F(z_1, z_2)] z_1^{n_1-1} z_2^{n_2-1} dz_1 dz_2 = \\
 &= \frac{1}{4\pi^2} \int_{-\pi}^{\pi} \int_{-\pi}^{\pi} \log[F(e^{i\omega_1}, e^{i\omega_2})] e^{i\omega_1 m} e^{i\omega_2 n} d\omega_1 d\omega_2 = \\
 &= \frac{1}{4\pi^2} \int_{-\pi}^{\pi} \int_{-\pi}^{\pi} [\log U(e^{i\omega_1}) + \log V(e^{i\omega_2})] e^{i\omega_1 m} e^{i\omega_2 n} d\omega_1 d\omega_2 = \\
 &= \hat{u}(m) \delta(n) + \hat{v}(n) \delta(m)
 \end{aligned} \tag{10.10}$$

We calculate then 1D log cepstrum of  $f^{(1)}(p)$ , the helical transform of  $f$ :

$$\begin{aligned}
 \log[F^{(1)}(z)] &= \log \left[ \sum_{p=0}^{\infty} f^{(1)}(p) z^{-p} \right] = \log[F(z, z^M)] = \\
 &= \log \left[ \sum_{m=0}^{M-1} u(m) z^{-m} \sum_{n=0}^{\infty} v(n) z^{-Mn} \right] = \\
 &= \log \left[ \sum_{m=0}^{M-1} u(m) z^{-m} \right] + \log \left[ \sum_{n=0}^{\infty} v(n) z^{-Mn} \right] = \\
 &= \log[U(z)] + \log[V(z^M)]
 \end{aligned} \tag{10.11}$$

Thus the cepstrum of a separable function is given by

$$\begin{aligned}
 \hat{f}^{(1)}(p) &= \frac{1}{2\pi i} \oint_{|z|=1} \log [F^{(1)}(z)] z^{p-1} dz = \\
 &= \frac{1}{2\pi} \int_{-\pi}^{\pi} \log [F^{(1)}(e^{i\omega})] e^{i\omega p} d\omega = \\
 &= \frac{1}{2\pi} \int_{-\pi}^{\pi} \{ \log [U(e^{i\omega})] + \log [V(e^{i\omega M})] \} e^{i\omega p} d\omega = \\
 &= \hat{u}(p) + \frac{1}{M} \hat{v} \left( \frac{p}{M} \right)
 \end{aligned} \tag{10.12}$$

□

The same conclusions hold for a separable function of three or more variables.

We also give an alternative proof of these facts in the Z-domain, in the case of separable functions of three variables: the periodization along one dimension corresponds to a re-mapping and increase in number of poles and zeros of the Z-transform, that nevertheless maintain the same modulus.

*Proof.* Let us calculate the Z-transform of a finite sequence of three variables,  $f(n_x, n_y, n_t)$ , with  $0 \leq n_x \leq N_x$ ,  $0 \leq n_y \leq N_y$  and  $n_t \in \mathbb{N}$ :

$$F(z_x, z_y, z_t) = \sum_{n_x=0}^{N_x-1} \sum_{n_y=0}^{N_y-1} \sum_{n_t=0}^{\infty} f(n_x, n_y, n_t) \cdot z_x^{-n_x} z_y^{-n_y} z_t^{-n_t} \tag{10.13}$$

Helical boundary conditions are defined through the helical bijection

$$\begin{aligned}
 \phi : [0 : N_x - 1] \times [0 : N_y - 1] \times \mathbb{N} &\longrightarrow \mathbb{N} \\
 (n_x, n_y, n_t) &\longmapsto n_z = N_x(N_y n_t + n_y) + n_x
 \end{aligned} \tag{10.14}$$

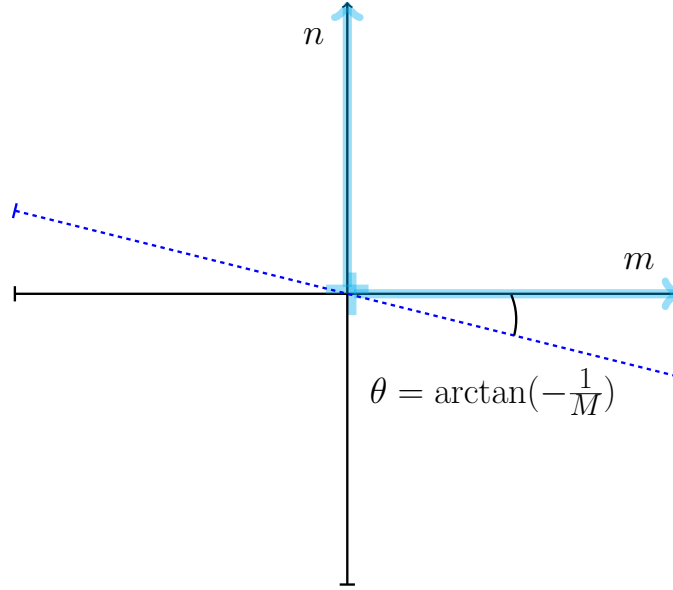


Figure 10.3.: Semi-causal cepstrum for a separable function

Starting from the original 3D function, we can thus define the 1D helical vectorization (or *helix*) as  $f^{(1)} = f \circ \phi$ , with Z-transform

$$F^{(1)}(z) = \sum_{n_z=0}^{\infty} f^{(1)}(n_z) z^{-n_z} \quad (10.15)$$

We can then express  $F^{(1)}$  in relation to  $F$  as

$$\begin{aligned} F^{(1)}(z) &= \sum_{n_x=0}^{N_x-1} \sum_{n_y=0}^{N_y-1} \sum_{n_t=0}^{\infty} f^{(1)}(N_x(N_y n_t + n_y) + n_x) \cdot z^{-(N_x(N_y n_t + n_y) + n_x)} = \\ &= \sum_{n_x=0}^{N_x-1} \sum_{n_y=0}^{N_y-1} \sum_{n_t=0}^{\infty} f(n_x, n_y, n_t) z^{-n_x} (z^{N_x})^{-n_y} (z^{N_x N_y})^{-n_t} \end{aligned} \quad (10.16)$$

Therefore,

$$F^{(1)}(z) = F(z, z^{N_x}, z^{N_x N_y}) \quad (10.17)$$

Let us consider the polynomial expression of  $F$ , in the case of a separable function  $f$ . For sake of simplicity, the polynomial function is assumed to be an all-zeros function, with a finite number of roots:

$$F(z_x, z_y, z_t) = A \prod_{i_x=1}^{N_{\alpha,x}} (z_x - \alpha_{i_x}) \prod_{i_y=1}^{N_{\alpha,y}} (z_y - \alpha_{i_y}) \prod_{i_t=1}^{N_{\alpha,t}} (z_t - \alpha_{i_t}) \quad (10.18)$$

On the other hand, from (10.17) we derive the polynomial expression of  $F^{(1)}$ :

$$F^{(1)}(z) = A \prod_{i_x=1}^{N_{\alpha,x}} (z - \alpha_{i_x}) \prod_{i_y=1}^{N_{\alpha,y}} (z^{N_x} - \alpha_{i_y}) \prod_{i_t=1}^{N_{\alpha,t}} (z^{N_x N_y} - \alpha_{i_t}) \quad (10.19)$$

The following remarks can be made:

1.  $F^{(1)}$  shares its zeros  $\alpha_{i_x}$  with  $F$ .
2. For each zero  $\alpha_{i_y}$  of  $F$ ,  $F^{(1)}$  has  $N_x$  corresponding new zeros,
 
$$\alpha_{i_y,k}^{(1)} = |\alpha_{i_y}|^{1/N_x} e^{i2\pi k/N_x}$$
3. For each zero  $\alpha_{i_t}$  of  $F$ ,  $F^{(1)}$  has  $N_x N_y$  corresponding new zeros,
 
$$\alpha_{i_y,l}^{(1)} = |\alpha_{i_y}|^{1/(N_x N_y)} e^{i2\pi l/(N_x N_y)}$$

Consequently, the zeros of  $F^{(1)}$  lie inside the unit circle if and only if the zeros of  $F$  are inside the unit circle. The same considerations can be made for a rational function  $F$  with poles at the denominator.  $\square$

Thus, this result can be easily generalized to  $dD$  and leads to the following statement:

**Proposition 10.4.** If the variables of  $f(n_1, n_2, \dots, n_d)$  separate, 1D minimum phase of its helical transform  $f^{(1)}$  is equivalent to strict  $dD$  minimum phase of the  $dD$  sequence  $f$ . This equivalence is always verified, not only asymptotically.

## 10.5. Helical Mapping for Wavefield Propagation

PDEs describing wave propagation generally have two possible solutions:  $f_+$  is forward propagating and then causal, whereas  $f_-$  is back propagating and then anti-causal; see Eq. (10.20) for an example. Let  $f(x, t)$  be the general solution of a PDE describing wave propagation, sampled in space  $x_m = m\Delta$  and time  $t_n = nT$ . We want to recover the causal solution of the wave equation through spectral factorization with helical mapping, on the basis of the following result:

**Proposition 10.5.** The helical processing of the data matrix  $f(m, n)$  can lead to the cancellation of the back propagating solution of the PDE, if the helical vectorization  $f^{(1)}(p)$  is performed column-wise, *i.e.*  $p = m + Mn$  (thus periodizing  $f(m, n)$  with respect to space).

*Proof.* Since the back-propagating term coincides with the forward (causal) propagating solution  $f_{\oplus+}$  reversed in time, it represents the semi-maximum phase component of the power spectral density,  $f_{\ominus-}$ . Now, thanks to Proposition 10.2, if the helix is constructed through periodization with respect to space, the minimum-phase term  $f_+^{(1)}$  will asymptotically correspond (for large  $M$  and after remapping to the 2D space), to the semi-minimum phase term of the two factor decomposition,  $f_{\oplus+}$ . Thus, according to Corollary 10.1, it will be minimum phase with respect to time and approximate the forward propagating solution.  $\square$

In the frequency domain, the extraction of the semi-minimum phase solution  $f_{\oplus+}$  is equivalent to applying an all-pass phase-only filter to the data. This is consistent with [48], where the boundary condition (at the surface) of the wave equation needs to cancel the back propagating solution through convolution with a semi-causal filter.

In order to illustrate Proposition 10.5 with a straightforward example, we make the assumption of an homogeneous medium, with constant propagation speed  $c$ . However, we

want to integrate the viscosity  $\alpha$  and the absorbance  $\beta$  of the medium into the 1D wave equation (this translates into attenuation of waves in space and time):

$$c^2 \frac{\partial^2 \Phi}{\partial x^2} = \frac{\partial^2 \Phi}{\partial t^2} + \alpha \frac{\partial \Phi}{\partial x} + \beta \frac{\partial \Phi}{\partial t} \quad (10.20)$$

The general solution of (10.20) is expressed by

$$\Phi(x, t) = \mathcal{F}(x - ct) + \mathcal{G}(x + ct) \quad (10.21)$$

For a plane wave equation corresponding to eigenmode  $\omega$ , this yields

$$f_\omega(x, t) = A_0 e^{i(kx - \omega t)} e^{-\alpha x} e^{-\beta t} + B_0 e^{i(kx + \omega t)} e^{-\alpha x} e^{\beta t} \quad (10.22)$$

The causal solution is embedded in the first term ( $B_0 = 0$ ). After sampling with periods  $\Delta$  for space and  $T$  for time, the continuous and discrete causal solutions of (10.20) take the expressions

$$\begin{cases} f(x, t) = A_0 e^{-\alpha x} e^{-\beta t} e^{ikx} e^{-i\omega t} \\ f(m, n) = A_0 e^{-\alpha m \Delta} e^{-\beta n T} e^{ikm \Delta} e^{-i\omega n T} \end{cases} \quad (10.23)$$

The attenuated propagating wave in (10.23) can be considered as the impulse response of the propagative system:  $f(m, n) = \delta(m, n) * h(m, n) = h(m, n)$ . Section 10.A details the computation of the poles and zeros of the Z-transform of the causal solution of the wave equation, and discusses the effects of the helical mapping in the Z domain. Furthermore, Section 10.A shows how the back-propagating solution of (10.20) corresponds to the minimum phase term, reversed in time.

## 10.6. Application to Physical Systems

Helical coordinates have been used in helioseismology [120] for the estimation of a minimum phase impulse response. More generally, physical environments involving the propagation of waves, like the interior of the sun for helioseismology or the Earth volume for passive seismic, can be represented as convolutive systems [143]. Simulated data are generated by a convolutive propagative system  $d(x, t) = s(x, t) * h(x, t)$  where  $s(x, t)$  refers to the excitation signature and  $h(x, t)$  to the impulse response. The FT of the data matrix is then expressed as the product  $D(k_x, \omega) = S(k_x, \omega) H(k_x, \omega)$ . In the examples presented in this chapter, we aim at estimating the acoustic impulse response of the Sun,  $h(x, t)$ , including internal reverberations. We make the assumptions that seismic excitation  $s(x, t)$ , generated by small *sunquakes*, is uncorrelated in space and time, so that the power spectral density of  $d(x, t)$ ,  $|S_d(\omega_x, \omega)|^2$ , equals  $|H(\omega_x, \omega)|^2$  up to a scale factor, and that  $h$  is semi-minimum phase. In 10.B we detail the two algorithms used for comparison: on one hand the *dD* spectral factorization (Algorithm 10.1), on the other hand the helical spectral factorization (Algorithm 10.2).

Figure 10.4 (a) and (b) show simulated data for  $M = N = 1024$  and the impulse response of the system, modeled as a Ricker wavelet [49]:

$$h(x, t) \propto \frac{1}{\sqrt{2\pi}\sigma^2} \left\{ 1 - \frac{[t - \tau(x)]^2}{\sigma^2} \right\} e^{-\frac{[t - \tau(x)]^2}{2\sigma^2}}, \quad (10.24)$$

where  $\tau(x) = \sqrt{x^2 + R^2}/v$ , and  $R$  and  $v$  indicate the distance and the propagation speed of the source, respectively. Temporal and spatial sampling periods are fixed at 20 ms and

5 m, and  $\sigma = 0.01$ . The random excitation is modeled as a Gaussian white noise with unit variance, in both dimensions:  $s \sim \mathcal{N}(0, \mathbb{I})$ .

Figures 10.5 (a) and 10.6 (a) show the estimated impulse responses  $\hat{h}$  through the helical procedure described in Algorithm 10.2, for a Dirac source and a random source, respectively. Correspondingly, Figures 10.5 (b) and 10.6 (b) show the distribution of the estimation error with respect to the true impulse response  $h$ .

Figure 10.7 (a) shows the total approximation error  $e^{tot} = \|f_+^{(1)}(p) - f_+(m, n)^{(1)}\|^2$  of the helical minimum phase solution (Algorithm 10.2) with respect to the 2D semi-minimum phase solution (Algorithm 10.1), as a decreasing function of the number of space samples  $M$ . This can be interpreted as a confirmation of the asymptotic equivalence of the two solutions stated in Proposition 10.2. Another measure of the quality of the approximation is expressed by the correlation coefficient  $R$  between the two solutions, illustrated in Figure 10.7 (b) as an increasing function of the number of space samples  $M$ .

The algorithm was then applied to 3D solar data in Figure 10.8 (for more information about the experimental setup, cf. [138]), and the Sun impulse response was estimated through helical spectral factorization: in Figure 10.9 (a) and (b), we present our results for a given time instant and space location. Figure 10.10 shows the correlation coefficient between the helical and the 3D solutions, as a function of the number of samples along the  $x$  and  $y$ -axes, and along the time axis. The estimated impulse response with multiple reflections is consistent with results in [120] and it seems to be related to a propagative system where seismic waves are reverberated at least three times within the Sun (cf. Figure 10.9 (b)).

## Conclusion

This chapter gives a theoretical foundation to the relevance of helical boundary conditions, *i.e.* a generalization of the vectorization of a multidimensional array, for the spectral factorization problem. Effects of this representation are detailed in the cepstral domain and in the  $Z$  domain, and the proposed technique is then illustrated through an example of blind deconvolution for a propagative system, and an application to helioseismology.

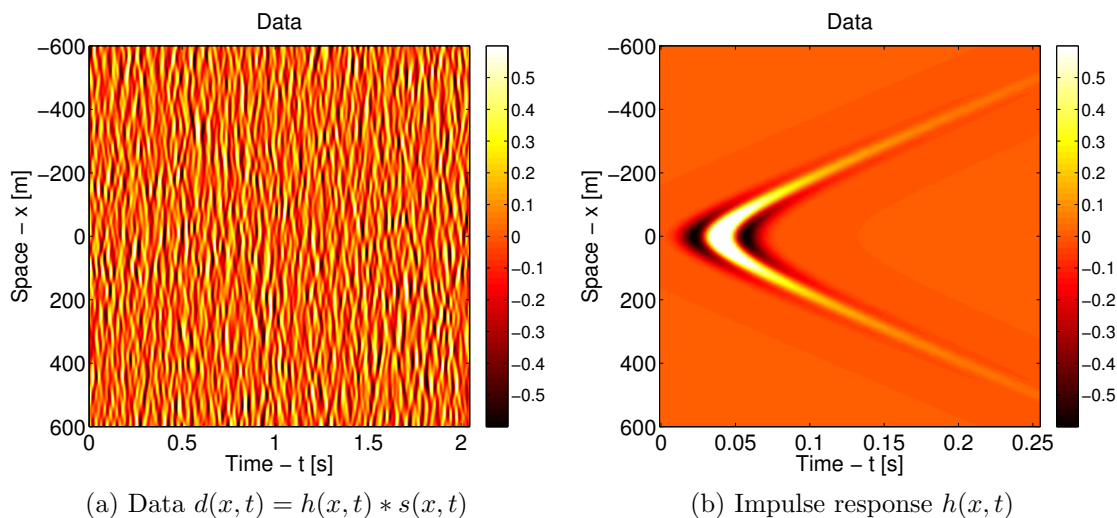


Figure 10.4.: Simulated 2D data and impulse response in the plane  $(x, t)$

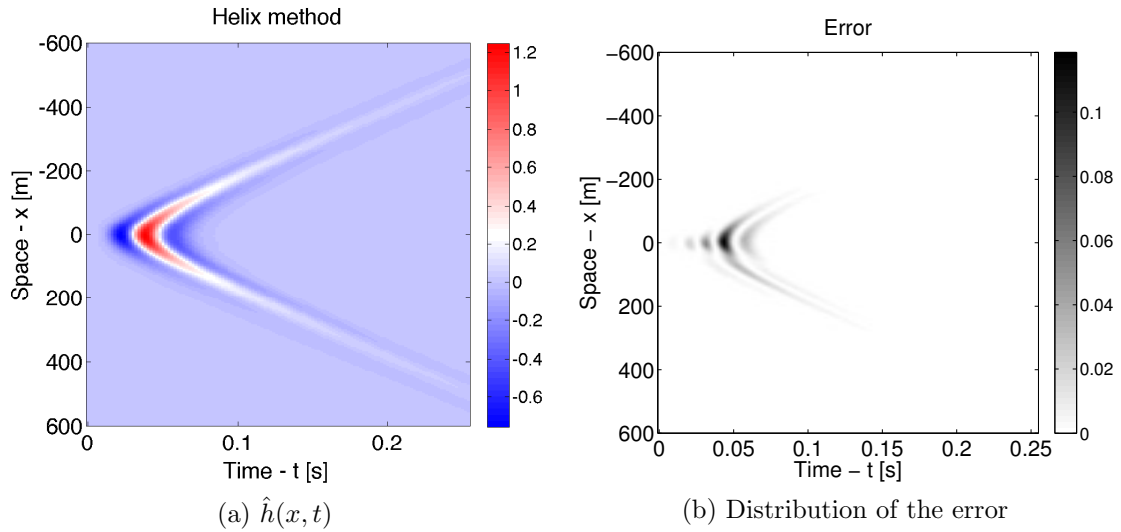


Figure 10.5.: Estimation of the impulse response - only one Dirac source  $\delta(x, t)$

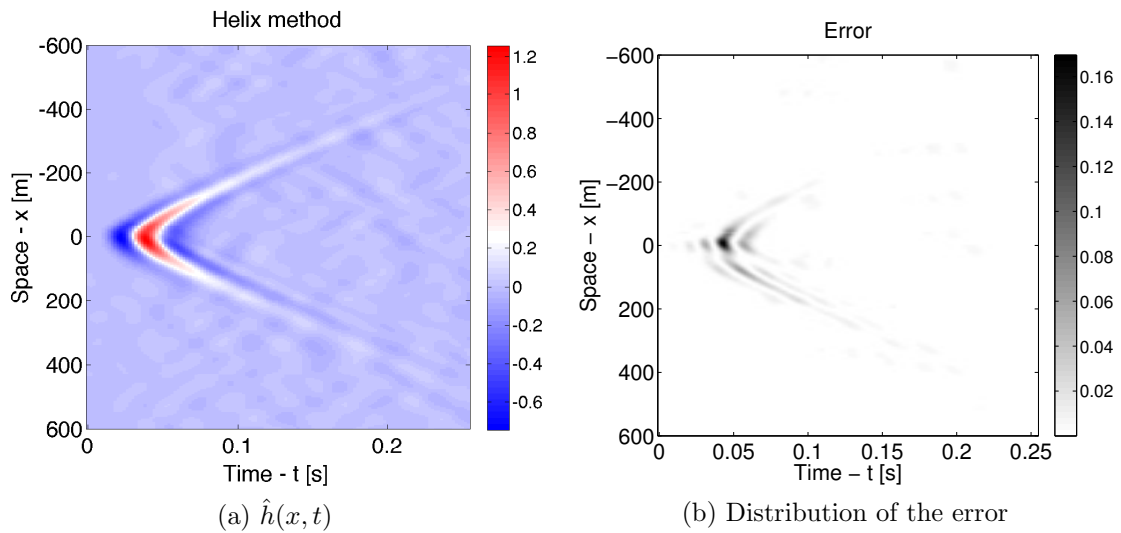


Figure 10.6.: Estimation of the impulse response - random excitation  $s(x, t)$

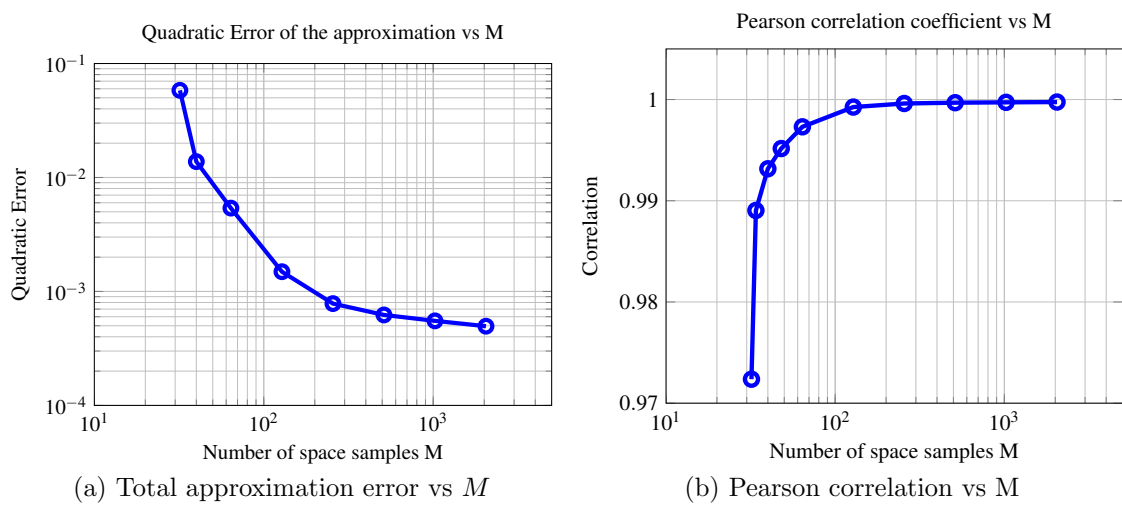


Figure 10.7.: Approximation error and correlation with respect to the 2D solution

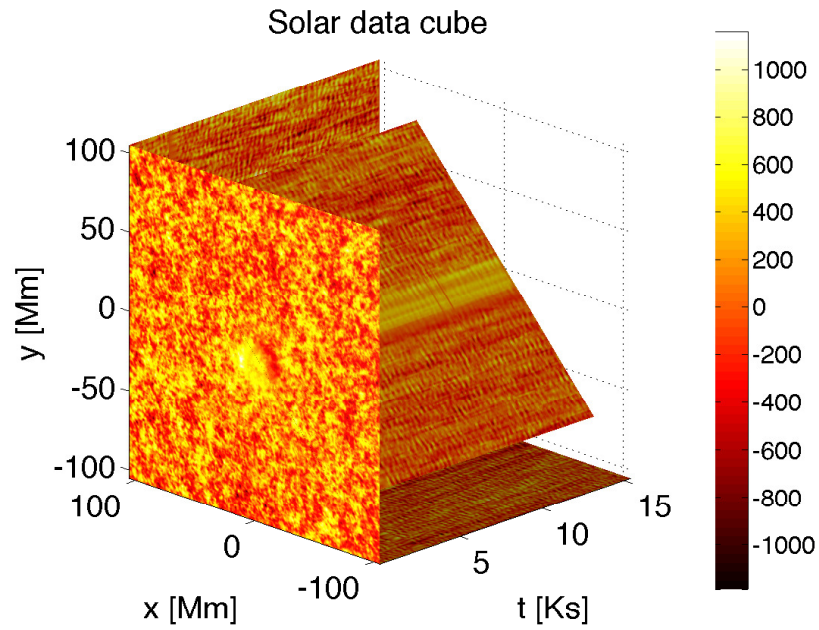


Figure 10.8.: Solar Data Volume (Courtesy by Jon Claerbout, Stanford University)

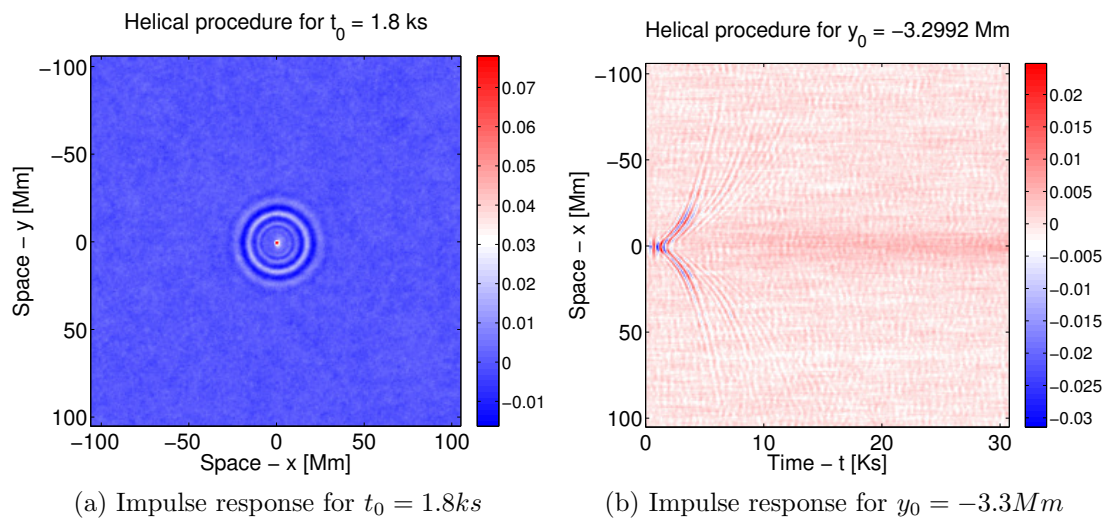


Figure 10.9.: Estimation of the impulse response of the reverberations of the Sun

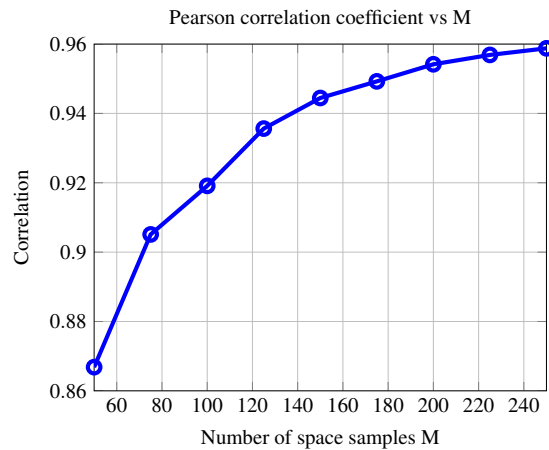


Figure 10.10.: Pearson correlation between the helical and the 3D solutions vs M.

# Appendix

## 10.A. Proof for Propagative Systems

We calculate the Z-transform of the forward propagating solution in (10.23),  $f(m, n) = A_0 e^{-\alpha m \Delta} e^{-\beta n T} e^{i k m \Delta} e^{-i \omega n T}$ . If we have  $m, n \in \mathbb{N}$ , the result is simple:

$$\begin{aligned}
 F(z_1, z_2) &= \sum_{m=0}^{\infty} \sum_{n=0}^{\infty} f(m, n) z_1^{-m} z_2^{-n} = \\
 &= A_0 \sum_{m=0}^{\infty} e^{-\alpha m \Delta} e^{i k m \Delta} z_1^{-m} \sum_{n=0}^{\infty} e^{-\beta n T} e^{-i \omega n T} z_2^{-n} \\
 &= A_0 \frac{1}{1 - e^{-\alpha \Delta} e^{i k \Delta} z_1^{-1}} \frac{1}{1 - e^{-\beta T} e^{-i \omega T} z_2^{-1}}
 \end{aligned} \tag{10.25}$$

The convergence zone is given by

$$\begin{cases} |e^{-\alpha \Delta} e^{i k \Delta} z_1^{-1}| < 1 \Rightarrow |z_1| > e^{-\alpha \Delta} \\ |e^{-\beta T} e^{-i \omega T} z_2^{-1}| < 1 \Rightarrow |z_2| > e^{-\beta T} \end{cases} \tag{10.26}$$

The poles of  $f(m, n)$  are given by

$$\begin{cases} z_1 = e^{-\alpha \Delta} e^{i k \Delta} \\ z_2 = e^{-\beta T} e^{-i \omega T} \end{cases} \tag{10.27}$$

If  $0 \leq m \leq M - 1$ , numerator has supplementary zeros:

$$z_{1k} = e^{-\alpha \Delta} e^{i k \Delta + k 2\pi/M}, \quad 0 \leq k \leq M \tag{10.28}$$

If  $0 \leq n \leq N - 1$ , numerator has supplementary zeros:

$$z_{2k} = e^{-\beta T} e^{-i \omega T + k 2\pi/N}, \quad 0 \leq k \leq N \tag{10.29}$$

Notice that  $f(m, n)$  is strictly 2D minimum phase, as its poles and zeros lie inside the unit bicircle. The back-propagating term would not be minimum phase with respect to time, due to poles  $z_2^- = e^{\beta T} e^{i \omega T}$  with  $|z_2^-| > 1$ , and zeros  $z_{2k}^- = e^{\beta T} e^{i \omega T + k 2\pi/N}$  with  $|z_{2k}^-| > 1, \forall k$ .

On the other hand, provided  $0 \leq m \leq M - 1$ , after the helical mapping in (10.2), the 1D Z-transform of the helix  $f^{(1)}(p)$  is given by

$$\begin{aligned}
 F^{(1)}(z) &= \sum_{p=0}^{\infty} f^{(1)}(p) z^{-p} = F(z, z^M) = \\
 &= \sum_{m=0}^{M-1} \sum_{n=1}^{\infty} f(m, n) z^{-m} z^{-Mn} = \\
 &= A_0 \sum_{m=0}^{M-1} e^{-\alpha m \Delta} e^{i k m \Delta} z^{-m} \sum_{n=1}^{\infty} e^{-\beta n T} e^{-i \omega n T} z^{-Mn} \\
 &= A_0 \frac{1 - e^{-\alpha \Delta M} e^{i k \Delta M} z^{-M}}{1 - e^{-\alpha \Delta} e^{i k \Delta} z^{-1}} \frac{1}{1 - e^{-\beta T} e^{-i \omega T} z^{-M}}
 \end{aligned} \tag{10.30}$$

The convergence zone for the Z-transform is  $\{|z| > e^{-\alpha\Delta}, |z| > \sqrt[M]{e^{-\beta T}}\}$ . The poles are given by

$$\begin{cases} z = e^{-\alpha\Delta} e^{ik\Delta} \\ z_k = \sqrt[M]{e^{-\beta T}} e^{-i\omega T/M+k 2\pi/M}, 0 \leq k \leq M \end{cases} \quad (10.31)$$

and the zeros by

$$z_k = e^{-\alpha\Delta} e^{ik\Delta+k 2\pi/M}, 0 \leq k \leq M \quad (10.32)$$

If  $0 \leq n \leq N - 1$ , numerator has supplementary zeros:

$$z_k = \sqrt[M]{e^{-\beta T}} e^{-i\omega T/M+k 2\pi/(MN)}, 0 \leq k \leq MN \quad (10.33)$$

Notice that  $f^{(1)}(p)$  is minimum phase, as its poles and zeros lie inside the unit circle. After helical mapping, the back-propagating term would not be minimum phase with respect to time, due to poles  $z_k^- = \sqrt[M]{e^{\beta T}} e^{i\omega T/M+k 2\pi/M}$  with  $|z_k^-| > 1$ , and zeros  $z_k^- = \sqrt[M]{e^{\beta T}} e^{i\omega T/M+k 2\pi/(MN)}$  with  $|z_k^-| > 1, \forall k$ .

## 10.B. Algorithms

---

### Algorithm 10.1 2D spectral factorization

---

1: Calculate 2D spectrum  $S(k, l)$ ,  $0 \leq k \leq M - 1$ ,  $0 \leq l \leq N - 1$ :

$$S(k, l) = \left| \sum_{m=0}^{M-1} \sum_{n=0}^{N-1} s(m, n) e^{-2\pi mk/M} e^{-2\pi nl/N} \right|^2 \quad (10.34)$$

2: Calculate 2D complex cepstrum

$$\hat{s}(m, n) = \frac{1}{MN} \sum_{k=0}^{M-1} \sum_{l=0}^{N-1} \log S(k, l) e^{2\pi mk/M} e^{2\pi nl/N} \quad (10.35)$$

3: Project the cepstrum on the upper NSHP

$$\mathcal{R}_{\oplus+} = \{m \geq 0, n \geq 0\} \cup \{m < 0, n > 0\}:$$

$$\hat{s}_{\oplus+}(m, n) = 0 \text{ for } (m, n) \in \mathcal{R}_{\ominus-} := \{m \leq 0, n \leq 0\} \cup \{m > 0, n < 0\} \quad (10.36)$$

4: Perform the inverse homomorphic transform on the semi-causal cepstrum to find the 2D semi-minimum phase component:  $s_{\oplus+}(m, n) = \mathcal{H}^{-1}[\hat{s}_{\oplus+}(m, n)]$

---



---

### Algorithm 10.2 Helical spectral factorization

---

1: Vectorize data  $s^{(1)}(p) = f(m, n)$  column-wise,  
with  $p = m + Mn$ ,  $0 \leq p \leq MN - 1$

2: Calculate 1D spectrum  $S^{(1)}(k)$ ,  $0 \leq k \leq MN - 1$ :

$$S^{(1)}(k) = \left| \sum_{p=0}^{MN-1} s^{(1)}(p) e^{-2\pi pk/(MN)} \right|^2 \quad (10.37)$$

3: Calculate 1D complex cepstrum

$$\hat{s}^{(1)}(p) = \frac{1}{MN} \sum_{k=0}^{MN-1} \log S(k) e^{2\pi pk/(MN)} \quad (10.38)$$

4: Project the cepstrum on the 1D causal admissible region  $\{p \geq 0\}$ :  $\hat{s}_+^{(1)}(p) = 0$  for  $p < 0$

5: Perform the inverse homomorphic transform on the causal cepstrum to find the 1D minimum phase component:  $s_+^{(1)}(p) = \mathcal{H}^{-1}[\hat{s}_+^{(1)}(p)]$

6: Back project the helical minimum phase solution to the 2D domain:  $s_+^{helix}(m, n) = s_+^{(1)}(m + Mn)$

---

## **Conclusion and Perspectives**



# Conclusion and Perspectives

During my PhD, I took a particular interest in the combination of two elements: the physics of wave propagation and sensor arrays on one hand, and the mathematical formalism for their interpretation on the other hand, in the context of source estimation and localization. Tensor analysis has been a natural way to integrate multiple dimensions into array processing, in addition to space and time of traditional techniques. In particular, while array processing added space as a relevant variable to the estimation problem, tensors are now able to extend the estimation problem to a multidimensional space, where each dimension corresponds to a physical variable.

In Part I, I introduced the basics of sensor arrays and of the tensor formalism in a simple and gradual way, from the signal reception to its processing for source localization. I explained how tensors can be an important tool to grasp the multidimensional relationships between variables of multi-way arrays.

The physical dimensions that I studied in Part II were polarization, directional gain patterns, propagation speed, and frequency diversity. In particular, gain patterns and propagation speed had never been used before in any tensor approach as sources of useful information on wave propagation. I also showed how tensor decompositions can be applied to the estimation of wideband sources, which are very common in many applications, such as sonar or seismology. In particular, we developed a coherent tensor preprocessing allowing to multi-linearize our data tensor directly in the frequency domain. The main practical difficulty of the tensor formalism is the requirement of multilinearity, corresponding to the separability of the underlying model. While in many situations, such as for narrowband polarized far-field sources, the physical model is separable, there are still many cases in which it is not. This thesis gives a major example on the possibility to use tensors in non standard situations, such as in the case of wideband processing.

Finally, in Part III, I explored the factorization of multidimensional data cubes, for the estimation of the impulse-response of the Sun.

I would be pleased if this thesis could provide a starting point to understand the basics and the benefits of the multi-way analysis of wave propagation. In the same vein, Table 10.1 summarizes the requirements and the advantages of various physical diversities in the tensor formulation.

Table 10.1.: Main diversities in array processing

---

<b>Diversities</b>	<b>Requirements</b>	<b>Information</b>
Time /Frequency	One sensor (pressure, electromagnetic, velocity, displacement)	

---

---

Time	One array of $L$ sensors.	Directions of Arrival (DoAs) can be estimated.
Space	The estimation of spatial statistics ( <i>e.g.</i> the spatial covariance). Sensor positions must be known. Sources must be narrowband.	Scalar source signatures can be estimated.

---

Frequency	One array of $L$ sensors.	DoAs can be estimated.
Space	Sources are wideband. Linear interpolation for a coherent array processing. Sensor positions must be known.	Source Fourier coefficients can be jointly estimated. Possible estimation bias due to interpolation at high SNR. Interpolation induces a correlation error, that is to be taken into account into the estimation.

---

Time	$M$ identical subarrays.	DoAs and source signatures can be jointly estimated.
Space	Sources must be narrowband.	
Space Shift	Either sensor positions or subarray positions must be known.	

---

Time	One vector sensor array, <i>i.e.</i> $L$ 3C sensors.	DoAs, polarization parameters, and source signatures can be jointly estimated.
Space	Sensor positions must be known for DoA estimation; they can be unknown for polarization estimation.	Polarization is useful to disambiguate closely spaced sources.
Polarization	Sources must be narrowband.	Information on the type of elastic or electromagnetic wave.

---

Time	$M$ identical (almost) overlapping subarrays with possibly unknown directional elements.	DoAs and source signatures can be jointly estimated.
Gain Patterns		
Space Shift	Space shifts must be known. Sources must be narrowband.	

---

Frequency	$M$ identical subarrays.	DoAs and source Fourier coefficients can be jointly estimated.
Space	Sources are wideband.	
Space Shift	Bilinear interpolation for a coherent tensor processing. Sensor and subarray positions must be known.	Possible estimation bias due to interpolation at high SNR. Interpolation induces a correlation error, that is to be taken into account into the tensor approximation routine.

---

---

Frequency	One vector sensor array,	DoAs, polarization parameters, and source
Space	<i>i.e.</i> $L$ 3C sensors.	Fourier coefficients can be jointly esti-
Polarization	Linear interpolation for a coherent tensor	mated.
	processing.	Information on the type of elastic or elec-
	Sensor positions must be known.	tromagnetic wave.
		Possible estimation bias due to interpola-
		tion at high SNR.
		Interpolation induces a correlation error,
		that is to be taken into account into the
		tensor approximation routine.

---

Time	One sensors array - $L$ sensors.	DoAs can be estimated.
Space	Sensor positions must be known.	Information on the type of seismic wave.
Propagation	Impinging sources are seismic volume	Loss of information due to narrowband fil-
Speed	waves (P and S waves).	tering.
	Narrowband filtering at frequencies ensur-	
	ing constant wavelength.	

---

Other combinations are also possible, such as the overall model developed in Chapter 6, using frequency, space, space shift, and polarization diversity. This only requires a slightly more complex notation, as it results in a fourth order tensor.

Time diversity is sufficient when signals are narrowband. This is often the case of electromagnetic waves for telecommunications. Frequency diversity needs to be taken into account when impinging waves are wideband, *i.e.* when the array aperture is not negligible compared with the signal spectral bandwidth. This is often the case of elastic or acoustic waves. If we filter these signals and treat them as narrowband, we lose most of the information on their propagation.

Polarization is another interesting property of waves that concerns the geometric orientation of particle motion, in the form of the polarization ellipse. Polarization can then be very useful to identify the kind of impinging waves, *e.g.* different types of seismic waves are also differently polarized.

Gain patterns offer an additional diversity allowing uniqueness when spatial invariance is not allowed, in the case of very small sub arrays.

The perspectives for future work are listed below. I would have liked to study all these subjects in more depth, but three years is a very short time.

- As for space and space shift diversities addressed in Chapter 4, an acquisition system might possess several space invariant structures, as in [142]. In this case, could the tensor formalism be exploited to determine the optimal combination of translated (and possibly overlapping) subarrays to include into the Canonical Polyadic Decomposition (CPD) model?
- It would be of interest to extend the simulations of Chapter 5 to more closely spaced sources. In particular, polarization diversity has a good potential to help distinguishing sources with similar DoAs. Comparisons of the proposed tensor CPD

and the algorithm proposed in [42] would be relevant in the context of polarization diversity.

- More generally, polarization diversity could be advantageous to use not only with vector sensor arrays as in Chapter 5, but also with differently polarized subarrays as in [42]. The latter configuration has the benefit of being less restrictive.
- Polarization diversity for vector sensor arrays could be seen as a particularly extreme case of gain pattern diversity. Connections between the two representations are promising to investigate.
- As for the computational aspects, major convergence issues of the ALS algorithm arise when the overall product of the coherences approaches one. This is not surprising, especially in the light of Section 3.7 on the existence of a solution to the tensor CPD approximation problem. From this perspective, the case of closely spaced sources or highly correlated sources have very similar numerical consequences.
- Spatial smoothing traditionally improve the estimation in the case of correlated sources [61]. Furthermore, a tensor-based spatial smoothing that creates a new dimension of the tensor has been introduced in [148]. The latter solution could be further studied in relation to the proposed tensor models.
- Other diversities that could be included into the tensor formulation of Chapter 5 are given by doppler shifts and path delays [163].
- The performance of the algorithms proposed in Chapter 6 could be compared to the exact Cramér-Rao Bound (CRB) of the wideband model, as explained in Section 7.4.
- The noise covariance structure induced by interpolation should be taken into account in Chapter 8, in a similar fashion as in Chapter 6, thanks to the algorithm ALSCOLOR in Section 6.5.
- Furthermore, the noise covariance structure induced by interpolation could be further studied. In Section 6.6 I only presented a qualitative analysis and a simple measure of this correlation strength. The same could be done for the sinc interpolation of regular array geometries in Chapter 8. It would be of great interest to compare both interpolations and their resulting noise correlation strengths.
- Closely related to source localization, we could address the problem of estimating the model order, *i.e.* the number of simultaneously impinging sources, via tensor tools. An example of multidimensional model order estimation can be found in [30]. An open question is whether it is helpful to use the tensor formalism to determine the number of sources.
- In the context of model order estimation, model order mismatch is also of great interest. We have such a mismatch whenever we fit a  $\hat{R}$ -rank CPD model with data originating from  $R \neq \hat{R}$  sources. See Sections 3.6 and 3.6.2 for details on the issues of tensor CPD approximation.
- An interesting perspective could be to conceive a multidimensional beamforming and interference rejection exploiting multiple diversities.

- Interpolation as a preprocessing step to study wideband waves induces an estimation bias, that is visible as a saturation of the MSE for high SNR. We did not take it into account in the proposed estimation algorithms in Chapters 6 and 8 nor in the derivation of the CRB in Chapter 7. A perspective of our work would be to take it into account in the same spirit as [70, 71].
- Calibration issues of the tensor formulation could be investigated, and sensor position errors could be introduced into the tensor model and into the performance bounds. Errors on sensor configuration can involve their position (translation errors) or orientation (rotation errors). The latter are significant in the case of vector sensors that are sensitive to wave polarization [35]. Calibration errors are typical of settings such as the glacier experimental setup described in Section 9.7, where the surface profile is not known in advance and may be difficult to measure. If we have some prior statistical knowledge on position and orientation errors available, we could derive hybrid CRBs including this information.
- This PhD thesis was about using several physical diversities. However, each diversity carries its uncertainty due to model errors. How do these errors combine into the tensor formulation? Which is the maximum number of diversities that we can add together without propagating too much uncertainty into the estimation problem? These questions are important in the context of data fusion: sometimes it might be better to separate two sets of diversities forming two tensors respectively, than to include them all into the same big tensor.
- Only recently, coupled tensor decompositions [2, 1] have been developed and applied to sensor arrays. This is the case when two data tensors can be coupled through one of their modes, because they share approximately the same factor matrix along that mode. In [12] this coupling is defined in a statistical sense, with corresponding Bayesian bounds. This subject is still open and full of potential in the context of data fusion [84, 94].
- A very interesting perspective is Bayesian tracking of moving sources through the tensor formulation of a Kalman filter. This could also involve signals whose parameters in general (*e.g.* DoA, polarization) vary over time.

An interesting challenge would be to solve this problem using coupled tensor decompositions. If signal parameters can be considered constant in a certain lapse of time, at each snapshot we can measure a data tensor. This would result in several data tensors that can be coupled through the parameters that do not vary, while the others are allowed to change and be dependent on the snapshot number.

As an example, we refer to [18] for time-varying multidimensional harmonic retrieval via a tensor subspace tracking algorithm based on Kronecker-structured projections and including forward-backward averaging.

- More generally, it would be of great interest to include into the tensor model some a priori information we might have on impinging sources. Also, the structure of factor matrices could be included into the estimation problem, for instance the Vandermonde structure of ULAs [55]. Finally, the coupling between factor matrices depending on the DoAs could be taken into account. For instance, space and space shift matrices, or space and polarization matrices both depend on DoAs.

- We could extend our results, in particular our tensor analysis of wideband waves, to multidimensional harmonic retrieval, as proposed in [163].
- In our simulations, we considered non-dispersive and non-dissipative media. In actual propagation media, dissipation is generally higher at higher frequencies, and dispersion takes place as well, *i.e.* propagation speed may depend on frequency. All these elements could be taken into account into the model or estimated in active experimental settings.
- Tensor decompositions could be applied to the estimation and localization of spread sources. In this thesis, we only tackled the problem of point-like sources in the far-field. However, in many scenarios, sources are spatially spread and are the result of an integral of an infinite number of spatially related point-like sources [7].
- Tensor analysis could be applied to the active multidimensional characterization of heterogeneous propagation media, in the context of exploration seismology. Some example of such an application are given by [76, 78, 77, 127].
- A great challenge would be to generalize tensor methods to process more complex waves, such as spherical waves in the near field [161]. A major issue of this kind of sources is the non separability of the corresponding physical model, due to the wavefront curvature.
- As a further step, an interesting perspective could involve a post-processing of estimated signal parameters for the classification of sources and propagation media. This information could then be used for dictionary learning.
- Finally, the helical coordinate system studied in Chapter 10 could be of interest for on-line applications, where the sequential order of data acquisition matters.

# Résumé en Français

## Traitement Spatio-Temporel

Au début du traitement du signal, les problèmes de statistiques et d'ingénierie étaient axés sur l'estimation de paramètres et sur la performance associée à cette estimation. Les paramètres d'intérêt étaient surtout liés au temps, car les données mesurées étaient essentiellement des fonctions du temps. Par conséquent, les signaux pouvaient être caractérisés dans le domaine du temps, ou de façon équivalente, dans le domaine des fréquences.

Par la suite, suivant l'expansion des applications, les signaux mesurés devinrent aussi fonction de la position des capteurs, ajoutant ainsi une dépendance spatiale. La composante spatiale du processeur est une ouverture (ou antenne) dans le domaine continu de l'espace, tandis qu'elle est un réseau de capteurs dans l'espace discret de l'espace [151]. Depuis que les signaux devinrent des processus dans le temps et l'espace, les paramètres à la fois spatiaux et temporels devinrent l'objet d'un véritable nouveau domaine, nommé traitement d'antenne. Le traitement d'antenne est un traitement couplé dans l'espace et le temps, avec pour objectif de combiner les données récoltées par plusieurs capteurs [79]. L'information *a priori* sur le système d'acquisition (*c.a.d.* la géométrie d'antenne, les caractéristiques des capteurs, etc.) est utilisée afin d'estimer les paramètres des signaux. Puisque un réseau de capteurs échantillonne les champs incidents dans l'espace et le temps, la fusion spatio-temporelle a lieu dans le domaine multidimensionnel de l'espace-temps. Les problèmes principaux du traitement d'antennes sont donnés par la configuration des capteurs, les caractéristiques des signaux et du bruit, et l'objectif de l'estimation [151], comme la direction d'arrivée (DoA) de sources potentiellement simultanées.

## Applications principales

L'estimation des paramètres des signaux en traitement d'antenne a donné lieu à une immense variété d'applications, comme mentionné dans la liste ci-dessous.

### Radar

La première application des réseaux de capteurs fut fournie par la localisation de sources en radar. La plupart des systèmes radar sont actifs, dans la mesure où le réseau est utilisé pour la transmission ainsi que la réception des signaux en même temps. La réflectivité du sol est un problème majeur que l'on appelle communément *clutter*, impliquant des interférences spatialement distribuées. Les applications non militaires du radar incluent le contrôle du trafic aérien. Les paramètres spatiaux d'intérêt peuvent varier : les systèmes actifs peuvent estimer la vitesse (la fréquence Doppler), la distance, et les directions d'arrivée, tandis que les systèmes passifs ne peuvent estimer que les directions d'arrivée (DoAs).

### **Astronomie**

En astronomie, les réseaux d'antenne sont constitués par des systèmes passifs très grands (la base peut rejoindre de milliers de kilomètres) qui mesure et étudie des objets célestes avec une résolution très élevée.

### **Sonar**

Les systèmes sonar actifs traitent les échos de signaux acoustiques transmis sous l'eau, alors que les systèmes sonar passifs étudient les ondes acoustiques incidentes par un réseau d'hydrophones. La différence principale entre le sonar actif et le radar réside dans les conditions de propagation : la propagation des ondes acoustiques dans l'océan est plus complexe et problématique que la propagation des ondes électromagnétiques dans l'atmosphère, à cause de la dispersion, de la dissipation, et de la variation de la vitesse de propagation avec la profondeur. Les raisons majeurs de bruits sont constituées par l'environnement, le système et la réverbération. L'application la plus importante est donnée par la détection et le repérage des sous-marins. Les réseaux déformables sont souvent remorqués sous l'eau et ont une structure linéaire [79].

### **Communications**

Un autre domaine majeur du traitement d'antenne est offert par les télécommunications (à la fois terrestres et satellitaires). Les signaux des communications sont typiquement des sources ponctuelles, et ils arrivent généralement au receveur distant sous forme d'onde planes, après avoir été réfléchies plusieurs fois par les bâtiments et les collines. Ces réflexions multiples, aussi appelées multipath, peuvent produire une atténuation sévère du signal. La performance d'estimation peut aussi être dégradée par d'autres signaux interférant, ou des interférences entre utilisateurs. Dans ce contexte, les *smart antennas* consistent en des réseaux adaptatifs pour les communications sans fils : elles implémentent un traitement spatial adaptatif en complément au traitement temporel adaptatif déjà utilisé [151].

### **Sismologie**

La sismologie d'exploration ou de réflexion est un autre domaine important du traitement d'antenne, destiné à dériver une image de la structure de la terre et des propriétés physiques de ses différentes couches. Les systèmes actifs, qui mesurent les réflexions à travers les diverses couches, sont conçus en fonction de la propagation des ondes élastiques à travers un milieu inhomogène. D'un autre côté, la sismique passive utilise plusieurs sismomètres, séparés par de centaine de mètres, afin de détecter les mouvements naturels de la terre sur des périodes d'heures ou de jours [151]. Cette dernière application est adressée dans le Chapitre 9.

### **Génie biomédicale**

Les applications biomédicales ont aussi offert un terrain très fertile pour le traitement d'antenne. L'électrocardiographie (ECG) est utilisée pour surveiller la santé du cœur ; l'électroencéphalographie (EEG) et la magnétoencéphalographie (MEG) sont utilisées pour localiser l'activité cérébrale [79]. La tomographie est la reconstruction par tranches du volume d'un objet par des ondes transmises ou réfléchies. Cette dernière a eu un succès considérable pour les diagnostics médicaux [151].

## Les Approches Classiques en 2D

Au début, l'approche originale pour le traitement spatio-temporel fût offert par le filtrage spatial, ou formation de voies, ou *beamforming* en anglais, consistant à amplifier les signaux provenant de certaines directions, tout en atténuant tous les autres [152]. Cependant, bien que très simple, la formation de voie souffre d'une limitation sévère : sa performance dépend directement de l'aperture d'antenne, indépendamment du nombre d'échantillons, et du rapport signal sur bruit (SNR). Cela limite sérieusement sa résolution, *c.a.d.* sa capacité à distinguer de sources spatialement rapprochées. La résolution est intuitivement facile à comprendre dans le contexte des méthodes spectrales, comme la formation de voies : lorsque deux pics sont visibles en correspondance de deux vraies sources, ils sont dits résolus.

Les données mesurées consistent en matrices, dont les lignes correspondent aux divers capteurs (espace) et les colonnes correspondent aux échantillons mesurés (temps), comme en Figure 10.11. Puisque les paramètres des signaux d'intérêt, comme les directions

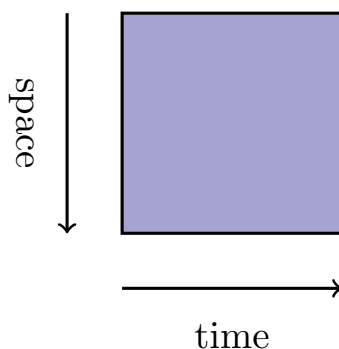


Figure 10.11.: Matrice de données en traitement d'antenne traditionnel

d'arrivée, ont une nature spatiale, la plupart des approches 2D sont fondés sur l'estimation de l'information d'inter-corrélation entre capteurs, *c.a.d.* la matrice de covariance spatiale. Cette estimation requiert donc des échantillons de très longue durée.

Une véritable percée dans le traitement d'antenne fût apportée par les méthodes à sous-espaces [131, 126]. La structure à valeurs propres de la matrice de covariance fût alors explicitement exploitée via des techniques de décomposition spectrale, comme la décomposition en éléments propres (EVD). Grâce à la structure de rang faible des données reçues, les vecteurs propres correspondant aux plus grand valeurs propres engendrent l'espace signal, tandis que les vecteurs propres restants engendrent l'espace bruit. En conséquence, les techniques haute résolution comme MUSIC [131] font appel à ces deux éléments de diversité : l'espace et le temps, afin d'estimer l'espace signal engendré par les sources incidentes, ainsi que leur directions d'arrivée. Cela est généralement accompli par l'estimation de la matrice de covariance d'antenne. Des statistiques d'ordre supérieur peuvent aussi être employées [83] pour supprimer le bruit gaussien et augmenter le nombre de sources détectables.

En outre, la structure invariante par translation du système d'acquisition peut être exploitée lorsque l'antenne globale est constituée par deux sous-antennes identiques, l'une étant une version translatée de l'autre. Ceci est l'essence de l'algorithme ESPRIT [126].

En l'absence d'erreur de modèle, la capacité de résolution des méthodes à sous-espaces n'est pas limitée par l'aperture d'antenne, pourvu que la taille des données et le rapport signal sur bruit soient suffisamment grands [79].

De plus, si les champs incidents ne sont pas scalaires, mais vectoriels, la polarisation des ondes dévient une propriété utile qui peut améliorer la localisation des sources, sous réserve que les capteurs soient sensibles à des composantes différentes et que ces dernières puissent être calibrées séparément. Cela est le cas du capteur vectoriel (*vector-sensor*), *c.a.d.* un capteur qui mesure toutes les composantes orthogonales des ondes élastiques ou électromagnétiques en même temps [95, 96].

Dans les méthodes traditionnelles, les composantes du capteur vectoriel sont généralement empilées l'une après l'autre dans un long vecteur, pour un instant donné, perdant ainsi leur structure multidimensionnelle.

Au début, la formation de voie et les méthodes à sous-espaces furent conçus pour les ondes à bande étroite, ce qui correspond à une hypothèse assez réaliste en radar et télécommunications, car la bande spectrale du signal est souvent négligeable, par rapport à l'aperture de l'antenne. Néanmoins, dans de nombreuses applications, comme en sonar et en sismologie, les signaux reçus sont intrinsèquement à bande large. L'extension naturel du traitement d'antenne au cas large bande est basée sur la Transformée de Fourier Discrète (TFD), suivie par une combinaison optimale ou sous-optimale de l'information sur les différents canaux de fréquence. Une solution optimale est apportée par le Coherent Signal Subspace (CSS) : toutes les contributions en fréquence sont alignées vers le même sous-espace de référence à une fréquence centrale, par des transformations linéaires [157].

## Les Méthodes Tensoriels

Nous remarquons que la décompositions en valeurs propres (EVD) de la matrice de covariance estimée est équivalente à la décomposition en valeurs singulières (SVD) des données brutes correspondantes. La SVD est une factorisation matricielle qui tire son unicité de deux contraintes : un noyau diagonal contenant des valeurs singulières non négatives distinctes, et des matrices orthogonales contenant les vecteurs singulières de gauche et de droite, respectivement. Cette contrainte d'orthogonalité est souvent arbitraire et physiquement injustifiée.

Les factorisations matricielles standard, comme la SVD, sont des outils très efficaces pour la sélection de caractéristiques, la réduction dimensionnelle, l'amélioration du signal, et la fouille des données (ou *data mining*) [22]. Toutefois, comme mentionné dans la section précédente, elles ne peuvent s'adresser qu'à deux modes seulement, *c.a.d.* les matrices d'espace et temps. Dans de nombreuses applications, comme la chimiométrie et la psychométrie, mais aussi la fouille de textes, le clustering, les réseaux sociaux, les télécommunications, etc., la structure des données est extrêmement multidimensionnelle, car elle contient modes d'ordre supérieur, comme les tests, les conditions expérimentales, les sujets, les groupes, en plus des modes intrinsèques données par l'espace et le temps/fréquence [22]. Manifestement, la perspective plate de la factorisation matricielle ne peut pas décrire une structure multidimensionnelle complexe. En revanche, les décompositions tensorielles sont une façon naturelle de saisir conjointement les relations multilinéaires entre les différents modes, et en extraire une information unique et physiquement significative.

La factorisation tensoriel consiste en l'analyse de cubes multidimensionnels d'au moins trois dimensions. Ceci est accompli par leur décomposition en une somme de composantes élémentaires, grâce à la multilinéarité et au rang faible du modèle sous-jacent. La Décomposition Canonique Polyadique (CPD), une des décompositions les plus répandues, développe un tenseur en une sommes de termes multilinéaires. Ceci peut être interprété

comme une généralisation des factorisations matricielles bilinéaires comme la SVD. Néanmoins, contrairement à la SVD, la CPD n'a pas besoin de contraintes d'orthogonalité, puisqu'elle est unique à des conditions légères. Cela veut dire que nous pouvons récupérer toutes les matrices facteurs qui correspondent aux différentes modalités du tenseur, à partir du tenseur de données bruitées [88].

Seulement récemment l'analyse tensorielle a-t-elle été appliquée au traitement d'antenne d'ondes à bande étroite en [136], en tant que généralisation déterministe d'ESPRIT [126] à plus qu'une translation, sans aucune nécessité d'estimer de quantités statistiques. Cela veut dire que le système d'acquisition doit se constituer d'une sous-antenne de référence, répétée dans l'espace par de translations multiples. Donc, le troisième mode ou diversité est fourni par la translation en espace, en plus de l'espace et du temps. Ensuite, le formalisme tensoriel a été étendu pour étudier les ondes polarisées en [57], via CPD, avec la polarisation comme troisième mode au lieu de la translation en espace. Voir Figure 10.12 pour une illustration d'un cube de données de dimension 3.

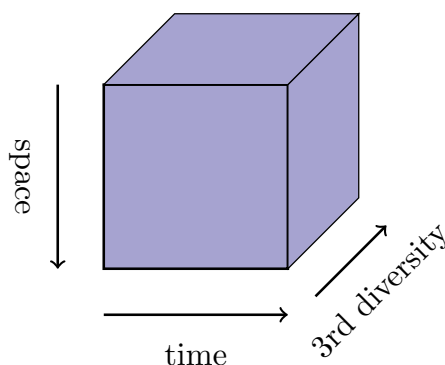


Figure 10.12.: Cube de données de dimension 3 en traitement d'antenne tensoriel

Les décompositions tensorielles permettent de récupérer conjointement et uniquement toutes les modalités reliées aux paramètres des signaux, *c.a.d.* les directions d'arrivée, les angles de polarisation, et les formes d'onde reçues. Ainsi, les méthodes tensorielles nous offrent une estimée des signaux des sources, avec leur directions d'arrivée, de façon déterministe. Ceci peut être accompli en vertu du modèle séparable et de rang faible suivi par les sources à bande étroite et en champ lointain. Puisque les méthodes tensorielles ne nécessitent ni d'estimation de la covariance des données ni de statistiques d'ordre supérieur, elles peuvent gérer des échantillons de données plus courtes.

## Contribution et Plan

Cette thèse a pour sujets l'estimation et la localisation de multiples sources par des méthodes tensorielles pour le traitement d'antenne, en exploitant plusieurs modalités. Nous incluons plusieurs diversités physiques dans le modèle tensoriel, outre l'espace et le temps : la translation en espace, les patterns de gains de capteurs directionnels, et la célérité ou vitesse de propagation des ondes sismiques. Au début de mon doctorat, j'étais intéressée au modèle tensoriel pour les ondes à bande étroite, en particulier les ondes polarisées et sismiques. Par la suite j'ai étendu tous nos résultats à l'étude des ondes à bande large en exploitant la diversité de fréquence, et en développant ultérieurement la formulation tensorielle correspondante.

La difficulté pratique principale du formalisme tensoriel est due à la condition de multilinéarité, correspondant à la séparabilité du modèle sous-jacent. Bien que, dans certaines situations, comme dans le cas de sources à bande étroite et en champ lointain, le modèle physique est séparable, il est toutefois de nombreux cas où il ne l'est pas. Cette thèse est un exemple de la possibilité d'utiliser les tenseurs même dans des situations difficiles, comme dans le cas des ondes à bande large, surmontant ainsi ce problème.

**Contributions** Tout au long de mon doctorat, mon travail a donné lieu aux contributions énumérées ci-dessous en ordre chronologique.

- Au début, nous avons étendu l'analyse tensorielle aux ondes de volume sismiques, en employant la diversité de leur vitesse de propagation comme troisième mode. Ce travail a été publié dans un article de journal pour *Signal Processing*, Elsevier [117].
- Nous avons aussi présenté notre travail sur le modèle tensoriel des ondes élastiques polarisées et à bande étroite, ainsi que les bornes sur sa performance, à une conférence nationale française en traitement du signal [115].
- Notre intérêt pour les ondes sismiques nous a conduit à publier un article de journal pour *Signal Processing*, Elsevier sur la factorisation multidimensionnelle de cubes de données sismiques pour l'héliosismologie [118].
- Nous avons introduit l'emploi de capteurs directionnels, en proposant les patterns de gain comme une véritable diversité physique dans un article pour *IEEE Signal Processing Letters* [116].
- Après s'être aperçus que la diversité de célérité des ondes sismiques dans notre article [117] pourrait être interprétée comme une diversité de fréquence, nous avons décidé d'étendre le formalisme tensoriel à des ondes à bande large génériques. Notre idée d'utiliser l'interpolation spatiale pour des antennes linéaires uniformes a été présentée pour la première fois à ICASSP 2016 à Shanghai [119].
- Nous avons ultérieurement développé l'idée originale de [119] en utilisant des transformations bilinéaires dans un article de journal, publié par *IEEE Transactions on Signal Processing* [114].

Cette thèse de doctorat est structurée comme détaillé ci-dessous. La présentation est divisée en trois parties : La Partie I décrit l'état de l'art du traitement d'antenne et de l'analyse tensorielle ; les Partie II et III expliquent ma contribution pour respectivement le traitement d'antenne tensoriel et la factorisation multidimensionnelle.

Le Chapitre 1 présente le modèle physique des sources élastiques à bande étroite et en champ lointain, ainsi que les définitions et hypothèses principales. Le Chapitre 2 passe en revue l'état de l'art sur l'estimation de la direction d'arrivée, avec un accent particulier sur les méthodes à haute résolution et à sous-espaces.

Le Chapitre 3 introduit le formalisme tensoriel, à savoir la définition d'hypercubes de coordonnées, les opérations et les décompositions multilinéaires principales. Le Chapitre 4 présente le sujet de traitement d'antenne tensoriel via invariance rotationnelle.

Le Chapitre 5 introduit un modèle tensoriel général pour les ondes élastiques à bande étroite, impliquant de multiples diversités physiques, comme l'espace, le temps, la translation en espace, la polarisation, et les patterns de gain de directivité.

Dès lors, les Chapitres 6 et 8 établissent un modèle tensoriel pour un traitement d'antenne large bande cohérent. Nous proposons une opération de focalisation cohérente séparable par des transformations bilinéaires et par un ré-échantillonnage spatial, afin d'assurer la multilinearité des données interpolées. Nous montrons par des simulations numériques que l'estimation proposée des paramètres des signaux s'améliore considérablement, par rapport au traitement tensoriel bande étroite existant et à MUSIC bande large. Tout au long des chapitres nous comparons aussi les performances de l'estimation tensorielle avec la borne de Cramér-Rao du modèle multilinéaire, que nous dérivons dans sa formulation plus générale dans le Chapitre 7. En outre, dans le Chapitre 9 nous proposons un modèle tensoriel via la diversité de célérité des ondes sismiques et nous illustrons une applications aux données sismiques réelles d'un glacier alpin.

Dernièrement, la partie finale de cette thèse dans le Chapitre 10 passe au sujet parallèle de la factorisation spectrale multidimensionnelle des ondes sismiques, et en illustre une application à l'estimation de la réponse impulsionnelle du Soleil pour l'héliosismologie.



# Bibliography

- [1] E. Acar, T. G. Kolda, and D. M. Dunlavy. All-at-once optimization for coupled matrix and tensor factorizations. *arXiv preprint arXiv:1105.3422*, 2011.
- [2] E. Acar, M. A. Rasmussen, F. Savorani, T. Næs, and R. Bro. Understanding data fusion within the framework of coupled matrix and tensor factorizations. *Chemo. Intell. Lab. Syst.*, 129:53–63, 2013.
- [3] S. Anderson and A. Nehorai. Analysis of a polarized seismic wave model. *IEEE Trans. Signal Process.*, 44(2):379–386, 1996.
- [4] S. Banerjee and A. Roy. *Linear algebra and matrix analysis for statistics*. CRC Press, 2014.
- [5] A. Barabell. Improving the resolution performance of eigenstructure-based direction-finding algorithms. In *Proc. IEEE Int. Conf. Acoust. Speech Signal Process.*, volume 8, pages 336–339, Boston, 1983.
- [6] H. Becker, L. Albera, P. Comon, R. Gribonval, F. Wendling, and I. Merlet. Brain source imaging: from sparse to tensor models. *IEEE Signal Process. Mag.*, 32(6):100–112, November 2015.
- [7] H. Becker, L. Albera, P. Comon, M. Haardt, G. Birot, F. Wendling, M. Gavaret, C.-G. Bénar, and I. Merlet. EEG extended source localization: Tensor-based vs. conventional methods. *NeuroImage*, 96:143–57, August 2014.
- [8] H. Becker, P. Comon, L. Albera, M. Haardt, and I. Merlet. Multi-way space-time-wavevector analysis for EEG source separation. *Signal Process.*, 92(4):1021–1031, April 2012.
- [9] E. Bedrosian. A product theorem for Hilbert transforms. *Research Memorandum, RM-3439-PR*, 1962.
- [10] J. W. Brewer. Kronecker products and matrix calculus in system theory. *IEEE Trans. Circuits Systems*, 25(9):114–122, September 1978.
- [11] R. Bro, R. A. Harshman, N. D. Sidiropoulos, and M. E. Lundy. Modeling multi-way data with linearly dependent loadings. *Journal of Chemometrics*, 23(7-8):324–340, 2009.
- [12] R. Cabral Farias, J. E. Cohen, and P. Comon. Exploring multimodal data fusion through joint decompositions with flexible couplings. *IEEE Trans. Signal Process.*, 64(18):4830–4844, 2016.
- [13] C. Chang, T. Cheng, and H. Lin. Fast direction finding algorithm for circular array based on directional antenna. In *IEEE Int. Workshop Microw. Millimeter Wave Circuits Syst. Technol.*, pages 1–4, 2012.

- [14] H. Chang and J. K. Aggarwal. Design of two-dimensional semicasual recursive filters. *IEEE Trans. Circuits Syst.*, 25(12):1051–1059, 1978.
- [15] E. Chaumette, J. Galy, A. Quinlan, and P. Larzabal. A new Barankin bound approximation for the prediction of the threshold region performance of maximum likelihood estimators. *IEEE Trans. Signal Process.*, 56(11):5319–5333, November 2008.
- [16] H. Chen and J. Zhao. Coherent signal-subspace processing of acoustic vector sensor array for DoA estimation of wideband sources. *Signal. Process.*, 85(4):837–847, 2005.
- [17] J. C. Chen, K. Yao, and R. E. Hudson. Source localization and beamforming. *IEEE Signal Process. Mag.*, 19(2):30–39, 2002.
- [18] Y. Cheng, F. Roemer, O. Khatib, and M. Haardt. Tensor subspace Tracking via Kronecker structured projections (TeTraKron) for time-varying multidimensional harmonic retrieval. *EURASIP J. Advances Signal Process.*, 2014:123–136, 2014.
- [19] L. Chiantini, G. Ottaviani, and N. Vannieuwenhoven. An algorithm for generic and low-rank specific identifiability of complex tensors. *J. Matrix Anal. Appl.*, 35(4):1265–1287, 2014.
- [20] M. Chryssomallis. Smart antennas. *IEEE Antennas Propag. Mag.*, 42(3):129–136, 2000.
- [21] A. Cichocki, D. Mandic, L. De Lathauwer, G. Zhou, Q. Zhao, C. Caiafa, and H. A. Phan. Tensor decompositions for signal processing applications: From two-way to multiway component analysis. *IEEE Signal Process. Mag.*, 32(2):145–163, 2015.
- [22] A. Cichocki, R. Zdunek, A. H. Phan, and S.-I. Amari. *Nonnegative matrix and tensor factorizations: applications to exploratory multi-way data analysis and blind source separation*. John Wiley & Sons, 2009.
- [23] H. Clergeot and O. Michel. New simple implementation of the coherent signal subspace method for wide-band direction of arrival estimation. In *Proc. IEEE Int. Conf. Acoust. Speech Signal Process.*, pages 2764–2767, 1989.
- [24] J. E. Cohen. *Environmental Multiway Data Mining*. PhD thesis, Université Grenoble Alpes, September 2016.
- [25] P. Comon. Estimation multivariable complexe. *Traitement du Signal*, 3(2):97–101, April 1986.
- [26] P. Comon. Tensors: a brief introduction. *IEEE Signal Process. Mag.*, 31:44–53, 2014.
- [27] P. Comon, X. Luciani, and A. L. F. De Almeida. Tensor decompositions, alternating least squares and other tales. *Journal of Chemometrics*, 23(7-8):393–405, 2009.
- [28] P. Comon, K. Minaoui, A. Rouijel, and D. Aboutajdine. Performance index for tensor polyadic decompositions. In *Proc. IEEE European Signal Process. Conf.*, pages 1–5, 2013.

- [29] J. P. C. L. Da Costa, K. Liu, H. C. So, S. Schwarz, M. Haardt, and F. Römer. Multidimensional prewhitening for enhanced signal reconstruction and parameter estimation in colored noise with Kronecker correlation structure. *Signal Process.*, 93(11):3209–3226, 2013.
- [30] J. P. C. L. da Costa, F. Roemer, M. Haardt, and R. T. de Sousa. Multi-dimensional model order selection. *EURASIP J. Advances Signal Process.*, 2011(1):26, 2011.
- [31] L. De Lathauwer. A link between the canonical decomposition in multilinear algebra and simultaneous matrix diagonalization. *J. Matrix Anal. Appl.*, 28(3):642–666, 2006.
- [32] L. De Lathauwer, B. De Moor, and J. Vandewalle. A multilinear singular value decomposition. *J. Matrix Anal. Appl.*, 21(4):1253–1278, 2000.
- [33] J. H. de Morais Goulart and P. Comon. A novel non-iterative algorithm for low-multilinear-rank tensor approximation. In *Proc. 25th European Signal Process. Conf.*, Kos, Greece, August 2017.
- [34] T. Do-Hong and P. Russer. Signal processing for wideband smart antenna array applications. *IEEE Microw. Mag.*, 5(1):57–67, 2004.
- [35] D. Donno, A. Nehorai, and U. Spagnolini. Seismic velocity and polarization estimation for wavefield separation. *IEEE Trans. Signal Process.*, 56(10):4794–4809, 2008.
- [36] M.A. Doran, E. Doron, and A. J. Weiss. Coherent wide-band processing for arbitrary array geometry. *IEEE Trans. Signal Process.*, 41(1):414, 1993.
- [37] D. E. Dudgeon. The computation of two dimensional cepstra. *IEEE Trans. Acoust. Speech Signal Process.*, 25(6):476–484, 1977.
- [38] D. E. Dudgeon and R. M. Mersereau. *Multidimensional digital signal processing*. Englewood Cliffs: Prentice-Hall, 1984.
- [39] C. Eckart and G. Young. The approximation of one matrix by another of lower rank. *Psychometrika*, 1(3):211–218, 1936.
- [40] M. P. Ekstrom and J. W. Woods. Two-dimensional spectral factorization with applications in recursive digital filtering. *IEEE Trans. Acoust. Speech Signal Process.*, 24(2):115–128, 1976.
- [41] J. E. Evans, J. R. Johnson, and D.F. Sun. Application of advanced signal processing techniques to angle of arrival estimation in ATC navigation and surveillance systems. Technical report, M.I.T. Lincoln Laboratory, 1982.
- [42] E. Ferrara and T. Parks. Direction finding with an array of antennas having diverse polarizations. *IEEE Trans. Antennas Propag.*, 31(2):231–236, 1983.
- [43] S. Fomel and J. F. Claerbout. Multidimensional recursive filter preconditioning in geophysical estimation problems. *Geophysics*, 68(2):577–588, 2003.
- [44] P. Forster, G. Ginolhac, and M. Boizard. Derivation of the theoretical performance of a Tensor MUSIC Algorithm. *Signal Process.*, 2016.

- [45] B. Friedlander. The root-MUSIC algorithm for direction finding with interpolated arrays. *Signal Process.*, 30(1):15–29, 1993.
- [46] B. Friedlander and A. J. Weiss. Direction finding for wide-band signals using an interpolated array. *IEEE Trans. Signal Process.*, 41(4):1618–1634, 1993.
- [47] O. L. Frost. An algorithm for linearly constrained adaptive array processing. *Proc. IEEE*, 60(8):926–935, 1972.
- [48] G. Garibotto. 2-D recursive phase filters for the solution of two-dimensional wave equations. *IEEE Trans. Acoust., Speech, Signal Process.*, 27(4):367–373, 1979.
- [49] A. Gholamy and V. Kreinovich. Why Ricker wavelets are successful in processing seismic data: Towards a theoretical explanation. In *IEEE Symp. Comput. Intell. Eng. Solut.*, pages 11–16, 2014.
- [50] L. C. Godara. Beamforming in the presence of correlated arrivals using structured correlation matrix. *IEEE Trans. Acoust. Speech and Signal Process.*, 38(1):1–15, 1990.
- [51] L. C. Godara. Application of antenna arrays to mobile communications. II. Beamforming and direction of arrival considerations. *Proc. IEEE*, 85(8):1195–1245, 1997.
- [52] L. C. Godara and M. R. S. Jahromi. Limitations and capabilities of frequency domain broadband constrained beamforming schemes. *IEEE Trans. Signal Process.*, 47(9):2386–2395, 1999.
- [53] G. H. Golub and C. F. Van Loan. *Matrix computations*. The John Hopkins University Press, 1989.
- [54] D. M. Goodman and M. P. Ekstrom. Multidimensional spectral factorization and unilateral autoregressive models. *IEEE Trans. Autom. Control*, 25(2):258–262, 1980.
- [55] J. H. de M. Goulart, M. Boizard, R. Boyer, G. Favier, and P. Comon. Tensor CP decomposition with structured factor matrices: Algorithms and performance. *IEEE J. Sel. Topics Signal Process.*, 10(4):757–769, 2016.
- [56] X. Guo, S. Miron, and D. Brie. The effect of polarization separation on the performance of CANDECOMP/PARAFAC-based vector sensor array processing. *Phys. Comm.*, 5(4):289–295, 2012.
- [57] X. Guo, S. Miron, D. Brie, S. Zhu, and X. Liao. A CANDECOMP/PARAFAC perspective on uniqueness of DoA estimation using a vector sensor array. *IEEE Trans. Signal Process.*, 59(7):3475–3481, 2011.
- [58] M. Haardt. Structured least squares to improve the performance of ESPRIT-type algorithms. *IEEE Trans. Signal Process.*, 45(3):792–799, 1997.
- [59] M. Haardt and J. A. Nossék. Unitary ESPRIT: How to obtain increased estimation accuracy with a reduced computational burden. *IEEE Trans. Signal Process.*, 43(5):1232–1242, 1995.

- [60] M. Haardt and J. A. Nossék. Simultaneous Schur decomposition of several nonsymmetric matrices to achieve automatic pairing in multidimensional harmonic retrieval problems. *IEEE Trans. Signal Process.*, 46(1):161–169, 1998.
- [61] M. Haardt, F. Roemer, and G. Del Galdo. Higher-order SVD-based subspace estimation to improve the parameter estimation accuracy in multidimensional harmonic retrieval problems. *IEEE Trans. Signal Process.*, 56(7):3198–3213, 2008.
- [62] K. Han and A. Nehorai. Nested vector-sensor array processing via tensor modeling. *IEEE Trans. Signal Process.*, 62(10):2542–2553, 2014.
- [63] A. Helmstetter, B. Nicolas, P. Comon, and M. Gay. Basal icequakes recorded beneath an Alpine glacier (Glacier d’Argentière, Mont Blanc, France): evidence for stick-slip motion? *Journal of Geophysical Research: Earth Surface*, 120(3):379–401, March 2015.
- [64] A. Helmstetter, B. Nicolas, P. Comon, and M. Gay. Intermediate-depth icequakes and harmonic tremor in an alpine glacier (Glacier d’Argentière, Mont Blanc, France): evidence for hydraulic fracturing? *Journal of Geophysical Research: Earth Surface*, 120(3):402–416, March 2015.
- [65] A. Hjørungnes and D. Gesbert. Complex-valued matrix differentiation: Techniques and key results. *IEEE Trans. Signal Process.*, 55(6):2740–2746, 2007.
- [66] B. Hochwald and A. Nehorai. Polarimetric modeling and parameter estimation with applications to remote sensing. *IEEE Trans. Signal Process.*, 43(8):1923–1935, 1995.
- [67] P. D. Hoff. Separable covariance arrays via the Tucker product, with applications to multivariate relational data. *Bayesian Analysis*, 6(2):179–196, 2011.
- [68] H. Hung and M. Kaveh. Focussing matrices for coherent signal-subspace processing. *IEEE Trans. Acoust. Speech and Signal Process.*, 36(8):1272–1281, 1988.
- [69] H. Hung and M. Kaveh. Coherent wide-band ESPRIT method for directions-of-arrival estimation of multiple wide-band sources. *IEEE Trans. Acoust. Speech Signal Process.*, 38:354–356, 1990.
- [70] P. Hyberg, M. Jansson, and B. Ottersten. Array interpolation and bias reduction. *IEEE Trans. Signal Process.*, 52(10):2711–2720, 2004.
- [71] P. Hyberg, M. Jansson, and B. Ottersten. Array interpolation and DoA MSE reduction. *IEEE Trans. Signal Process.*, 53(12):4464–4471, 2005.
- [72] B. R. Jackson, S. Rajan, B. J. Liao, and S. Wang. Direction of arrival estimation using directive antennas in uniform circular arrays. *IEEE Trans. Antennas Propag.*, 63(2):736–747, 2015.
- [73] T. Jiang, N. D. Sidiropoulos, and J. M. F. Ten Berge. Almost-sure identifiability of multidimensional harmonic retrieval. *IEEE Trans. Signal Process.*, 49(9):1849–1859, 2001.
- [74] A. Kizilkaya. On the parameter estimation of 2-D moving average random fields. *IEEE Trans. Circuits Syst. II, Exp. Briefs*, 54(11):989–993, 2007.

- [75] T. G. Kolda and B. W. Bader. Tensor decompositions and applications. *SIAM Review*, 51(3):455–500, September 2009.
- [76] N. Kreimer and M. D. Sacchi. A tensor higher-order singular value decomposition for prestack seismic data noise reduction and interpolation. *Geophysics*, 77(3):V113–V122, 2012.
- [77] N. Kreimer and M. D. Sacchi. Nuclear norm minimization and tensor completion in exploration seismology. In *Proc. IEEE Int. Conf. Acoust. Speech Signal Process.*, pages 4275–4279, 2013.
- [78] N. Kreimer, A. Stanton, and M. D. Sacchi. Tensor completion based on nuclear norm minimization for 5D seismic data reconstruction. *Geophysics*, 78(6):V273–V284, 2013.
- [79] H. Krim and M. Viberg. Two decades of array signal processing research: the parametric approach. *IEEE Signal Process. Mag.*, 13(4):67–94, 1996.
- [80] J. Krolik and D. Swingler. Focused wide-band array processing by spatial resampling. *IEEE Trans. Acoust. Speech Signal Process.*, 38(2):356–360, 1990.
- [81] J. B. Kruskal. Three-way arrays: rank and uniqueness of trilinear decompositions, with application to arithmetic complexity and statistics. *Linear algebra and its applications*, 18(2):95–138, 1977.
- [82] J. B. Kruskal. Rank, decomposition, and uniqueness for 3-way and 4-way arrays. *Multway Data Analysis*, 1989.
- [83] J.-L. Lacoume, P.-O. Amblard, and P. Comon. *Statistiques d’ordre supérieur pour le traitement du signal*. Masson, 1997.
- [84] D. Lahat, T. Adali, and C. Jutten. Multimodal data fusion: an overview of methods, challenges, and prospects. *Proc. IEEE*, 103(9):1449–1477, 2015.
- [85] S.E. Leurgans, R.T. Ross, and R.B. Abel. A decomposition for three-way arrays. *J. Matrix Anal. Appl.*, 14(4):1064–1083, 1993.
- [86] J. Li and R.T. Compton Jr. Angle and polarization estimation using ESPRIT with a polarization sensitive array. *IEEE Trans. Antennas Propag.*, 39:1376–1383, 1991.
- [87] L.-H. Lim and P. Comon. Nonnegative approximations of nonnegative tensors. *Journal of Chemometrics*, 23(7-8):432–441, 2009.
- [88] L.-H. Lim and P. Comon. Blind multilinear identification. *IEEE Trans. Inf. Theory*, 60(2):1260–1280, February 2014.
- [89] W. Liu and S. Weiss. *Wideband beamforming: concepts and techniques*, volume 17. John Wiley & Sons, 2010.
- [90] X. Liu and N. D. Sidiropoulos. Cramér-Rao lower bounds for low-rank decomposition of multidimensional arrays. *IEEE Trans. Signal Process.*, 49(9):2074–2086, 2001.

- [91] R. M. Mersereau and D. E. Dudgeon. The representation of two-dimensional sequences as one-dimensional sequences. *IEEE Trans. Acoust. Speech Signal Process.*, 22(5):320–325, 1974.
- [92] S. Miron, N. Le Bihan, and J. I. Mars. Vector-sensor MUSIC for polarized seismic sources localization. *EURASIP J. Advances Signal Process.*, 1:74–84, 2005.
- [93] S. Miron, Y. Song, D. Brie, and K. T. Wong. Multilinear direction finding for sensor-array with multiple scales of invariance. *IEEE Trans. Aerosp. Electron. Syst.*, 51(3):2057–2070, 2015.
- [94] K. Naskovska, A. A. Korobkov, M. Haardt, and J. Haueisen. Analysis of the Photic Driving Effect via joint EEG and MEG data processing based on the Coupled CP decomposition. In *Proc. IEEE European Signal Process. Conf.*, pages 1325–1329, 2017.
- [95] A. Nehorai and E. Paldi. Acoustic vector-sensor array processing. *IEEE Trans. Signal Process.*, 42(9):2481–2491, 1994.
- [96] A. Nehorai and E. Paldi. Vector-sensor array processing for electromagnetic source localization. *IEEE Trans. Signal Process.*, 42(2):376–398, 1994.
- [97] M. Niknazar, H. Becker, B. Rivet, C. Jutten, and P. Comon. Blind source separation of underdetermined mixtures of event-related sources. *Signal Process.*, 101:52–64, August 2014.
- [98] P. J. Ooninex. The discrete wavelet transform as a tool for automatic phase pickers. In *Proc. IEEE-SP Int. Symp. Time-Freq. Time-Scale Anal.*, pages 201–204, 1998.
- [99] A. V. Oppenheim and R. W. Schaffer. From frequency to quefrequency: A history of the cepstrum. *IEEE Signal Process. Mag.*, 21(5):95–106, 2004.
- [100] A. V. Oppenheim, R. W. Schaffer, and J. R. Buck. *Discrete-time signal processing*. Prentice Hall, Inc., New Jersey, 1989.
- [101] A. V. Oppenheim, R. W. Schaffer, and T. G. Stockham. Nonlinear filtering of multiplied and convolved signals. *Proc. IEEE*, 56(8):1264–1291, 1968.
- [102] B. Ottersten and T. Kailath. Direction-of-arrival estimation for wide-band signals using the ESPRIT algorithm. *IEEE Trans. Acoust. Speech Signal Process.*, 38(2):317–327, 1990.
- [103] B. Ottersten, M. Viberg, and T. Kailath. Performance analysis of the total least squares ESPRIT algorithm. *IEEE Trans. Signal Process.*, 39(5):1122–1135, 1991.
- [104] C. F. Pedersen, O. Andersen, and P. Dalsgaard. Separation of mixed phase signals by zeros of the z-transform - A reformulation of complex cepstrum based separation by causality. In *Proc. IEEE Int. Conf. Acoust. Speech Signal Process.*, pages 5050–5053, 2010.
- [105] S.-C. Pei and H.-S. Lin. Two-dimensional partially differential cepstrum and its applications on filter stabilization and phase unwrapping. *IEEE Trans. Circuits Syst. I, Reg. Papers*, 58(4):737–745, 2011.

- [106] A. Pereira da Silva, P. Comon, and A. L. F. de Almeida. A finite algorithm to compute rank-1 tensor approximations. *IEEE Signal Process. Lett.*, 23(7):959–963, 2016.
- [107] M. Pesavento and J.F. Bohme. Direction of arrival estimation in uniform circular arrays composed of directional elements. In *Proc. IEEE Workshop Sensor Array Multichannel Sig. Process.*, pages 503–507, 2002.
- [108] M. Pesavento, A. B. Gershman, and M. Haardt. Unitary root-MUSIC with a real-valued eigendecomposition: A theoretical and experimental performance study. *IEEE Trans. Signal Process.*, 48(5):1306–1314, 2000.
- [109] M. Pesavento, A. B. Gershman, and K. M. Wong. Direction finding in partly calibrated sensor arrays composed of multiple subarrays. *IEEE Trans. Signal Process.*, 50(9):2103–2115, 2002.
- [110] S. U. Pillai and B. H. Kwon. Forward/backward spatial smoothing techniques for coherent signal identification. *IEEE Trans. Acoust. Speech Signal Process.*, 37(1):8–15, 1989.
- [111] E. A. Podolskiy and F. Walter. Cryoseismology. *Reviews of Geophysics*, 54(4):708–758, December 2016.
- [112] D. Rahamim, J. Tabrikian, and R. Shavit. Source localization using vector sensor array in a multipath environment. *IEEE Trans. Signal Process.*, 52(11):3096–3103, 2004.
- [113] T. Rahim and D.E.N. Davies. Effect of directional elements on the directional response of circular antenna arrays. *IEE Proc. H Microw. Optics Antennas*, 129(1):18–22, 1982.
- [114] F. E. D. Raimondi, R. Cabral Farias, O. J. Michel, and P. Comon. Wideband multiple diversity tensor array processing. *IEEE Trans. Signal Process.*, 65(20):5334–5346, 2017.
- [115] F. E. D. Raimondi and P. Comon. Tensor decomposition of polarized seismic waves. In *XXV Colloque GRETSI*, Lyon, France, September 8-11 2015. hal-01164363.
- [116] F. E. D. Raimondi and P. Comon. Tensor DoA estimation with directional elements. *IEEE Signal Process. Letters*, 24(5):648–652, 2017.
- [117] F. E. D. Raimondi, P. Comon, O. Michel, S. Sahnoun, and A. Helmstetter. Tensor decomposition exploiting diversity of propagation velocities: Application to localization of icequake events. *Signal Process.*, 118:75–88, 2016.
- [118] F. E. D. Raimondi, P. Comon, O. J. Michel, and U. Spagnolini. Multidimensional factorization through helical mapping. *Signal Process.*, 131:171–180, feb 2017.
- [119] F. E. D. Raimondi, P. Comon, and O. Michel. Wideband multilinear array processing through tensor decomposition. In *Proc. IEEE Int. Conf. Acoust. Speech Signal Process.*, 2016.

- [120] J. E. Rickett and J. F. Claerbout. Calculation of the sun's acoustic impulse response by multi-dimensional spectral factorization. *Solar Physics*, 192(1-2):203–210, 2000.
- [121] F. Roemer and M. Haardt. A semi-algebraic framework for approximate CP decompositions via simultaneous matrix diagonalizations (SECSI). *Signal Process.*, 93(9):2722–2738, 2013.
- [122] F. Roemer, M. Haardt, and G. Del Galdo. Analytical performance assessment of multi-dimensional matrix-and tensor-based ESPRIT-type algorithms. *IEEE Trans. Signal Process.*, 62(10):2611–2625, 2014.
- [123] S. Rost and C. Thomas. Array seismology: methods and applications. *Reviews of geophysics*, 40(3):2–1, 2002.
- [124] P.-F. Roux. *Méthodes sismologiques pour l'étude de la fracturation dans les glaciers alpins: glaciers d'Argentière et du Gorner*. PhD thesis, Université de Savoie, 2008.
- [125] P.-F. Roux, D. Marsan, J.-P. Métaixian, G. O'Brien, and L. Moreau. Microseismic activity within a serac zone in an alpine glacier (Glacier d'Argentière, Mont Blanc, France). *Journal of Glaciology*, 54(184):157–168, 2008.
- [126] R. Roy and T. Kailath. ESPRIT-estimation of signal parameters via rotational invariance techniques. *IEEE Trans. Acoust. Speech Signal Process.*, 37(7):984–995, 1989.
- [127] M. D. Sacchi, J. Gao, A. Stanton, and J. Cheng. Tensor factorization and its application to multidimensional seismic data recovery. In *Technical Program Expanded Abstracts*, pages 4827–4831. Society of Exploration Geophysicists, 2015.
- [128] S. Sahnoun and P. Comon. Joint source estimation and localization. *IEEE Trans. Signal Process.*, 63(10):2485–2495, 2015.
- [129] S. Sahnoun, E.-H. Djermoune, D. Brie, and P. Comon. A simultaneous sparse approximation method for multidimensional harmonic retrieval. *Signal Process.*, 131:36–48, 2017.
- [130] S. Sarpal and E. Chilton. ARMA modelling based on root cepstral deconvolution. In *Proc. IEEE Int. Conf. Digit. Signal Process.*, volume 2, pages 745–748, 2002.
- [131] R. O. Schmidt. Multiple emitter location and signal parameter estimation. *IEEE Trans. Antennas Propag.*, 34(3):276–280, 1986.
- [132] T.-J. Shan, M. Wax, and T. Kailath. On spatial smoothing for direction-of-arrival estimation of coherent signals. *IEEE Trans. Acoust. Speech Signal Process.*, 33(4):806–811, 1985.
- [133] R. E. Sheriff and L. P. Geldart. *Exploration seismology. Volume 1: History, theory, and data acquisition*. Cambridge University Press, New York, NY, 1983.
- [134] R. E. Sheriff and L. P. Geldart. *Exploration seismology*. Cambridge University Press, New York, NY, 1995.
- [135] N. D Sidiropoulos and R. Bro. On the uniqueness of multilinear decomposition of N-way arrays. *Journal of Chemometrics*, 14(3):229–239, 2000.

- [136] N. D. Sidiropoulos, R. Bro, and G. B. Giannakis. Parallel factor analysis in sensor array processing. *IEEE Trans. Signal Process.*, 48(8):2377–2388, August 2000.
- [137] N. D. Sidiropoulos and X. Liu. Identifiability conditions for deterministic blind beamforming in the presence of incoherent multipath with small delay spread. In *Proc. IEEE European Signal Process. Conf.*, pages 1–4, 2000.
- [138] Stanford-Lockheed Institute for Space Research. *The Solar Oscillations Investigation project / The Michelson Doppler Imager*.
- [139] K. Steiglitz and B. Dickinson. Computation of the complex cepstrum by factorization of the z-transform. In *Proc. IEEE Int. Conf. Acoust. Speech Signal Process.*, volume 2, pages 723–726, 1977.
- [140] P. Stoica and A. Nehorai. MUSIC, maximum likelihood, and Cramér-Rao bound. *IEEE Trans. Acoust. Speech Signal Process.*, 37(5):720–741, 1989.
- [141] P. Stoica and A. Nehorai. MUSIC, maximum likelihood, and Cramer-Rao bound: further results and comparisons. *IEEE Trans. Acoust. Speech Signal Process.*, 38(12):2140–2150, 1990.
- [142] A. L. Swindlehurst, B. Ottersten, R. Roy, and T. Kailath. Multiple invariance ESPRIT. *IEEE Trans. Signal Process.*, 40(4):867–881, 1992.
- [143] A. K. Takahata, E. Z. Nadalin, R. Ferrari, L. T. Duarte, R. Suyama, R. R. Lopes, J. M. T. Romano, and M. Tygel. Unsupervised processing of geophysical signals: A review of some key aspects of blind deconvolution and blind source separation. *IEEE Signal Process. Mag.*, 29(4):27–35, 2012.
- [144] K.-C. Tan, K.-C. Ho, and A. Nehorai. Linear independence of steering vectors of an electromagnetic vector sensor. *IEEE Trans. Signal Process.*, 44(12):3099–3107, 1996.
- [145] K.-C. Tan, K.-C. Ho, and A. Nehorai. Uniqueness study of measurements obtainable with arrays of electromagnetic vector sensors. *IEEE Trans. Signal Process.*, 44(4):1036–1039, 1996.
- [146] T. Taxt and G. V. Frolova. Noise robust one-dimensional blind deconvolution of medical ultrasound images. *IEEE Trans. Ultrason. Ferroelect. Freq. Control*, 46(2):291–299, 1999.
- [147] T. Taxt and J. Strand. Two-dimensional noise-robust blind deconvolution of ultrasound images. *IEEE Trans. Ultrason. Ferroelect. Freq. Control*, 48(4):861–866, 2001.
- [148] A. Thakre, M. Haardt, F. Roemer, and K. Giridhar. Tensor-based spatial smoothing (TB-SS) using multiple snapshots. *IEEE Trans. Signal Process.*, 58(5):2715–2728, 2010.
- [149] P. Tichavsky, A. H. Phan, and Z. Koldovsky. Cramér-Rao-induced bounds for CANDECAMP/PARAFAC tensor decomposition. *IEEE Trans. Signal Process.*, 61(8):1986–1997, 2013.

- [150] M. Vallon. *Contribution à l'étude de la Mer de Glace - Alpes françaises*. PhD thesis, Faculté des Sciences de l'Université de Grenoble, May 1967.
- [151] H. L. Van Trees. *Detection, estimation, and modulation theory, optimum array processing*. John Wiley & Sons, 2004.
- [152] B. D. Van Veen and K. M. Buckley. Beamforming: A versatile approach to spatial filtering. *IEEE Acoust. Speech Signal Process. Mag.*, 5(2):4–24, 1988.
- [153] M. Viberg and B. Ottersten. Sensor array processing based on subspace fitting. *IEEE Trans. Signal Process.*, 39(5):1110–1121, 1991.
- [154] V. Vigneron, A. Kodewitz, M. N. da Costa, A. M. Tome, and E. Langlang. Non-negative sub-tensor ensemble factorization (NsTEF) algorithm. A new incremental tensor factorization for large data sets. *Signal Processing*, 144:77–86, 2018.
- [155] C. Vincent, A. Soruco, D. Six, and E. Le Meur. Glacier thickening and decay analysis from 50 years of glaciological observations performed on Glacier d'Argentière, Mont Blanc area, France. *Annals of glaciology*, 50(50):73–79, 2009.
- [156] F. Walter, N. Deichmann, and M. Funk. Basal icequakes during changing sub-glacial water pressures beneath Gornergletscher, Switzerland. *Journal of Glaciology*, 54(186):511–521, 2008.
- [157] H. Wang and M. Kaveh. Coherent signal-subspace processing for the detection and estimation of angles of arrival of multiple wide-band sources. *IEEE Trans. Acoust. Speech Signal Process.*, 33(4):823–831, 1985.
- [158] A. J. Weiss and B. Friedlander. Performance analysis of spatial smoothing with interpolated arrays. *IEEE Trans. Signal Process.*, 41(5):1881–1892, 1993.
- [159] K. T. Wong and M. D. Zoltowski. Uni-vector-sensor ESPRIT for multisource azimuth, elevation, and polarization estimation. *IEEE Trans. Antennas Propag.*, 45(10):1467–1474, 1997.
- [160] K. T. Wong and M. D. Zoltowski. Self-initiating MUSIC-based direction finding and polarization estimation in spatio-polarizational beamspace. *IEEE Trans. Antennas Propag.*, 48(8):1235–1245, 2000.
- [161] Y. I. Wu, K. Thomas Wong, and S.-K. Lau. The acoustic vector-sensor's near-field array-manifold. *IEEE Trans. Signal Process.*, 58(7):3946–3951, 2010.
- [162] Y.-H. Yang and J.-H. Lee. Design of 2-D recursive digital filters using nonsymmetric half-plane allpass filters. *IEEE Trans. Signal Process.*, 55(12):5604–5618, 2007.
- [163] J. Zhang, I. Podkurkov, M. Haardt, and A. Nadeev. Efficient multidimensional parameter estimation for joint wideband radar and communication systems based on OFDM. In *Proc. IEEE Int. Conf. Acoust. Speech Signal Process.*, 2017.
- [164] M. D. Zoltowski, M. Haardt, and C. P. Mathews. Closed-form 2-D angle estimation with rectangular arrays in element space or beamspace via unitary ESPRIT. *IEEE Trans. Signal Process.*, 44(2):316–328, 1996.



# Index

- Alignment
  - Seismic Waveform, 159
- ALSCOLOR, 112
- Beamforming, 33
- Cepstrum
  - 1D, 177
  - 2D, dD, 178
- Coherence
  - Constraint, 67
  - Polarization, 92
  - Space Shift, 77
- Coherences
  - Gain patterns, 98
- Coherent Sources, 18, 46
  - CPD
    - Polarization, 92
    - Space Shift, 76
- Complex Derivative, 127
- Complex Envelope, 30
- Contraction, 53
- Correlated Noise, 45
  - Tensor, 109
- Correlated Sources, 18, 46
- CPD
  - Definition, 56
  - Indeterminacies, 58
  - Uniqueness, 59
- Cramér-Rao Bounds, 31
  - Tensor, 125
- Direction of Arrival, 13
  - Azimuth, 15
  - Elevation, 15
- Diversity
  - Frequency
    - Polarization, 105
    - Space Shift, 104
  - Gain Patterns, 96
  - Multiple, 85
  - Wideband, 106
  - Polarization, 90
  - Propagation Speed, 151
  - Repetition, 165
  - Space Shift, 72
- DoA Estimation
  - 1D, 80
  - 2D, 79
  - 3D, 79
  - Main Approaches, 33
  - Tensor
    - Gain Patterns, 98
    - Polarization, 92
    - Space Shift, 78
- ESPRIT, 37
- Estimation
  - Performance, 31
- Exact Decomposition, 63
- Far Field, 12
- Fisher Information Matrix, 32
  - Tensor, 126
- Gain Patterns, 96
- Harmonic Retrieval, 71
- Helical Transform, 176
  - Multidimensional Factorization, 181
  - Wavefield Propagation, 185
- Helioseismology, 186
- HOSVD, 56
- Icequake, 160
- Identifiability
  - Space Shift, 74
- Likelihood, 32
- Log-Likelihood, 32
  - Tensor, 125
- Mean Square Error, 32
- Multilinear Product, 54

- Multilinear Rank, 55
- MUSIC, 35
  - Long Vector, 88
  - Polarization, 88
  - Tensor, 89
- Narrowband
  - Definition, 13
  - Propagation Model, 12
  - Shift Invariance, 72
- Non Symmetric Half Plane, 179
- Parameter Estimation
  - Definition, 28
  - Tensor
    - Gain Patterns, 98
    - Polarization, 92
    - Propagation Speed, 153
    - Space Shift, 78, 81
    - Wideband, 113
  - Wideband
    - ULA, 139
- Polarization
  - Definition, 20
  - Ellipticity Angle, 20
  - Orientation Angle, 20
  - Signal Subspace, 41
  - Tensor
    - Estimation, 92
  - Tensors, 90
  - Wideband, 25
- Reshaping, 52
- Scaling Indeterminacies
  - Frequency, 110
  - Gain Patterns, 96
  - Polarization, 91
  - Space Shift, 73
- Seismic Waves, 26
  - P Waves, 22, 27
  - Rayleigh Waves, 22, 27
  - S Waves, 27
- Sensor Arrays
  - Array Manifold, 19
  - Model, 15
  - Uniform Circular Arrays, 17
  - Uniform Linear Arrays, 16
  - Uniform Rectangular Arrays, 17
  - Vector Sensor Arrays, 22
- Signal Copy
  - ESPRIT, 40
  - Tensors, 81
- Signal Subspace
  - Assumptions, 18
  - Definition, 18
  - Multidimensional, 71
- Signal to Noise Ratio
  - Definition, 33
- Sinc Interpolation, 148
- Spatial Covariance
  - Definition, 19
  - Estimation, 29
- Spatial Smoothing, 46
- Spectral Factorization
  - 1D, 177
  - Multidimensional, 178
- Sunquake, 186
- Tensor Approximation
  - Algorithms, 66
  - ALS for Correlated Noise, 112
  - Alternating Least Squares, 66
  - Correlated Noise, 111
  - Definition, 64
  - Existence, 65
- Tensor Product, 53
- Tensors
  - Advantages
    - General, 61
    - Sensor Arrays, 81
  - Decomposable, 54
  - Definition, 49
  - Fibers, 52
  - Normal Distributions, 61
  - Notations, 50
  - Operations, 53
  - Slices, 52
  - Tensor Norm, 52
  - Tensor Rank, 55
  - Unfolding, 52
- Tucker Decomposition, 55
- Vectorization, 53
  - Kronecker Product, 53
- White Noise, 18
- Wideband
  - Bilinear Interpolation, 107

- Polarization, 110
- Bilinear Interpolation
  - Space Shift, 109
- Coherent Signal Subspace, 41
- Definition, 24
- Linear Interpolation, 43
- Multiple Diversities, 106
- Polarization, 25, 45, 105
- Regular Arrays, 137
  - Tensor Resampling, 138
- Resampling, 44
  - Space Shift, 104
    - Regular Arrays, 133
    - Tensor Resampling, 137
- Virtual Arrays, 42
- Virtual Subarrays, 107